

2023

Structural analysis and design of semi-submersible platform for floating offshore wind turbines

Ye, Qi

<https://pearl.plymouth.ac.uk/handle/10026.1/21440>

<http://dx.doi.org/10.24382/5098>

University of Plymouth

All content in PEARL is protected by copyright law. Author manuscripts are made available in accordance with publisher policies. Please cite only the published version using the details provided on the item record or document. In the absence of an open licence (e.g. Creative Commons), permissions for further reuse of content should be sought from the publisher or author.

This copy of the thesis has been supplied on condition that anyone who consults it is understood to recognise that its copyright rests with its author and that no quotation from the thesis and no information derived from it may be published without the author's prior consent.



**UNIVERSITY OF
PLYMOUTH**

**STRUCTURAL ANALYSIS AND DESIGN OF SEMI-SUBMERSIBLE PLATFORM
FOR FLOATING OFFSHORE WIND TURBINES**

by

QI YE

A thesis submitted to the University of Plymouth
in partial fulfilment for the degree of

DOCTOR OF PHILOSOPHY

School of Engineering, Computing and Mathematics

August 2023

ABSTRACT

Structural analysis and design of semi-submersible platform for floating offshore wind turbines

Qi Ye

To solve the issues of energy shortages and environmental pollution, renewable energy is increasingly exploited. As one of the most promising new energy resources, wind energy is actively developed and utilized around the world. To increase the use of offshore wind, there is a need to develop floating platforms to support wind turbines in deep water. However, the cost of floating platform needs to be reduced sharply to be competitive with the traditional energy sources and fixed wind turbines. Moreover, the design code for floating wind turbines (FWTs) is primarily based on offshore ships, oil & gas industry, which still needs to be assessed and evaluated. To both ensure the safety and avoid overdesign of offshore wind, the structural behaviour and the evaluation of the design guideline of FWTs need to be studied. Because of the combined actions of the aerodynamic load, hydrodynamic load and tension of mooring lines, the structural behaviour of a FWT becomes extremely complicated in the marine environment. Previous studies for FWTs mainly focused on the dynamic response due to the environmental load, while the structural performance has not been well addressed. In this context, the aim of this thesis is to improve understanding of the nonlinear structural behaviour of a semi-submersible platform for FWTs, and compare and evaluate the relevant design codes.

Firstly, the structural behaviour of a semi-submersible platform (SSP) for an offshore wind turbine is studied. A novel one-way coupled fluid structure interaction simulation that combines hydrodynamic and structural analysis is undertaken, with a focus on structural nonlinearity – especially the geometrical nonlinearity. The analysis is divided into four steps. First, the hydrodynamic response is simulated in the frequency domain using ANSYS AQWA to generate the wave pressures acting on the floating platform. Second, the wave pressures are transferred from ANSYS AQWA to ANSYS Mechanical

to study the structural performance. Third, linear elastic analysis is carried out to identify the critical load cases. Finally, geometrically and materially nonlinear analysis is adopted to investigate the failure modes and corresponding critical failure locations in comparison with the linear elastic analysis. The effects of azimuthal angles of environmental loads, wave-wind misalignment and boundary conditions on the overall structural performance are also investigated.

Secondly, the structural design of the main component of a floating platform for a FWT are carried out by hand calculations based on the worst load case from the global structural analysis. The prevailing design guidelines, the DNVGL (Det Norske Veritas and Germanischer Lloyd), and two versions of EN1993-1-6 (2007 and the latest, 2017) have been adopted for carrying out the structural design. The design process of a shell structure based on the three codes is presented in detail. The unstiffened and stiffened cylindrical shells are designed separately, and a cost-effective design for stiffened cylindrical shell is proposed to reduce the levelized cost of energy.

Lastly, but not least, the buckling behaviour and ultimate strength of cylindrical shells under combined axial compression and bending are investigated by means of the finite element method (FEM), in conjunction with the design codes for reference. Starting from the geometry of the main component of a floating platform, a series of FE models considering geometrical and material nonlinearities with a wide geometric range and different types of initial geometric imperfections are simulated. The effects of geometric imperfection profiles and amplitudes on the ultimate strength of the unstiffened cylindrical shells are examined. The typical buckling modes due to the different initial imperfections are discussed. Moreover, a stiffened cylinder is proposed as a case study and compared with an unstiffened cylinder in respect of buckling behaviour and effects of initial imperfections. The accuracy of three design codes for plain shell structures, the DNVGL and EN1993-1-6 (2007 and 2017 versions), are evaluated using the FEM results. Then, a reliability analysis is adopted to propose modified partial safety factors γ_M to ensure that these design codes possess the required level of safety for offshore structures.

Keywords: aerodynamic load; buckling resistance; design guideline; finite element method; floating platform; hydrodynamic load; imperfection; nonlinear analysis; offshore wind; reliability; shell structure; structural behaviour; ultimate strength.

ACKNOWLEDGMENT

I would like to express my sincere thanks to my director of studies, Dr Shanshan Cheng, who gives me the precious chance to study for a doctorate and provides invaluable advice and support during my PhD study. Her precise attitude and immense knowledge encourage me in my academic research. I would like to acknowledge my other supervisors, Prof. Gregorio Iglesias, Dr Keri Collins and Dr Boksun Kim, for their kind help and support. I appreciate all of them being my supervisors.

Many thanks to my friends especially to Dr Nanting Yu, Dr Daming Wang, Dr Qinwei Ding and Dr Chenyu Zhao for their support and encouragement during my PhD study.

Thanks also to the University of Plymouth and China Scholarship Council (CSC) for providing me the scholarships and financial support for my PhD study in Plymouth.

Finally, I am deeply grateful to my family, especially to my father, mother and grandma for their unconditional love and support. I will be your firm support soon.


AUTHOR'S DECLARATION

At no time during the registration for the degree of Doctor of Philosophy has the author been registered for any other University award without prior agreement of the Doctoral College Quality Sub-Committee.

Work submitted for this research degree at the University of Plymouth has not formed part of any other degree either at University of Plymouth or at another establishment.

This PhD study was financed with the aid of School of Engineering, Computing and Mathematics, University of Plymouth, and China Scholarship Council for the UK PhD scholarship.

Word count of main body of thesis: 40,851

Signed:  _

Date: 15 August 2023

CONTENTS

ABSTRACT.....	5
ACKNOWLEDGMENT.....	8
AUTHOR’S DECLARATION.....	10
CONTENTS.....	12
LIST OF FIGURES.....	16
LIST OF TABLES.....	22
NOMENCLATURE.....	24
CHAPTER 1 – Introduction.....	28
1.1 Introduction to offshore wind turbines.....	28
1.1.1 Bottom-fixed wind turbines.....	29
1.1.2 Floating wind turbines (FWTs).....	34
1.2 Classification of FWTs.....	36
1.2.1 Spar-buoys.....	38
1.2.2 Tensioned-leg platforms.....	40
1.2.3 Semi-submersible platforms.....	42
1.3 Research scope and objectives.....	45
1.4 Outline of the thesis.....	47
CHAPTER 2 – Literature Review.....	50
2.1 Modelling of environmental forces for offshore structures.....	50
2.1.1 Numerical modelling of environmental forces.....	50
2.1.2 Experimental study under environmental forces.....	60

2.2	Global structural analysis of offshore structures.....	66
2.2.1	Optimization design and strength analysis.....	66
2.2.2	Design codes of environmental loads for offshore structure	70
2.3	Failure mechanism of components in offshore wind industry	71
2.3.1	Ultimate strength and buckling of offshore structures.....	71
2.3.2	Fatigue study of offshore structures.....	76
2.3.3	Design codes of structural design for offshore structure	78
2.4	Research gaps.....	83
2.5	Methodology	85
CHAPTER 3 – Nonlinear Structural Analysis of a Floating Wind Platform.....		87
3.1	Research object	87
3.2	Materials and Methods.....	89
3.2.1	Environmental loads.....	89
3.2.2	Case studies of global model.....	94
3.2.3	Numerical modelling using ANSYS.....	96
3.3	Results.....	112
3.3.1	Equivalent static structural analysis.....	112
3.3.2	Geometrically and materially nonlinear analysis (GMNA).....	121
3.4	Discussion	133
3.5	Conclusions.....	135
CHAPTER 4 – Code-based Cylindrical Shell Design Comparison.....		137
4.1	Problem Definition.....	137
4.1.1	Objectives.....	138

4.2	Obtainment of design loads.....	138
4.3	Unstiffened shell structure design.....	140
4.4	Stiffened shell structure design	141
4.4.1	DNVGL-RP-C202	141
4.4.2	EN1993-1-6 (2007) & (2017)	145
4.5	Conclusions.....	147
CHAPTER 5 – Ultimate Strength of Unstiffened Cylindrical Shell Under Combined		
Compression and Bending		
		149
5.1	Code-based approach	149
5.1.1	Tolerances of initial geometric imperfection	150
5.2	Description of the numerical model.....	152
5.2.1	Material properties	152
5.2.2	Geometric imperfection	152
5.3	Finite element modelling	153
5.3.1	Case study of a FE model	154
5.3.2	Test matrix	156
5.3.3	Mesh convergence study.....	158
5.3.4	Validation of the model.....	159
5.4	Results and discussion of unstiffened cylindrical shells.....	163
5.4.1	Effect of imperfection profiles	163
5.4.2	Effect of imperfection amplitudes.....	164
5.4.3	Comparison between design codes	167
5.4.4	Failure modes of cylindrical shells	174

5.5	Reliability analysis	180
5.6	Case study of stiffened cylindrical shells.....	187
5.6.1	Axial compression capacity	188
5.6.2	Effect of imperfection amplitudes.....	190
5.7	Conclusions	191
CHAPTER 6	Conclusions and Future Works	194
6.1	Summary of contributions.....	194
6.2	Summary of findings.....	195
6.3	Future works	197
APPENDIX A	Introduction of Design Codes for Shell Structure.....	199
A.1	Unstiffened shell structure design.....	199
A.1.1	DNVGL-RP-C202	199
A.1.2	EN1993-1-6 (2007)	201
A.1.3	EN1993-1-6 (2017)	207
A.2	Stiffened shell structure design	208
A.2.1	DNVGL-RP-C202	208
A.2.2	EN1993-1-6 (2007) & (2017)	211
APPENDIX B	Spreadsheet for Shell Structure Design.....	212
REFERENCE	267
PUBLICATIONS	285

LIST OF FIGURES

Figure 1.1 Typical bottom-fixed offshore foundation (Ding, 2019).....	29
Figure 1.2 Typical floating offshore foundation (Ding, 2019)	29
Figure 1.3 Geometry of (a) tripod, (b) jacket and (c) monopile (Hao and Liu, 2017)....	32
Figure 1.4 Suction bucket foundation for OWTs (Gao et al., 2021).....	34
Figure 1.5 Deep Water Offshore Platforms for Oil and Gas Exploration (a) & (b) tension leg platform, (c) taut-moored spar, (d) & (e) catenary-moored semi-submersible (Shukla and Karki, 2016)	37
Figure 1.6 Draft for a multiple-array wind turbine structure (Heronemus, 1972)	37
Figure 1.7 Hywind (Muliawan et al., 2013).....	38
Figure 1.8 Hybrid (Rhodri James, 2015)	39
Figure 1.9 Advanced Spar (Edwards et al., 2023, Ishihara, 2016)	39
Figure 1.10 Blue H TLP (EWEA, 2013)	40
Figure 1.11 GICON TLP: (a) Initial concept of the platform (Adam et al., 2015), (b) Latest concept of the platform (Rhodri James, 2015), (c) Experimental model (Walia et al., 2021)	41
Figure 1.12 Glosten PelaStar(Park et al., 2016).....	42
Figure 1.13 WindFloat (Rhodri James, 2015).....	43
Figure 1.14 IDEOL platform (EWEA, 2013)	43
Figure 1.15 Compact Semi-Sub (Rhodri James, 2015)	44
Figure 1.16 V-Shape Semi-Sub (Rhodri James, 2015).....	45
Figure 1.17 Study process of this PhD thesis.....	47
Figure 2.1 The semi-submersible VAWT (Liu et al., 2018).....	53
Figure 2.2 Abbreviations for members of DeepCwind (Lee et al., 2020)	54
Figure 2.3 Perspective view of the semi-submersible platform (Ding et al., 2020)	61
Figure 2.4 Experimental model (1:15 scale) of a jacket-type foundation (Liu et al., 2014)	61
Figure 2.5 The 1:37 scaled TLP platform (Adam et al., 2014).....	62

Figure 2.6 Model with reinforced heave plate (left), with solid plain one (middle) and sketch of entire FWT (right)	63
Figure 2.7 Tri-floater platform provided by Lefebvre and Collu (2012).....	68
Figure 2.8 Four imperfection profiles from Kumar Yadav and Gerasimidis (2019).....	73
Figure 2.9 Loading conditions in the experiments (Evkin et al., 2019).....	74
Figure 2.10 Comparison of Equation (2.1) and experimental results (Jawad, 2004).....	79
Figure 2.11 Shell buckling reduction factor curves for axial compression, external pressure and torsion in different design codes (Winterstetter and Schmidt, 2002)	80
Figure 2.12 Buckling reduction factor curves for axial compression based on EN1993-1-6 (2017) and EN1993-1-1 (2005).....	83
Figure 2.13 Circular hollow tubular section classification in (EN1993-1-1, 2005).....	83
Figure 3.1 WindFloat concept: (a) floating wind turbine, (b) platform shown without the external columns, (c) section A.....	88
Figure 3.2 Wave and wind acting on the WindFloat	89
Figure 3.3 Thrust of a fixed NREL 5 MW wind turbine simulated with various methods (Dong et al., 2019)	93
Figure 3.4 Gravitational and inertial forces on a rotor.....	93
Figure 3.5 Wave and wind directions	95
Figure 3.6 Positions of connections: (a) components numbers, (b) connections numbers	96
Figure 3.7 Hydrodynamic model of the WindFloat floating platform.....	97
Figure 3.8 The speed of wind of LC21	99
Figure 3.9 The speed of wind of LC26	99
Figure 3.10 The rotor thrust of LC21 and LC26.....	100
Figure 3.11 3D structural model of the platform implemented in ANSYS (with mesh)	101
Figure 3.12 Stress-strain curve of S355	102
Figure 3.13 Mesh convergence of structural model.....	103

Figure 3.14 Comparison of the maximum equivalent stresses of the connections with and without considering inertia force in LC21-25.....	104
Figure 3.15 Comparison of the maximum equivalent stresses of the connections with and without considering inertia force in LC26-30.....	105
Figure 3.16 Comparison of the maximum equivalent stress of connections using different supports (LC27)	106
Figure 3.17 Load mapping process	107
Figure 3.18 Load mapping from hydrodynamic mesh to structural mesh	108
Figure 3.19 Hydrodynamic pressure profile of (a) hydrodynamic model and (b) structural model under a regular wave of height $H = 3$ m, period $T = 8$ s, and direction: 0° ; wave phase: 0°	109
Figure 3.20 RAO in (a) surge, (b) heave and (c) pitch at wave direction 0° without wind	112
Figure 3.21 Individual effect of wave and wind on the maximum equivalent stress of connections.....	114
Figure 3.22 Individual effects of wave and wind on the maximum equivalent stress of connections.....	117
Figure 3.23 The maximum equivalent stress of connections in moderate conditions (LC21-25).....	119
Figure 3.24 The maximum equivalent stress of connections in rated conditions (LC26-30)	119
Figure 3.25 The maximum equivalent stress of P3R in rated conditions subjected to misaligned wave and wind.....	120
Figure 3.26 Stress contour of the platform in LC27, wave 45° +wind 45° (shown without external columns and heave plates) (Unit: Pa).....	124
Figure 3.27 Stress contour of connections (Unit: Pa)	126
Figure 3.28 Stress performance of components (LC27)	128
Figure 3.29 Displacement and deformation performance of components (LC27)	130
Figure 3.30 Deformation comparison of the floating platform (scaled by 20 times) ...	130

Figure 3.31 The maximum stress of ICs and ECs in LC12 (wave only)	132
Figure 3.32 The maximum stress of ICs and ECs in LC27 (wave and wind alignment)	132
Figure 3.33 The maximum stress of ICs (left) and ECs (right)	133
Figure 4.1 Edge section of external and internal columns	139
Figure 4.2 Fillet weld	142
Figure 4.3 Geometries of (a) external column Case 1, (b) external column Case 2, (c) internal column Case 1 and (d) internal column Case 2	144
Figure 4.4 Geometries of (a) external column, (b) internal column based on EN1993-1-6 (2017).....	146
Figure 5.1 Definition of (a) δ and g , (b) s , l and r (DNVGL, 2020)	150
Figure 5.2 Gauge length l_g measured on (a) meridian and (b) circumferential circle (EN1993-1-6, 2017)	151
Figure 5.3 Imperfection profiles subjected to (a) axial compression load, (b) lateral pressure, (c) bending moment and (d) lateral point load (amplified by 50 times).....	153
Figure 5.4 Boundary condition and loading mode.....	154
Figure 5.5 Sketch of WindFloat platform shown in beam element	155
Figure 5.6 Results of mesh convergence study	159
Figure 5.7 Test arrangement for cylinder provided by Ifayefunmi (2016)	161
Figure 5.8 Load-displacement curves of the present model and existing studies.....	162
Figure 5.9 Ultimate capacity of cylinders under combined compression and bending moment.....	164
Figure 5.10 Comparison of the buckling resistance of cylinders under different imperfection amplitudes.....	166
Figure 5.11 Ratio of the buckling strength between small imperfection amplitude and large imperfection amplitude	167
Figure 5.12 Buckling capacity of FEA results versus characteristic buckling capacity of (a) DNVGL (b) EN1993-1-6 (2007) (c) EN1993-1-6 (2017) subjected to eccentric compression (red and green data point obtained from Group A and B)	171

Figure 5.13 Comparison of M-N curve under different design guideline (DG-DNVGL, EC07- EN1993-1-6 (2007), EC17- EN1993-1-6 (2017), S-Short cylinder, M-Medium cylinder, L-Long cylinder).....	172
Figure 5.14 Value of F_{FE}/F_{ksd} based on (a) DNVGL (b) EN1993-1-6 (2007) (c) EN1993-1-6 (2017).....	173
Figure 5.15 Failure modes of Series 1 (deformation is amplified by 50 times)	175
Figure 5.16 Failure modes of Series 2 (deformation is amplified by 50 times)	176
Figure 5.17 Load-displacement curve for unstiffened shell with different imperfection amplitude.....	177
Figure 5.18 Strain-displacement curve for unstiffened shell $L/r = 5.4$ and $r/t = 100$ with different imperfection profiles and amplitudes (Series 1 & 2)	179
Figure 5.19 Partial safety factor-load ratio curves for (a) DNVGL (b) EN1993-1-6 (2007) (c) EN1993-1-6 (2017).....	185
Figure 5.20 Value of F_{FE}/F_{ksd} based on (a) DNVGL (b) EN1993-1-6 (2007) (c) EN1993-1-6 (2017) using revised γ_M	187
Figure 5.21 Comparison of F_{FE}/F_{ks} and F_{FE}/F_{ksd} between the stiffened and unstiffened shells.....	189
Figure 5.22 Load-displacement curve for stiffened shell with different imperfection amplitudes	190
Figure 5.23 Strain-displacement curve for stiffened shell with different imperfection amplitudes	191
Figure 7.1 Flowchart of shell buckling calculation according to DNVGL (Ye et al., 2019)	200
Figure 7.2 Buckling modes of (a) meridional buckling, (b) circumferential buckling, (c) Shear buckling obtained from FEA	202
Figure 7.3 Flowchart of meridional buckling calculation according to EN1993-1-6 (2007)	202
Figure 7.4 Flowchart of circumferential buckling calculation according to EN1993-1-6 (2007).....	204

Figure 7.5 Flowchart of shear buckling calculation according to EN1993-1-6 (2007)	206
Figure 7.6 Flowchart for buckling interaction checking according to EN1993-1-6 (2007)	
.....	207
Figure 7.7 Stiffened cylindrical shell (DNVGL-RP-C202, 2019)	209
Figure 7.8 Buckling modes of (a) shell buckling, b) panel stiffener buckling, c) panel ring buckling, d) general buckling, e) column buckling (DNVGL-RP-C202, 2019)	209
Figure 7.9 Flowchart of panel stiffener buckling calculation according to DNVGL	210
Figure 7.10 Flowchart of panel ring buckling calculation according to DNVGL	211

LIST OF TABLES

Table 1.1 General geometries of tripod, jacket and monopile foundation (Hao and Liu, 2017)	31
Table 2.1 Summary of experimental tests of FWT	64
Table 2.2 Types of boundary conditions (Evkin et al., 2019).....	74
Table 2.3 Summary of structural design standards for substructure of OWT	81
Table 3.1 WindFloat main dimensions (unit: m)	88
Table 3.2 5 MW turbine characteristics (Roddir et al., 2010a).....	88
Table 3.3 40 Load cases definition	95
Table 3.4 Dynamic Characteristics of the WindFloat in Heave, Roll and Pitch.....	98
Table 3.5 Dynamic Characteristics of the WindFloat in Surge, Sway and Yaw	98
Table 3.6 Material parameters of the platform	101
Table 3.7 Stiffness of spring for the mooring lines.....	105
Table 3.8 Summary of maximum stress of the eight connections under various directions of wave and wind	117
Table 3.9 Comparison of the maximum stress between misaligned and aligned wave-wind	120
Table 3.10 Thickness of the main components of the floating platform (mm)	122
Table 3.11 The critical connections in LC26-30.....	124
Table 4.1 Environmental condition of LC27	138
Table 4.2 Design loads for external and internal columns.....	140
Table 4.3 Design results of external and internal columns (Unit: mm).....	140
Table 4.4 Costs considered in the fabrication analysis (Quintana, 2016, Shen et al., 2010, Li et al., 2017).....	142
Table 4.5 Optimised results of the structural dimensions (unit: mm).....	143
Table 4.6 Costs considered in the fabrication analysis (unit: €)	145
Table 4.7 Structural dimensions of stiffened shell (unit: mm)	146

Table 5.1 Recommended values for dimple imperfection amplitude parameters U_{n1} and U_{n2}	151
Table 5.2 Summary of internal forces and stresses of IC1	156
Table 5.3 Geometrical properties of Group A	157
Table 5.4 Geometrical properties of Group B.....	157
Table 5.5 Geometries of validation model (Li et al., 2017, Ifayefunmi, 2016, Wang et al., 2019)	160
Table 5.6 Comparison of ANSYS predictions with the existing experimental and numerical predictions	163
Table 5.7 Statistical properties of design variables.....	181
Table 5.8 Summary of reliability analysis results (note that the values in parentheses represent the original partial safety factor)	185
Table 5.9 Structural scantlings of the stiffened cylindrical shell (unit: mm).....	188
Table 5.10 Comparison of standard deviation, mean and COV for Figure 5.17	189
Table A.1 Elastic critical circumferential buckling stress	203
Table A.2 Factor $C\tau$	205

NOMENCLATURE

CFD	computational fluid dynamics
FEA	finite element analysis
FEM	finite element method
FWT	floating wind turbine
HAWT	horizontal axis wind turbine
OWT	offshore wind turbine
SSP	semi-submersible platform
TLP	tension leg platform
VAWT	vertical axis wind turbine
A_R	cross sectional area
b_{eff}	effective breadth (stringer)
b_f	geometric proportions requirement (flange)
b_f	geometric proportions requirement (flange)
b_r	ring flange width
b_s	stringer flange width
C	reduced buckling coefficient
C_θ	circumferential buckling factor
C_τ	shear buckling factor
E	Young's modulus
f_{akd}	design local buckling strength
f_E	elastic buckling strength
f_{E1}	Euler buckling strength
f_{E2}	Euler buckling strength
f_{Ea}	elastic buckling strength for axial force
f_{Eh}	elastic buckling strength for hydrostatic pressure, lateral pressure and circumferential compression
f_{Em}	elastic buckling strength for bending moment
$f_{E\tau}$	elastic buckling strength for shear force
f_{kcd}	design column buckling strength
f_{ks}	characteristic buckling strength of a shell
f_{ks}	characteristic buckling strength of a shell

f_{ksd}	design buckling strength of a shell
f_{ksd}	design buckling strength of a shell
f_y	yield strength of the material
G	dead load
h_r	ring flange width
h_r	geometric proportions requirement (web)
h_s	stringer web width
h_s	geometric proportions requirement (web)
i_c	radius of gyration of cylinder section
I_h	moment of inertia subjected to external lateral pressure
I_R	effective moment of inertia of a ring frame
I_x	moment of inertia subjected to axial compression and bending
I_{xh}	moment of inertia subjected to shear
k	effective length factor, column buckling
k_i	buckling interaction parameter
k_x	meridional buckling interaction parameter
k_θ	circumferential buckling interaction parameter
k_τ	shear buckling interaction parameter
K_R	model uncertainty of resistance effect in reliability analysis
K_S	model uncertainty of load effect in reliability analysis
l	distance between ring frames
L	distance between effective supports of the cylinder
L_c	total cylinder length
l_{ef}	effective width of shell
l_{eo}	equivalent length
M	design bending moment
N	design axial force
p_{sd}	design lateral pressure
P_f	function of failure probability
q_{eq}	external water pressure
q_s	internal water pressure
Q	live load
r	shell radius
R	resistance effect

R_d	design resistance
R_{Ed}	design load effect
s	spacing of stringer
S_e	effective shell width
t	shell thickness
t_e	equivalent thickness
t_{fr}	ring flange thickness
t_{fs}	stringer flange thickness
t_{wr}	ring web thickness
t_{ws}	stringer web thickness
V	design shear force
W_A	wave load
W_I	wind load
Z	basic limit state function in reliability analysis
Z_l	curvature parameter
Z_s	curvature parameter
$\bar{\lambda}_s^2$	reduced shell slenderness
$\bar{\lambda}_x$	meridional shell slenderness parameters
$\bar{\lambda}_{x0}$	meridional squash limit slenderness
$\bar{\lambda}_{xp}$	meridional plastic limit relative slenderness
$\bar{\lambda}_\theta$	circumferential shell slenderness parameters
$\bar{\lambda}_{\theta0}$	circumferential squash limit slenderness
$\bar{\lambda}_{\theta p}$	circumferential plastic limit relative slenderness
$\bar{\lambda}_\tau$	shell slenderness parameters of shear
$\bar{\lambda}_{\tau0}$	shear squash limit slenderness
$\bar{\lambda}_{\tau p}$	shear plastic limit relative slenderness
α_x	meridional elastic imperfection reduction factor
β	reliability index
β_x	plastic range factor
γ_M	partial factor
δ_0	initial out-of-roundness parameter
Δw_k	characteristic imperfection amplitude
ζ	coefficient

η	interaction exponent
ξ	coefficient
ρ	coefficient
$\sigma_{xE,A}$	design value of the meridional stress due to axial force
$\sigma_{xE,M}$	design value of the meridional stress due to bending
$\sigma_{\theta,Ed}$	circumferential design stress
$\sigma_{\theta,Rcr}$	elastic critical circumferential buckling stress
$\sigma_{\theta,Rd}$	circumferential design buckling stress
$\sigma_{\theta,Rk}$	circumferential characteristic buckling stress
$\tau_{x\theta,Ed}$	design value of shear stress
$\tau_{x\theta,Rcr}$	elastic critical shear buckling stress
$\tau_{x\theta,Rd}$	shear design buckling resistance stress
$\tau_{x\theta,Rk}$	shear characteristic buckling stress
ν	Poisson's ratio = 0.3
χ_x	meridional buckling reduction factor
χ_θ	circumferential buckling reduction factor
χ_τ	shear buckling reduction factor
ψ	coefficient
ω	length parameter
Φ	cumulative distribution function

CHAPTER 1 – INTRODUCTION

1.1 Introduction to offshore wind turbines

An offshore wind turbine consists mainly of rotor blades, nacelle, tower, and foundation or platform. Rotor blades and nacelle are used to capture wind energy to generate electricity. Based on the direction of the axis of the rotor, wind turbines can be classified as vertical axis wind turbines (VAWTs) and horizontal axis wind turbines (HAWTs). The foundation type is also an important criterion for offshore wind turbines (OWTs). Considering water depth, feasibility of economy and technology, the foundation can be designed as a bottom-fixed foundation or a floating platform. At present, most of offshore wind power is based on bottom-fixed OWTs (Jiang, 2021), including pile-type (monopile, tri-pile), tripod, gravity-based, suction bucket and jacket. The floating platform can be classified as tension leg platform (TLP), semi-submersible, spar buoy, and barge. The bottom-fixed foundation is not suitable in deep water (approximately > 50 m) but the floating platform is extended in water depth to approximately 60 – 900 m (Hussein et al., 2013). The general shapes of bottom-fixed and floating offshore foundations are presented in Figure 1.1 and Figure 1.2, respectively.

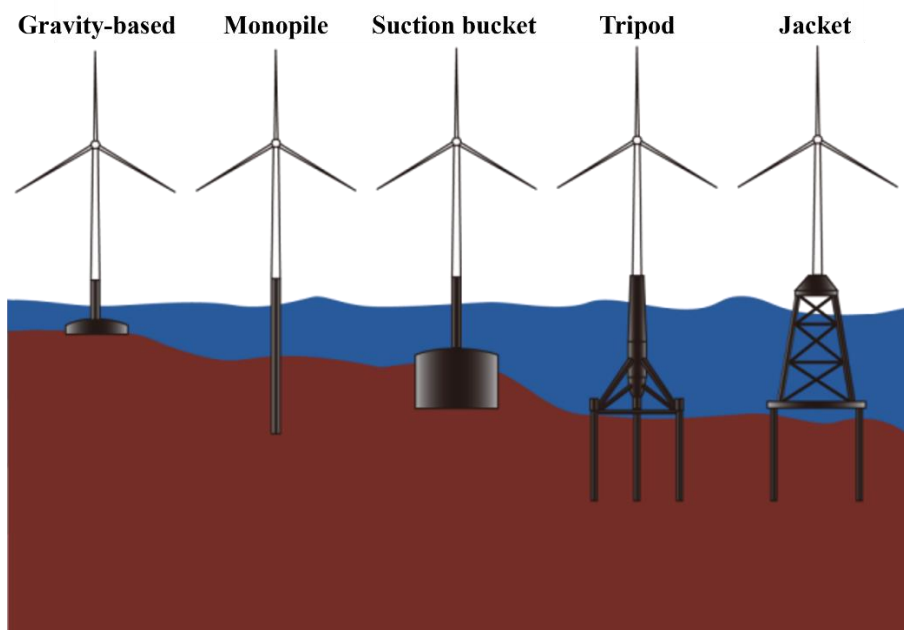


Figure 1.1 Typical bottom-fixed offshore foundation (Ding, 2019)

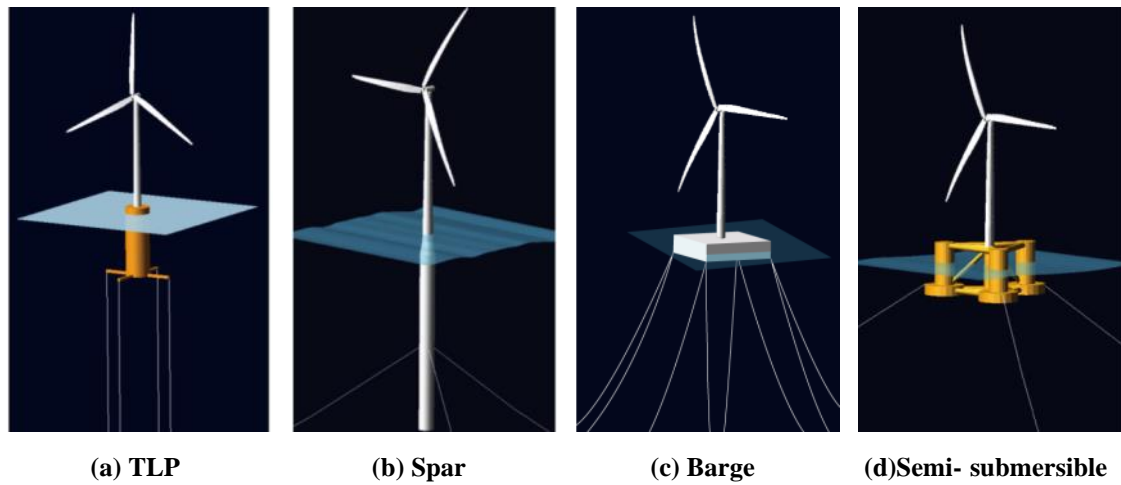


Figure 1.2 Typical floating offshore foundation (Ding, 2019)

1.1.1 Bottom-fixed wind turbines

(1) Monopile

The monopile foundation is made up of the monopile itself, a transitional piece, connection, shaft and work platform. Because of its simplicity in design, fabrication, and installation processes (Gupta and Basu, 2020), the monopile is still the most popular substructure type. It was reported that there were about 3720 foundations in Europe in 2017, accounting for 81.7% of all installed substructures (WindEurope, 2018). The foundation was made of a hollow steel cylinder with a diameter of 4 - 8 m, a length of 20 - 40 m and a wall thickness of $D/80$ - $D/120$ (Malekjafarian et al., 2021), in which 40 - 50% of the length was inserted into seabed to provide support conditions (Wang et al., 2018b). Note that the monopile is not cost effective in water deeper than 30 m (Pérez-Collazo et al., 2015) due to its high fabrication and installation cost. Furthermore, the scour effect around the monopile foundation can affect its support conditions and should be considered when designing the monopile.

(2) Tripod

To support big wind turbines in deep water, where the monopile would not be suitable, the tripod foundation (in water 20-80 m deep ([Sarker and Faiz, 2016](#))) has emerged. A tripod foundation is a three-legged steel structure supporting a monopile foundation. The forces and moments from the upper part due to winds and waves are delivered to the three steel piles. The main advantage of the tripod foundation is its larger base, which provides great resistance and thus improves the stiffness and stability of supported wind turbines ([Pérez-Collazo et al., 2015](#)). However, its cost in relation to the transportation and installation increases because of its large size ([Wang et al., 2018b](#)).

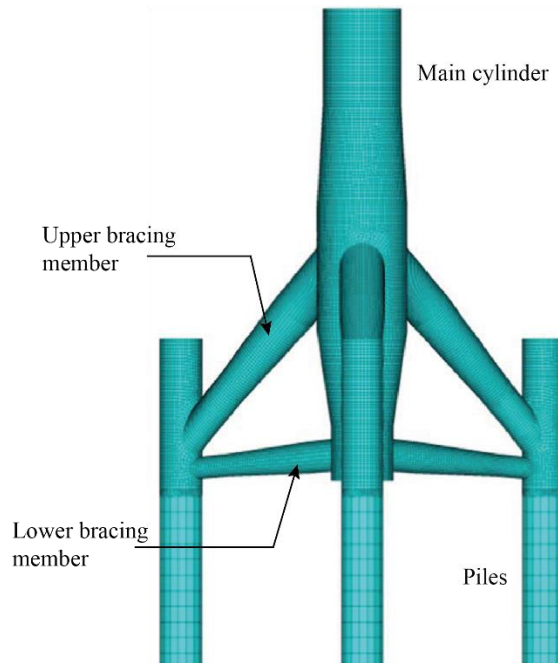
(3) Jacket

In general, a jacket foundation consists of a lattice truss with three or four leg piles which are driven into the seabed. It can be used at a relatively deeper water depth of 20-80 m ([Sarker and Faiz, 2016](#)). The jacket support structures were originally used in the offshore oil and gas industry ([Lee et al., 2016](#)). The foundation is usually fabricated by welding in factory and then transported by barge to the designated location. Finally, the jacket is lifted by heavy lift vessel and installed into the foundation piles which have been driven by hammer in advance ([Jiang, 2021](#), [Wu et al., 2019](#)). Operating in deeper waters and relatively cheap material costs are the main advantages of the jacket foundation when compared with the monopile or tripod foundation. The disadvantage of the jacket foundation is its construction and installation costs, which are rather high due to the complexity of welding connections and large dimensions. Compared with tripod foundations ([Yeter et al., 2015](#)), fatigue damage is more critical to the structural design of the jacket foundations, as a jacket structure has more welded connections, which suffer more defects and stress concentrations, and thus leads to a fatigue damage under the action of cyclic wave and wind loads.

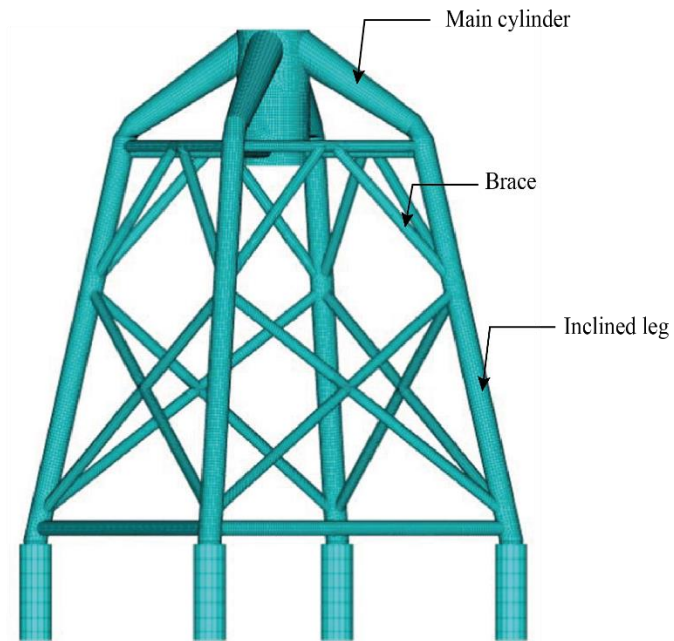
The general geometries of tripod, jacket and monopile foundations (Hao and Liu, 2017) for a 4 MW wind turbine are shown in Table 1.1. The corresponding schematic diagrams are presented in Figure 1.3.

Table 1.1 General geometries of tripod, jacket and monopile foundation (Hao and Liu, 2017)

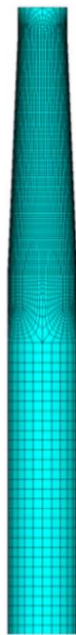
		Diameter (m)	Thickness (mm)
Tripod	Main cylinder	4.0-5.8	50-80
	Three piles	2.7	35-40
	Upper bracing member	2.2-3.0	35-55
	Lower bracing member	1.4-1.9	28-35
Jacket	Main cylinder	5	65-85
	Inclined legs	1.6	35-45
	Four piles	2.2	32-36
	X-braces, K-braces	0.8-1.0	25-30
Monopile		5.0-7.1	65-80



(a)



(b)



(c)

Figure 1.3 Geometry of (a) tripod, (b) jacket and (c) monopile (Hao and Liu, 2017)

(4) Gravity-based

Compared to the deep insertion of a monopile in the seabed, gravity-based foundations normally use heavy reinforced concrete with ballast (Koh and Ng, 2016) to maintain the stability of supported wind turbines, in which case the cost of the transportation and installation take up a great proportion in the whole process. The water depth ranges from 0 to 30 m (Wang et al., 2018b). A large barge and crane are needed to transport the gravity-based structure. In addition, to have a flat base, excavating and backfilling the original seabed is necessary before the installation. Therefore, the total cost of the gravity-based foundation is usually higher than that of the monopile, although the structure itself is less expensive (Wang et al., 2018b).

(5) Suction bucket

The suction bucket was first introduced to the offshore oil and gas industry in 1982 (Gao et al., 2021). Now, it is considered as an effective option for OWTs, shown in Figure 1.4. During the installation, the suction bucket is inserted into the seabed with the bucket filled by water and soil. The suction pressure is produced to provide a high bearing capacity and overturning capacity (Faizi et al., 2019, Lian et al., 2014, Wang et al., 2017a). This type of foundation has the advantages of large bearing capacity, repeated use, easy transportation and installation, and low cost (Wang et al., 2017b). Because the suction bucket is still in the early stages of development for wind energy, its commercialization requires more research studies.

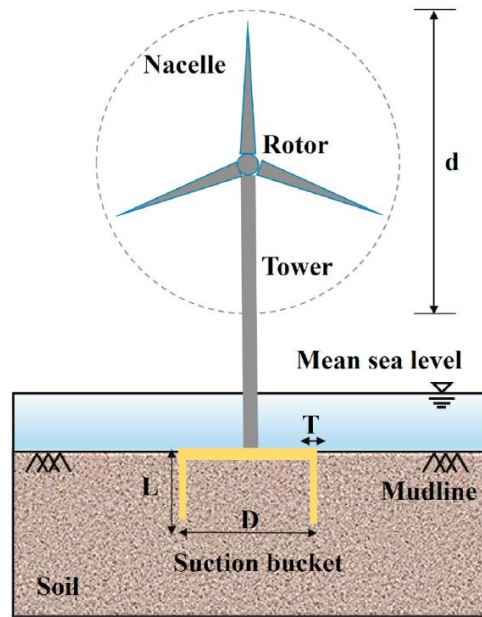


Figure 1.4 Suction bucket foundation for OWTs (Gao et al., 2021)

1.1.2 Floating wind turbines (FWTs)

FWTs are proposed to capture wind energy in deep waters. A FWT consists of a floating platform, a wind turbine and a mooring system. The four dominant types of floating wind structures are semi-submersible platform, spar-buoy, TLP and barge (see Figure 1.2). To maintain the stability of structures in deep water under wind and wave actions, FWTs use buoyancy, ballast, mooring lines, tension legs or a large water plane area.

(1) Semi-submersible platform

A semi-submersible platform normally uses a number of floaters connected by trusses to form a relatively large hull compared with the others. It relies on a large water plane area and heavy ballast to counter overturning (Karimirad and Michailides, 2015), although the draft is shallow compared to spar-buoys (Lamei and Hayatdavoodi, 2020). The main merit of the semi-submersible platform is its flexibility, as the platform can be constructed onshore and easily towed by a basic tug boat (Pérez-Collazo et al., 2015). However, the cost of design and fabrication of the semi-submersible platform is normally higher than

that of the other platform types because of its relatively complex structure. The platform motions and structural behaviour, considering buckling strength and fatigue, under different wind and wave conditions should be considered when designing the semi-submersible platform.

(2) Spar-buoy

Normally, a spar-buoy foundation is composed of a long steel cylinder connected to seabed by mooring lines and anchors. It is easy to fabricate the spar-buoy foundation, which benefits from the few components and simple structure (Zountouridou et al., 2015). Furthermore, the stability of this foundation is excellent during the operation phase on account of the deep draft and low position of the ballast, which provides a large restoring moment against overturning when the spar is inclined. However, because of the deep draft, a large water depth is required not only during the transportation but also at the final deployment site.

(3) Tension leg platform (TLP)

TLP is characterized by their vertical pre-tensioned tendons, which provide the stability of the platform (Nejad et al., 2015). It does not require a large structural weight and ballast; and therefore, the structure is simple, with fewer connections. Both the simplicity and excellent stability of the structure are beneficial in terms of fatigue (Nejad et al., 2015). However, as the pre-tensioned mooring cables would sustain a great tension, especially under extreme environmental loading, TLPs remain challenging. Moreover, the transportation (Han et al., 2017), installation and maintenance of TLPs will require additional consideration during the free-floating phase.

(4) Barges

The barge-type platform is made up of a wide and shallow body. The large water plane area provides the required restoring moment for stabilizing the platform (Kopperstad et al., 2020). The barge has the advantages of a simple structure, low cost, easy transportation and installation. However, it is sensitive to incident waves and wind because of its shallow draft and high gravity centre, which render it unsuitable for harsh sea environments.

1.2 Classification of FWTs

The concepts of the above-mentioned four types of floating foundation used for FWT are based on the traditional oil and gas industry (shown in Figure 1.5) (Rhodri James, 2015). Heronemus (1972) proposed a concept of a multiple-array wind turbine structure (shown in Figure 1.6) at the University of Massachusetts in 1972. In 2008, the first test of FWT (rated capacity of 80 kW) was installed by Blue H technologies off the Italian coast (Diaz-Casas, 2016). Followed by the Poseidon 37 projects in 2009, a FWT foundation that supports a 37 m wide wind energy plant was tested at DONG's offshore wind farm at Onsevig (Diaz-Casas, 2016). The main concepts of floating foundation used for FWT are introduced as follows.

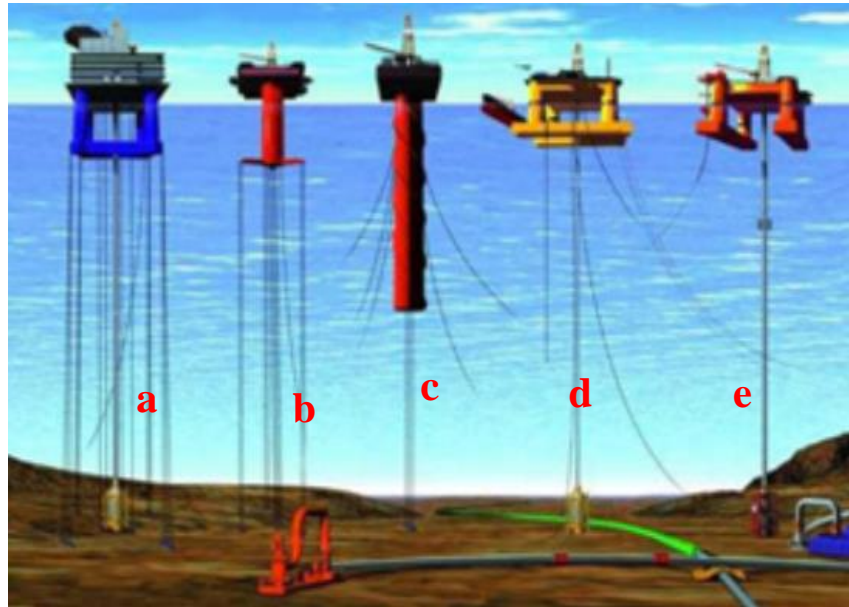


Figure 1.5 Deep Water Offshore Platforms for Oil and Gas Exploration (a) & (b) tension leg platform, (c) taut-moored spar, (d) & (e) catenary-moored semi-submersible (Shukla and Karki, 2016)

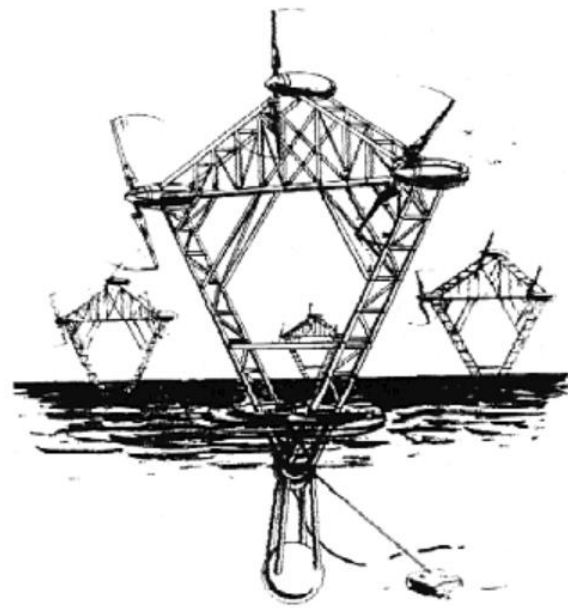


Figure 1.6 Draft for a multiple-array wind turbine structure (Heronemus, 1972)

1.2.1 Spar-buoys

In 2009, as a first large-capacity, 2.3 MW FWT, Hywind was developed by Equinor (then: Statoil) in Norway. The deep draft (70-90 m) of the spar buoy structure, a heavy ballast at the bottom, and a catenary 3-line mooring system provides sufficient stability to support the wind turbine. The water range of Hywind is 100-500 m (Muliawan et al., 2013).



Figure 1.7 Hywind (Muliawan et al., 2013)

In 2013, a concrete-steel hybrid spar developed by Toda Construction was installed off Kabashima Island, Japan (Rhodri James, 2015). In this case, concrete was used as the ballast material to lower the centre of gravity and also to reduce the costs. In April 2016, this concept was operated commercially in Japan. The FOWT has a draft of 76 m and a hub height of 56 m, and a 2-MW wind turbine with a rotor diameter of 80 m is installed on the platform (Tanaka et al., 2020).



Figure 1.8 Hybrid (Rhodri James, 2015)

A spar-buoy called Advanced Spar was proposed by Japan Marine United and installed in July 2016 (Edwards et al., 2023). This platform, shown in Figure 1.9, is divided into multiple discrete hulls. The wider plate increases the waterplane area to have a small pitch motion. Compared to the traditional Spar, Advanced Spar has a smaller draft to make construction, transportation, and installation easily.



(a) Concept of Advanced Spar

(b) Installation of Advanced Spar

Figure 1.9 Advanced Spar (Edwards et al., 2023, Ishihara, 2016)

Furthermore, some concepts of Spar buoy platforms were proposed to support VAWTs, for example DeepWind Spar, SeaTwirl and Spinwind (Edwards et al., 2023). The prototypes of these concepts have been launched.

1.2.2 Tensioned-leg platforms

In 2008, the Blue H company installed the first prototype (80 kW wind turbine supported by TLP) off the coast of Italy (Bilgili et al., 2011). As can be seen from Figure 1.10, the buoyant platform is connected to three heavy ballast blocks by mooring tethers. After this prototype, the design was changed to the lowerable gravity anchors, but there has been no news on the platform for a few years.



Figure 1.10 Blue H TLP (EWEA, 2013)

The GICON Group started a research project on tensioned-leg platforms (TLP) in 2009 (Adam et al., 2015). A TLP with vertical and angled tensioned ropes was developed. Like the usual TLP, the GICON TLP uses vertical mooring lines to constrain heave. The unique feature of this new TLP is that additional angled mooring lines were provided to

limit sway and surge (Adam et al., 2014). After various modifications and optimizations, the final prototype of this new TLP consisting of four linked columns with four vertical and four angled mooring lines (a total of eight mooring lines) was proposed in 2015 (Figure 1.11). In 2017, a 1:50 scale model of the platform was carried in a test tank in France to validate the computational model and to determine the natural frequencies of the platform (Walia et al., 2021). This concept will be further developed to reduce the levelized cost of energy.

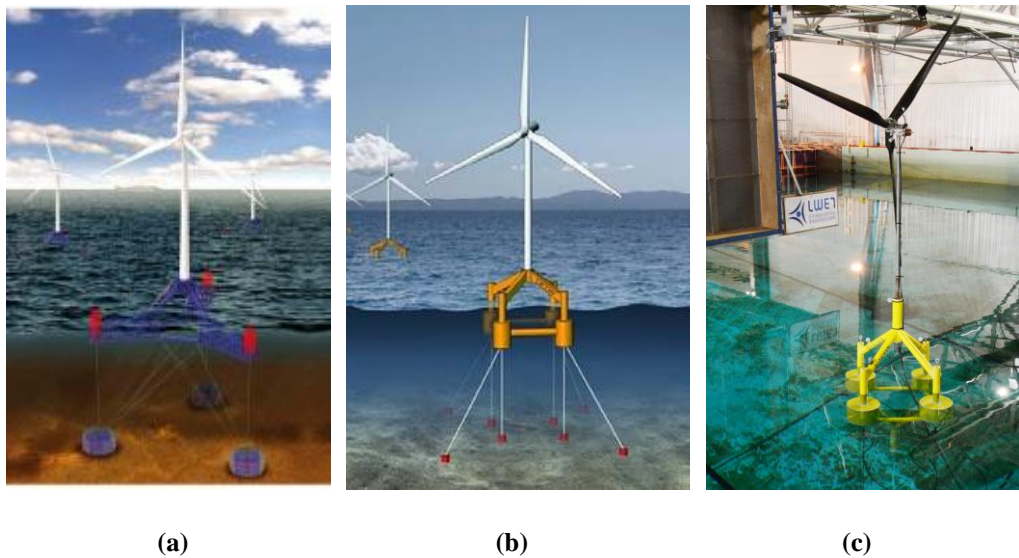


Figure 1.11 GICON TLP: (a) Initial concept of the platform (Adam et al., 2015), (b) Latest concept of the platform (Rhodri James, 2015), (c) Experimental model (Walia et al., 2021)

Glosten PelaStar (Figure 1.12) is a five-armed TLP with synthetic tendons. The platform is centralized and thin compared to the above TLP platform, which minimizes wave loads and mooring loads. The synthetic tendon has high strength to bear tremendous tension in extreme weather conditions. A demo of Glosten PelaStar was carried out with a 0.1 MW in 2011 (Bento and Fontes, 2019). The design for a full-scale demonstration turbine is still developing.

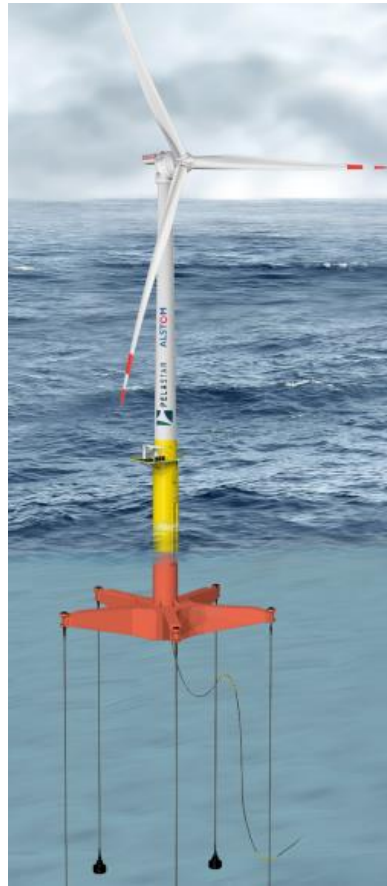


Figure 1.12 Glosten PelaStar(Park et al., 2016)

1.2.3 Semi-submersible platforms

WindFloat is a comparatively mature semi-submersible platform, having a three-legged floating foundation with water-entrapment plates at the bottom of every column. In 2011, the first full-scale prototype of WindFloat was developed by Principle Power to accommodate a 2 MW wind turbine and installed off the coast of Portugal. In this concept, permanent water ballast was installed to lower the centre of gravity. Furthermore, an active ballast system moves water from the three columns by using a water pump to improve the stability of platform (Roddiier et al., 2010b).



Figure 1.13 WindFloat (Rhodri James, 2015)

The IDEOL platform is a square ring floater constructed of prestressed reinforced concrete. The advantage of the IDEOL platform is the cheaper material cost of concrete. However, considering that the concrete is weak in tension, pre-stressed reinforced concrete is necessary to ensure crack control and water-tightness. There is an opening in the centre of the square floater, i.e., a moonpool, called ‘damping pool’. The purpose of this ‘damping pool’ is to expand the foundation and minimise the motion of floater (EWEA, 2013).



Figure 1.14 IDEOL platform (EWEA, 2013)

In 2013, Mitsui Engineering & Shipbuilding developed the Compact semi-sub floater with a 2 MW wind turbine off the coast of Fukushima, Japan. There are four columns connected by steel trusses and a pontoon to provide buoyancy for whole structure. The wind turbine is located on the central column.



Figure 1.15 Compact Semi-Sub (Rhodri James, 2015)

In 2015, Mitsubishi Heavy Industries developed the V-Shape Semi-Sub floater with the 7 MW MHI SeaAngel turbine (Rhodri James, 2015). There are three columns connected by a pontoon to provide buoyancy. Unlike the Compact semi-sub floater, the turbine in the V-Shape Semi-Sub floater is located on one column rather than at the centre of hull, which leads to fewer steel members and connections to be required. However, this may also cause different weight of the ballast in the three columns which should be considered in order to keep the stability of the platform.

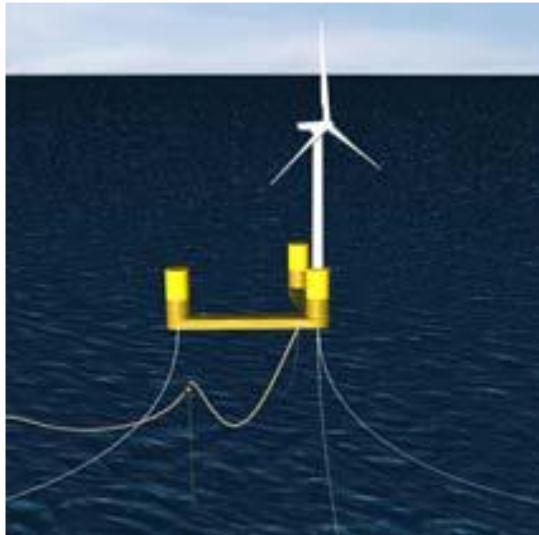


Figure 1.16 V-Shape Semi-Sub (Rhodri James, 2015)

1.3 Research scope and objectives

Although many concepts of FWTs have been adopted, the levelized cost of energy (LCOE) for semi-submersible platforms is still high (Johnston et al., 2020). The LCOE calculation includes the capital expense (the costs related to development, manufacturing, transportation and installation) and the costs of operation, maintenance and decommissioning (Lerch et al., 2018). Compared with the bottom-fixed substructures, the material consumption of semi-submersible platforms is high. Due to the complexity of manufacturing, the manufacturing cost of semi-submersible platforms is the highest among the substructures of offshore wind, whereas the differences among the operation & maintenance costs, grid costs and turbine costs seem small. As for 5 MW floating wind turbine, the LCOE of semi-submersible platforms is around 160 £/MWh, which is higher than the LCOE of Spar-buoy (around 145 £/MWh) and TLP (around 155 £/MWh) (ABS, 2021). However, it should be pointed out that there is still plenty of room for improvements in the structural optimization and cost-reduction of semi-submersible platforms. The existing research work on semi-submersible platforms has mainly focused on the hydrodynamic behaviours, but little on the structural behaviours. In this context, the work undertaken in this thesis aims to improve understanding of the nonlinear

structural behaviour of a semi-submersible platform for FWTs, compare and evaluate the relevant design codes. Both the entire platform and individual components are to be studied by considering geometric and material nonlinearities. In order to clearly explain the objectives of the research, the objects to be investigated and corresponding study process are provided in Figure 1.17. Firstly, the entire floating system including platform, mooring, tower and the impact of wave and wind is established for carrying out the global structural analysis. Secondly, as an important component of the floating platform, the largest cylindrical column is adopted to conduct the structural design under the loading conditions used in the global analysis. Finally, to have a comprehensive understanding of the buckling behaviours of cylindrical shells, a wide range of geometry including the design of cylindrical columns in the second step is considered and corresponding design codes for shell structures are discussed and evaluated. The specific objectives are listed as follows:

Literature review

- To review the work published so far on offshore structures and especially on the structural performance of FWTs.

Global structural analysis

- To investigate the dynamic motions and forces of the entire floating platform due to wave and wind loads, which will serve to establish the loading conditions for structural analyses in later stages.
- To develop a new structural finite element model coupling the hydrodynamic model with the wave-induced pressure and inertia force, which is used to investigate the structural behaviour of the floating platform.
- To study the effect of wave and wind loadings on the ultimate strength of the connections and structural components of the floating platform.
- To study the structural nonlinearity effect on the stress and deformation performance of the floating platform.

Component structural design

- To compare the various code-based approaches and the FE simulation based on the main structure of the floating platform under an environmental load condition used in the global structural analysis.
- To provide a cost-effective stiffened shell considering material consumption and labour of welding.

Component structural analysis

- To carry out the buckling analysis of unstiffened and stiffened cylindrical shells under combined axial compression and bending.
- To study the influence of geometric imperfection profiles and amplitude on the buckling behaviour of cylindrical shells.
- To assess the accuracy of various shell design codes.
- To assess the reliability of the relevant shell design codes and propose modifications if necessary.

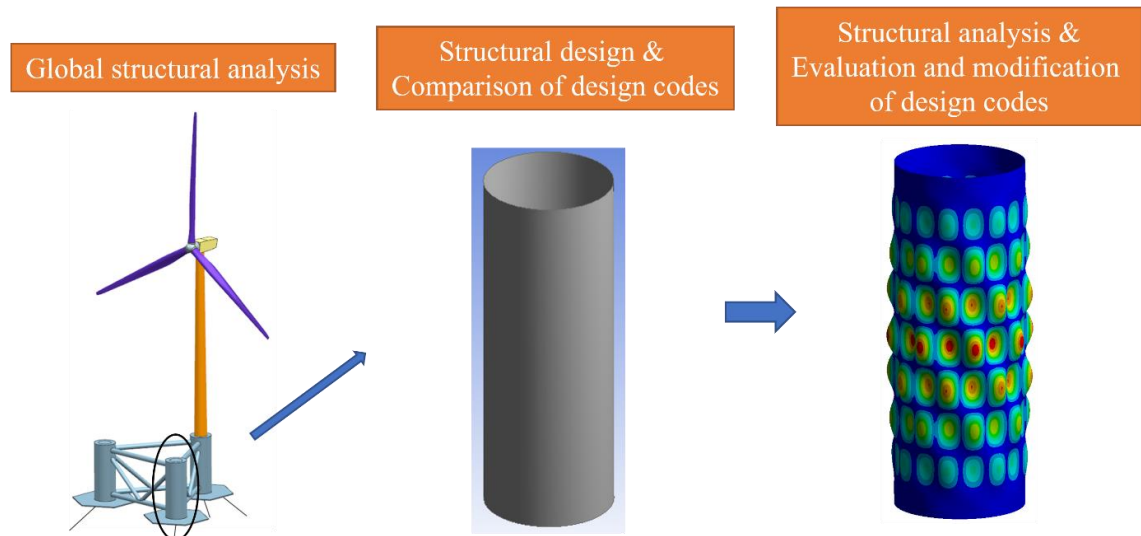


Figure 1.17 Study process of this PhD thesis

1.4 Outline of the thesis

This thesis is organised in six chapters:

Chapter 1 gives a general introduction and research background of OWTs, followed by the research objectives and methods adopted in the study.

Chapter 2 presents a detailed literature review of offshore structures, including analysis methods of hydrodynamic and aerodynamic forces for offshore structures, global structural analysis for bottom-fixed foundations and floating platforms, ultimate strength, buckling behaviour and fatigue study for cylindrical shells, and the corresponding design guidelines adopted for offshore structures. The knowledge gap and the contributions of this research are presented at the end.

Chapter 3 investigates the nonlinear structural response for WindFloat's platform. A novel one-way coupled fluid-structure interaction simulation is undertaken by integrating a series of wave phases to create a full wave, which enables the investigation of structural behaviour of a floating platform under a complete wave cycle. Linear elastic analysis is firstly carried out to identify the critical load case, and then geometrically and materially nonlinear analysis is adopted to investigate the failure modes and the critical locations in comparison with the linear elastic analysis. The effects of azimuthal angles of environmental loads, wave-wind misalignment and boundary conditions on the failure modes are also investigated. The present structural modelling method could also be adopted by other FWTs if they have similar design consideration.

Chapter 3 focuses on the global structural analysis of a platform, while Chapter 4 presents various design procedures of the large cylindrical shell, which is the main structural component used in semi-submersible platforms, in order to compare the design codes and propose a cost-effective solution for the stiffened shell. Firstly, the design process of three code-based approaches (the DNVGL guideline and the EN1993-1-6 (2007 and 2017 versions)) are discussed. After the structural design of the unstiffened and stiffened cylindrical shell, a comparison of the design results based on the above three codes is presented. The design spreadsheets are developed as shown in Appendix.

Chapter 5 presents the buckling and ultimate strength analyses of cylindrical shells under combined loading conditions using finite element modelling. The analysis includes the effects of geometric imperfections, as well as global slenderness (L/r) and local slenderness (r/t) of the shell. The numerical prediction of the ultimate strength of cylindrical shells is compared with the design results obtained from the design codes presented in Chapter 4 to assess the accuracy of the design codes. A reliability analysis of the design codes is provided and the recommended modification is proposed to ensure these design codes possess the required level of safety. A case study of stiffened cylindrical shell with different geometric imperfections under axial compression is provided.

Chapter 6 summarizes the main findings obtained and the conclusions drawn from this study. Future work is also suggested in the end of this chapter.

CHAPTER 2 – LITERATURE REVIEW

2.1 Modelling of environmental forces for offshore structures

Environmental forces may cause dynamic response of offshore structures, which may lead to structural failures and operating challenges. A predictable status is essential for FWTs during the transportation, installation and operation. Therefore, the assessment of environmental forces is necessary.

2.1.1 Numerical modelling of environmental forces

2.1.1.1 *Hydrodynamic force*

The effect of environmental forces on the dynamic response of FWTs has been widely studied. Potential flow theory is a popular one to consider the hydrodynamic force, which assumes that the flow is incompressible, inviscid, and irrotational, with negligible surface-tension effects.

The following hydrodynamic software are commonly used for offshore structures based on the potential flow theory: AQWA (Ren et al., 2018, Ren et al., 2020), WAMIT (Simos et al., 2018), MOSES, Hydrostar, HydroD (Sesam) (Xu et al., 2018), Orcaflex (Zhao et al., 2021), etc. Numerical models of FWTs have been proposed using these software to investigate the dynamic performance of platforms under the action of hydrodynamic force.

In literature the effects of linear and nonlinear waves on OWTs have been investigated widely. Linear wave theory, also known as sinusoidal wave theory or Airy theory, is the simplest wave theory, which has a sinusoidal surface profile. The nonlinear wave can be defined using Stokes wave theory, Cnoidal wave theory, Solitary wave theory, or Stream function wave theory based on different nonlinear properties. Most numerical models for FWTs only consider the first-order wave effect. It may be less reliable for hydrodynamic simulation when compared with the fully nonlinear wave in extreme wave conditions. Xu

[et al. \(2019\)](#) studied the nonlinear wave effect on the platform motions and mooring tension of a semi-submersible FWT. It was found that in the extreme wave conditions (significant wave heights of 9.77m and 15.75m) the surge motion of the platform and the tension force of mooring line predicted by a nonlinear wave model are both 25% larger than that of a linear wave model. [Zhao et al. \(2020\)](#) adopted the second-order ANSYS-AQWA solution to investigate the second-order effects of hydrodynamics on a semi-submersible FWT. It showed that neglecting the second-order wave underestimated the pitch motion by about 16% in the frequency domain at extreme wave condition (significant wave height of 15.6m). However, the difference of the platform motion between the first-order and second-order wave is not evident at moderate sea state (significant wave heights of 2.5m and 5m). [Mei and Xiong \(2021\)](#) studied the effect of second-order hydrodynamics on a semi-submersible FWT using AQWA. Similarly, compared with the second-order hydrodynamics, the pitch, heave, and yaw motions are underestimated if the first-order hydrodynamics are adopted under an extreme wave (significant wave heights of 9.7m and 16.7m). Moreover, due to the pitch and yaw motions induced by the second-order hydrodynamic loads, the fatigue damage of the tower base can be increased by 57.1%.

Different from semi-submersible platforms, the heave motion of the TLP platform is restricted by the high tension leg load. The nonlinear wave excites a higher pitch and surge motion at extreme wave conditions and has a further great influence on the bending moment of the tower base and the tension leg load. For example, the tension leg load caused by the second-order wave load increases by 100% in high frequency response under an extreme condition (13.8m significant wave height) ([Han et al., 2022](#)). Under the nonlinear wave impact, the standard deviation of the tower base bending moment increases by 24% compared to the linear wave ([Vardaroglu et al., 2022](#)).

As for a Spar platform, the higher order of the hydrodynamic loads is rarely considered. This is because its impact on the dynamic response of the Spar is relatively small ([Roald](#)

et al., 2013). However, the nonlinear effect of viscosity is significant. Hence, potential flow theory combined with Morison's equation to consider the viscous effect is a suitable option to study nonlinear hydrodynamics. Compared with the nonlinear wave, the surge, pitch motions and the bending moment of the tower base would be underestimated by the linear wave (Hegseth and Bachynski, 2019).

In summary, neglecting the nonlinear effect of hydrodynamics may underestimate the platform motions of FWTs especially at extreme wave conditions. The larger the wave, the more obvious the nonlinear effect. The platform motions would have further influence on the bending moment of the tower base, the tension force of the mooring lines, and the fatigue damage of the platform. However, the linear wave theory is still applicable for small and medium amplitude waves because the second-order hydrodynamic loads are relatively small when compared with the first-order hydrodynamic loads.

As the main environmental forces, the misalignment of wave and wind during operational conditions has been considered by some scholars. Normally, the misalignment between wind and wave is within 30° , and it is rarely larger than 60° (Wang et al., 2016a). Therefore, the angles between wind and wave directions were up to 90° in some studies (Mitra et al., 2021). It was found that except for the pitch, the other motions (Wang et al., 2016a) and the tower base bending moment (Li et al., 2020b) increased if wave and wind were misaligned for a semi-submersible floater. In this thesis, the misalignment of wave and wind loads is considered to study its effect on the structural behaviour of the floating platform in Chapter 3.

However, the effect of environmental forces on the structural performance of the floating platform is not well understood. Qi et al. (2018), Ma et al. (2019a) used AQWA to calculate the wave pressure on the semi-submersible offshore platform in order to obtain the data such as the stresses in structural components and connections and their fatigue

behaviours. The hot spot and fatigue crack growth in critical locations were predicted. However, these floating structures are not designed for offshore wind turbines.

Liu et al. (2018) carried out the structural strength analysis of a semi-submersible VAWT. Their results showed that the highest structural stress occurs when the wave, wind, and current are in a collinear direction and is located in the main and secondary supporting bars as shown in Figure 2.1. In the wave loading calculation, the first-order wave forces were considered based on the potential flow theory for the large-scale components. For the small-scale components, the wave loads were calculated by using Morrison formula. However, the structural behaviour simulation was simplified. For instance, the material was assumed to be linearly elastic; the environmental loads were equivalently applied to the MASS element, and the mooring systems were neglected. This kind of simplification used in the structural model may affect the accuracy of the calculated wave loads.

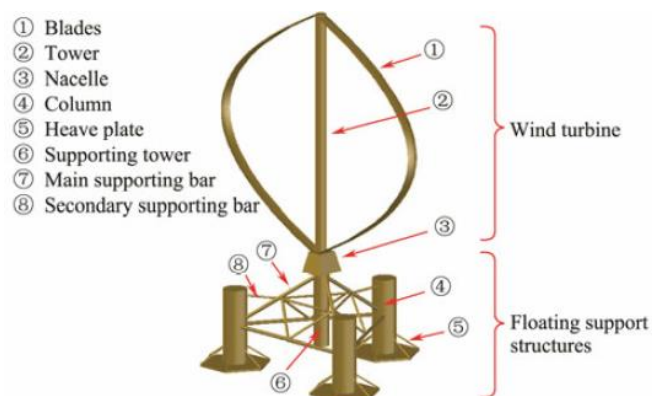


Figure 2.1 The semi-submersible VAWT (Liu et al., 2018)

Lee et al. (2020) evaluated the structural strength of a semi-submersible platform called DeepCwind using structural finite element modelling technique. They found that the structural components YU and YL (shown in Figure 2.2) were most likely to occur structural failure. In their study, one-way hydrodynamic structure interaction analysis in AQWA was used for conducting the hydrodynamic diffraction analysis to calculate the pressure. Then, a pressure load mapping was performed to transfer the pressure from the

hydrodynamic model to the structural model. However, the inertia force and the geometric and material nonlinearities were not considered in the load transfer and the structural strength evaluation.

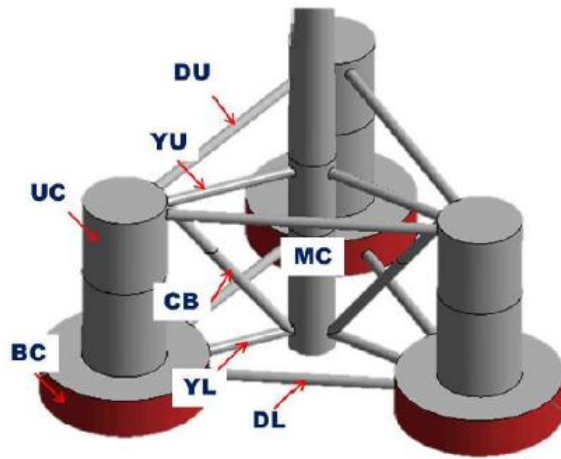


Figure 2.2 Abbreviations for members of DeepCwind (Lee et al., 2020)

For slender structural members ($\lambda > 5D$, where λ is the wave length and D is the diameter of the member) (DNVGL-RP-C205, 2020) the drag force and inertia force are dominant in the wave and current induced loads. The total wave loads can be calculated using Morison's load formula (J. Morison, 1950). Morison's equation is a semi-empirical formula in which the hydrodynamic coefficients should be obtained from water tank tests or design guidelines, such as API or DNVGL. Morison's equation was used by Mitra et al. (2021) to estimate the inertia and drag forces on a spar and torus to study the vibration of spar-torus combination. Suja-Thauvin et al. (2018) adopted the modified Morison's equation to estimate the extreme responses such as the stress distribution of a monopile offshore wind turbine. For structures whose dimensions are between the slender and large members, the potential flow can be combined with Morison's equation to consider the important dynamic features (Li and Bachynski-Polić, 2021, Hu et al., 2022, Cheng et al., 2019b, Zhang et al., 2020).

Although potential flow theory is widely used in hydrodynamic analysis ranging from linear theories to fully nonlinear methods (Hirdaris et al., 2014), it is unable to identify the viscous forces. CFD (computational fluid dynamics) codes developed by solving Navier–Stokes equations are more accurate, but they are computational expensive. Benitz et al. (2014), Benitz et al. (2015) performed CFD simulations in OpenFOAM to predict the hydrodynamic forces on the semi-submersible platform called DeepCwind (Figure 2.2). Their results showed that the multimember arrangement leads to a decrease of the drag loads. Note that the oscillatory loads from the inline and transverse flow directions due to vortex shedding captured in CFD simulation cannot be captured by using the potential flow theory and Morison’s equation. Bruinsma et al. (2018) compared a physical model test and a fully nonlinear numerical modelling performed by a CFD solver to study the dynamic response of a rigid floating structure for FWTs in waves. The vertical loading, the heave and pitch motion of the platform due to the regular incoming waves from CFD results compare well with the physical model. As for structural analysis, the bending moment of tower base and the tension force of the tension legs of a TLP wind turbine were studied by Nematbakhsh et al. (2015) using CFD modelling and potential flow approach. A regular wave considering the nonlinear effects was adopted in this study. It was found that, when compared with the surge and heave, the tension force of the tension legs was mainly governed by the pitch response. The bending moment of tower base was used to validate the CFD method and the potential flow theory with finite element method and good agreement was demonstrated. Chen and Hall (2022) used the coupled CFD solver OpenFOAM with the mooring dynamic solver MoorDyn to predict the mooring line tension of a floating structure. It should be stressed herein that, CFD simulation is mainly used to analyse the wave loads and motion responses of FWTs.

In literature there are some studies on hydro-structure coupling of CFD and FEA, but the works are largely on ship hulls. The key issue in the coupling analysis of CFD and FEA is the transfer of the hydrodynamic load from the CFD model to the FE model. The coupling method of CFD and FEA can be divided into one-way coupling and two-way

coupling. In the former, the wave-induced pressure and inertia force calculated in the CFD solver are directly transferred to the FE model in which the structure is determined as a rigid body and the structural deformation is neglected. In the latter, the structural deformation is considered and fed back into the next step of CFD simulation. For example, [Huang et al. \(2022\)](#), [Jiao et al. \(2021\)](#) used CFD-FEA (STAR-CCM+ for CFD solver and Abaqus for FEA) two-way coupled method to predict the ship motions and wave load under a nonlinear regular wave. The fluid pressure and wall shear force calculated by the CFD solver were transferred to the FE solver, and then the node displacement is calculated and exported to the CFD solver to update the geometry of the hull. The FE model consists of a massless surface shell and a backbone beam. The backbone beam provides the total longitudinal stiffness and feeds back the deformation to the surface shell. Thus, the structural behaviours of the shell under wave loads cannot be captured. [Bakica et al. \(2020\)](#) developed CFD-FEA (OpenFOAM for CFD solver and NASTRAN for FEA) one-way coupled method to transfer the hydrodynamic loads from the CFD mesh to the FE mesh of a hull. A novel method of the load transfer, which increases the structural integration points to capture the pressure area having the large pressure gradients, is provided. However, only linear elastic structural analysis was carried out to reduce the computational expense. [Volpi et al. \(2017\)](#) developed both CFD-FEA (CFDShip-Iowa for CFD solver and ANSYS for FEA) one-way and two-way coupled methods to study the structural behaviour of a composite hull. It was found that when compared with the one-way coupled method, the pressure and maximum strain value on the hull was reduced by 12% in the two-way coupled method. In theory, the hydro-structure coupling of CFD and FEA mentioned above can be also applied to FWTs to consider the structural load transfer. However, unlike the ship hulls, the effect of the wind loading on FWTs is significant as the wave loading, which may have a more complicated dynamic behaviour. Thus, the coupling of wind turbine aerodynamics, hydrodynamics and structural response will be a special concern in the analysis of FWTs. Moreover, the structural model is simplified as beam element or linear material to reduce the

computational cost in the coupling method. These barriers are considered in this thesis to study the structural behaviour of a floating platform for FWT in Chapter 3.

2.1.1.2 Aerodynamic force

Except for the hydrodynamic force, the aerodynamic force is another important environmental force for FWTs. The Blade Element/Momentum method (BEM) is a popular method for studying the aerodynamic force because of its simplicity (Borg and Collu, 2015, Chen et al., 2019, Jessen et al., 2019). The BEM theory consists of the momentum theory and the blade element theory. Rankine (1865) and Froude (1889) proposed the one-dimensional momentum theory of the propeller which used an actuator disc to represent the propeller. Drzewiecki developed the blade element theory in 1892 in which the blades of propellers were divided into several sections in order that the aerodynamic forces can be calculated independently (Okulov et al., 2015). Finally, Glauert combined these two theories and developed the BEM theory in 1926 (Mian et al., 2021).

Liu et al. (2017) used BEM theory to estimate the aerodynamic loads and the fatigue loads of the tower for an offshore horizontal axis wind turbine supported by a bottom-fixed foundation. BEM theory was amended by introducing the dynamic inflow and dynamic stall models to account for the transient aerodynamics. It was concluded that the bending moment of the tower base calculated without considering aerodynamic damping is more than five times that considering aerodynamic damping, and thus the interaction between structural motion and rotor aerodynamics is recommended to evaluate the aerodynamic damping. Since the dynamic response of the floating platform is relatively large the mechanical behaviour of the bottom-fixed foundation may not be applicable to the floating platform.

Ma et al. (2017), Li et al. (2018c), Borg and Collu (2015), Chen et al. (2019), Jessen et al. (2019) studied the motions of floating platform using BEM to calculate the aerodynamic force. In the corresponding structural analysis, the tensile forces of the mooring lines (Li et al., 2018c, Chen et al., 2019) were studied.

Although the BEM theory is simple and requires less computational effort, the accuracy of the calculated results decreases with the increase of wind speed. The main reason for this is because the realistic 3D geometry of the blades cannot be considered in the 2D aerodynamic characteristics of BEM and thus spanwise flow is neglected, which leads to an overprediction of the spanwise distribution of forces and pressures due to wind near the rotational tip of blades when the wind speed is larger than 15 m/s (Plaza et al., 2015). Moreover, the BEM theory assumes the wind flow is steady and neglects the turbulent inflow. However, air movement is usually turbulent. Thus, the performance of turbine blades under the turbulence is not considered in the BEM theory. In spite of these limitations, the BEM theory has been used widely as a high-efficiency and reliable model for calculating the aerodynamic loads on wind turbine.

In order to obtain the aerodynamic data from 3D flow, the vortex methods and potential flow can be adopted. Vortex methods include Free Vortex Model (FVM), Vortex Lattice Model (VLM), Vortex Panel Method (VPM) (Shi et al., 2021). Most of them were adopted to study the relationship between wake and dynamic behaviours or power performance of FWTs. For example, Lee and Lee (2019) found that the platform motion of a spar-buoy FWT result in varying the peak values of the power output and thrust forces from 17.82 to 58.64% and 7.16 to 28.46% respectively. Wen et al. (2018) obtained the curves of the power variation with the pitch motion of FWT by using FVM in order to investigate a better power performance. Farrugia et al. (2016) determined the relationship between the surge conditions of platform and the rotor operating conditions based on free-wake vortex. Jeon et al. (2014) used VLM to predict the aerodynamic load

under unsteady aerodynamics of FWTs and their results have shown good agreement with experimental data.

The aerodynamic force sometimes can be simplified as equivalent thrusts (Ren et al., 2020) according to the design data of rotor thrust provided by the National Renewable Energy Laboratory (NREL). Although this simplified method is computationally efficient, it might not be suitable when a wind turbine is in an extreme environmental condition with high frequency platform motions (Lee and Lee, 2019, Dong et al., 2019).

The viscous effects are not considered in the above methods. To overcome this limitation, CFD method can be used to undertake a more accurate solution for aerodynamic force. Based on the literature review, a coupled CFD-FEM method was used to study the impact of aerodynamic force on the blades. This method has been integrated and developed by some software such as Ansys Fluent + Ansys mechanical module (Wang et al., 2016b), Ansys CFX + Ansys mechanical module (Khalid et al., 2013), OpenFOAM + BeamFOAM (Dose et al., 2018), in which the one-way or two-way coupled fluid-structure interaction simulation can be achieved. Specifically, the aerodynamic force on the blade was transferred from CFD to FEM and after the structural analysis, the new geometry of the deformed blade is imported to CFD software to conduct the next simulation. The above two complete analyses are called a two-way coupled simulation. If the second step is not considered, it is called a one-way coupled simulation. The deformations (Dose et al., 2018, Lee et al., 2017), internal forces (Santo et al., 2020) and stresses (Wang et al., 2016b) of the blade have been studied by some scholars. However, the hydrodynamic force and the foundations or the platforms of OWTs have not been considered in their coupling models.

As for the effect of aerodynamic force on the floating platforms, the existing studies mainly focus on the aerodynamic performance under the motions of FWT induced by wave loads. Pitch and surge motions (Chen et al., 2021, Tran and Kim, 2015) would be

significantly affected by the incoming wave. Therefore, they are most commonly considered in the CFD simulations. The motions of FWTs may cause the varying thrust loading, power generation (Shi et al., 2021) and additional fatigue loads in the structural components of wind turbines such as blades and rotor. Conversely, the aerodynamic forces can have an effect on the hydrodynamic response of FWTs too (Cheng et al., 2019a). Currently, the study of the structural performance of floating platforms for FWTs using CFD simulation is still rare. This is because it is a complex study which needs to consider wave, wind, fluid structure interaction, wave-wind coupling, etc. A huge computational resource and time are required to carry out CFD simulation although it can provide a more accurate prediction compared with other methods such as BEM. Therefore, the requirement for accuracy and computational effort will be synthetically considered to choose a suitable simulation method in Chapter 3.

2.1.2 Experimental study under environmental forces

Experimental tests have been widely used to investigate the structural response of FWT structures and to validate the numerical models of FWTs under various different conditions of wave and/or wind actions.

Chen et al. (2018) conducted an experiment to study the structural behaviours, particularly the forces and moments on the components, of a floating platform subjected to wave forces only. It was found that the forces and moments increase linearly with the wave amplitude. Ding et al. (2020) studied the hydrodynamic and structural characteristics of a floating platform (Figure 2.3) under wave forces. The loads on the connections were assessed and it was found that the maximum load occurred on the interior connection.

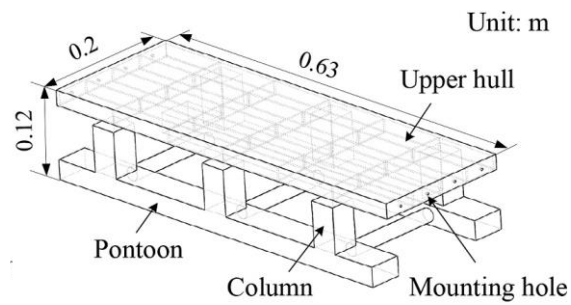


Figure 2.3 Perspective view of the semi-submersible platform (Ding et al., 2020)

An experimental study of a jacket-type offshore wind turbine (Figure 2.4) was carried out by Liu et al. (2014). Considering environmental forces of wind, wave and current, the buckling failure of the jacket-type offshore structures was examined, the results of which could be used to support the structural design of the steel jacket-type offshore structures. Similarly, Asgarian et al. (2016) built a scaled offshore platform to identify the position in the structure where the buckling occurs.



Figure 2.4 Experimental model (1:15 scale) of a jacket-type foundation (Liu et al., 2014)

The tests of structures mentioned above can be classified as bottom-fixed foundations and floating platforms without wind turbine. It may not be applicable for the FWTs which involve wind forces and aerodynamic response.

A wave tank experiment of a TLP platform for wind turbines (Figure 2.5) was developed by [Adam et al. \(2014\)](#) to study the internal force evolution in the structure. It was found that the internal forces subjected to single wind and wave loads could be superposed when the horizontal movement of the platform was not significant. However, this outcome was not suitable for the semi-submersible structures because their dynamic behaviour was sensitive to the environmental loads.



Figure 2.5 The 1:37 scaled TLP platform ([Adam et al., 2014](#))

A physical model of one column of a semi-submersible platform for FWT (Figure 2.6) was built by [Lopez-Pavon and Souto-Iglesias \(2015\)](#) to investigate the hydrodynamic coefficients and pressure loads on the heave plates with or without radial and circular reinforcements (shown in Figure 2.6) which is used to reinforce the heave plates. In hydrodynamic part, the results showed that the circular reinforcement sharply reduces the hydrodynamic damping when compared with the solid plain plates; and the motion amplitude has a great effect on damping and added mass coefficients. In structural part, the pressures on the top and bottom sides of the heave plate with reinforcements are

similar in magnitude. However, the radial and circular reinforcements caused a larger pressure difference in its local position.

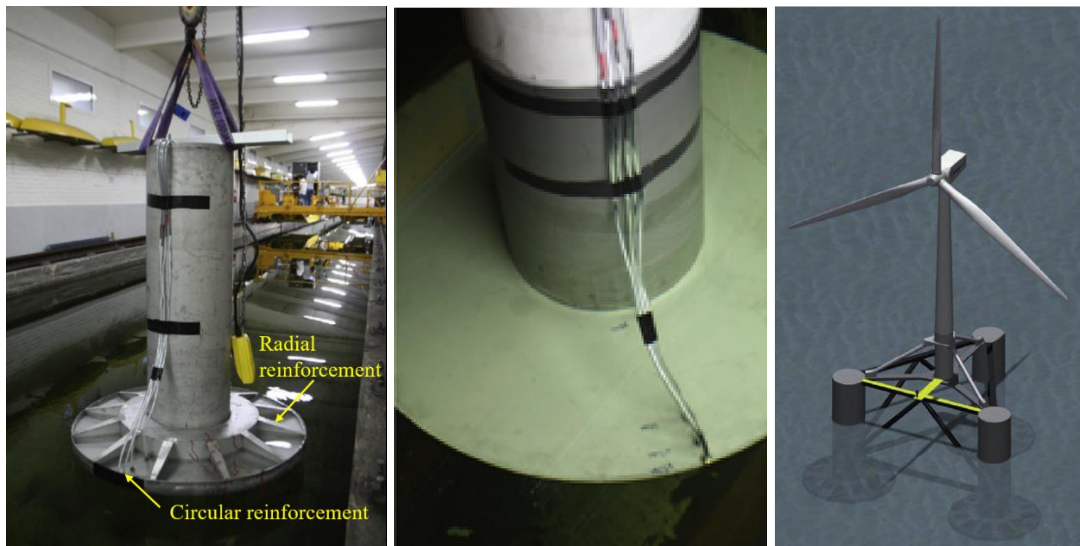


Figure 2.6 Model with reinforced heave plate (left), with solid plain one (middle) and sketch of entire FWT (right)

The experimental test on the structural behaviours of FWTs is difficult to conduct. The main challenges of basin experiment technology are the highly specific facilities including wave tank, measurement devices, wind-wave generation system, manufacture of FWTs and etc. Furthermore, compared with the hydrodynamic data, the structural data such as the stresses and deformations are more difficult to obtain. This is why there are not many test data available in literature. Nevertheless, Table 2.1 lists some experimental tests of FWTs reported in literature.

Table 2.1 Summary of experimental tests of FWT

Experiment Name	Scale	Platform Type	Wind turbine	Hydrodynamic setup	Aerodynamic Setup	Hydrodynamic outcome	Structural outcome
Fukushima-FORWARD (Ishihara and Zhang, 2019)	1:50	Semi-submersible	2 MW	towing speeds: 0.2 m/s, 0.5 m/s and 1.0 m/s)	-	Added mass coefficient, drag coefficient	Tension of mooring lines
HiPRWind (Simos et al., 2018)	1:19.8	Semi-submersible	1.5 MW	regular, bichromatic and irregular waves	-	First-order motions, amplitudes	-
Concrete star (Azcona et al., 2014)	1:40	Semi-submersible	6 MW	Regular, irregular waves	12.7 m/s, 5 m/s, 8.5 m/s, 25 m/s, turbulent wind	Surge, pitch, heave	-
UMaine-Hywind (Ruzzo et al., 2016)	1:30	Spar-buoy	-	field site (max. tidal amplitude: 0.20 m)	-	Six degree of freedom (DOF) motions	-
Spar at NRMI (Utsunomiya et al., 2009)	1:22.5	Spar-buoy	2 MW	Regular, irregular waves	35.6 m/s (29.4N)	Six DOF motions	-
Tension-leg of MARIN (Koo et al., 2012, Goupee et al., 2014)	1:50	Tension-Leg Platform	5MW	regular and irregular waves	Steady, Dynamic Wind	Surge, heave, pitch	Tower base bending moment, mooring line tension

Spar buoy of MARIN (Koo et al., 2012, Goupee et al., 2014)	1:50	Spar Buoy	5MW	regular and irregular waves	Steady, Dynamic Wind	Surge, heave, pitch	Tower base bending moment, mooring line tension
Semi-submersible of MARIN (Koo et al., 2012, Goupee et al., 2014)	1:50	Semi-submersible	5MW	regular and irregular waves	Steady, Dynamic Wind	Surge, heave, pitch	Tower base bending moment, mooring line tension
WindFloat (Roddier et al., 2010b)	1:105	Semi-submersible	5MW	100-year wave, regular wave	Actuator Disk + Rotating Mass	Surge, heave, pitch	Fatigue life of truss, tower
ConFloat (Zhou et al., 2017)	1:60	Semi-submersible	5MW	regular and irregular waves	11.5 m/s Drag discs	Heave, pitch, surge	-
Semi-submersible in SINTEF Ocean (Luan et al., 2018)	1:30	Semi-submersible	5MW	Irregular wave, JONSWAP wave spectrum	Turbulent wind, Kaimal wind spectrum	Surge, heave, pitch	sectional forces and moments of columns
TLP of Korea Institute of Energy Research (Madsen et al., 2020)	1:60	TLP	10MW	Irregular wave $H_s=3.3$ to 10 m (full scale)	Steady wind 8.5 to 33 m/s (full scale)	surge and nacelle accelerations	mooring line tension
TLP with heave-type WEC (Ren et al., 2020)	1:50	TLP		Height: 0.02 m to 0.45 m, period: 0.5 s to 5.0 s	Speed: 0 to 27 m/s	Six DOF motions	-

2.2 Global structural analysis of offshore structures

2.2.1 Optimization design and strength analysis

2.2.1.1 *Bottom-fixed structures*

The studies on the optimization design and strength analysis of OWTs mainly focus on bottom-fixed structures, particularly the jacket substructures. Optimum structural design on offshore wind turbine jacket substructure, based on the analytical gradient-based method, was reported by [Chew et al. \(2015\)](#). It was shown that the mass of the optimized jacket substructure could be reduced by 52 % when compared with the initial design.

The structural design of steel gravitational support for an offshore wind turbine was carried out by [Niklas \(2017\)](#), in which the maximal stress level, the maximal column deflection and the total mass of the structure were reduced by 71%, 11% and 9% respectively, when compared with the initial design that was planned to be operated on North Sea or Baltic Sea waters.

Based on the structural optimization design of jacket substructures, [Häfele et al. \(2019\)](#) and [Kok Hon Chew \(2014\)](#) found that the three-legged structure was more preferable than the four-legged structure. [Häfele et al. \(2019\)](#) optimized the jacket substructures using a cost modelling which included material costs, fabrication costs, coating costs, transport costs and installation costs. [Kok Hon Chew \(2014\)](#) considered the different angles of wind-wave incident and substructures minimization of structural mass and concluded that the three-legged jacket substructure was a better concept, which reduced 17% of the structural mass and 25% of welded joints.

Based on the solid isotropic microstructure with penalization method, topology optimization design for jacket structures was developed by [Tian et al. \(2019\)](#). Their results showed that the mass and the maximum equivalent stress of the jacket structure could be reduced by 13.7% and 46.31%, respectively.

Meanwhile, [Natarajan et al. \(2019\)](#), [Kaveh and Sabeti \(2018\)](#), [Oest et al. \(2018\)](#) carried out the optimization design of jacket structures for offshore wind turbines to reduce the structural mass.

As for strength analysis, the structural damage of a jacket-type platform due to earthquake was assessed by [M. Aghajani Delavar \(2018\)](#) based on a 3-D analytical model. It was shown that the lower storey had the greater shear force and the structural behaviour of the offshore platform was similar to that of a steel braced frame.

[Yu and Amdahl \(2018\)](#) studied the structural response of offshore tubular members subjected to ship impact using finite element modelling and design standard DNV-GL RP C204. A new concept, named as “transition indentation ratio” used to define the deformation from local denting to global bending, was introduced to better understand the deformation patterns of the tubular members.

[Arany et al. \(2017\)](#) provided a structural design procedure for monopile foundation including the use of three design criteria, namely Ultimate Limit State (ULS), Serviceability Limit State (SLS) and Fatigue Limit State (FLS).

2.2.1.2 *Floating structures*

The structural analysis of the truss and tower of a semi-submersible platform called WindFloat (shown in Figure 1.13) using FE analysis was given by [Roddi et al. \(2010b\)](#), who demonstrated that the main horizontal bracing elements were the critical parts and the wind load was the leading factor in the structural design of the tower. A deficiency of using truss element in FEM is that the local buckling of the components cannot be captured especially for the large cylinders. Note that the local buckling design is important for the large cylinders, and it probably dominates the structural design of the cylinders.

With regard to floating structures, a methodology of the dimensions calculation of a semi-submersible platform called WindFloat and a 3D FEM based on ANSYS for the static strength assessment were provided by [Hussein et al. \(2013\)](#). The study obtained the new dimensions of the semi-submersible platform with a minimum geometry and showed that

the middle part of column supporting the tower had the highest stress in the three supporting columns. It should be pointed out here that, the dynamic response is important for offshore structures. The structural static analysis without considering the dynamic effect may underestimate the stress results.

[Lefebvre and Collu \(2012\)](#) used the static numerical simulation to assess the structural strength of a tri-floater platform shown in Figure 2.7. They found that the strength fulfilled the requirements of structural design (the strength utilization of columns and bracings were 67% and 47%). The environmental loads considered in their study were relatively simple. For example, the effect of the direction of the environmental loads has not been considered, and the constant thrust force was adopted which cannot reflect the dynamic motion in the marine environment.

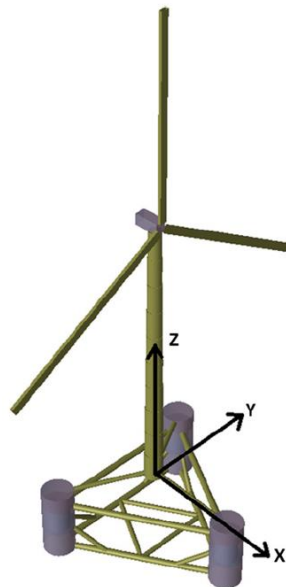


Figure 2.7 Tri-floater platform provided by [Lefebvre and Collu \(2012\)](#)

The structural strength of a tri-floater floating platform supporting vertical axis wind turbines was studied by [Liu et al. \(2018\)](#) using finite element method. They demonstrated that the wind load leads to high stresses in the structure when compared to the wave and current loads, and the direct compressive stress is more critical than the bending stress in supporting tubes.

[Kim and Paik \(2017\)](#) developed an optimization technique for hull structures to minimize structural weight, time cost for the design process and maximize structural safety. In the traditional hull structural design, the scantlings of hull need to be revised by designers to carry the yield and buckling strength evaluation. In this paper, an automated procedure was developed to carry out the ultimate strength analysis of hull and efficiently obtain the scantlings of hull. Moreover, the non-linear finite-element method was used to accurately calculate the internal force in order to reduce the overdesign and underestimate of structural elements. The result shows that the required time cost of the finite element analysis and the mass weight of the hull are reduced by 20% and by 3% respectively. Note that, it is important and also valuable to consider the manual labour of construction, transportation and installation in practical projects because these labour costs account for a large proportion in the project costs.

[Hu et al. \(2016\)](#) performed the finite element analyses to assess the structural stresses of the Spar type FWT. FAST and SESAM code were used to conduct fully-coupled dynamic simulations and finite element analysis. It was found that the stress concentration occurred in the top and base of the tower. The wind turbine has a higher stress value in the rated operational condition than that in the extreme sea state condition, due to the large wind effect under the rated operational condition.

Sectional forces and moments of a semi-submersible FWT modelled by using finite element method and a 1:30 scaled model test were studied by [Luan et al. \(2017\)](#) and [Luan et al. \(2018\)](#). The study demonstrated that the wind load contributed most to the stresses in structural components and identified the location of the most critical structural components.

Apart from foundation, other components such as wind turbine tower, mooring design and wind turbine blades have also been studied in terms of the structural analysis and design. For example, the structural reliability of the wind turbine blade and tower of a bottom-fixed wind turbine under extreme loading conditions is investigated by [Abdallah et al. \(2016\)](#). The optimization and design of a wind turbine tower for a semi-submersible floating platform is provided by [Young et al. \(2017\)](#). The mooring system for FWTs was designed by [Campanile et al. \(2018\)](#) considering the wind turbine in parked condition and mooring line fault condition. A preliminary cost, the line number and line scope of

mooring system were investigated in this study. The mooring line tension and fatigue for a FWT were predicted by [Cevasco et al. \(2018\)](#). The reliability assessment of the blades of wind turbines in the ultimate limit state was carried out by [Toft et al. \(2011\)](#). Different distribution of defects in blades were considered in this assessment.

The study of optimization design of offshore structures mainly focusses on mass reduction, although other factors should also be considered in the optimization, such as the labour cost, the construction method and transportation of the structures. Moreover, the structural analysis is simply based on the simplified assumptions. For example, the linear material properties and/or small displacement assumptions are normally used in the structural FE model to facilitate the numerical simulation. In addition, the static structural analysis is usually carried out in the optimization, which neglects the inertia force induced by the dynamic response. These simplifications may lead to inaccurate results obtained in the structural analysis and corresponding structural optimization. In Chapter 3, the geometrical and material nonlinearities, mooring system and the inertia force will be taken fully into account.

2.2.2 Design codes of environmental loads for offshore structure

At present, analysis, design and installation of OWTs usually rely on the existing guidelines developed by the offshore ships, oil and gas industry ([API, 2014](#), [DNVGL, 2015](#), [DIN, 2005](#)). However, the current experience and design codes used for relatively large scale structures such as gas & oil platforms and ship hulls may not be applicable for small-diameter component of OWTs (such as spar-buoys and some semi-submersible platforms). Furthermore, these standards were developed by mainly considering the wave loads only, while for OWTs the wave and wind load coupling effect needs to be considered. Hence, some specific guidelines are also developed for design of wind turbine structures.

The standards [ABS \(2020\)](#), [BV \(2019\)](#) and [DNVGL-RP-C205 \(2020\)](#) present the calculation methods of environmental loads applied to FWTs. In wind loading calculation, rotor thrust force and wind forces on exposed structural components are mainly considered in these codes. Wind loads and pressures are determined based on analytical methods or wind tunnel tests using a representative model of FWTs. Wave forces acting

on the FWT can be categorised into those acting on slender members and those on large members. For calculation of wave forces on slender members that do not significantly alter the incident wave field, semi-empirical formulations, such as Morison's equation may be used. As for a large structure, potential flow theory based on wave diffraction-radiation models is generally employed.

In order to maximize or minimize a loading effect for the FWT, design load cases are defined. The standards [ABS \(2020\)](#), [\(IET, 2019\)](#) [BV \(2019\)](#) and [DNVGL-RP-C205 \(2020\)](#) give the design load cases with different load combinations and safety factors including normal case, accidental case, fatigue case, installation, maintenance and repair case, etc.

2.3 Failure mechanism of components in offshore wind industry

Section 2.2 mainly presents the optimization design and structural analysis of entire offshore devices. In this section, the structural performance of individual components, which are widely used in offshore wind industry, is discussed.

2.3.1 Ultimate strength and buckling of offshore structures

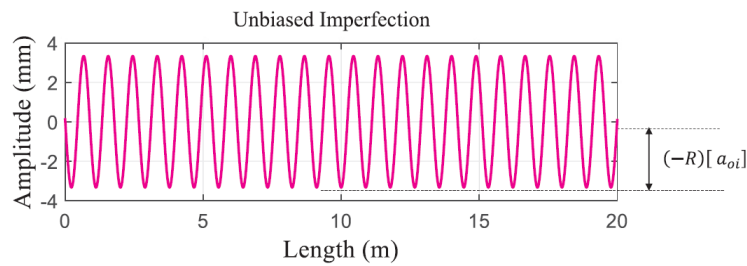
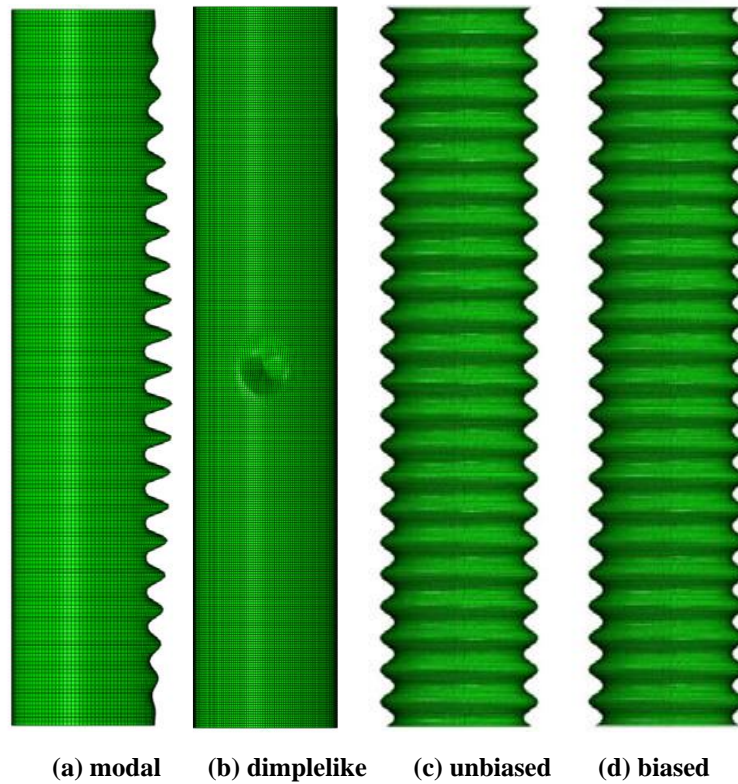
Shell structure is a popular structure adopted in offshore structures, for example, the wind turbine towers and foundations or platforms. In the complex marine environment, the shell structure would bear axial force, bending moment, torsion, shear, internal or external pressure. In order to enhance the stability and strength of a curved shell, stiffeners are adopted extensively in offshore structures. Ring stiffeners are proportioned to act against external pressure. Longitudinal stiffeners usually called stringers are used to provide additional strength and stiffness in the axial direction.

Since the early twentieth century, theoretical analysis method was the main tool to investigate the structural behaviour of cylindrical shells. [Windenburg and Trilling \(1934\)](#), [Von and Gunther \(1952\)](#), [Von and Windenburg \(1933\)](#) provided the theoretical equations to calculate the buckling load of cylindrical shells. Since then, the boundary layer theory ([Shen, 1998](#)), the structural orthotropic theory ([Andrianov et al., 2006](#)), the energy method, Galerkin's method, the perturbation method ([Shen, 2004](#)), the refined beam theory ([She et al., 2017](#)) and the Donnell shell theory etc. have been proposed and used in the study of buckling behaviours of the shell structures.

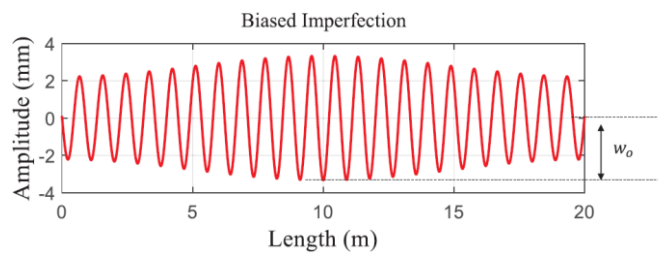
With the rapid development of computer technology, numerical modelling has been developed for analysing the buckling behaviours and ultimate strength of complicated shell structures. There are numerous studies on the buckling behaviours of cylindrical shells subjected to one loading condition. The loading of uniform axial compression is a common loading case. The first theoretical prediction of cylindrical shell buckling was carried out based on axial compression in the early 20th century (Southwell, 1914). However, the results of experiment and theoretical prediction vary dramatically in early tests and the former could be 30% lower than the latter (ECCS, 2013). Therefore, in order to have an accurate prediction of ultimate strength and buckling behaviours of cylindrical shells, many aspects have been studied by using numerical modelling and/or experiments.

- Effect of imperfection

Kumar Yadav and Gerasimidis (2019) used finite element modelling to study the effects of four geometric imperfection profiles including modal, dimple like, unbiased and biased shapes (Figure 2.8) under bending. They found that the influence of the dimple like imperfection was minimum (6% reduction in load carrying capacity compared with perfect cylinder) and the reduction in load capacity due to biased imperfection was maximum (18% reduction in load carrying capacity compared with perfect cylinder). Li and Kim (2022) studied the effect of initial geometric imperfection on the ultimate buckling strength of cylindrical shell under axial compression based on numerical modelling and design codes. It was found that the prediction of the ultimate strength was conservative, and the ultimate collapse and capacity were sensitive to the initial geometric imperfection. The experiments of cylindrical shells with different magnitudes of imperfections under uniform external pressure were tested by Fatemi et al. (2013). It was found that, when the depth of imperfection became larger, the buckling capacity reduced more sharply, and the imperfection had the smallest effect on the specimens with lowest height/radius and highest radius/thickness ratio. Imperfection sensitivity of an elastic cylinder under partial axial compression was carried out by Song et al. (2004). Their results, obtained based on the nonlinear finite element analysis, showed that the imperfection with weld depressions caused the lowest buckling load.



(f) imperfection amplitude for unbiased profile



(g) imperfection amplitude for biased profile

Figure 2.8 Four imperfection profiles from Kumar Yadav and Gerasimidis (2019)

- Effect of boundary conditions

The effect of boundary conditions is important in the structural study of cylindrical shells. Because of experimental difficulties, there are relatively few studies focussing on the boundary conditions. Simply-supported and clamped conditions are the two classical boundary conditions in experimental studies. In the simply-support conditions the

displacement is radially restrained, while in clamped conditions all displacements and rotations are restrained. Therefore, the deflection of the unstiffened shells with clamped conditions is reduced by 80% when compared with those with simply-support conditions, and the deflection is reduced at least 45% when compared with the stiffened cylindrical shells (Temami et al., 2018). Due to the less restraint of a simply-supported boundary, the buckling capacity of the shells drops faster with increasing length (Fajuyitan et al., 2018, Fajuyitan et al., 2015). As for the other types of boundary conditions, Evkin et al. (2019) studied the local buckling of cylinders under axial compression with six different boundary conditions. The types of boundary conditions are shown according to Figure 2.9 and Table 2.2. It was shown that the cylinder with type 4, the stiffest boundary condition, has the highest buckling load among these boundary conditions. While the cylinder with type 1 boundary condition has the lowest buckling load which is 11.7% lower than that of the cylinder with type 4.

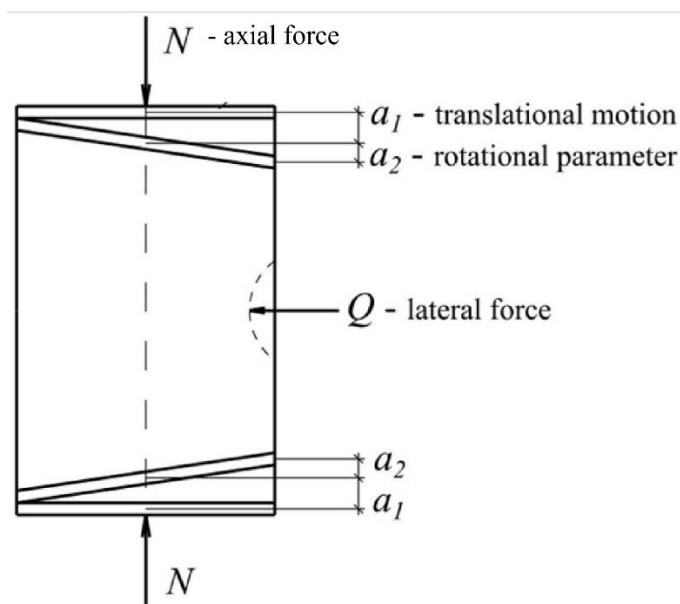


Figure 2.9 Loading conditions in the experiments (Evkin et al., 2019)

Table 2.2 Types of boundary conditions (Evkin et al., 2019)

Type 1	Type 2	Type 3	Type 4	Type 5	Type 6
Nonuniform a_1, a_2	$a_1=0, a_2$	Nonuniform $a_1, a_2=0$	Uniform $a_1, a_2=0$	Uniform $a_1, a_2=0$, release radial displacements	fixed and uniformly distributed compressive load

- Effect of length to radius ratio & radius to thickness

The length (L), radius (r) and thickness (t) are the basic geometric parameters to investigate the structural behaviour of cylindrical shells. According to a parameter $\omega = L/\sqrt{rt}$ defined in [EN1993-1-6 \(2007\)](#), the cylinder can be categorised to short cylinders ($\omega \leq 17$), medium cylinders ($1.7 < \omega \leq 0.5(\frac{r}{t})$) and long cylinders ($\omega > 0.5(\frac{r}{t})$). For a short cylinder under axial compression, the failure mode is dominated by local column buckling, and the buckling capacity reaches to a relatively high level. As for a medium one, the middle part cannot be restrained strongly and the maximum stress is slightly lower than the classical elastic critical buckling stress (with about 15% reduction) ([Fajuyitan et al., 2018](#)). Similarly, the buckling capacity of long cylinders experience a larger reduction. The thickness has a great effect on the stability of cylindrical shells, which significantly influences their ultimate strength. Some experimental and FE results have shown that with the change of r/t and L/r , the deviation of the buckling load was changed dramatically ([Ifayefunmi, 2016](#), [Zhu et al., 2018](#)).

A few studies have been carried out on the combined effect of axial loads and bending. [Jin et al. \(2021\)](#) studied the buckling behaviour of steel cylindrical shells under combined axial compression and bending. They found that the buckling behaviour of the shells was significantly affected by different imperfection profiles, radius to thickness ratio, slenderness ratio and eccentricity. In this study, the ratios of diameter-to-thickness are restricted to 40 and 97. The buckling behaviour of the thinner cylinders has not been studied.

In summary, above-described studies mainly focussed on the buckling strength of unstiffened cylindrical shells subjected to one loading condition to examine the effects of different parameters, e.g. length-to-radius ratio, radius-to-thickness, imperfection profiles, boundary conditions. Thus, these parameters need to be considered when the ultimate strength and buckling behaviour of the cylindrical shell under the combined load effect are carried out.

As for stiffened shell, [Zhao et al. \(2017\)](#) proposed a hierarchical grid-stiffened cylindrical shell under axial compression to avoid local buckling. [Thang Do et al. \(2018\)](#), [Do et al. \(2021\)](#) and [Cerik \(2015\)](#) studied the ultimate strength of locally damaged steel stiffened

cylinders. It is shown that the strength reduction of stringer-stiffened cylinders with local damage subjected to external pressure was extremely low when compared to that of the intact stringer-stiffened cylinders (Thang Do et al., 2018), while the strength of ring-stiffened cylinders under external pressure was significantly reduced compared to that of the intact ring-stiffened cylinders (Do et al., 2021). The strength reduction of ring-stiffened cylinders with local damage under axial compression was significantly reduced compared to that of the intact ring-stiffened cylinders, while that of the orthogonally stiffened cylinders was not dramatic (Cerik, 2015). Shi et al. (2018) investigated the effect of pitting on the stiffened panels under compression and derived a formula to predict the ultimate strength of the stiffened panels with pits.

2.3.2 Fatigue study of offshore structures

Most fatigue studies have focused on the fatigue analysis and fatigue life predictions for bottom-fixed wind turbines, such as jacket structures. Chatziioannou et al. (2019) and Chatziioannou et al. (2021) carried out the low-cycle fatigue study of the steel welded tubular X-joints and components used in offshore wind energy structural systems by using experiments and numerical modelling, which provided a further understanding on fatigue behaviours and theoretical support for fatigue life prediction of piping components.

To reduce the fatigue load set for bottom-fixed wind turbine, a probabilistic load set (2048 design load cases) with realistic environmental data and a systematic reduced load set (1560 design load cases) with unidirectional wind, wave, and current were carried out by Häfele et al. (2018). It was concluded that the systematic reduced load set can be adopted to evaluate the fatigue damage for jacket substructures, and then the numerical effort of the jacket design process can be reduced by reducing the design load cases.

After static structural design according to an ultimate strength criterion, the redesign process of fatigue verification of a lattice-type foundation for offshore wind turbines based on frequency domain method was carried out by Long and Moe (2012). The impact on fatigue of thrust and wave loading were carried out separately and the fatigue cycles were counted using the Dirlik method. In order to meet the fatigue life requirement, the thickness of the tubes was increased so that the result showed that the mass of the jacket foundation increased more than 30% compared with the ultimate strength result.

The effect of damping (structural, aerodynamic, hydrodynamic and soil damping) on the fatigue life of monopile foundation for FWTs was studied by [Rezaei et al. \(2018\)](#). Using time-domain finite element modelling, the result demonstrated that an increase in overall damping reduces fatigue damage by up to 67% among all operational and non-operational conditions.

Fatigue loads of a bottom-supported offshore wind turbine were studied by [Marino et al. \(2017\)](#). Miner's rule, S-N curves and rainflow cycle-counting were used for fatigue damage accumulation and damage estimations. The result showed that, firstly, the aerodynamic loads were dominant in fatigue damage when compared with the nonlinear wave in operational condition, and secondly, the linear wave approach underestimates fatigue loads by a maximum of 15% when compared to the nonlinear wave.

In order to compare the fatigue assessment by using traditional methods, the thermographic measurement used to predict the fatigue limit was presented by [Corigliano et al. \(2017\)](#). The temperature of the S355 grade specimen was detected by an infrared camera during the fatigue test. The fatigue life predicted by the thermographic method was in good agreement with the experimental result of the steel specimens.

Meanwhile, there are some investigations of fatigue on FWTs. The fatigue life of the connections of WindFloat was analysed by [Roddier et al., 2010b](#)). Twelve sea states with the significant wave height ranging from 1.5 m to 12.5 m were adopted to obtain the stress of the connection. The results showed that critical fatigue damage occurred at the connections between bracings. After calculation, the minimum fatigue life of the connections was 670 years, which was more conservative than the target design life of 20 years. However, the stress value was assumed to be linear with the wave height. The stress of the connections between components is based on beam theory which may not capture the realistic stress of the tubular or shell elements.

[Kvittem and Moan \(2015\)](#) performed the time domain analyses of the nominal stress for the fatigue assessment of a semi-submersible platform for FWTs. In this study, the fatigue loads due to aerodynamic loads and hydrodynamic loads were calculated using BEM and potential flow theory with Morison's formula, respectively. Using Miner's rule, S-N

curves and rainflow counting, the fatigue assessment showed that the dominant cause of fatigue damage in the tower and pontoon was pitch motion. Moreover, misaligned wind and wave led to less fatigue damage of the tower and pontoon than the aligned load conditions.

Some other components of FWTs such as mechanical components inside the gearbox (Nejad et al., 2015), tower (Kvittem and Moan, 2015, Cheng et al., 2017, Li et al., 2018a, Li et al., 2018b), mooring lines (Li and Choung, 2016, Chen and Basu, 2018, Li et al., 2018b) were also studied by researchers. It has been found that the fatigue damage in FWTs is more serious than that in land-based wind turbines owing to the more complex and unstable environment (Nejad et al., 2015). So far, the realistic structural behaviours of the floating platform for FWTs have not been fully understood, which need to consider nonlinear environmental loads, nonlinear structural response, fluid-structure interaction and etc. It has been found that the linear wave assumption (Marino et al., 2017) or linear structural model (Qu et al., 2020) would significantly underestimate fatigue loads of OWT. Moreover, the realistic environmental conditions for fatigue need to be fully considered. The inadequate and excess design load cases may underestimate and overestimate the fatigue damage. Therefore, suitable environmental data and design load cases need to be investigated to perform a more accurate fatigue analysis.

2.3.3 Design codes of structural design for offshore structure

For a short perfect cylindrical shell subjected to uniform axial compression, the classical elastic critical buckling stress σ can be expressed as:

$$\sigma = \frac{E}{\sqrt{3(1-\nu^2)}} \cdot \frac{t}{r} \approx \frac{0.6E}{r/t} \quad (2.1)$$

or in terms of strain

$$\varepsilon = \frac{0.6}{r/t} \quad (2.2)$$

where E is the Young's modulus, ν is the Poisson's ratio 0.3, r and t are the radius and thickness of the cylindrical shell. However, with the increase of r/t , the stress result of above equations trends to be inaccurate. The comparison of the critical buckling capacity between the theoretical prediction and test data based on different r/t is shown in Figure 2.10. Considering the strength reduction due to large r/t ratio, an empirical equation (Jawad, 2004) for the elastic critical buckling stress σ based on Eq. (2.1) can be expressed as:

$$\sigma = \frac{0.6CE}{r/t} \quad (2.3)$$

where C is a reduction factor for the elastic critical buckling stress induced by imperfection and slenderness of the cylindrical shell. It can be expressed as:

$$C = 1 - 0.9 \left(1 - e^{(-1/16)\sqrt{(r/t)}} \right) \quad (2.4)$$

It should be noted that the effect L/r ratio has not been considered in Eq. (2.3). Euler's equation could be used to check the global column buckling. Hence, the equation can be modified as:

$$\sigma = \frac{\pi^2 EI}{(KL)^2 A} \quad (2.5)$$

where A is the cross sectional area, I is the moment of inertia, L is the length of cylinder and K is the factor accounting for the end conditions.

Similar with the reduction factor of Eq. (2.5) for the critical buckling stress due to axial compression, the other reduction factors due to different load effects such as external pressure and torsion recommended by various design codes are shown in Figure 2.11.

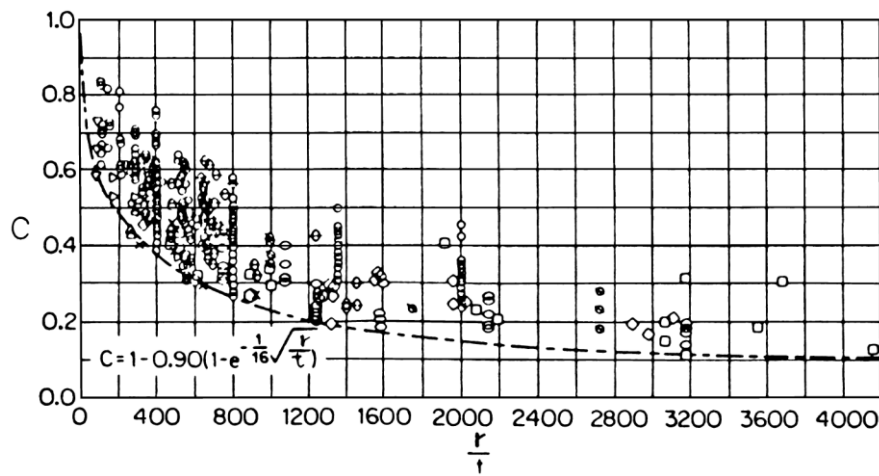


Figure 2.10 Comparison of Equation (2.1) and experimental results (Jawad, 2004)

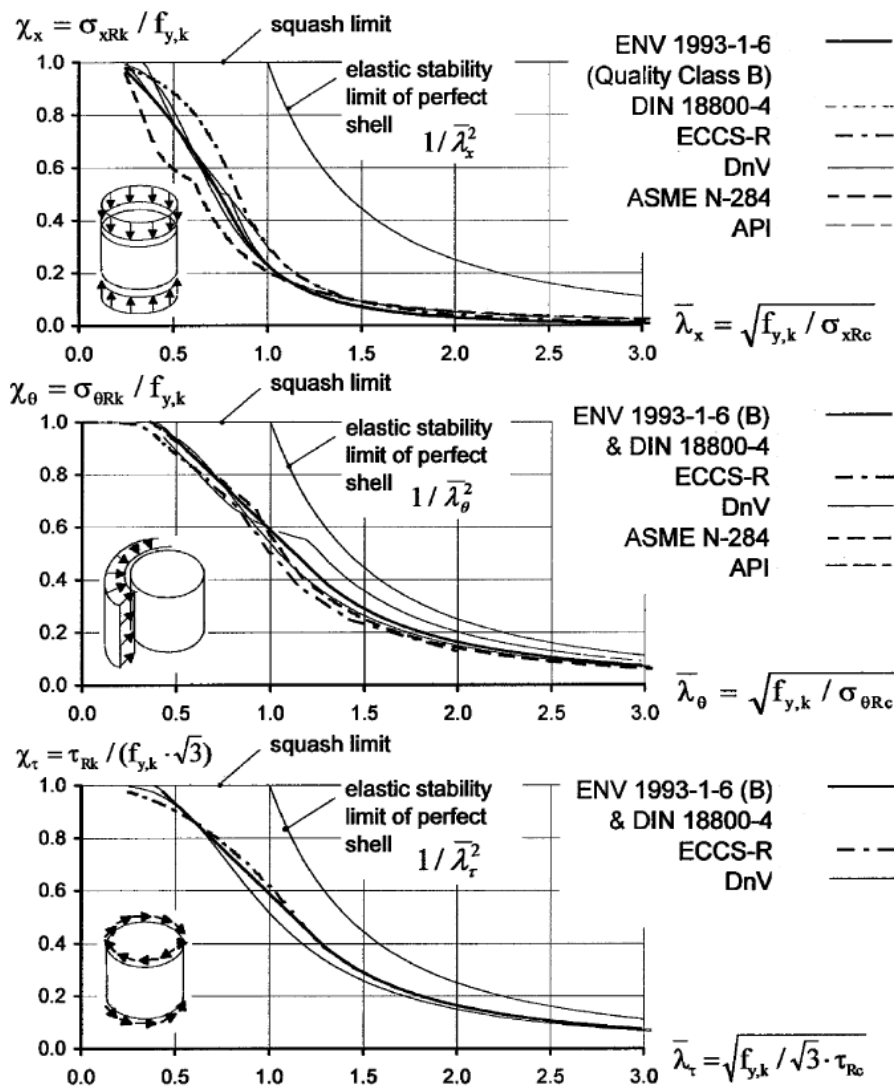


Figure 2.11 Shell buckling reduction factor curves for axial compression, external pressure and torsion in different design codes (Winterstetter and Schmidt, 2002)

The design load cases are used in structural analysis and design as the input loads. It should be noted that only the substructure of OWTs is covered by this section, and the superstructures such as rotor, nacelle, blade and tower are not covered. Generally, the choice of structural design codes depends on the material and structure types. Steel and concrete are popular materials for the substructure. Moreover, steel structure can be categorized into shell structures, tubular members, non-tubular beams, columns, and frames, plate structures, lattice structures, bolted and welded connections (DNVGL-ST-0126, 2018). DNVGL, which is an international accredited registrar and classification society, provides many design standards and guidelines for OWTs. EN (the European Union), ISO (International Standard) and BV (Bureau Veritas) have also published relevant specifications.

The main design process and the applications of various design codes for OWT are shown as follows: 1) understand environmental conditions: assess the environmental conditions at the offshore site, including factors such as wave loads, wind loads, and current velocities; 2) determine loadings: calculate the various loadings acting on the structure, including environmental loads, gravity loads, and other loads. The design code provided in section 2.2.2 will provide guidance on how to calculate and combine these loads. 3) select structural configuration: determine the appropriate structural configuration for the offshore structure. 4) perform structural analysis: conduct structural analysis using appropriate methods and software to evaluate the structural response under different loadings. 5) design structural elements: design the individual structural elements of the offshore structure, including members, connections, and foundations. The relevant design code needs to be selected based on the various material and elements. The summary of the structural design standards for substructure of OWTs is presented in Table 2.3. Follow the design code guidelines for sizing and detailing these elements to ensure that they meet the required safety and performance criteria.

Table 2.3 Summary of structural design standards for substructure of OWT

Steel	Plated structures	DNV-RP-C201 (DNVGL, 2010), EN 1993-1-5 (EN, 2006), EN 1993-1-7 (EN, 2007), NI 615 (BV, 2021)
	Shell structures	DNVGL-RP-C202 (DNVGL-RP-C202, 2019), EN 1993-1-6 (EN1993-1-6, 2017)
	Tubular structures	EN 1993-1-1 (EN1993-1-1, 2005), ISO19902 (ISO, 2020), NORSOK N-004 (N-004, 2004)
	Non-tubular beams, columns and frames	DNV-RP-C201 (DNVGL, 2010), EN 1993-1-1 (EN1993-1-1, 2005), EN 1993-1-5 (EN, 2006).
	Steel grades	DNVGL-OS-B101 (DNVGL, 2019), EN 10025
	Connection (bolt and weld)	ISO 898-1 (ISO, 2013), DNVGL-OS-C401 (DNVGL, 2020), DNVGL-OS-B101 (DNVGL, 2019), EN 1090-2
	Corrosion	DNVGL-RP-0416 (DNVGL, 2016),
	Fatigue	DNVGL-RP-C203 (DNVGL-RP-C203, 2016), EN 1993-1-9 (EN, 2005)

- Design codes for cylindrical shell and tubular structure

With a similar circular hollow section, the cylindrical shell is thinner (smaller ratio of diameter to thickness) than the tubular structure. Thus, the local buckling should be taken into full consideration in cylindrical shell structure design, which may dominate the entire design. Figure 2.12 shows the buckling reduction factor curves for axial compression based on shell structure design code EN1993-1-6 (2017) and tubular structure design code EN1993-1-1 (2005). The non-dimensional slenderness $\bar{\lambda}_x$ is related to the thickness and length of the cylindrical shell. The thicker the thickness or the shorter the length, the smaller the $\bar{\lambda}_x$. Figure 2.12 shows that, when the non-dimensional slenderness $\bar{\lambda}_x$ is larger than 0.2, the reduction factor of tubular structure is larger than that of cylindrical shell. This means that the buckling resistance of cylindrical shell is more sensitive to the variation of slenderness $\bar{\lambda}_x$. Therefore, the structural design for cylindrical shells and for tubular structures should use different guidelines based on their different structural behaviours.

According to the circular hollow tubular section classification provided by EN1993-1-1 (2005) in Figure 2.13, if $d/t > 90\epsilon^2 = 59.4$ (where yield strength $f_y = 355$ MPa), the structure is defined as shell structure and therefore the shell structure design code EN1993-1-6 should be adopted. In this thesis, shell structure is adopted to study in Chapter 4 and 5.

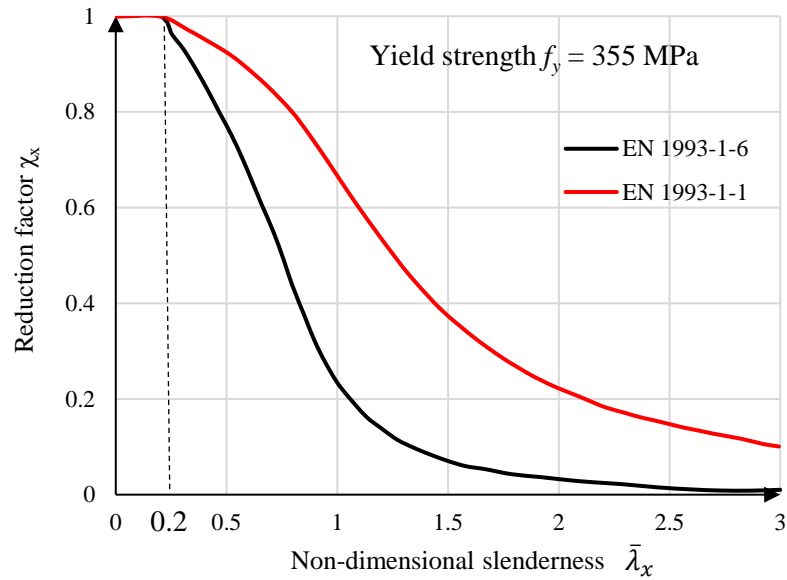


Figure 2.12 Buckling reduction factor curves for axial compression based on EN1993-1-6 (2017) and EN1993-1-1 (2005)

Tubular sections						
Class	Section in bending and/or compression					
1	$d/t \leq 50\varepsilon^2$					
2	$d/t \leq 70\varepsilon^2$					
3	$d/t \leq 90\varepsilon^2$					
	NOTE For $d/t > 90\varepsilon^2$ see EN 1993-1-6.					
$\varepsilon = \sqrt{235/f_y}$	f_y	235	275	355	420	460
	ε	1,00	0,92	0,81	0,75	0,71
	ε^2	1,00	0,85	0,66	0,56	0,51

Figure 2.13 Circular hollow tubular section classification in (EN1993-1-1, 2005)

2.4 Research gaps

This literature review presents the effect of environmental forces on offshore structures, current research on the structural analysis, design and specifications of FWTs, as well as the structural behaviours of the components used in FWTs.

The effect of environmental forces on the dynamic response of FWTs has been extensively studied, however the structural performance induced by those forces are less

well understood. The existing studies on the structural behaviours of offshore structures are mainly on the bottom-fixed wind turbine or floating platform for gas/oil industry. Due to the severe environmental forces and wave-wind interaction, floating platforms for the wind turbines have more complex structural behaviour compared to the bottom-fixed foundation and floating platform for gas/oil industry. The structural behaviours of the components and their connections used in the floating platforms have not been well studied. The relevant studies mainly use simplified environmental forces or structural models, for example, aerodynamic force is simplified as a constant point load; beam element is used to replace the structure of the platform; linear material properties and linear geometric analysis are adopted in the structural model. In this thesis, a more accurate input of environmental force (considering the effect of fluid structure interaction and the motion of the platform), and shell structure considering geometrical and material nonlinearity are adopted for the semi-submersible platform.

In regard to structural analysis, the structural optimization was commonly regarded as an element dimensioning problem for minimizing the total structural weight. The purpose of minimizing the weight is to reduce the cost of the offshore project. Thus, the cost can be affected by human resources, transport, and future O&M cost, which are considered to improve the financial management.

In terms of numerical simulation, although the traditional hydrodynamic and structural analysis software are available, the integrated modules of structural analysis for FWTs is still relatively rare. Normally, the hydrodynamic and structural analysis are conducted independently. The main issue is the load transfer from the hydrodynamic analysis to the structural analysis. Although there are some studies of hydro-structure coupling of CFD and FEA, the objects studied mainly focus on ship hulls or turbine blades. Moreover, it requires high computer configuration and expensive computational efforts. Therefore, an efficient load transfer mechanism from hydrodynamic model to structural model for FWTs is developed in this study.

Cylindrical shell structures are widely used in the offshore industry. The existing research mainly focuses on their response to a single load such as the axial compression, external pressure or bending. The failure mode of the cylindrical shells under the action of combined loads is heavily dependent on the geometry of the shell and the combination of

the loadings. There is a lack of research on the ultimate buckling strength and buckling behaviours of large cylindrical shells with specific physical parameters such as imperfections and radius-to-thickness ratios when subjected to various combined loads. The structural design of FWTs is derived from the offshore ships, oil and gas industry. The design methods, calculation process and safety factors thus need to have more evaluations.

Based on the above literature review, it is clear that further research is needed for the analysis and design of semi-submersible platform for FWTs under complex marine environments. The aim of this PhD project is to fill the above identified research gaps. The investigations carried out in this PhD project include: (1) A coupled fluid structure interaction simulation for global structural analysis of the semi-submersible platform is developed. This simulation method considers the structural nonlinearity, wave-wind interaction, fluid-structure interaction, mooring system and inertia force induced by dynamic motions of the platform. This simulation method could have a wider usage in the relevant research or industry such as the effect of irregular waves on the structural behaviours of the floating structure or other types of FWTs. (2) After the global structural analysis, the cylindrical shells, as the main structural component of the platform, is targeted to assess the code-based structural design. The different design standards for shell structures are compared. (3) In order to have a comprehensive understanding of the buckling behaviour of cylindrical shells, a wide geometric range covering short, medium and long cylinders with various radius to thickness (r/t) ratios are used to study the ultimate strength and buckling behaviours under combined load effects. (4) Based on the results obtained in (3), the accuracy of the relevant design codes for FWTs are evaluated. Finally, a reliability analysis of the relevant design codes is conducted and the recommended modification of partial safety factor γ_M is proposed to ensure the target reliability level for offshore structures are achieved.

2.5 Methodology

Different theories and methods are adopted to attain the research objectives:

- Morison's equation is adopted to calculate the wave load when the wave length is five times larger than the cross-sectional dimension of the member.

- EN1993-1-6 (2007), EN1993-1-6 (2017) and DNVGL-RP-C202 are adopted in shell structure design.
- Potential flow theory with additional damping is used to calculate the hydrodynamic response and wave pressure on the floating platform.
- The Finite Element Method (FEM) is used to carry out the linear and nonlinear structural analyses of the entire floating structure as well as the individual structural components.
- Linear elastic analysis is carried out to identify the critical load case, the critical stress positions and the effects of waves, winds and wave-wind misalignment on the structural behaviour.
- Geometrically and materially nonlinear analysis is adopted to study the buckling behaviour and failure modes in comparison with the linear elastic analysis.
- The first order reliability method is adopted to carry out the reliability analysis of the code-based approach.

The methodology used in this study could be applied to offshore structures which have similar design considerations. For example, Morison's equation and potential flow theory can be adopted for other platform types to calculate the hydrodynamic loads. The coupled fluid structure interaction simulation can be adopted to accurately transfer the environmental load in the finite element modelling. Geometrically and materially nonlinear analysis can be used for similar structures to study the structural performance.

CHAPTER 3 – NONLINEAR STRUCTURAL ANALYSIS OF A FLOATING WIND PLATFORM

Floating wind turbines (FWTs) operate in the complex marine environment and sometimes encounter extreme load conditions. The floating foundations that support the FWTs can be categorised into tension leg platforms (TLP), spar buoys, barges and semi-submersible platforms (SSPs). Compared with the others, SSPs have the best performance on pitch and roll motions as they have a large water plane and heavy ballast to counter (Karimirad and Michailides, 2015), which is important to achieve stability of the entire system. Moreover, SSPs are more flexible to be transported and adaptable to large water depths (Zhao et al., 2020, Pérez-Collazo et al., 2015). However, due to their structural complexity and heavy self-weight, they still have a relatively high fabrication cost. This means that SSPs can be further improved with structural optimization to achieve cost-reduction. The aim of this Chapter is to investigate the nonlinear structural behaviour of the floating platform for FWT considering both material and geometrical nonlinearities. The combined effects of wind and wave will be studied, which will provide a baseline for structural component design and analysis in Chapters 4 and 5.

3.1 Research object

The WindFloat (Rodder et al., 2010a) developed by Principle Power is used as the structural system of FWTs in this study, as shown in Figure 3.1. The three columns connected by the pontoons and bracings have the same dimensions. Referring to the existing literature (Aubault et al., 2018, Aubault et al., 2011), the following assumptions are made: each column consists of two cylindrical shells, called internal and external columns (Figure 3.1); the internal columns, pontoons and bracings are connected as a load-bearing frame (Figure 3.1 (b)); the external columns cover the internal columns and withstand wave loads. Table 3.1 provides the main dimensions of WindFloat according to Aubault et al. (2011). The National Renewable Energy Laboratory (NREL) offshore 5 MW baseline wind turbine (Jonkman et al., 2009) is designed to be installed on one of the columns of the floating foundation and the main parameters of this wind turbine are shown in Table 3.2.

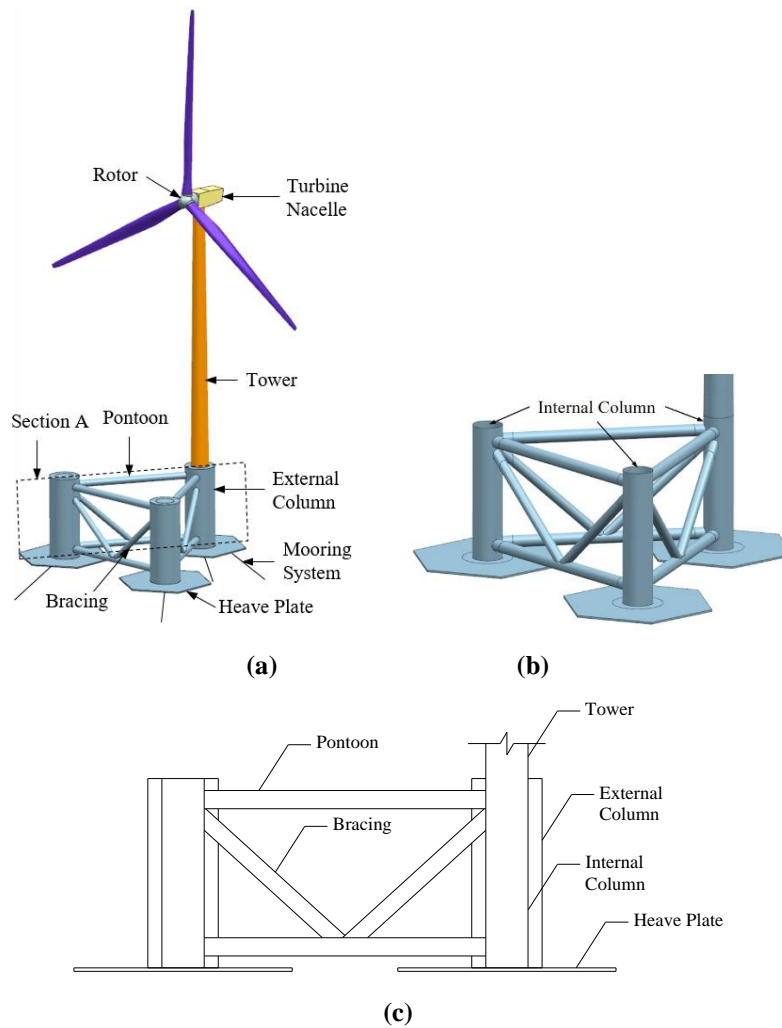


Figure 3.1 WindFloat concept: (a) floating wind turbine, (b) platform shown without the external columns, (c) section A

Table 3.1 WindFloat main dimensions (unit: m)

External column diameter	10
Internal column diameter	6
Length of heave plate edge	15
Column separation, centre to centre	46
Pontoon diameter	2.6
Bracing diameter	2.2
Tower diameter	4 – 6
Tower length	88
Rotor diameter	126

Table 3.2 5 MW turbine characteristics (Rodder et al., 2010a)

Rotor mass	135 mt
Nacelle mass	294 mt
Tower mass	425 mt
Tower diameter	4-6 m
Rotor diameter	126 m

3.2 Materials and Methods

3.2.1 Environmental loads

Environmental loads to be used for structural analysis and design should be based on the sea environment that the FWT will be located, and obtained by using relevant methods applicable for the target geometry of the structure (DNVGL-ST-0119, 2018). The following loads may need to consider over the service life of FWTs: wind load, hydrodynamic load induced by waves and current, earthquake loads, tidal effects, marine growth, snow and ice loads. In general, wind and wave loads dominate the structural design of a semi-submersible FWT, so they will be discussed in detail in this study. The sketch of the wave and wind on the FWT is shown in Figure 3.2.

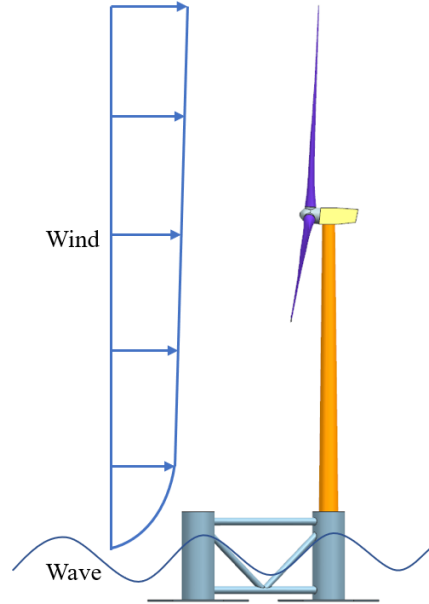


Figure 3.2 Wave and wind acting on the WindFloat

The loads acting on the FWT are the wave, wind, mooring line, gravitational and buoyancy forces. Therefore, the response of the floating platform can be described by:

$$m\ddot{x} = F_{hd} + F_{wind} + F_m + F_g + F_b + F_{hs} \quad (3.1)$$

where m is the mass of the system, \ddot{x} is the acceleration, F_{hd} is the hydrodynamic force including exciting force and radiation force, F_{wind} is the wind load, F_m is the mooring line load, F_g is the gravitational load, F_b is the buoyancy load, and F_{hs} is the hydrostatic load.

3.2.1.1 Wave load

The simulation of wave effect is carried out by potential flow theory. As mentioned in Section 2.1.1, this theory assumes that the fluid is incompressible, inviscid and irrotational.

The hydrodynamic force comprises the exciting force (including the Froude-Krylov force F_I and diffraction force F_d) and radiation force F_r :

$$F_{hd} = F_I + F_d + F_r \quad (3.2)$$

The wave potential due to incident, diffraction, and radiation waves can be written as:

$$\varphi(\vec{x})e^{-i\omega t} = \{(\varphi_1 + \varphi_e) + \sum_6^{j=1} \varphi_{rj}x_j\}e^{-i\omega t} \quad (3.3)$$

where φ_1 is the first order incident wave potential with unit wave amplitude, φ_e is the corresponding exciting wave potential, and φ_{rj} is the radiation wave potential due to the j -th motion with unit motion amplitude.

The total first-order hydrodynamic force can then be written as:

$$F_j = [(F_{Ij} + F_{dj}) + \sum_{k=1}^6 F_{rjk}] \quad (3.4)$$

The semi-submersible platform does not affect the incident wave potential, but it does influence the platform's radiational and diffraction potentials. As a result, the j -th component of the Froude-Krylov force due to the incident wave is:

$$F_{Ij} = -i\omega\rho \int_{S_{wet}} \varphi_I(\vec{X})n_j dS \quad (3.5)$$

The j -th component of the diffraction force is:

$$F_{dj} = -i\omega\rho \int_{S_{wet}} \varphi_d(\vec{X})n_j dS \quad (3.6)$$

The j -th component of the radiation force induced by the k -th unit amplitude motion is:

$$F_{rjk} = -i\omega\rho \int_{S_{wet}} \varphi_{rk}(\vec{X})n_j dS \quad (3.7)$$

The radiation potential φ_{rk} is divided into real and imaginary parts that produce added mass and radiation damping.

$$a(\omega) = \frac{\rho}{\omega} \int_{S_{wet}} Im[\varphi_{rk}(\vec{X})]n_j dS \quad (3.8)$$

$$b(\omega) = \frac{\rho}{\omega} \int_{S_{wet}} Re[\varphi_{rk}(\vec{X})]n_j dS \quad (3.9)$$

3.2.1.2 Wind load

The wind load acting on the wind turbine and tower is considered. In a structural analysis, the wind force on a structural component is affected by the shape, wind pressure and the projected area of the structural member (DNVGL-RP-C205, 2020). The shape coefficient can be obtained from wind tunnel tests or design guidelines. Similar to the wave loads, the wind loads can also be evaluated by solving the Navier-Stokes equations using CFD method.

A comparison of various methods to calculate the rotor thrust of a bottom-fixed wind turbine for wind speeds varying from the cut-in value of 3 m/s to the cut-out value of 25 m/s was carried out by Dong et al. (2019) and is shown in Figure 3.3. The comparison shows good agreement with regard to the trend of the rotor thrust across the various wind speeds. With the increase in the wind speed, the rotor thrust increases sharply, peaking at the rated wind speed (11.4 m/s) and, after that, drops sharply. The data provided by NREL and BEM stands for Blade Element Momentum which offers lowest computing cost among the other models, since this method assumes the wind flow is steady and the blades is divided into several sections to calculate the 2D aerodynamic loads. Note that the wake aerodynamics and the realistic 3D geometry of the blades are not considered in the model, which may have a large impact on the aerodynamics of the blade tip (Plaza et al., 2015) and the impact on the thrust is relatively small in the case of a small motion of the platform (Tran and Kim, 2015). In comparison, the Reynolds-averaged Navier-Stokes (RANS) method is based on a CFD model, which deals with the fully coupled dynamics and theoretically provides a more realistic prediction. However, the RANS method is the most costly and time-consuming among these models because the whole flow field around the 3D geometry of the wind turbine is simulated. Another approach called the vortex method is more accurate than BEM and less costly than CFD, which is used to investigate the unsteady flow with wake aerodynamics. The nonlinear vortex lattice method (NVLM) and the free wake vortex ring method (FWVR) are vortex methods, which consider the coupled rotor and wake aerodynamics. In NVLM, the wake flow is represented by vortex filaments. In comparison, the wake is simulated by vortex rings in FWVR to reduce the computing cost while retaining the basic physical properties of wake. Figure 3.3 shows a good agreement of the thrusts calculated by the different methods including FWVR, BEM,

RANS and NVLM. It should be noted that the thrust from NREL is slightly bigger than the other thrusts because the effects of the gravity (due to the rotor mass and shaft tilt) and inertial forces (due to the rotor inertia and acceleration/deceleration) of the rotor are considered. Specifically, according to Figure 3.4, the shaft tilt leads to the gravitational load F_g that is the component of gravity along the tilt angle. The acceleration/deceleration of the rotor leads to the inertial force $F_i=ma$ (m is the mass of the rotor, and a is the acceleration of the rotor). Both of the gravitational inertial forces are accumulated in the rotor thrust. In contrast, all the other models only consider the pure aerodynamic thrusts. Thus, for the sake of accuracy and on the conservative side, NREL's data are used in this study.

In this study, wind speeds of 7 m/s and 11.4 m/s are adopted as the moderate and rated wind speed condition respectively, in order to produce two very different magnitudes of rotor thrust that can be used to efficiently gain an initial understanding of the structural behaviour of the complex system. As the focus of this study is to test the effects of material and geometric nonlinearities on the global structural behaviour of a floating platform, a rigorous wind load prediction by taking into account the fluctuation of wind speed or a more realistic wind condition is unnecessary and considered as over costly. Therefore, simplified calculations of thrust based on NREL's data taking into account the unsteady thrust due to the motion of the FWT have been adopted. It should be noted that if the wind speed is larger than 11.4 m/s, the blades of the 5 MW wind turbine would rotate to reduce their projected area normal to the direction of the wind speed to reduce the rotor thrust, which is a protection scheme for the blades. Thus, the wind speed of 11.4 m/s is adopted to calculate the maximum rotor thrust.

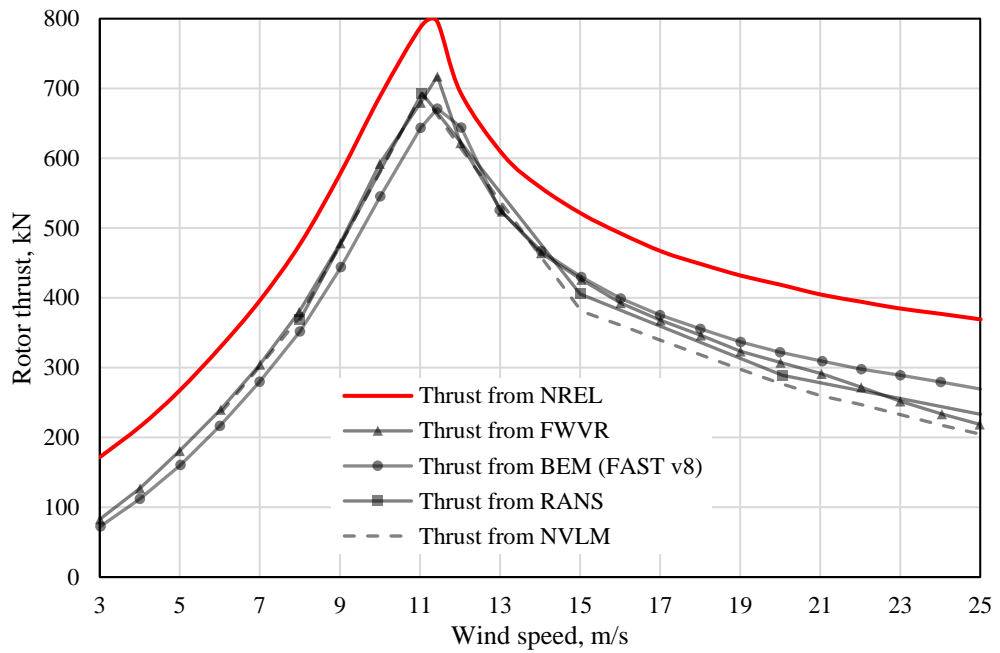


Figure 3.3 Thrust of a fixed NREL 5 MW wind turbine simulated with various methods (Dong et al., 2019)

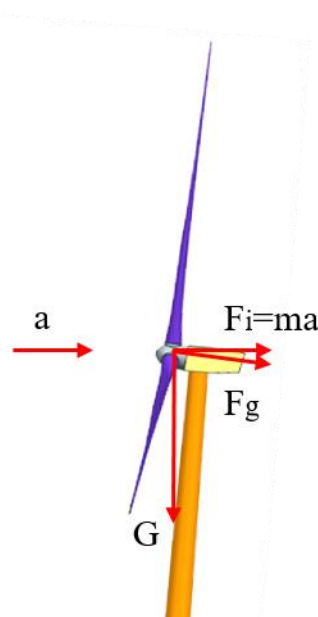


Figure 3.4 Gravitational and inertial forces on a rotor

The platform motion also contribute to the rotor thrust in FWTs (Wen et al., 2017, Li et al., 2018b, Lee and Lee, 2019, Tran and Kim, 2015). Cheng et al. (2019a) found that oscillating regularity on aerodynamic loads of wind turbine has the similar oscillating period as the incoming wave. To simulate the unsteady aerodynamic force, the thrust of

the FWTs is calculated under a set of sinusoidal winds. The speed of the sinusoidal wind, $V(t)$, is defined as:

$$V(t) = V_0 + V' \sin(\omega t) \quad (3.10)$$

where V_0 is the mean wind speed, V' is the wind speed due to platform motions of pitch and surge motion, and is being extracted straight from the numerical model, ω is the frequency of the platform.

The thrust of the FWT under a sinusoidal wind is defined as:

$$F(t) = F_0 + F' \sin(\omega t) \quad (3.11)$$

where F_0 is the mean rotor thrust of a FWT, which can be calculated by the rotor thrust of a fixed wind turbine (Figure 3.3), and F' is the thrust due to platform motions. This approach is limited by steady wind flow and regular waves, hence wind loading under a more complex or realistic wind and wave condition has not been considered.

3.2.2 Case studies of global model

A series of simulations are performed at different azimuthal angles under aligned and misaligned wave-wind conditions. As the floating platform is a symmetrical structure, five directions of wave and wind are considered: 0° , 45° , 90° , 135° and 180° defined in Figure 3.5. In addition to the five aligned wind-wave directions, a misalignment effect is considered with a wave-wind misalignment angle of 22.5° (Michailides et al., 2016). Referring to previous hydrodynamic analyses of FWTs using AQWA (Ren et al., 2020, Ma et al., 2019b), two environmental conditions, moderate and rated conditions, are considered in this study. In the rated condition, the wave condition with 9 m height is more extreme than the wind condition with 11.4 m/s wind speed. This is because that, as discussed before, the rotor thrust is reduced if the wind speed is larger than 11.4 m/s. Therefore, to evaluate the structural behaviour of the FWT under a combination of extreme environmental loads, these environmental conditions are selected.

Different wind speeds (U_w), regular wave heights (H), periods (T), directions of wave (α) and wind (β) are shown in Table 3.3. There are in total 40 load cases (LC) to investigate the individual effects of wave and wind, the critical connection positions, the most dangerous load cases of wind and wave, wave-wind misalignment effects and the different contribution of stress and deformation due to wave and wind.

Table 3.3 40 Load cases definition

No.	H (m)	T (s)	U_w (m/s)	α	β	Comments	Environmental conditions
LC1-5	3	8	0	0°, 45°, 90°, 135°, 180°	-	Wave only	-
LC6-10	0	0	7	-	0°, 45°, 90°, 135°, 180°	Wind only	-
LC11-15	9	10	0	0°, 45°, 90°, 135°, 180°	-	Wave only	-
LC16-20	0	0	11.4	-	0°, 45°, 90°, 135°, 180°	Wind only	-
LC21-25	3	8	7	0°, 45°, 90°, 135°, 180°			Moderate
LC26-30	9	10	11.4	0°, 45°, 90°, 135°, 180°			Rated (aligned conditions)
LC31, 32	9	10	11.4	0°	-22.5°, 22.5°	Wave and	Rated (misaligned conditions)
LC33, 34	9	10	11.4	45°	22.5°, 67.5°	Wind	
LC35, 36	9	10	11.4	90°	67.5°, 112.5°		
LC37, 38	9	10	11.4	135°	112.5°, 157.5°		
LC39, 40	9	10	11.4	180°	157.5°, 202.5°		

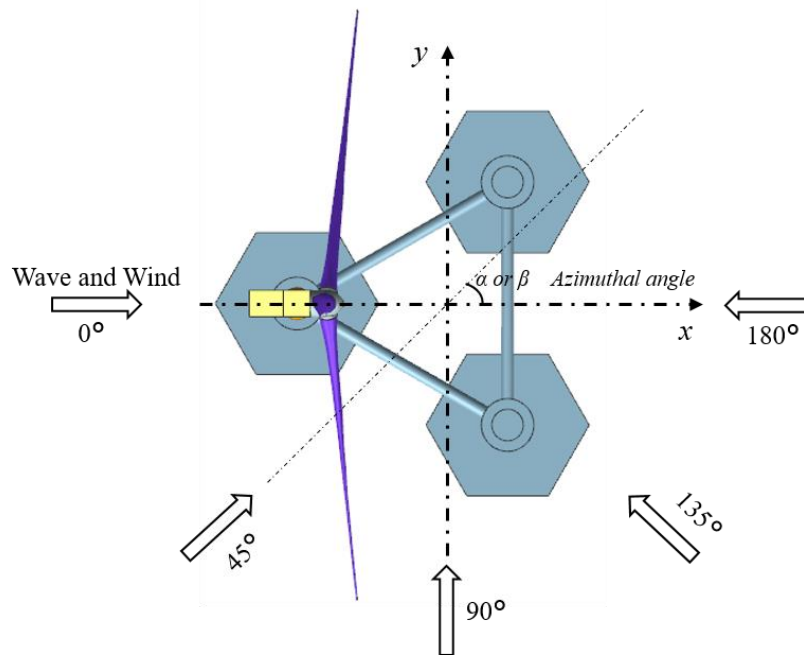


Figure 3.5 Wave and wind directions

The structural behaviours of the tubular components, tower base and the connections between components subjected to wave, wind and wave-wind alignment are examined in this study. The symbols/labels used to represent the sixteen connections and individual structural components are shown in Figure 3.6. The position label P1L stands for the left

end side connection of pontoon P1; the position label P4M stands for the middle connection of pontoon P4; EC1 stands for the external column 1; IC1 stands for the internal column in EC1, and TB stands for the tower base. In addition, ‘left’ and ‘right’ are defined for the target component in the planimetric position of Figure 3.6. If a connection is located on the left of a component, the connection is named as ‘L’.

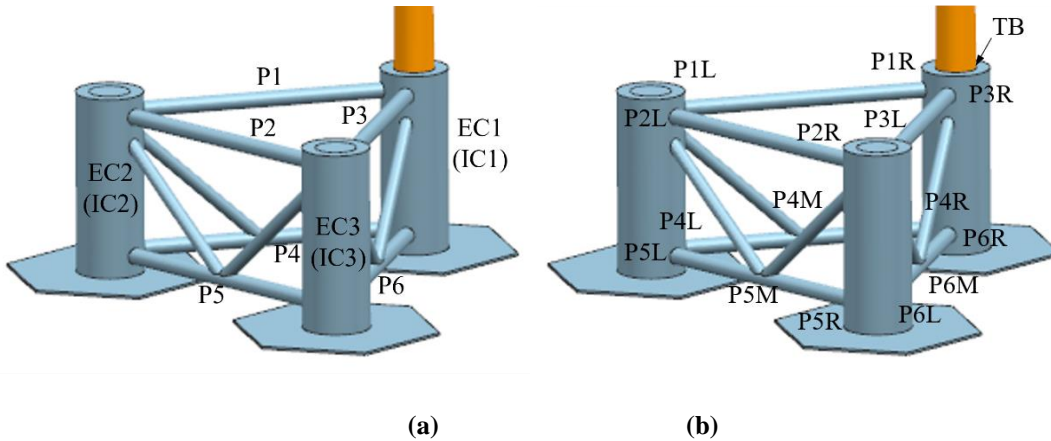


Figure 3.6 Positions of connections: (a) components numbers, (b) connections numbers

3.2.3 Numerical modelling using ANSYS

The hydrodynamic analysis is carried out by using ANSYS AQWA based on frequency domain. After that, a load-mapping program called AQWA-WAVE is used to transfer the wave pressure data to a structural analysis model, which is then used to investigate the structure behaviour of the FWT platform under combined wind and wave loads. The hydrodynamic, rotor thrust and structural FEA model (including mass model) are presented as follows:

3.2.3.1 Hydrodynamic model

The hydrodynamic model of the WindFloat floating platform is shown in Figure 3.7. Different from the structural model which needs to consider the internally reinforced structures, only the external surface is adopted in the hydrodynamic model. Furthermore, the external wetted surface elements (green part) are used to calculate the hydrodynamic force.

Morison's equation is commonly used to calculate the wave load on a slender member. According to this method, the cross section of the cylinder is neglected and the wave pressure on the elements cannot be obtained. Thus, potential flow theory is adopted in this study to generate the hydrodynamic data and detailed wave pressure on the shell element. The incident, diffracted and radiated wave forces acting on the structure are calculated by AQWA-LINE for selected wave periods and directions. In order to simulate viscous damping due to the heave plate, the equivalent linear damping values (Table 3.4) are input in the hydrodynamic calculation. A linear spring is used to replace the mooring system to offer a restoring force. Based on the constant stiffness K_G and the fairlead displacement X_F , the mooring force F_G can be obtained by:

$$F_G = -K_G \times X_F \quad (3.12)$$

This method is commonly used in the other studies due to its ease of modelling (Waris and Ishihara, 2012, Li et al., 2020a). In this study, the equivalent linear stiffnesses in surge, sway and yaw motion are provided in Table 3.5 to simulate the springs. In order to obtain an accurate hydrodynamic performance of the FWT, the dynamic characteristics of RAOs of this model are validated with the results provided by Aubault et al. (2011) in Section 3.2.3.7. Thus, it is believed that the hydrodynamic model has well captured the motion of the platform, which lays the foundation for accurate calculation of wave pressure coupled with platform motion.

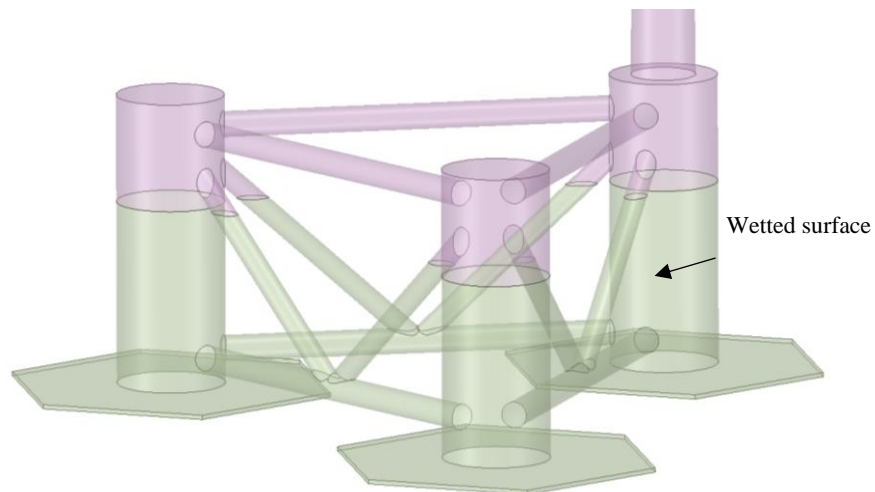


Figure 3.7 Hydrodynamic model of the WindFloat floating platform

Table 3.4 Dynamic Characteristics of the WindFloat in Heave, Roll and Pitch

	Period of Resonance (s)	Added Mass (kg) or Inertia (kg.m ²)	Hydrostatic Stiffness (N/m or N*.m/rad)	Critical Damping (kg/s)
Heave	19.2	1.90E+07	2.53E+06	1.57E+07
Roll	45.7	7.84E+09	2.97E+08	3.99E+09
Pitch	45.2	7.88E+09	3.05E+08	3.99E+09

Table 3.5 Dynamic Characteristics of the WindFloat in Surge, Sway and Yaw

	Period of Resonance (s)	Added Mass (kg) or Inertia (kg.m ²)	Equivalent mooring stiffness (N/m or N*.m/rad)
Surge	108.7	4.17E+06	29,270
Sway	136.6	4.17E+06	18,730
Yaw	71.5	2.80E+09	4.677E+7

3.2.3.2 Rotor thrust

In this section, the input rotor thrust is presented. It should be noted that the static curve is used to represent dynamic thrust, hence the impact of the turbine controller and turbulence near the blades has not been considered in this study. In terms of LC21 (a regular wave $H = 3$ m, $T = 8$ s with wind speed $U_w = 7$ m/s) shown in Table 3.3, due to the platform motions induced by the wave, the velocity of the rotor is $V\sin(\omega t) = 0.32 \sin\left(\frac{\pi}{4}t\right)$ m/s obtained from AQWA. Therefore, the speed of wind is:

$$V(t) = 7 + 0.32 \sin\left(\frac{\pi}{4}t\right) \text{ m/s} \quad (3.13)$$

which is shown in Figure 3.8. The minimum and maximum wind speed are 6.68 m/s and 7.32 m/s, respectively. According to Figure 3.3, the minimum and maximum rotor thrust can be obtained, which are 374.6 kN and 478.3 kN, respectively. According to Eq. (3.11), the rotor thrust of LC21 thus is:

$$F(t) = 427 + 52 \sin\left(\frac{\pi}{4}t\right) \text{ kN} \quad (3.14)$$

which is shown in Figure 3.10.

Similarly, the rotor thrust of LC26 follows the same calculation procedure. The wind speed of LC26 is:

$$V(t) = 11.4 + 1.5 \sin\left(\frac{\pi}{5}t\right) \text{ m/s} \quad (3.15)$$

which is shown in Figure 3.9. According to Figure 3.3, the rotor thrust for the wind speed of LC26 experiences decrease, increase, decrease, and then increase, which leads to a non-sinusoidal behaviour. Thus, the rotor thrust of LC26 is:

$$F(t) = 709 + 89 \cos\left(\frac{2\pi}{5}t\right) \text{ kN}, t \in (0s, 5s) \quad (3.16)$$

$$F(t) = 737 + 60 \cos\left(\frac{2\pi}{5}t\right) \text{ kN}, t \in (5s, 10s) \quad (3.17)$$

Figure 3.10 shows the rotor thrust of LC26.

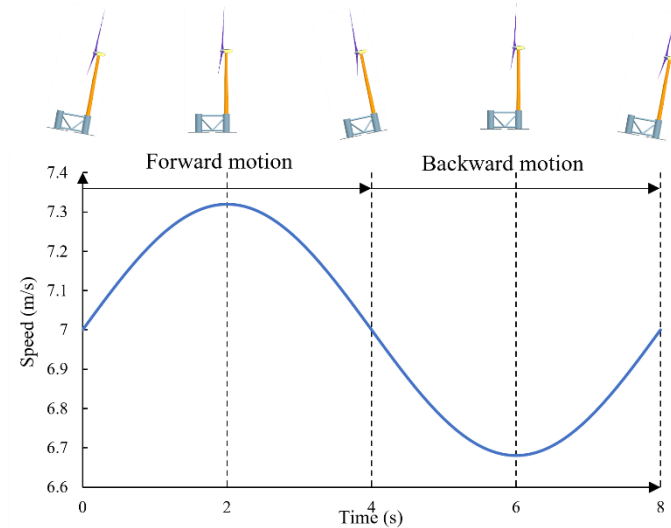


Figure 3.8 The speed of wind of LC21

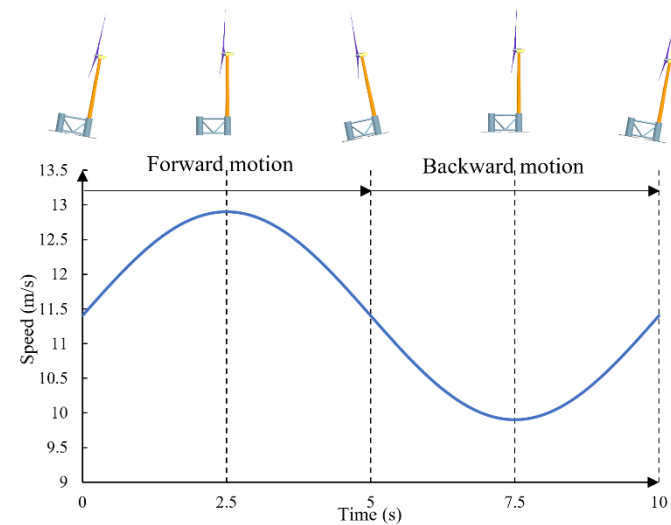


Figure 3.9 The speed of wind of LC26

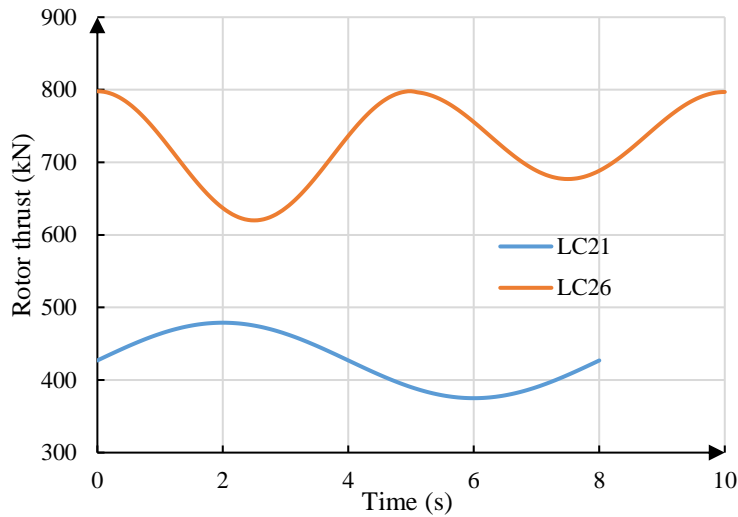


Figure 3.10 The rotor thrust of LC21 and LC26

3.2.3.3 Mass model

The mass model is used to describe the mass distribution of the entire structure, which is necessary to investigate the hydrodynamic response and structural behaviour of an FWT. In order to simplify the model and increase the computational efficiency, a point mass is used to represent the rotor and nacelle mass since these two structural components are not the focus of this study. In reality, there is an active ballast system in the platform, which is used to transfer water from column to column to lower the platform to its target operational draft and keep the tower vertical to improve the turbine performance (Roddier et al., 2010a). However, to simplify the modelling, the water ballast is also modelled as a point mass located at the bottom of each column.

3.2.3.4 Structural model

Equivalent static structural analysis was used to investigate the structural performance as such an analysis is less demanding in terms of computational cost compared with a dynamic analysis (Kim et al., 2021, Kim and Kwak, 2022). Unlike the static structural analysis, the equivalent static structural analysis considers the effect of the inertia force. The equilibrium equation could be expressed as $Kx = F_{external} = F_{wave} + F_{wind} - M\ddot{x}$, in which Kx represent the mooring line force, K is the equivalent stiffness matrix of the entire structure, F_{wave} is the wave pressure distribution, \ddot{x} and x are the acceleration and displacement of the system and F_{wind} is the wind load.

Shell 181 element in ANSYS mechanical module, which is suitable for analysing thin-walled shell structures with large deformations, is adopted to create the structural model (shown in Figure 3.11). This element can be used with three or four nodes, with six degrees of freedom at each node: translations in the x, y, and z directions, and rotations about the x, y, and z-axes. For regular cylindrical shells, a four-node element is more computationally cost-effective compared with a triangular mesh, thus it is used in this study. High strength structural steel, S355 (Moghaddam et al., 2020), is used for the platform, excluding the rigid heave plates, and its mechanical properties are given in Table 3.6. Considering material nonlinearity, the nonlinear stress-strain relationship shown in Figure 3.12 is adopted from Cheng and Becque (2016). The heave plate is attached on the bottom of each column to improve the stability of floating system by decreasing the pitch and heave motions. As the heave plates are not the focus of this study, they are assumed to be rigid bodies to reduce simulation time. The linear analysis (LA), geometrically nonlinear analysis (GNA), and geometrically and materially nonlinear analysis (GMNA) of the structural model are carried out respectively, the details of which are reported in Section 3.3.2.

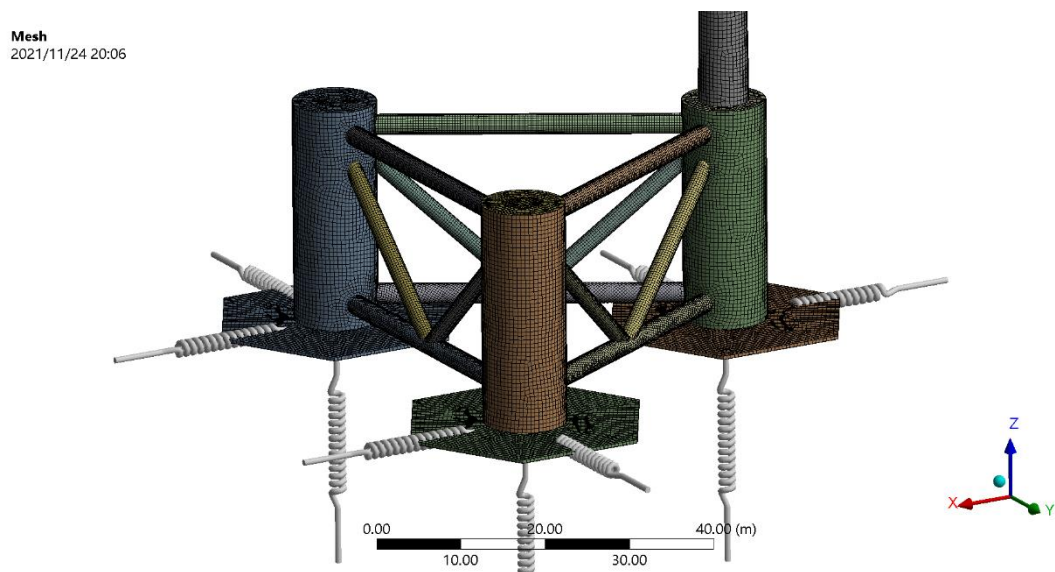


Figure 3.11 3D structural model of the platform implemented in ANSYS (with mesh)

Table 3.6 Material parameters of the platform

Item	Value
Material	S355
Yield strength (MPa)	355
Density (kg/m ³)	7850

Elastic modulus (MPa)	210,000
Poisson's ratio	0.3
Stiffness of mooring in x direction (N/m)	1.4159 e6
Stiffness of mooring in y direction (N/m)	1.3415 e6
Stiffness of mooring in z direction (N/m)	3.4935 e6

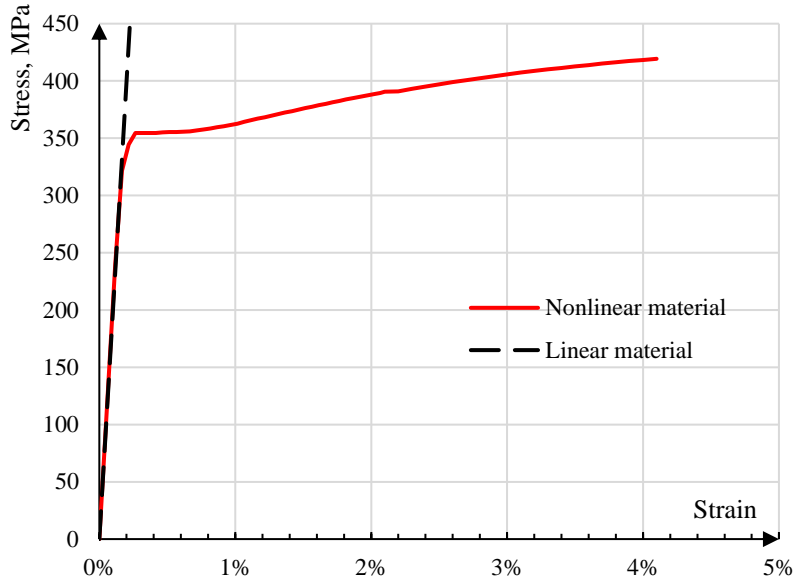
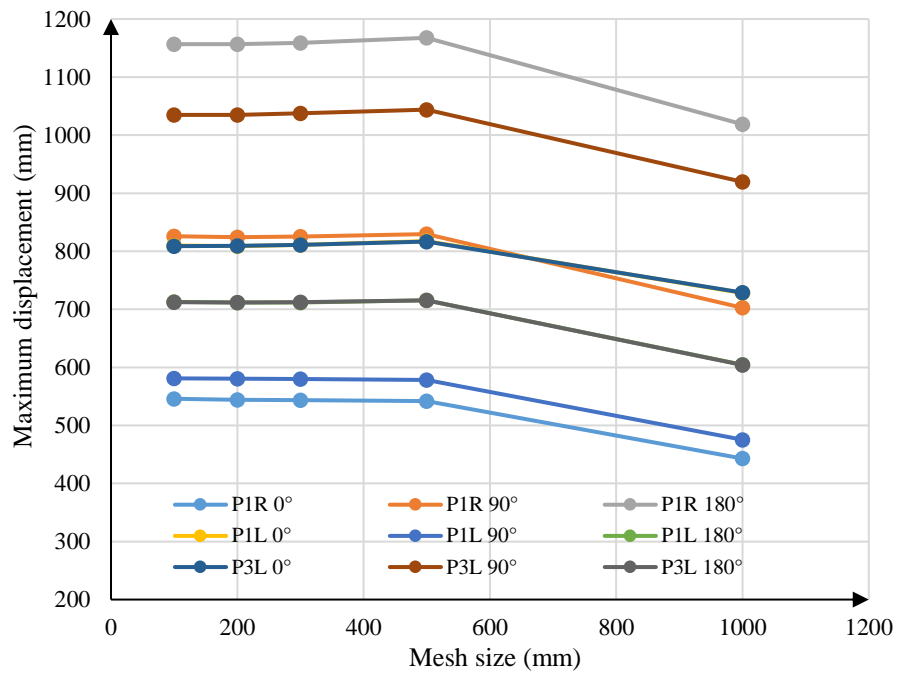
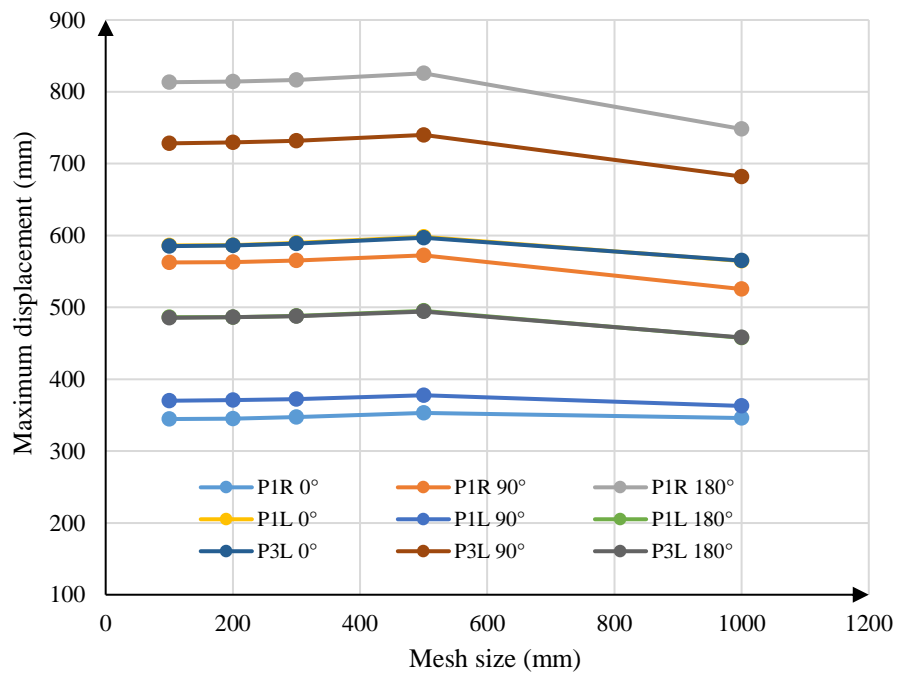


Figure 3.12 Stress-strain curve of S355

The size selection of mesh is an important issue in FEA. Reducing the mesh size is a classical strategy to achieve mesh convergence. Figure 3.13 shows the mesh convergence curves of the structural model. In this mesh convergence study, both moderate and rated environmental conditions introduced in Table 3.3 are adopted. 0° , 90° and 180° of environmental loads are adopted to consider the direction effect. Three connections P1R, P1L and P3L, which are located in the different columns, are used to consider the location effect. In Figure 3.13, the data of P1R 0° represents the maximum displacement of P1R under the 0° environmental loads. The maximum displacement is converged when the mesh size is smaller than 300 mm. The maximum errors between the mesh size of 100 mm and 300 mm are 0.77% and 0.45% for moderate and rated environmental conditions, respectively. Thus, a mesh size of 300 mm is adopted in FE modelling in this chapter.



(a) Wave: $H=9$ m, $T=10$ s; wind: $U_w=11.4$ m/s (rated condition)



(b) Wave: $H=3$ m, $T=8$ s; wind: $U_w=7$ m/s (moderate condition)

Figure 3.13 Mesh convergence of structural model

After determining the boundary condition, material properties and mesh size, the effect of inertia force is studied as follows based on a comparison of two models: one model considering inertia force (equivalent static structural analysis) and the other one neglecting inertia force (static structural analysis). Figure 3.14 and Figure 3.15 reflects the effect of inertia force on the maximum stress levels within the connections. In this

study, equivalent stress is adopted to evaluate the structural behaviour in stress level. Equivalent stress (also called von Mises stress) allows the three-dimensional stress state to be represented as a single positive stress value. In terms of the principal stresses σ_1 , σ_2 , σ_3 , the equivalent stress is expressed as: $\sigma_e = \sqrt{\frac{(\sigma_1 - \sigma_2)^2 + (\sigma_2 - \sigma_3)^2 + (\sigma_3 - \sigma_1)^2}{2}}$. It is found that, although the inertia force could increase the maximum equivalent stress in a connection by up to 32%, it will not affect the location of the worst loaded connection, and the increase of the maximum equivalent stress in the worst loaded connection is less than 10%.

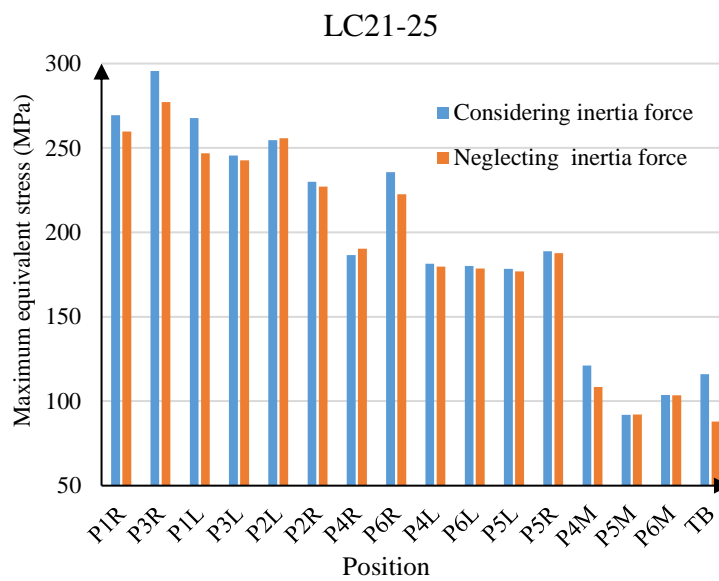


Figure 3.14 Comparison of the maximum equivalent stresses of the connections with and without considering inertia force in LC21-25

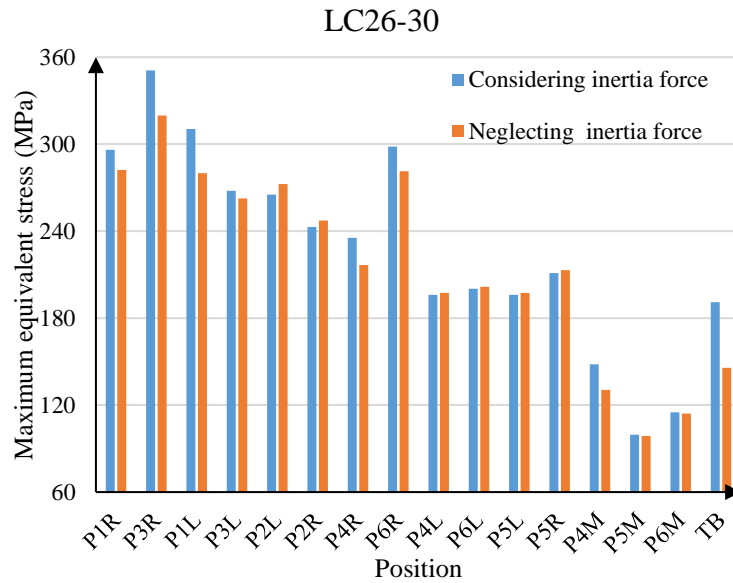


Figure 3.15 Comparison of the maximum equivalent stresses of the connections with and without considering inertia force in LC26-30

3.2.3.5 Boundary condition

In the existing literature, the mooring system were either modelled as a linear spring (Li et al., 2020a, Felix-Gonzalez and Mercier, 2016), or replaced by simply supported boundary conditions in the structural analysis to remove structural rigid movement (Qi et al., 2018, Liu et al., 2018). This section is to compare the two different boundary conditions, i.e., simple supports and springs, and select the more suitable one. GMNA of LC27 is adopted again in this section. Simply supported boundary conditions are applied to the bottom of each heave plate. The constraint conditions of the three heave plates are: constraint 1 (heave plate 1) $U_x=U_y=U_z=0$; constraint 2 (heave plate 2) $U_y=U_z=0$; constraint 3 (heave plate 3) $U_z=0$. The stiffness of linear springs is shown in Table 3.6, whose stiffness is equivalent to the restoring stiffness based on force-displacement behaviour of the mooring system in AQWA time-domain simulation.

Table 3.7 Stiffness of spring for the mooring lines

Item	Value
Stiffness of spring in x direction (N/m)	1.4159 e6
Stiffness of spring in y direction (N/m)	1.3415 e6
Stiffness of spring in z direction (N/m)	3.4935 e6

The maximum equivalent stress of connections using different supports is shown in Figure 3.16. The spring conditions provide larger stress values than the simple supports do, especially for P1R, P4R, P6R and TB. This is because self-weight plays a key role in structural behaviour, especially that of the wind turbine and tower (Ye et al., 2019). The large displacement caused by the spring boundary conditions induces a much larger second-order effect on the structure, thus causing an even higher stress than that with simply supported boundary conditions. Using simply supported boundary condition underestimates the internal stress of the platform. Therefore, the mooring lines represented by linear springs are adopted in this thesis.

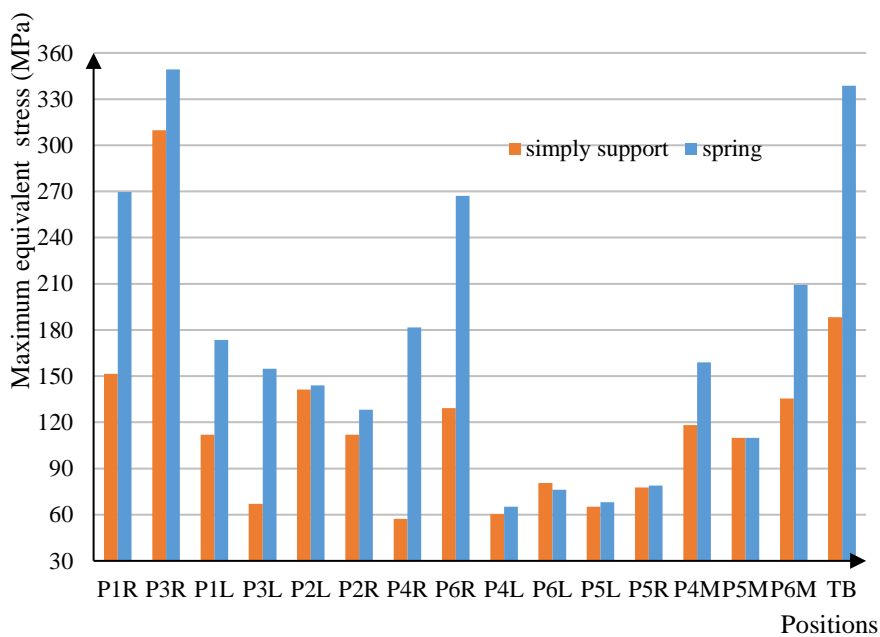


Figure 3.16 Comparison of the maximum equivalent stress of connections using different supports (LC27)

3.2.3.6 Load mapping

AQWA-WAVE is used to calculate the surface pressures at the facet centroids and the wave-induced translational and rotational accelerations, and transfer them from AQWA to the structural FEA model. The process of the load mapping is shown in Figure 3.17 and can be described as follows: 1) Create hydrodynamic geometry, 2) Run AQWA-line to generate wave loads and acceleration, 3) Create structural geometry, and 4) Run AQWA-WAVE to extract the pressures and accelerations that are calculated from the hydrodynamic model and then to map them into the structural model.

The nodes and elements used in the hydrodynamic model and structural model do not need to be exactly matched as the forces can be interpolated in the structural model. Figure 3.18 shows the load mapping from a hydrodynamic mesh to a structural mesh. Finite element nodal pressures (M1) are computed from weighted averaging of hydrodynamic nodal values (N1 to N4). An example of load mapping under a regular wave (height $H = 3$ m, period $T = 8$ s, and direction: 0° ; wave phase: 0°) is shown in Figure 3.19. As can be seen, the wave pressure of the structural model agrees well with that of the hydrodynamic model. An equivalent static analysis is carried out owing to its computational efficiency. A set of wave phases, 0° , 45° , 90° , 135° , 180° , 225° , 270° and 315° , are selected to evaluate a complete cycle of a regular wave to obtain the maximum wave impact. All wave phases are considered in every load case in Table 3.3, and the overall maximum stress value of the structure under a full cycle of wave (with various wave phases) is presented in this Chapter. The rotor thrust $F(t)$, which has been presented in 3.2.3.2, is applied on top of the tower. The ANSYS parametric design language (APDL) is adopted to input the hydrodynamic and aerodynamic forces in the structural analysis.

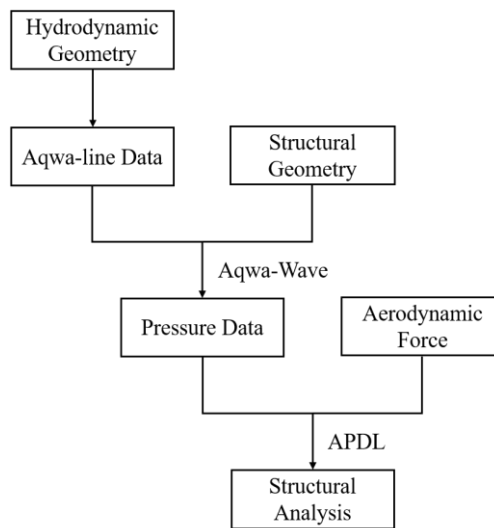


Figure 3.17 Load mapping process

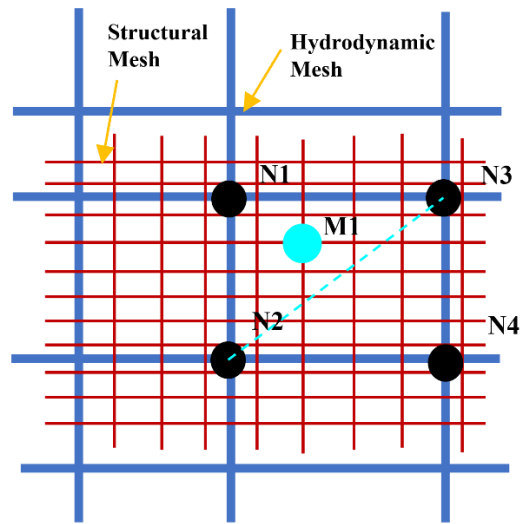
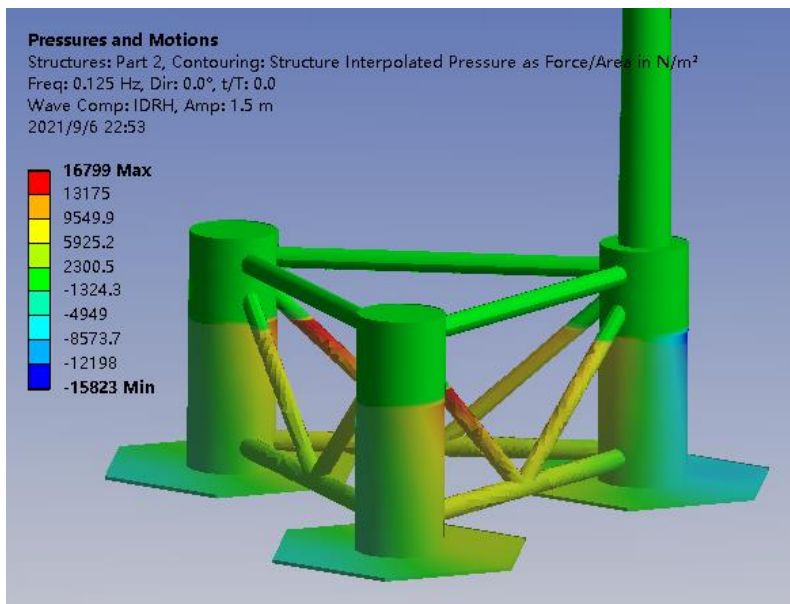
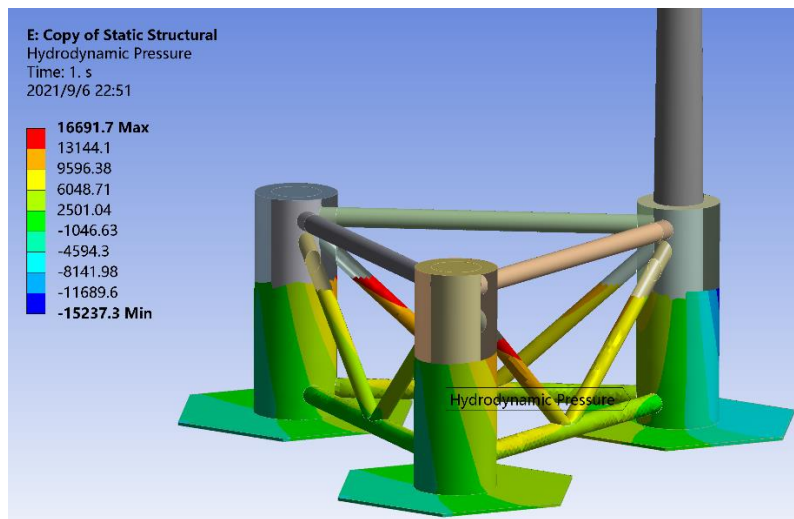


Figure 3.18 Load mapping from hydrodynamic mesh to structural mesh



(a)



(b)

Figure 3.19 Hydrodynamic pressure profile of (a) hydrodynamic model and (b) structural model under a regular wave of height $H = 3$ m, period $T = 8$ s, and direction: 0° ; wave phase: 0° .

3.2.3.7 Model validation

The present model described above is validated against previous experimental and numerical studies of WindFloat platform (Aubault et al., 2011, Peiffer and Roddier, 2012). In this validation section, the aerodynamic loads have not been considered. In experimental modelling, a 1:78 scale model is tested in a 61 m long, 2.4 m wide and 1.5 m deep towing tank. The full scale of the towing tank is 4755 m long, 190 m wide and 119 m deep. An equivalent linear mooring system is adopted for the platform model to match the global stiffness of the numerical model in surge, sway and yaw. Regular waves were generated with a constant steepness $1/80$ with the maximum wave height of 6 m. The full scale numerical model of WindFloat was built under frequency domain with numerical tools, WAMIT and AQWA (the presented model). Regular linear waves are generated with varying wave periods ranging from 5 to 20 s.

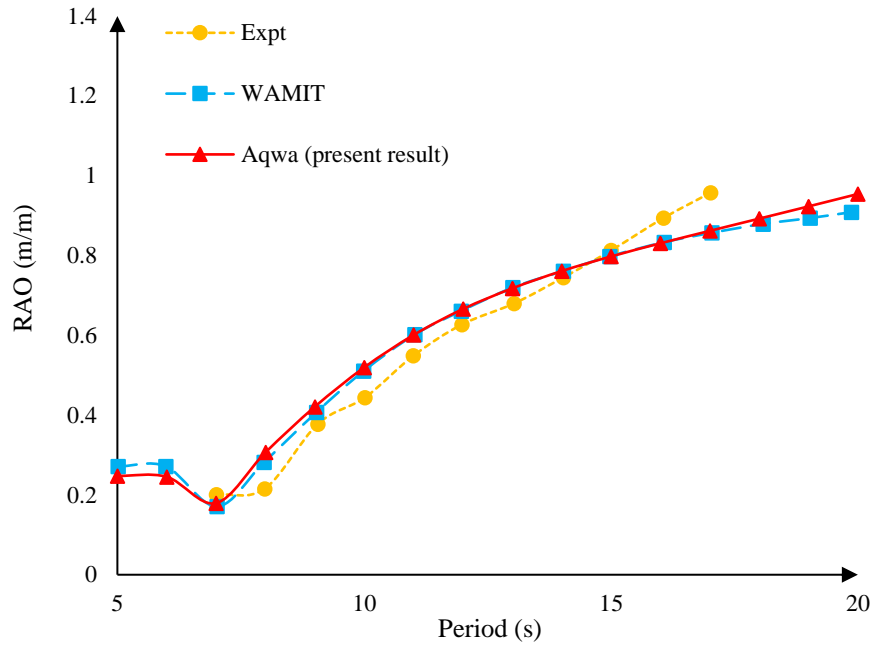
Figure 3.20 compares the surge, heave and pitch RAOs of the present model against experimental data and published numerical results of the WindFloat (Aubault et al., 2011). According to the linear potential flow theory, the motions of the platform would be increased or decreased linearly under different incident wave amplitudes. Excellent agreement was found between the present results (based on AQWA) and the previous results obtained with WAMIT, owing to the same theory used. Good agreement was also found with the experimental data except for the heave motion at large wave periods, although some small discrepancies can be found such as the surge beyond 15 s, the pitch at 6 s and beyond 12 s. The possible reasons can be concluded as: i) the size of the towing tank used in the basin test is not large enough, which may have effect on wave propagation. The depth of the full scale wave tank is only 119 m. With water depth increasing from 50m to 200m, the surge and pitch motions of floating platform would decrease, especially in the low-frequency region (period larger than 10 s) (Shi et al., 2023). This is because that second-order hydrodynamics have a larger impact on the dynamic responses of floating platform for shallow water depth, which leads to a larger wave excitation load. In the AQWA model, the water depth is 350 m ($h > 0.5\lambda$, where h is water depth and λ is

water length (DNVGL-RP-C205, 2020)) to avoid the impacts of water depth. Furthermore, wave reflections from the side walls may also cause differences between numerical and physical results. Because wave reflections were not considered in the numerical model; ii) the nonlinear effects of hydrodynamics are considered in the experiment, e.g. higher order wave effect and nonlinear damping due to the heave plates, which were linearized or ignored in the numerical model.

The significant difference of the heave motion between experimental and numerical results is found when wave period exceeds 15 s. The platform experiences a minimum heave motion at 18 s based on the WAMIT and AQWA models, which is called wave cancellation period (Bots, 2020). This is because, at this period, the wave excitation force of the top of the heave plate is equal to that of the bottom surface. Hence, the potential flow theory would underestimate the heave motion at long period if the floater has a heave plate. However, the above numerical method can still be adopted at periods smaller than 15 s. Accordingly, the wave periods of 8 s and 10 s are used in this study. On this basis, the AQWA model is adequate for the calculation of the hydrodynamic forces.

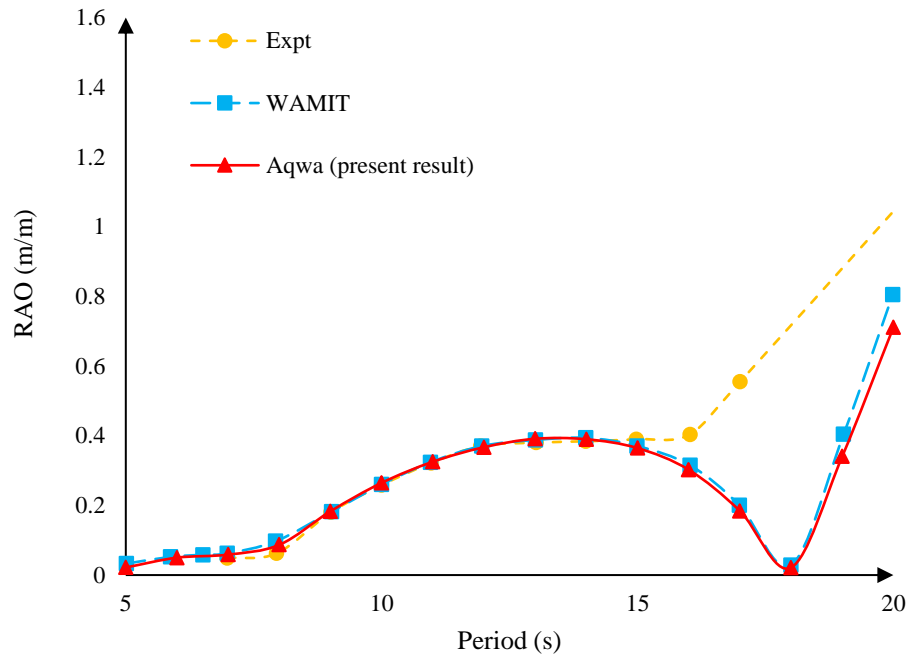
Although the maximum wave height of 6 m with 1/80 steepness was adopted in the validation of the experimental and numerical studies, the numerical model using potential flow theory is still valid for various wave height with a similar steepness in existing studies. For example, a set of regular waves including a wave height of 2 m with 1/78 steepness was used by (Ma et al., 2019b) to study the dynamic response of a tension leg platform based on the potential flow theory; a regular wave with 7.57 m wave height and 1/82.42 steepness was adopted by Ghafari et al. (2021) to validate the experimental and numerical model (based on AQWA) of a semi-submersible floating platform, and there was a good agreement between the experimental and numerical results.

Surge RAO

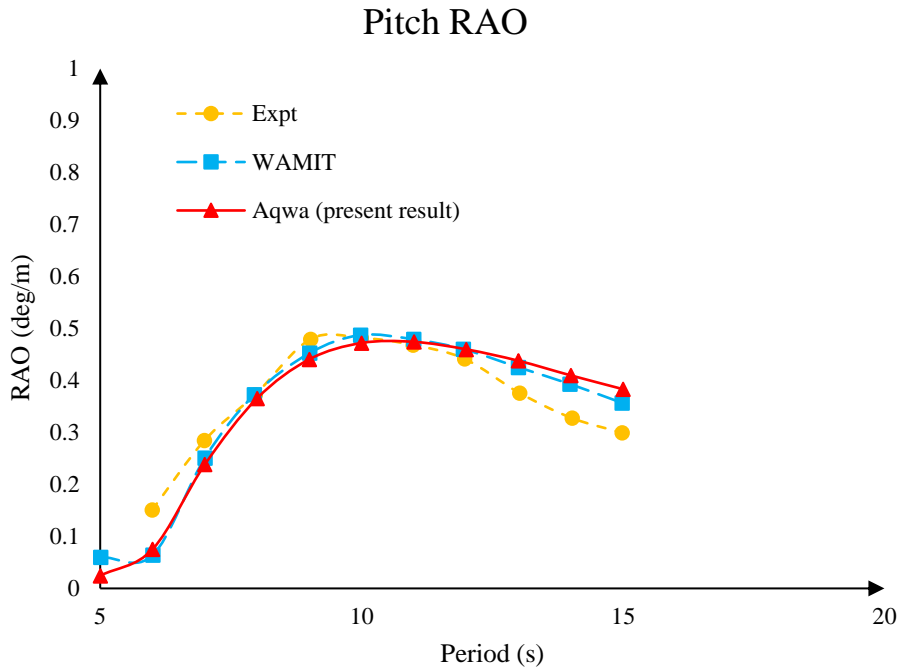


(a)

Heave RAO



(b)



(c)

Figure 3.20 RAO in (a) surge, (b) heave and (c) pitch at wave direction 0° without wind

3.3 Results

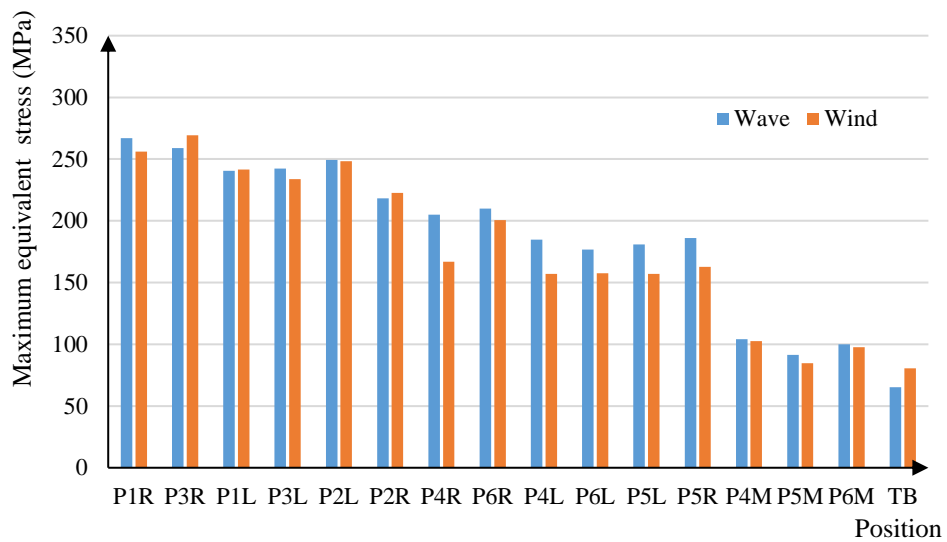
The results of the numerical modelling from both the linear and nonlinear analyses are presented in this section. A total of 40 loading cases introduced in Table 3.3 are used to carry out linear analysis, from which the worst case is selected to develop the nonlinear analysis models to study the nonlinear structural response of the platform.

3.3.1 Equivalent static structural analysis

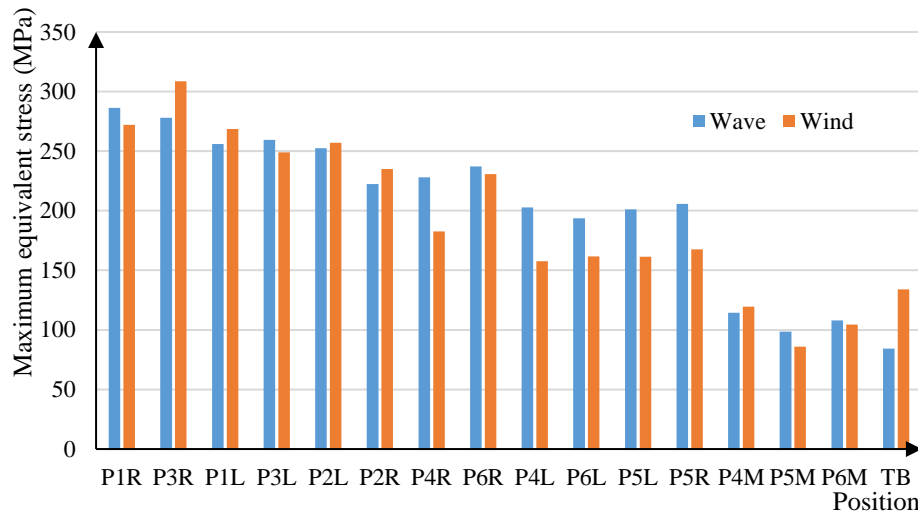
Nine different wave phases (0° , 45° , 90° , 135° , 180° , 225° , 270° and 315°) are considered to simulate the whole movement of wave to obtain the maximum wave impact. The stress result due to the wave impact comes from the comparison of all phases and the largest one is adopted. Different azimuthal angles under wave and wind conditions are considered as well. The maximum stress is found to always occur at the connections; and for this reason, their structural behaviour is highlighted.

3.3.1.1 Individual impact of wave and wind

Figure 3.21 demonstrates the maximum equivalent stresses of all 16 connections induced by the different wave or wind conditions using the largest stress among all angles (0° , 45° , 90° , 135° and 180°) that mentioned in Table 3.3. After comparing all connections, the maximum equivalent stresses of connections P1R, P3R, P1L, P3L, P2L, P2R, P4R and P6R are identified to be particularly critical due to the individual impact of wave and wind. These maximum stresses are all located on the column supporting the wind turbine and the upper pontoons. As for the structural behaviour of the tower base, Figure 3.21 shows greater susceptibility to wind-induced thrust loads compared to wave loads, with around 66.1% increase, which is in agreement with what was reported by [Xu et al. \(2019\)](#). Different from the direct impact of wind, the stress in TB induced by waves is mainly because of the dynamic motion induced by waves and the inertia force of the wind turbine.



(a) LC1-10



(b) LC11-20

Figure 3.21 Individual effect of wave and wind on the maximum equivalent stress of connections

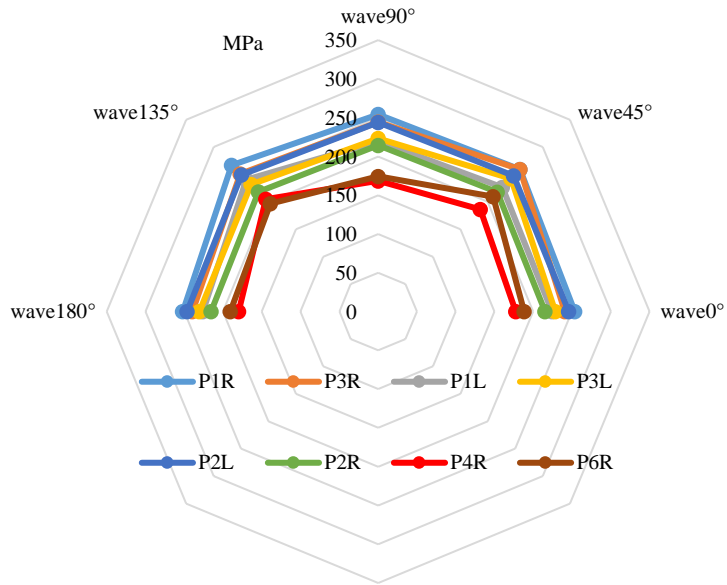
Figure 3.22 shows the individual effects of wave and wind directions on the equivalent stress of these eight critical connections (P1R, P3R, P1L, P3L, P2L, P2R, P4R and P6R). The dot data are the maximum stresses of the connections under the wind or wave with a specific direction. The dots of every connection are connected by using straight lines to demonstrate its variation. It is found that the impact of wave direction on the stress of these eight connections is relatively small compared to that of the wind direction. According to Figure 3.22 (a) and (c), among the eight connections P4R is mostly affected by the wave directions. For the equivalent stress of P4R under the small wave ($H=3\text{m}$), the minimum one is 169 MPa when the wave comes from 90° and the maximum one is 205 MPa when the wave comes from 135° . Thus, change of wave directions would make a maximum difference of 21.3% under a small wave ($H=3\text{m}$), compared with a 34.1% difference under a large wave ($H=9\text{m}$). Similar difference of stress change is found for P6R with 20.3% and 32.7% under the small wave and the large wave respectively. However, apart from P4R and P6R, the stress change of the other connections is lower than 12%. This is because both connections, P4R and P6R, are under the water level, which are directly impacted by the wave. The other connections are above the water level thus the impact of the wave directions is less obvious.

In contrast, the wind direction has more significant effect on the maximum equivalent stress of connections compared with the wave directions, especially for P1R and P3R.

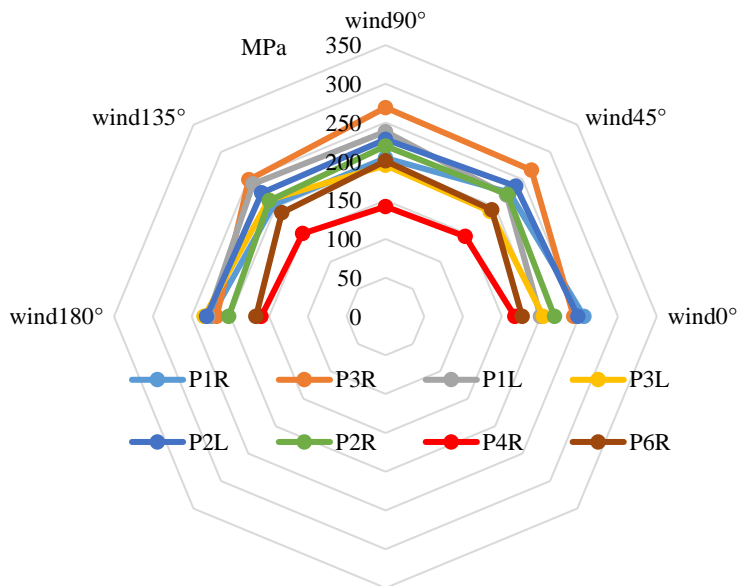
The stronger the wind condition, the greater difference of the stress of connections. According to Figure 3.22 (b) and (d), the greatest difference in the stress is found to be in P1R, where a difference of 25.8% and 60.6% is seen under the small wind ($U_w=7\text{m}$) and the large wind ($U_w=11.4\text{m}$), respectively. P3R, as a symmetrical position of P1R, has a similar structural behaviour: the greatest difference in the stress under the small wind and the large wind is 23.7% and 50.2%, respectively. Moreover, P2L and P2R, which are furthest away from the tower base, have the minimum stress difference under different wind directions. This is because that the wind load is transferred from the tower to the tower base, then to the platform. Due to the load distribution during the load transfer, the impact of the wind direction is reduced.

The maximum stresses of the eight connections under various directions of wave and wind are summarized in Table 3.8. It is found that there is no single wind direction which is adverse to all connections. Different from the wind direction, the most adverse directions of the wave directions on the maximum stress of all eight connections are 45° and 135° . The reason that the most critical wave directions are the lateral direction (45° and 135°) rather than the direction along the axis of symmetry (0° or 180°) could be that, when the wave comes from 0° or 180° , the wave load is transferred between columns by the pontoons performing as the axial forces and the axial forces are relatively even. However, when the wave comes from 45° and 135° , the axial forces are relatively uneven in the pontoons, which causes additional torsion and a larger normal stress. Thus, the equivalent stress of the connections increase.

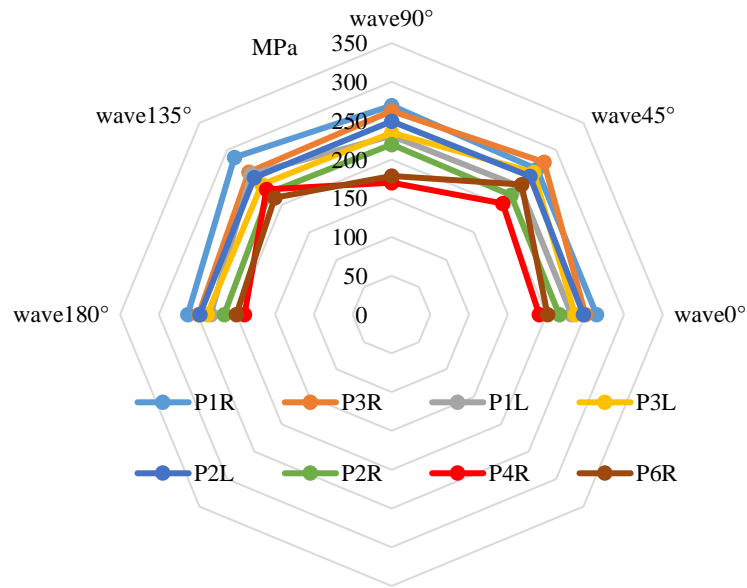
In summary, the wind direction appears to have a larger effect on the stress of the critical connections compared with the wave direction. As regards the stress level, the connections under the water level are more affected by wave directions, and the connections closing the tower base are more affected by wind directions. 45° and 135° are the most adverse wave directions on the maximum stress among the eight connections. However, there is no adverse direction of wind for all connections.



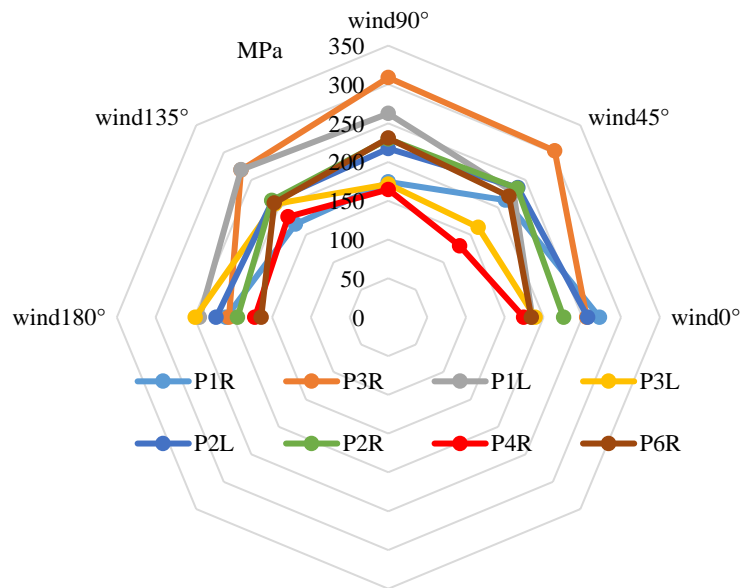
(a) LC1-5 (wave only, H=3m, T=8s)



(b) LC6-10 (wind only, Uw=7m/s)



(c) LC11-15 (wave only, $H=9\text{m}$, $T=10\text{s}$)



(d) LC16-20 (wind only, $U_w=11.4\text{m/s}$)

Figure 3.22 Individual effects of wave and wind on the maximum equivalent stress of connections

Table 3.8 Summary of maximum stress of the eight connections under various directions of wave and wind

Connections	LC1-5 (wave only, $H=3\text{m}$, $T=8\text{s}$)	LC6-10 (wind only, $U_w=7\text{m/s}$)	LC11-15 (wave only, $H=9\text{m}$, $T=10\text{s}$)	LC16-20 (wind only, $U_w=11.4\text{m/s}$)

	Max. stress (MPa)	Wave direction (°)	Max. stress (MPa)	Wind direction (°)	Max. stress (MPa)	Wave direction (°)	Max. stress (MPa)	Wind direction (°)
P1R	267	135	256	0	269	90	272	0
P3R	259	45	269	90	278	45	309	90
P1L	241	135	242	135	256	135	269	135
P3L	242	45	234	180	259	45	249	180
P2L	249	135	248	0	252	45	257	0
P2R	218	135	223	45	222	135	235	45
P4R	205	135	167	0	228	135	183	135
P6R	210	45	200	90	237	45	231	90

3.3.1.2 Wave-wind alignment

Figure 3.23 and Figure 3.24 show the maximum stresses in connections when considering the combined effects of wave and wind. Note that no safety factors are considered, either for materials or load combinations. In general, the critical stresses occur at connections P3R, P1R, P1L, P6R, P3L, P2L and P2R, which are also the critical connections when the platform is under the action of the wave or wind alone. These connections are mainly located on the column supporting the wind turbine and between the upper pontoons and columns. Comparing the maximum stresses of all 16 connections, P3R has the largest stress under the 45° environmental forces regardless of whether moderate condition or rated conditions are considered. The stresses of the connections between bracings and pontoons (P4M, P5M and P6M) are relatively small especially for P5M. According to Figure 3.23 and Figure 3.24, the lateral impact of wave and wind (45°, 90° and 135°) should be paid more attention because 75% of connections reach the maximum stress when the wind and wave loads come from 45°, 90° or 135°. This is because that the platform is symmetrical along the primary axis (0° and 180°), where load is more evenly distributed and normal stress is dominant. The lateral wave and wind force create uneven load distribution, i.e. additional torsion to compression, thus the connections suffer large shear stress in addition to the normal stress, and are more likely to cause stress concentration. The connections under the two environmental conditions have similar trends in stress level, although the difference is larger under the rated condition.

Although the tower base carries considerably high self-weight of the wind turbine and tower and the bending moment due to the wind thrust force, the maximum stress in the tower base is still lower than those in the connections (see Figure 3.23 and Figure 3.24).

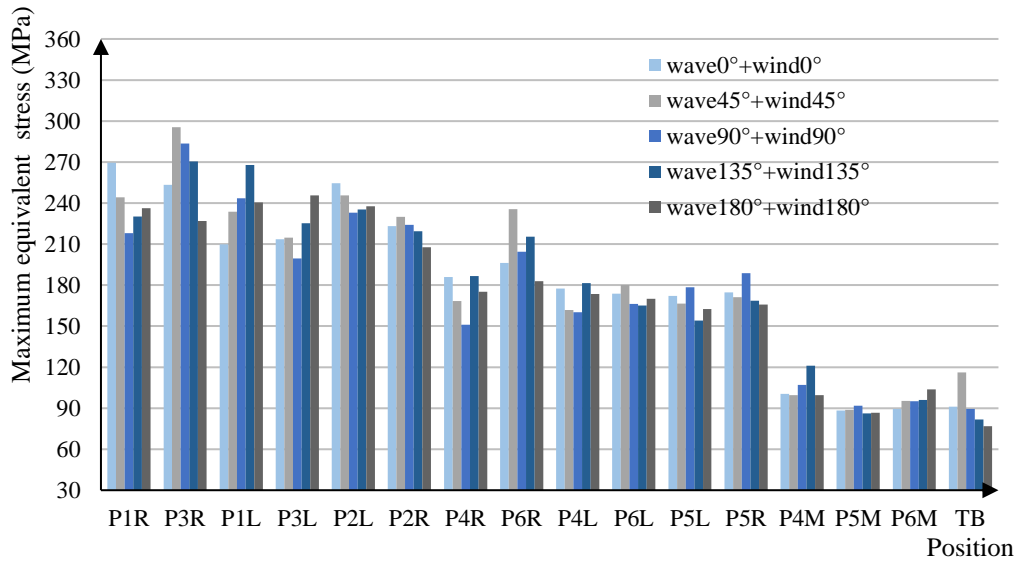


Figure 3.23 The maximum equivalent stress of connections in moderate conditions (LC21-25)

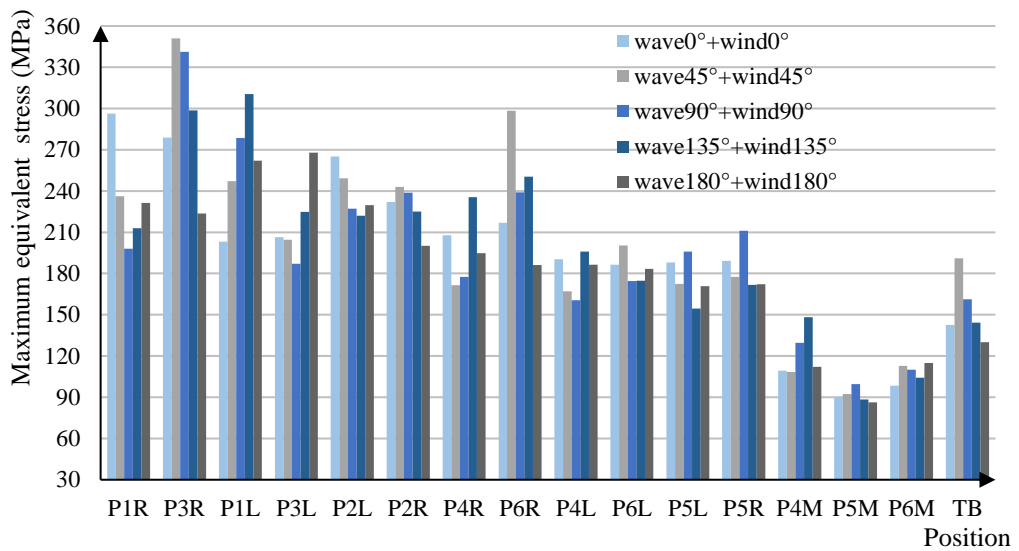


Figure 3.24 The maximum equivalent stress of connections in rated conditions (LC26-30)

3.3.1.3 Wave-wind misalignment

To investigate the effect of wave-wind misalignment, the angle between wave and wind is set to 22.5° (Michailides et al., 2016), which is a typical value used to investigate the structural response of platforms in misaligned conditions. Taking P3R as an example, Figure 3.25 shows that the comparison of the maximum equivalent stresses between misaligned and aligned wave and wind loads. The misalignment angle can be divided into

clockwise and anticlockwise directions, which has an adverse effect on the results: one reduces the maximum equivalent stresses and the other increases the results. There is always one misaligned wave-wind case which has larger maximum equivalent stress than the aligned wave-wind case; and the aligned wave-wind case always has the middle class of the connection stress between the two misaligned wave-wind cases. This means that the aligned wave-wind case is not the most critical loading case in terms of the stress level. The misaligned wave and wind loads may cause additional torsion and shear force leading to a larger equivalent stress compared with the aligned load case.

Table 3.9 shows the comparison of maximum stresses between the misaligned and aligned wave-wind cases in rated condition. The maximum stresses in all connections of both aligned and misaligned wave and wind conditions usually come from the same wave direction, except for P2R. It can be seen that the wave-wind misalignment would increase the maximum stress of the connection by up to 8.5%. Therefore, the effect of misalignment of environmental condition needs to be considered in the practical structural design to avoid underestimating of design stress.

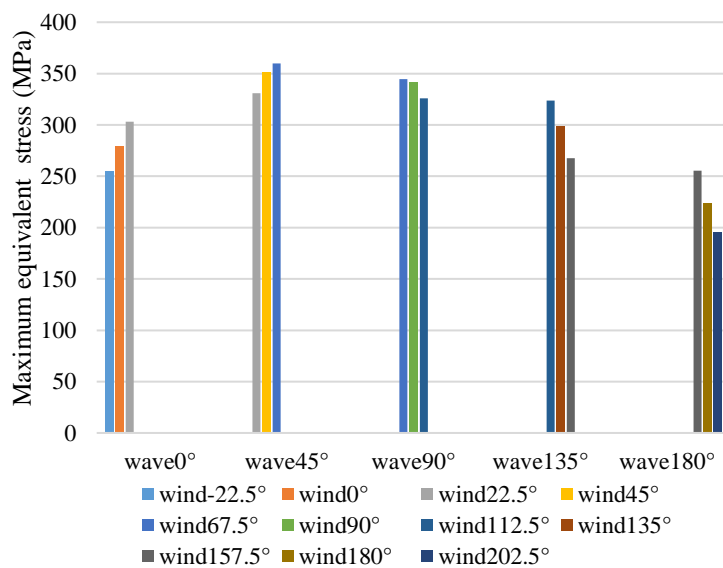


Figure 3.25 The maximum equivalent stress of P3R in rated conditions subjected to misaligned wave and wind

Table 3.9 Comparison of the maximum stress between misaligned and aligned wave-wind

	misaligned wave-wind (LC31-40)	aligned wave-wind (LC26-30)	Is $\sigma_1 > \sigma_2$?	Is $\alpha_1 = \alpha_2$?	Increase of stress

	Max. stress σ_1 (MPa)	Load case		Max. stress σ_2 (MPa)	Load case				$((\sigma_1 - \sigma_2)/\sigma_2)$ (%)
		Wave α_1 (°)	Wind β_1 (°)		Wave α_2 (°)	Wind β_2 (°)			
P1R	321	0	-22.5	296	0	0	Yes	Yes	8.48
P3R	355	45	67.5	351	45	45	Yes	Yes	1.45
P1L	312	135	112.5	310	135	135	Yes	Yes	0.36
P3L	284	180	202.5	268	180	180	Yes	Yes	5.94
P2L	272	0	22.5	265	0	0	Yes	Yes	2.69
P2R	243	90	67.5	243	45	45	Yes	No	0.16
P4R	241	135	112.5	235	135	135	Yes	Yes	2.26
P6R	307	45	67.5	298	45	45	Yes	Yes	2.93
P4L	198	135	157.5	196	135	135	Yes	Yes	1.16
P6L	202	45	67.5	200	45	45	Yes	Yes	0.71
P5L	200	90	67.5	196	90	90	Yes	Yes	1.87
P5R	214	90	67.5	211	90	90	Yes	Yes	1.31
P4M	151	135	112.5	148	135	135	Yes	Yes	1.55
P5M	100	90	67.5	99	90	90	Yes	Yes	0.63
P6M	119	180	202.5	115	180	180	Yes	Yes	3.46
TB	192	45	67.5	191	45	45	Yes	Yes	0.45

3.3.2 Geometrically and materially nonlinear analysis (GMNA)

According to the literature review, linear analysis has been widely used in the structural analysis of offshore structures, primarily attributed to its computing effectiveness. However, linear elastic analysis will not be able to accurately predict the post-yielding nonlinear behaviour, thus leads to conservative design solutions which have a negative impact on the levelised cost of energy (LCOE). In this section, three types of finite element models are used to study the effects of structural nonlinearities including material nonlinearity and geometric nonlinearity: linear analysis (LA), geometrically nonlinear analysis (GNA), geometrically and materially nonlinear analysis (GMNA). The linear and nonlinear material properties are given in Figure 3.12. The linear geometric analysis is based on the small displacement assumption of shells, i.e. linear bending and stretching shell theory with a constant stiffness matrix, which leads to a linear relation between the strain and displacement. The nonlinear geometric analysis is based on the nonlinear shell theory which is able to consider the change of stiffness matrix due to large displacement and leads to the nonlinear relation between displacement and strain (Rao et al., 2015). According to the linear global model presented in Section 3.3.1, although the misaligned cases are the most critical, they are still not common cases compared with the aligned cases. Moreover, this chapter mainly studies the structural behaviour of the platform

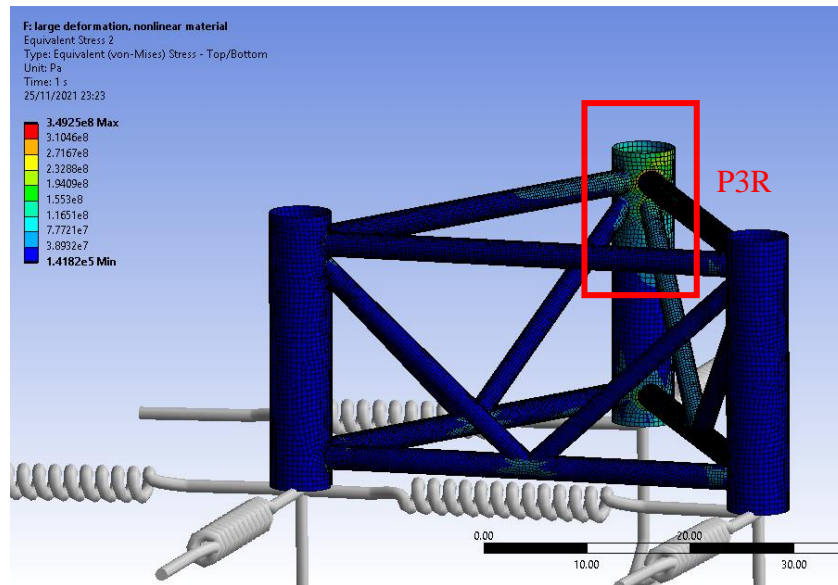
rather than the ultimate strength of the structure. Thus, LC27 (wave45°+wind45°), as the most critical case in the aligned cases, is then used in the study. Thickness reduction is adopted as an economy indicator of the structural design in this study, as smaller thickness usually leads to lower mass and less labour cost, particularly for the welding cost. Note that, in order to keep the same hydrodynamic response, no other dimensions were changed apart from the thickness.

3.3.2.1 Structural behaviour of the connections

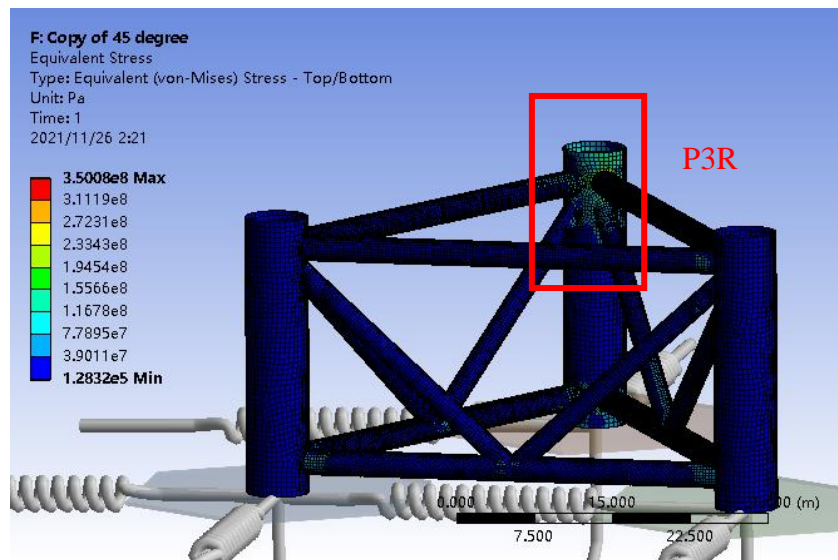
The minimum thickness of the components to resist the environmental forces under LC27 (as presented in Section 3.3.1) is obtained using three simulations (LA, GNA and GMNA), and the corresponding results are shown in Table 3.10. The minimum required thicknesses obtained using GMNA and GNA are 60% and 85% of that obtained using LA, respectively. As can be seen from Figure 3.26, the stress distribution of the GMNA is more uniform compared with that of the LA, especially in the connection P3R where the largest equivalent stress occurs. This is because that the GMNA allows stress redistribution when the maximum stress approaches the yield strength. In other words, the strength of the material is best utilized in a GMNA. It is concluded that LA would lead to overdesigning, unnecessary use of materials and increased labour cost. Therefore, the nonlinearity should be taken into consideration in offshore floating platform design.

Table 3.10 Thickness of the main components of the floating platform (mm)

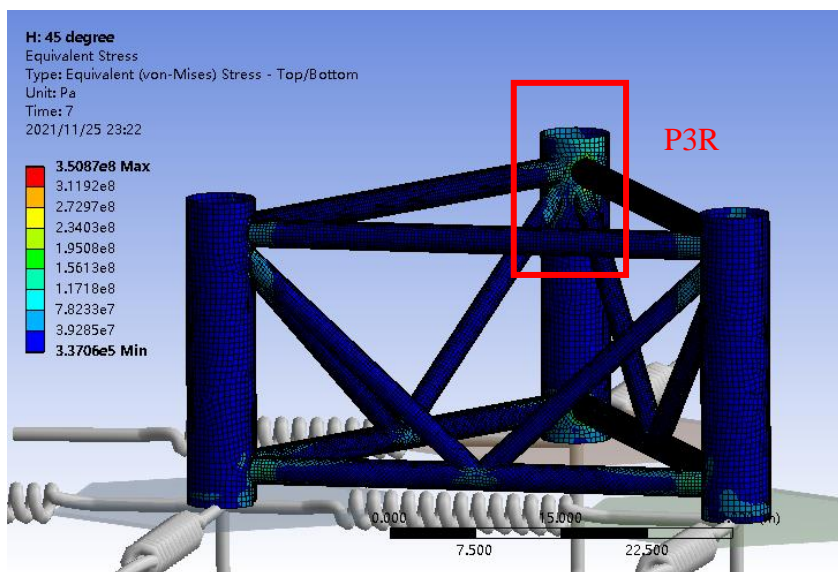
	External column	Internal column	Pontoon	Bracing
GMNA	36.0	30.0	22.0	22.0
GNA	51.0	42.5	31.1	31.1
LA	60.0	50.0	36.6	36.6



(a) Geometrically and materially nonlinear model



(b) Geometrically nonlinear model



(c) Linearly elastic model

Figure 3.26 Stress contour of the platform in LC27, wave 45°+wind 45° (shown without external columns and heave plates) (Unit: Pa)

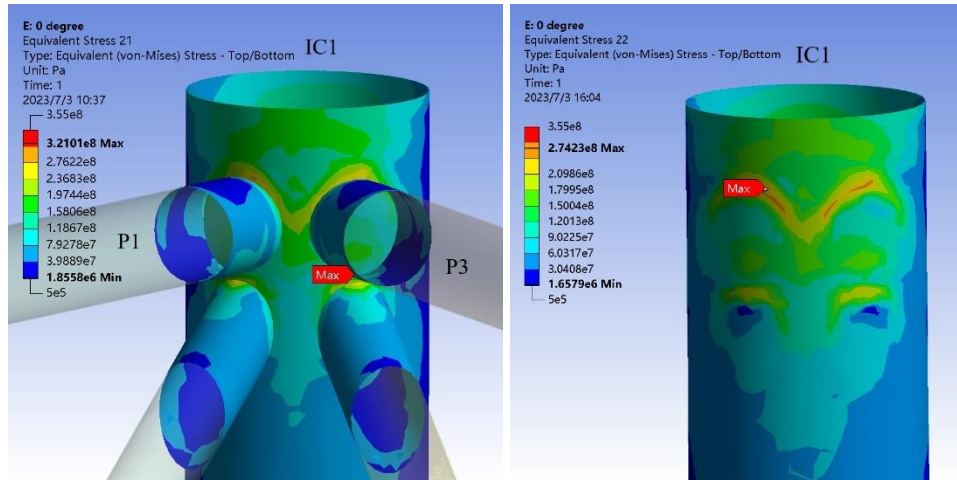
Different environmental forces could cause different failure modes. All critical connections under the rated conditions (LC26-30) have been summarized in Table 3.11. It is noted that the structural performance between LC27 and LC28 is quite similar so the results of LC28 are not presented further. It is found that the most likely failure position is always located in the connection region, especially in the connections between internal columns and pontoons. To highlight the presentation, all other components such as the tower and the external column are not shown in Figure 3.27. The stress concentration areas are mainly located in the top or bottom edge of the connections, despite the change of the direction of the environmental forces. Punching shear failure in the radial direction and tearing failure in the circumferential direction are likely to occur. Hence, in the actual design and fabrication, these stress concentration areas should be paid more attention and stiffeners are needed to strengthen these areas.

In Section 3.3.1.2, it was concluded that the direction of 45°, 90° or 135° of the environmental loads are more adverse to the structures in terms of maximum stress level when compared with the direction of 0° or 180° in LA. A similar outcome can also be found in GMNA, which can be demonstrated graphically in Figure 3.27 (a) and (b). When the direction of the environmental loads is 0° (LC26), the stress contour of P1R and P3R is relatively symmetrical and evenly distributed – the reason being that the environmental loads are averagely transferred to P1 and P3. However, when the direction of the environmental loads is 45° (LC27), the large stress mainly concentrates on P3R. Combining with Figure 3.5, it can be concluded that the 45° wind force induces a large shear force between P3R, and hence, the large stress in P3R occurs. Moreover, the largest stress under LC27 is 354.8 MPa, which is higher than that under LC26 (321.0 MPa). Therefore, it can be concluded that the direction of 45° of the environmental loads is more adverse to the structures as regards stress level than the direction of 0° in GMNA.

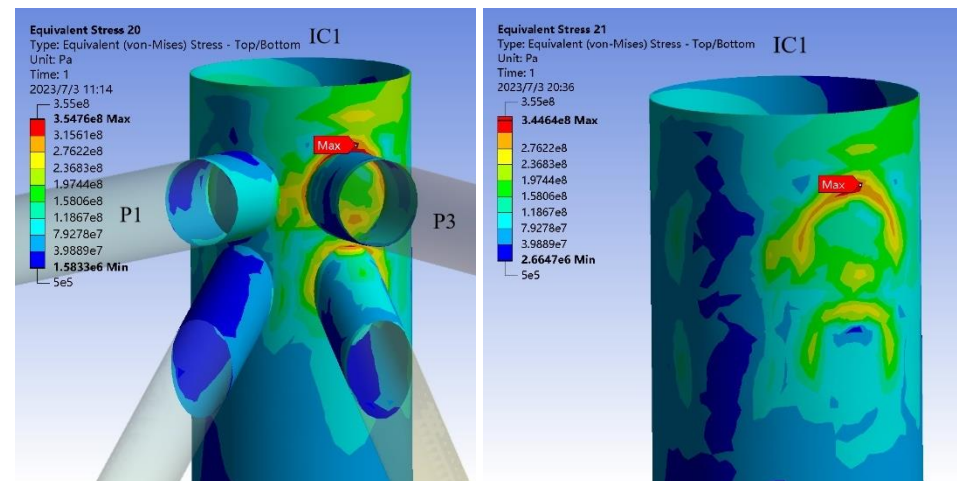
Table 3.11 The critical connections in LC26-30

	GMNA	LA
--	------	----

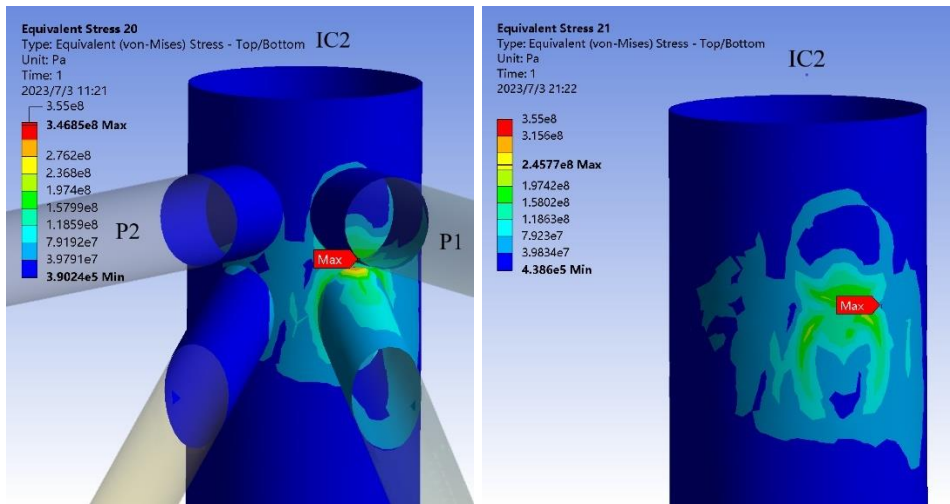
Load case No.	Maximum equivalent stress (MPa)	Occurred position	Maximum equivalent stress (MPa)	Occurred position
LC26	321.0	P1R	296.2	P1R
LC27	354.8	P3R	350.9	P3R
LC28	336.6	P3R	341.1	P3R
LC29	346.9	P1L	310.4	P1L
LC30	247.7	P1L	267.9	P3L



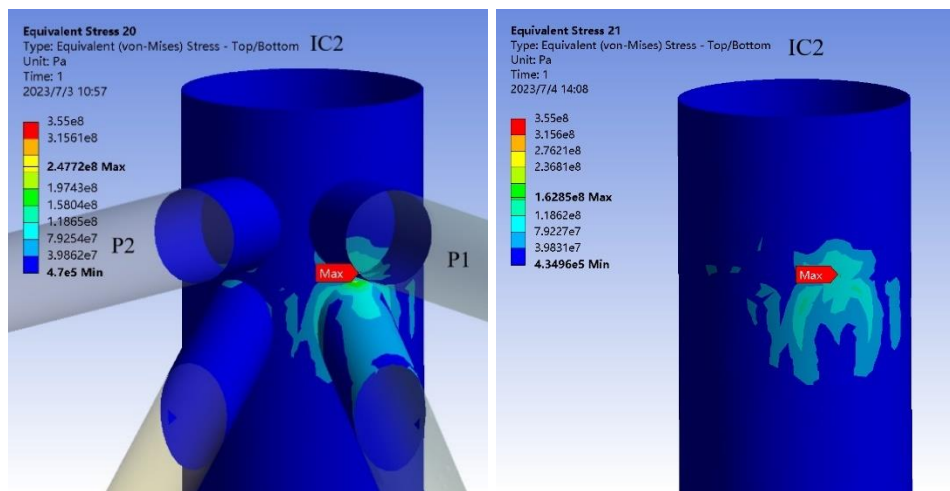
(a) Stress contour of PIR in LC26



(b) Stress contour of P3R in LC27



(c) Stress contour of P1L in LC29



(d) Stress contour of P1L in LC30

Figure 3.27 Stress contour of connections (Unit: Pa)

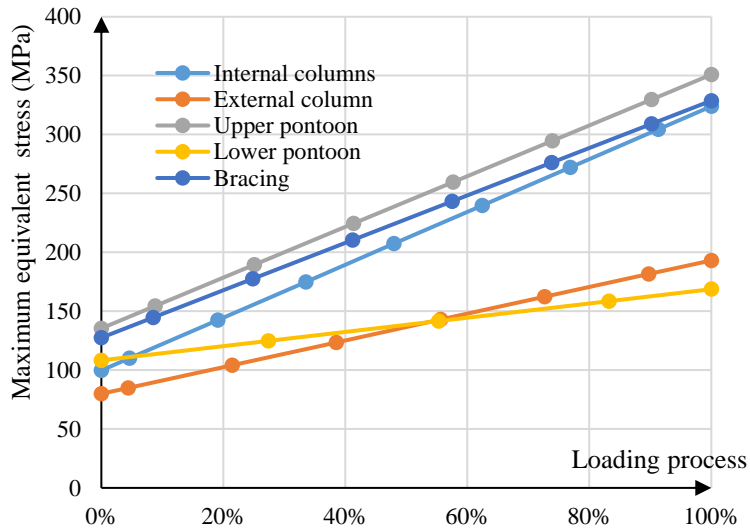
3.3.2.2 Structural behaviour of cylindrical components

This section focuses on the structural behaviour of the cylinders in the platform. Figure 3.28 and Figure 3.29 show the stress, global displacement and local deformation of all types of components in different loading process starting from calm sea condition in which FWT bears self-weight and hydrostatic force only. The global displacement is induced by the environmental forces and spring supports relative to the original location. 100% loading process means the environmental loads are fully applied on the platform. In GMNA (Figure 3.28 (b), Figure 3.29(b) and Figure 3.29(d)), when the structure is loaded less than 60% of the ultimate load, the total displacement and maximum equivalent stress increase almost linearly. After that, the displacement increases sharply and reaches to a peak of 1.55m. In addition, the results of linear analysis (LA) increase linearly

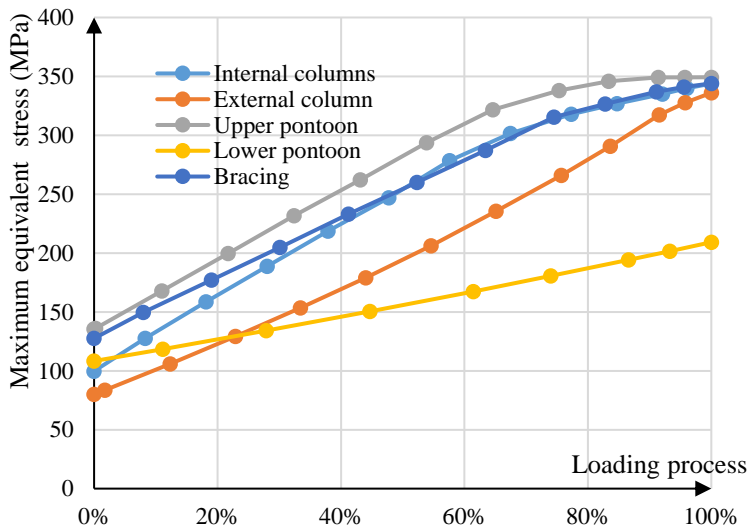
through the whole loading process. The maximum displacement of LA is 0.8m which is around half of the result of GMNA. It can be seen that the displacement of components is underestimated by LA. A large displacement may cause a large deformation, especially for slender structures. It has been known that shell structure is sensitive to large deformation. To be specific, under the vertical load (gravitational load) and lateral displacement, the slender structure will experience additional bending moment generated by the combined action of the vertical load and lateral displacement, which is called second-order effect due to geometric nonlinearity on the structure. Thus, the stresses of the components under GMNA increase faster than under LA.

According to Figure 3.28 (a) and (b), the structural nonlinearity has the largest effect on the external column in terms of the stress level, which has the largest ratio of diameter to thickness among the components. The final stress of the external column increases by 74% to 336 MPa from LA to GMNA. According to Figure 3.28 (b), the stresses of the components except for the lower pontoon get closer with the increase of loading, which means that these components have a large interaction especially when the load approaches the maximum. This is because that, according to Section 3.3.2.1, the connection is the most critical part and the structural nonlinearity allows the components to share the external forces and redistribute the stress within the connection part. In other words, there is a strain-hardening stage near the yield strength because of the effect of material nonlinearity. In this stage, plastic deformation is produced by the increased stress. However, this phenomenon cannot be obtained in the LA in Figure 3.28 (a). In sum, under GMNA in this study, geometric nonlinearity and material nonlinearity play important roles in pre 80% and last 20% of loading process, respectively. Hence, structural nonlinearity should be considered in the structural analysis of such large-volume steel structures.

According to Figure 3.29(c), Figure 3.29(d) and Figure 3.30, although these two models based on LA and GMNA bear the same environmental forces, the model with GMNA has a larger deformation. The main reason is that the thickness of the model with GMNA is thinner than the model with LA. The thinner thickness has a weaker stiffness, and it is more deformable. The deformation is likely to be the initial imperfection of the structure to trigger buckling damage, which should be paid attention in future work and the actual project.

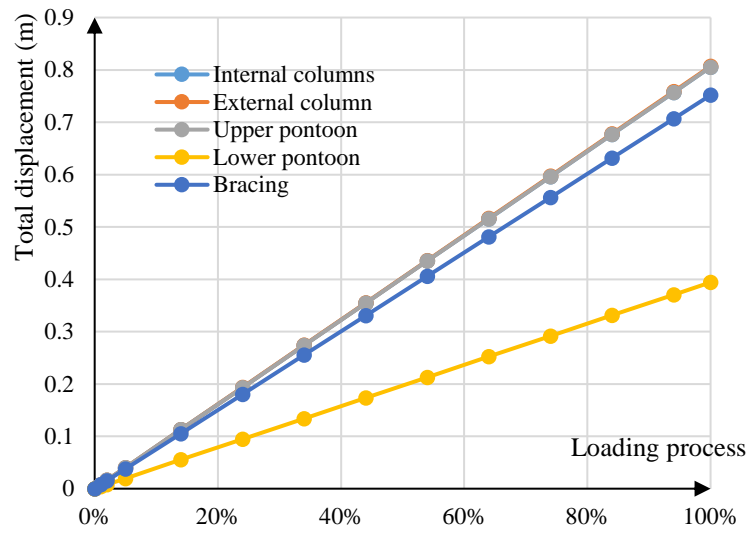


(a) The maximum equivalent stress of components in LA

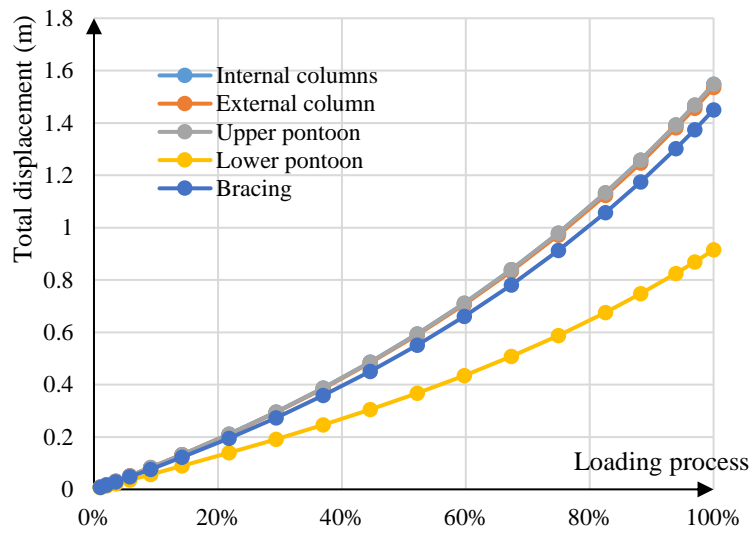


(b) The maximum equivalent stress of components in GMNA

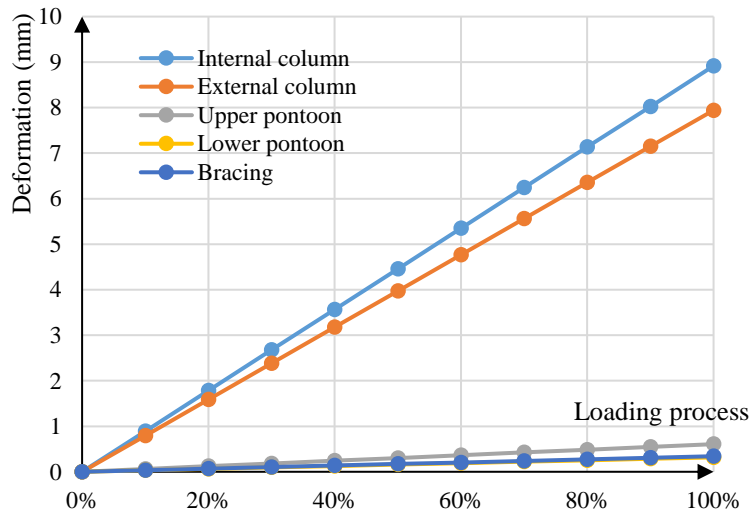
Figure 3.28 Stress performance of components (LC27)



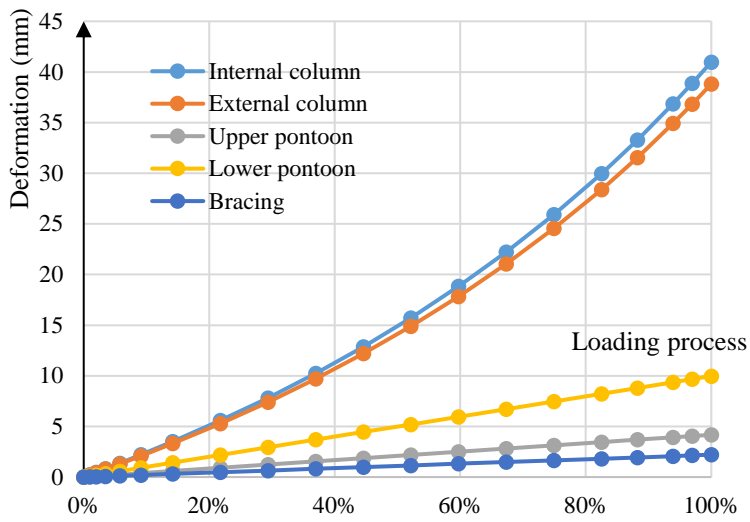
(a) The global displacement of components in LA



(b) The global displacement of components in GMNA

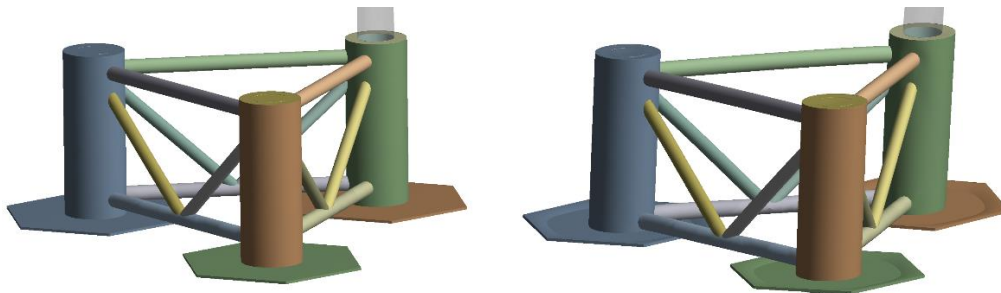


(c) The local deformation of components in LA



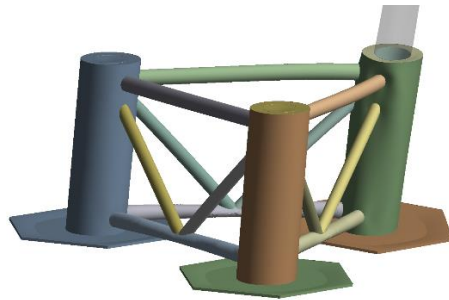
(d) The local deformation of components in GMNA

Figure 3.29 Displacement and deformation performance of components (LC27)



(a) Undeformed structure

(b) Deformed structure in LA (LC27)



(c) Deformed structure in GMNA (LC27)

Figure 3.30 Deformation comparison of the floating platform (scaled by 20 times)

3.3.2.3 Structural behaviour of the external and internal columns

As a main component of this platform, the column consists of an external column and an internal column, as shown in Figure 3.6. The structural design philosophy is to let the internal columns (ICs), which are connected with pontoons and bracings, primarily bear

the wind force from tower, while the external columns (ECs) covering the internal columns bear wave force only. However, although the external columns are not connected with the tower and internal columns directly, it is expected that a certain amount of wind or wave force would be shared by both the external and internal columns due to composite action transferred from pontoons and bracings to themselves. Therefore, the stress profiles on both the external and internal columns under wave or wind effects are investigated in this section.

GMNA is used to study the load distribution between external and internal columns under wave only condition (LC12) and wave-wind alignment (LC27) condition. Figure 3.31 and Figure 3.32 show the stress development of IC and EC in different loading processes starting from calm sea condition. In general, the stresses of IC are larger than that of EC in the same position especially for IC1 and EC1. Although the EC is assumed to mainly bear wave force, the stresses in ICs increase even more rapidly under wave loading (LC12). For example, the maximum equivalent stresses of IC1 and IC2 are 77% and 30% larger than those of EC1 and EC2, respectively.

In LC27, after the IC1 approaches yielding, the EC1 starts to bear more load. The stress difference between IC1 and EC1 reduces from 30% (loading process in 60%) to 2.3% (loading process in 100%) at the ultimate stage. This stress behaviour demonstrates the interaction and load transfer between IC1 and EC1. As mentioned before, IC1 is connected with EC1 by pontoons and bracings. Under the relatively large impact of environmental forces, EC1 is affected by IC1 to take more responsibility for sharing environmental loads. IC2, IC3, EC2 and EC3 have low maximum equivalent stress levels compared to IC1 and EC1. The maximum stresses of IC2 and IC3 are 49% and 35% higher than that of EC2 and EC3, respectively, when the loading process is 100%.

Figure 3.33 compares the final stress of ICs and ECs separately. It is found that the stresses in ICs and ECs under LC27 are generally higher than those under LC12, meaning that a certain amount of wind force will also be transferred to ICs and ECs due to composite action. The effect is more obvious on EC1 and IC1 than the others. Moreover, EC1 and IC1 undertake the most load from the turbine including the self-weight of the turbine and the rotor thrust in LC27. Although EC2, EC3, IC2 and IC3 are connected with IC1 and EC1, they have limited effect on transferring and bearing the loads from the wind

turbine. Thus, for structural design it is suggested that: 1) different structural design need to be provided for different columns to avoid overdesign and material waste, 2) the design could be improved to facilitate the load transfer and have a more even distribution of stress contour.

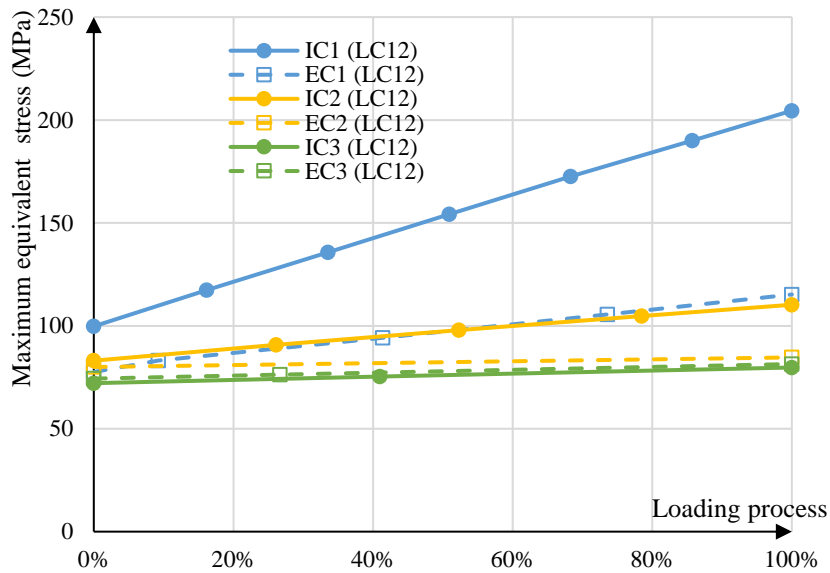


Figure 3.31 The maximum stress of ICs and ECs in LC12 (wave only)

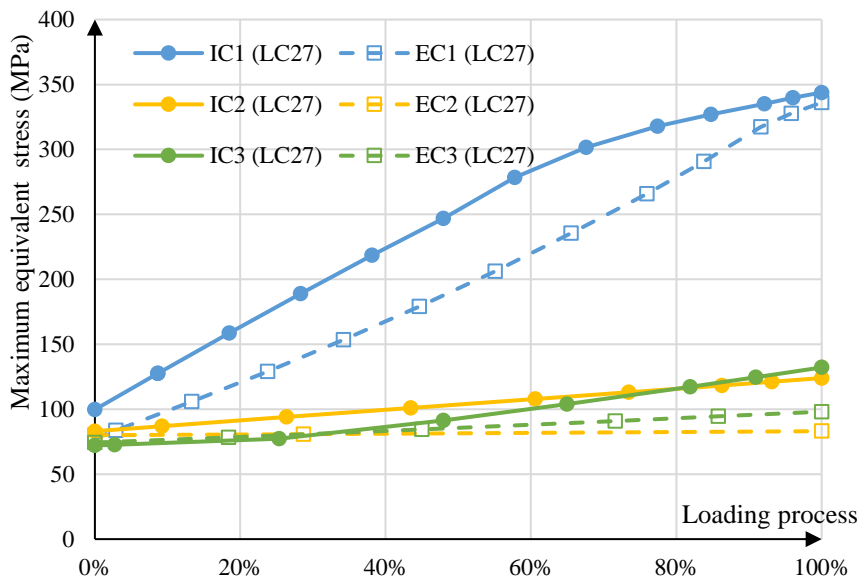


Figure 3.32 The maximum stress of ICs and ECs in LC27 (wave and wind alignment)

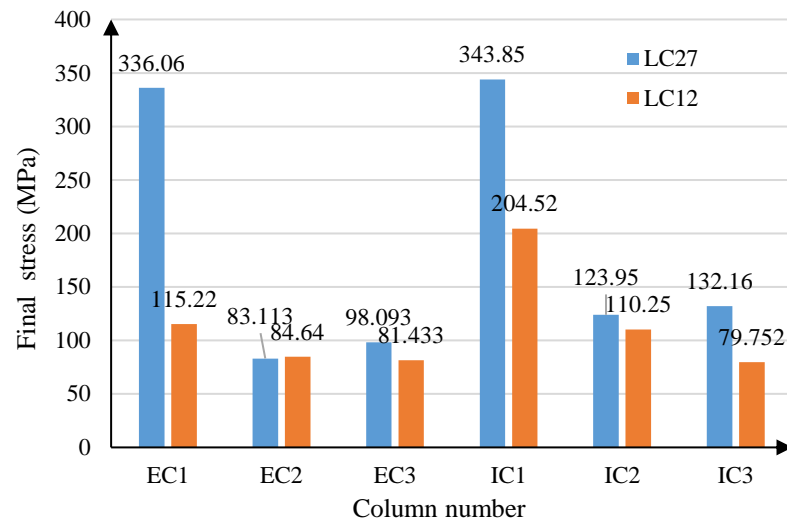


Figure 3.33 The maximum stress of ICs (left) and ECs (right)

3.4 Discussion

Prior studies (Michailides et al., 2016, Lee and Lee, 2019, Jiang et al., 2019) documented the effect of wave or wind on dynamic response. However, these studies did not include the structural performance due to wind, wave, wave-wind alignment, or misalignment. Therefore, these aspects have been focused on in this study. The wave direction of the environmental conditions was found to have less effect on the equivalent stress of the critical connections compared with the wind direction. Although wave-induced stress does vary on the surface of the columns, it is less critical than the stress at the connections.

On the contrary, the wind direction is found to play a key role in the stress level of the connections. The critical connections are located at the top of the column (P3R). Irrespective of the wind direction, the critical stresses are always in compression, where buckling is likely to occur.

Wave-wind misalignment has a considerable adverse effect on structural behaviour, especially with respect to the stress level. Therefore, the practical environmental data of the targeted sea area is essential in simulating FWTs.

Geometrical and material nonlinearities have seldom been considered in investigating the structural behaviour of FWT platforms. As a multi-body system, when the stress is approaching yield strength, geometrical and/or material nonlinearity would help

structures to redistribute the internal stress and maximize the utilisation of the material. According to geometrically and materially nonlinear analysis (GMNA), the thickness of the floating platform could be reduced by 40% when compared with a linear analysis. In other words, the total mass could be reduced by about 1023 tons, which is 14.4% of the self-weight of whole floating wind turbine including ballast (Roddier et al., 2010a).

During the design process, more attention should be paid to the connections. The internal columns may have punch-shear failure or local buckling due to the large axial force of pontoons. The ends of pontoons and bracing may have stress concentrations which could lead to local buckling. Therefore, strengthening is recommended for the connection region.

An assumption that the external columns are mainly bearing wave load should be reconsidered especially for EC1. IC1 not only bears the self-weight of wind turbine and wind load but also bears a large portion of wave load. The composite action between internal and external columns should not be ignored.

Although this study uses the WindFloat prototype to investigate the structural behaviour of SSPs, this approach is applicable to other SSP concepts, especially those with a steel truss platform. Like most approaches, the present study also has certain limitations. First, it relies on potential flow theory for the wave loads, which may not be accurate for extreme waves. In this respect, this approach may be complemented in future with CFD or experimental study to investigate the nonlinear effect of wave. Second, equivalent static structural analysis is used to save computing cost. In future work, a time-dependent (transient) analysis should be undertaken. Third, regular waves are adopted in a hydrodynamic model which cannot represent a realistic marine environment, though modelling of regular waves can save computer resources and is widely used in the hydrodynamic analysis. Compared to a regular wave, the irregular wave has a more complicated amplitude. This is because that an irregular wave can be composed of the linear superposition of several regular waves with different wave period and height. Parts of an irregular wave time series might have a larger/steeper amplitude or smaller/gentler amplitude according to the superposition of different regular waves. Therefore, the irregular wave may lead to a more complicated motion of the FWT and more extreme load cases compared to the regular wave. However, this study mainly focuses on the

direction of the wave, the combined effect of a wave with wind, and structural nonlinearity. Fourth, the rotor thrust provided by NREL is adopted to consider the wind load. Although the impact of platform motions on the rotor thrust is considered, the calculated rotor thrust is yet to be validated using monitored data of rotor thrust in operation. Other methods of aerodynamic force calculation could also be compared with the proposed calculation. Fifth, GMNA is adopted and compared to LA to reduce the structural mass of the floating platform. Reducing the mass will impact the platform dynamics and resonance frequencies which is not being considered with this optimisation. The impact of reducing mass on the dynamic behaviour of FWT will be considered comprehensively with structural optimisation in future work. Note that the results were drawn on the basis of the WindFloat concept used in this study. Further research would be necessary to extend the validity of these analyses to other concepts or environmental conditions.

3.5 Conclusions

The nonlinear structural analysis of a floating offshore wind platform was undertaken considering both material and geometric nonlinearities. Potential flow theory was used to calculate the hydrodynamic response, and ANSYS APDL was adopted to transfer wave data including surface pressures and wave induced acceleration from AQWA to the ANSYS mechanical module. Based on the equivalent static structural analysis, 40 load cases were analysed to investigate the effect of various load combinations, and to determine the most critical load case. Finally, fully nonlinear finite element models were established to study the effect of material and geometric nonlinearities. The following conclusions have been drawn:

1. Considering the individual effects of waves and wind, both play a significant role in the equivalent stress of the connections. The stress of the tower base is dominated by the wind force.
2. The critical positions are located on the connections of pontoons and internal columns on the upper level of the platform, the column supporting the turbine. Geometric or material nonlinearities will not alter these critical locations.
3. Considering the effect of wave and wind directions, the maximum equivalent stresses of the connections with relatively large stress are more sensitive to the wind direction than the wave direction.

4. The azimuthal angle under aligned wave and wind condition should be an important consideration. Because the angle especially for 45° , 90° and 135° has a significant effect on the stress distribution in structures. However, the effect may be different from case to case. The wave-wind misalignment effect would increase the maximum equivalent stress of structures by up to 8.5%.
5. In the worst design case of this study, the thickness of structures could be reduced by up to 40% in buckling limit state by considering geometric and material nonlinearity. The nonlinear models prove the significance of considering the geometrical and material nonlinearity in modelling and designing floating offshore wind platforms, especially for large volume shell structures.
6. Geometrical and material nonlinearities would help structures to redistribute the internal stress and maximize the strength of the material. The maximum stress in connections and components is reduced due to material yielding and structural nonlinear deformations.
7. Mooring system should be considered and simulated accurately to avoid underestimating structural behaviour.

CHAPTER 4 – CODE-BASED CYLINDRICAL SHELL DESIGN COMPARISON

In Chapter 3, the nonlinear global structural behaviour of the floating platform of WindFloat has been studied under various environmental conditions in order to identify the critical failure modes and investigate the effects of geometric and material nonlinearities. To simplify the global model, no geometric imperfections nor internal stiffeners were considered. As they have significant effects on the buckling load capacity of a cylindrical shell, particularly the thin-walled shell, which is gaining increasing demand with the industry pushing towards larger and larger turbines, buckling behaviour of cylindrical shells will be targeted in the next two chapters (Chapter 4 & 5). The current chapter, Chapter 4, will focus on the code-based design solution comparisons of primary load bearing components, e.g. the external and internal columns in the WindFloat platform, while Chapter 5 will focus on buckling behaviour of a generic cylindrical shell, and the key influential factors to the buckling load capacity.

The worst environmental load case from Chapter 3, which causes the largest stress on the internal and external columns, will be adopted as the design load case. The shell structure design codes, [DNVGL-RP-C202 \(2019\)](#) (abbreviated as DNVGL), [EN1993-1-6 \(2007\)](#) and [EN1993-1-6 \(2017\)](#) are adopted in structural design. It should be noted that EN1993-1-6 (2007) was the latest version at the time when this research was carried out, which was overwritten by a newer version (EN1993-1-6 (2017)) in later stage of this PhD study. Although EN1993-1-6 (2007) is still used in the most recent literature ([Evkin and Lykhachova, 2021](#), [Li and Kim, 2022](#)), a considerable difference has been found in the buckling design of cylindrical shells, particularly on how imperfection effect is incorporated. Therefore, both the predecessor and the latest version of EN1993-1-6 have been adopted in this Chapter.

4.1 Problem Definition

The WindFloat developed by Principle Power is used as the concept of FWT in this study, which has been shown in Figure 3.1. The main geometric dimensions of WindFloat are provided in Table 3.1. It is a semi-submersible floating foundation composed of three columns to provide buoyancy and support a wind turbine. The structural assumptions of the platform have been presented in Section 3.1. The columns, pontoons, bracings and tower are all within the category of shell structures. To meet the engineering demands for

strength and stability, different limit states such as ultimate limit state, accidental limit state and fatigue limit state are considered in the structural design. In this study, the buckling resistance of steel shell structures is investigated and the related industry criteria, DNVGL standard and EN1993-1-6, are compared to develop a more economical design. The standards used in this study are as follows:

- DNVGL-RP-C202 Buckling strength of shells (DNVGL-RP-C202, 2019)
- EN 1993-1-6 (2007): Eurocode 3: Design of steel structures – Part 1-6: Strength and stability of shell structures (EN1993-1-6, 2007)
- EN 1993-1-6: 2007+A1: 2017: Eurocode 3: Design of steel structures – Part 1-6: Strength and stability of shell structures (EN1993-1-6, 2017)

4.1.1 Objectives

As one of the most important components of the platform, the external and internal columns are used to carry out the structural analysis and design. The objectives of the work include:

- To calculate the internal forces of the elements using the results of the analysis of the global structural model.
- To study and compare the DNVGL standard and Eurocode by analysing the buckling resistance of steel cylindrical shell structures.
- To propose a cost-effective solution for the stiffened shell to reduce the weight and cost of the hull.

4.2 Obtainment of design loads

According to the global structural analysis in Chapter 3, LC27 is the most critical case in stress level within all wave-wind aligned cases, which is then used to design the external columns and the internal columns. The details of LC27 are listed in Table 4.1 and the direction of the environmental load is shown in Figure 3.5.

Table 4.1 Environmental condition of LC27

Regular wave height	9 m
Wave period	10 s

Wave direction	45°
Wind speed at 10 m elevation	11.4 m/s
Wind direction	45°

The stress data of each individual structural components can be obtained from Chapter 3, which were integrated over the whole cross-section to obtain the design loads, e.g. axial force, bending moment, and shear force induced by shear and torsion. It is found that the largest design loads occur in the end of the external column and the internal column which support the wind turbine. The internal force of the connections between the pontoon, heave plate, external and internal columns affects the internal force of external and internal columns. Thus, in order to avoid the disturbance of the internal force between the connections, the edge sections (Figure 4.1) between the top of the heave plate and the bottom of the pontoon are adopted to obtain the largest stresses for the design of the external and internal columns. After calculation, the design loads are listed in Table 4.2. It should be noted that the factors of load combination have not been considered so that the results of design codes and FEA can be compared under the same load case.

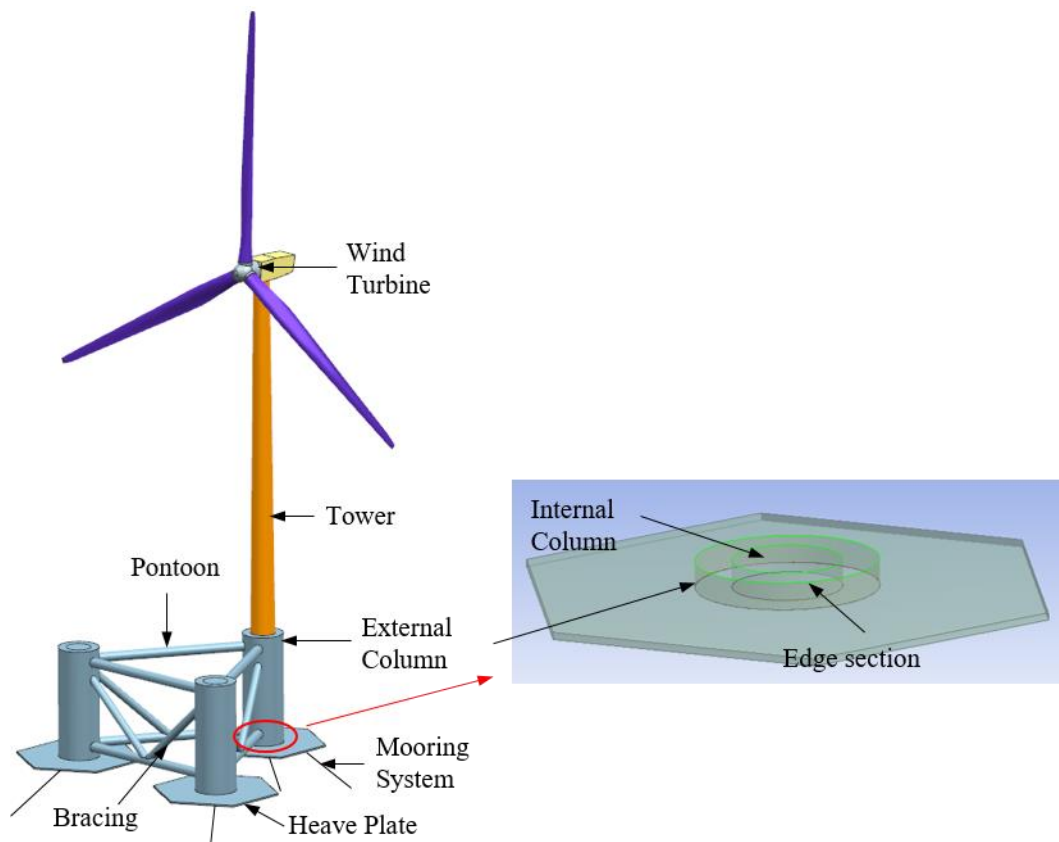


Figure 4.1 Edge section of external and internal columns

Table 4.2 Design loads for external and internal columns

	Axial force (kN)	Shear force (kN)	Bending moment (kNm)
External column	4354	1398	13664
Internal column	11180	1005	8867

4.3 Unstiffened shell structure design

The design processes of an unstiffened shell structure based on three design codes, the DNVGL, EN1993-1-6 (2007) and EN1993-1-6 (2017), are presented in Appendix A. In this section, the unstiffened shell structure is designed based on these three codes, and the design results are compared.

An Excel spreadsheet (Appendix B) has been developed to calculate the structural dimensions according to the DNVGL, EN1993-1-6 (2007) and EN1993-1-6 (2017) rules. The calculation procedure follows the flowchart proposed above. To obtain the minimum shell thickness, the other parameters (e.g. shell length and radius, yield strength of structural steel, etc.) remain unchanged. The design results of the external and internal columns based on various design standards are presented in Table 4.3

Table 4.3 Design results of external and internal columns (Unit: mm)

	DNVGL	EN1993-1-6 (2007)	EN1993-1-6 (2017)
Thickness of external column	43	37	37
Thickness of internal column	33	28	28

The solutions of the three design standards are rather similar, and they are all semi-empirical when considering the effect of geometric imperfections. The DNVGL uses the reduced buckling coefficient C and the reduced shell slenderness $\bar{\lambda}_s$ to calculate the buckling strength of a shell. By contrast, EN1993-1-6 proposes the imperfection reduction factor α and the buckling reduction factor χ to calculate the design stress value. The DNVGL code uses a larger partial safety factor $\gamma_M = 1.45$ compared with $\gamma_M = 1.1$ of

the EN1993-1-6 (2007) and EN1993-1-6 (2017). Thus, the required thicknesses of the cylinder based on two versions of EN1993-1-6 are smaller than that of the DNVGL. It should be noted that reducing or increasing the thickness of the column will impact the platform dynamics and resonance frequencies which is not being considered with this optimisation.

As can be seen from the design spreadsheet, in this study, the cylindrical shell is dominated by the circumferential (hoop) buckling. The EN1993-1-6 (2007) and EN1993-1-6 (2017) have the same design process on circumferential buckling, so they predict the same shell thickness to resist the external pressure on the column surface.

4.4 Stiffened shell structure design

Shell buckling is usually the major failure mode of a shell structure and geometric imperfection is usually the main cause of shell buckling failure. Therefore, stiffeners are commonly used on a shell surface to reduce the imperfection, improve stability and reduce the material usage. The design processes of stiffened shell structure based on three design codes, the DNVGL, EN1993-1-6 (2007) and EN1993-1-6 (2017), are presented in Appendix A. In this section, the design results based on these three codes are presented.

4.4.1 DNVGL-RP-C202

In the structural design of unstiffened shell, if the design loads are obtained and the length and radius of the cylindrical shell are determined, the thickness can be designed by using the design codes. The design loads, which have been used to design the external and internal columns, are also adopted to design the external and internal columns with stiffeners. Different from the structural design of unstiffened shells, more variables besides the thickness need to be considered in the stiffened shell design. Thus, there is no unique result for the structural design of stiffened shells.

Under the literature review of optimization design of offshore structures, the existing studies mainly focus on mass reduction, however other factors of fabrication should also be considered. Therefore, to carry out an effective design, two objectives are proposed as two design cases. Design case 1 is used to minimize the mass of shell structure and design case 2 is used to minimize the cost in the fabrication analysis shown in Table 4.4, such as

labour welding and filler material. In this section, fillet weld (Figure 4.2) is adopted to connect the stiffeners and shell. Assumptions of welding speed are provided as 100 mm/min based on friction stir welding (Shen et al., 2010, Li et al., 2017). The leg length l of weld is $0.7t$ (t is the thickness of panel) (MCA, 2020). According to the structural scantlings, the length, dimensions and material weight of filler rod can be determined. The weight of filler rod m_w is calculated as:

$$m_w = AL_w\rho_w = 0.5l^2L_w\rho_w \quad (4.1)$$

where A is the cross sectional area of weld, L_w is the length of weld and ρ_w is the density of weld using 7.85 g/cm^3 . Thus, based on the length of welding and the welding speed, the required labour time of welding can be calculated. The total costs of the fabrication include the material costs of steel plate and filler rod and labour welding are estimated.

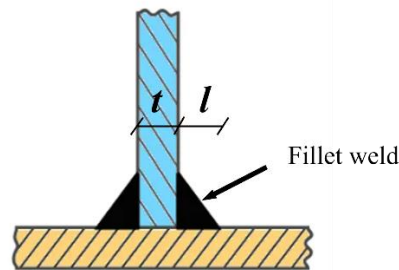


Figure 4.2 Fillet weld

Table 4.4 Costs considered in the fabrication analysis (Quintana, 2016, Shen et al., 2010, Li et al., 2017)

Cost voice	Specification	Unit cost
Steel plate	Structural steel	1 €/kg
Labour welding	Welding speed: 100 mm/min	20 €/h
Filler rod	Solid wire	2 €/kg

An Excel spreadsheet (Appendix B) using the Solver add-in function has been developed to carry out the structural design of the stiffened shell. The solver is used to find an optimal value for formulas in one cell (called the objective cell) by changing the design variables. The objective value is subjected to constraints, or limits, on the values of other formula cells on a worksheet. The specific process and the definition of the objective, constraints, and design variables are as follows. Firstly, the objective and the constraints

need to be determined in the spreadsheet. The objectives have been provided for two design cases. The constraints are as following: 1) the design buckling strength of every part is larger than the design stress induced by the design loads; 2) the structural dimensions meet the geometric proportions requirement; and 3) the structure meets the stability requirement which has been introduced in Section A.1.1. In addition, the design variables (the shell thickness, the dimensions of ring and longitudinal stiffeners) are adjusted to satisfy the constraints and produce the best result for the objectives.

Table 4.5 summarizes the dimensions results of the stiffened shells used as the external and internal columns based on the two design cases. As can be seen from Table 4.5 and Figure 4.3, the thickness of the shell, the web and flange of the longitudinal stiffener in Case 1 are thin and narrow. The philosophy of optimised structural dimensions based on Case 1 considering mass reduction only is to decrease the steel thickness and to utilise the strength of material as much as possible. The ring stiffeners are mainly used to bear the external pressure, while the longitudinal stiffeners are used to increase the axial compression capacity. In case 1, the web thickness of the ring stiffeners is much thicker than the web thickness of the longitudinal stiffeners; whereas in case 2 it is not necessary to have the longitudinal stiffeners. This is because the ring stiffeners are used to resist the circumferential buckling as the external column and the internal column bear a large pressure induced by wave and ballast water, respectively. However, the longitudinal stiffeners and ring stiffeners need more filler material and labour to weld, so the longitudinal stiffeners are not adopted in Case 2 to save costs.

According to Table 4.6, although the cost of structural steel is cut down to 37,102 € and 23,719 € in Case1 for the external and internal columns, which account for 40% and 25% cost of them in Case 2. However, the costs of labour welding and filler material of cases 1 are surprisingly high. When the fabrication of connections is considered, the cost decreases 69% from 311,201 € to 96,396 € and 44% from 177,141 € to 98,711 € for the external and internal columns, respectively. It is found that the external column has more potential to reduce the cost of fabrication when compared with the internal column.

Table 4.5 Optimised results of the structural dimensions (unit: mm)

	External Column	Internal Column

	Case 1	Case 2	Case 1	Case 2
Shell thickness t	2.9	11	2.9	12
Distance of ring frames l	2098	1420	1705	1970
Longitudinal stiffener web width h_s	18.8	0	20.8	0
Longitudinal stiffener web thickness t_{ws}	0.6	0	0.6	0
Longitudinal stiffener flange width b_s	9.6	0	11.2	0
Longitudinal stiffener flange thickness t_{fs}	0.6	0	0.6	0
Spacing of longitudinal stiffener s	42.1	0	45.8	0
Ring web width h_r	399.8	360	379.9	388
Ring web thickness t_{wr}	12.2	11	11.6	11.8
Ring flange width b_r	0	0	11.6	0
Ring flange thickness t_{fr}	0	0	5	0

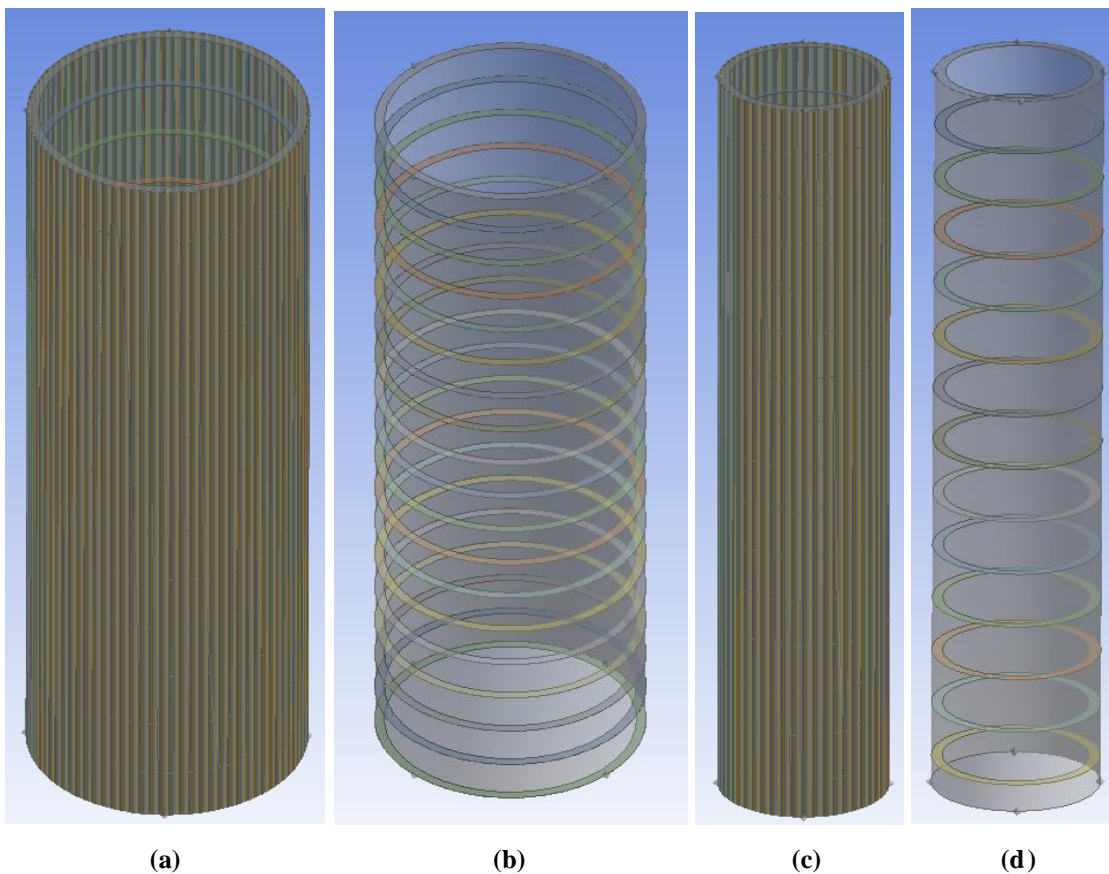


Figure 4.3 Geometries of (a) external column Case 1, (b) external column Case 2, (c) internal column Case 1 and (d) internal column Case 2

Table 4.6 Costs considered in the fabrication analysis (unit: €)

Cost item	External Column		Internal Column	
	Case 1	Case 2	Case 1	Case 2
Steel	37,102	91,814	23,719	95,406
Labour welding	271,541	3,982	151,990	2,872
Filler material	2,558	600	1,432	433
Total Cost	311,201	96,396	177,141	98,711

4.4.2 EN1993-1-6 (2007) & (2017)

After calculation, Table 4.7 summarizes the dimensions results of the stiffened shells used as the external and internal columns based on EN1993-1-6 (2007) and EN1993-1-6 (2017). Figure 4.4 shows the geometries of the external and internal columns EN1993-1-6 (2017) (EN1993-1-6 (2007) and EN1993-1-6 (2017) provide similar results, thus the results of EN1993-1-6 (2017) are shown only). As can be seen from Table 4.7, EN1993-1-6 (2007) provides a more conservative result with a shorter distance of ring frames. The main reason is that the plastic resistance of bending moment is considered in EN1993-1-6 (2017) based on the RRD method, however, EN1993-1-6 (2007) uses a purely elastic analysis to calculate the structural resistance due to bending. The strength of the material is better utilized in EN1993-1-6 (2017).

Compared with the dimensions of the cylinder with ring stiffeners predicted by DNVGL in Table 4.5 and EN1993-1-6 (2017) in Table 4.7, DNVGL provides a more conservative result with a shorter distance (1970mm for internal column) of ring frames and a thicker ring thickness (11mm and 12mm for the external and internal column respectively). As with EN 1993-4-1 (EN1993-4-1, 2007) and EN 1993-4-2 (EN1993-4-2, 2007), EN1993-1-6 is normally used to design tanks and silos which contain liquid and solid with internal pressure. The external ring frame would be extended by the cylinder thus the ring buckling does not need to be checked. However, offshore structures are used in the marine environment and for bearing large external forces. The ring frame is going to undertake the inward pressure, which may cause ring buckling. Thus, the buckling mode of the ring frame is required to carry out a safe structural prediction. Moreover, longitudinal stiffeners are suggested to add to these design codes of the stiffened shell. For these

reasons, EN1993-1-6 (2007) and EN1993-1-6 (2017) still need to be improved to be more applicative for the stiffened shell of offshore structures.

Table 4.7 Structural dimensions of stiffened shell (unit: mm)

	EN1993-1-6 (2007)		EN1993-1-6 (2017)	
	External column	Internal column	External column	Internal column
Radius r	5000	3000	5000	3000
Shell thickness t	11	12	11	12
Distance of ring frames l	1250	2700	1420	2950
Ring web width h_r	360	388	360	388
Ring web thickness t_{wr}	6	3	6	3

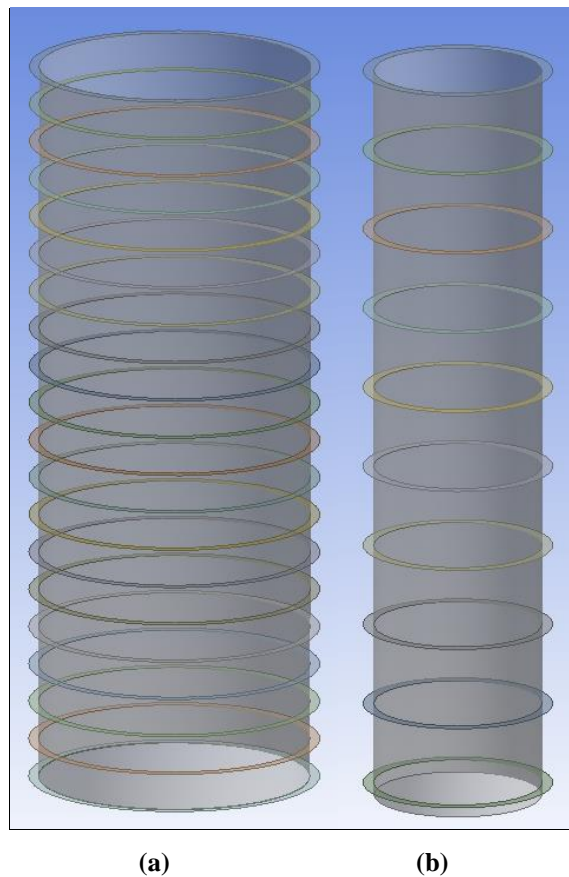


Figure 4.4 Geometries of (a) external column, (b) internal column based on EN1993-1-6 (2017)

4.5 Conclusions

Combined with this chapter and the previous chapter, a complete process from structural analysis to structural design for the components of a floating platform is presented. This chapter has presented the design loads for the structural design of the shell structure based on the previous study. The design process based on three design codes (DNVGL-RP-C202, EN1993-1-6 (2007) and EN1993-1-6 (2017)) is introduced. The structural design and design comparison of the external and internal columns with and without stiffeners are provided based on these design codes.

Compared with EN1993-1-6 (2007) and EN1993-1-6 (2017), DNVGL predicts a thicker unstiffened cylinder because of a larger partial safety factor. As EN1993-1-6 (2007) and EN1993-1-6 (2017) provide the same design process of circumferential buckling, they predict the same thickness for the unstiffened cylinders when the cylindrical shell is dominated by circumferential buckling. Furthermore, the FE model predicts a larger thickness for the external and internal columns of a floating platform to resist the local buckling compared with the results of the code-based approaches. Thus, for this type of complex offshore structure, the different analysis and design methods need to be considered synthetically to provide a comprehensive and safe structural analysis and design.

According to the stiffened shell design, the shell thicknesses of both the external and internal columns are cut down significantly if the longitudinal and ring stiffeners are adopted according to the DNVGL code. The stiffeners can improve the stiffness and reduce the material mass, but excessive stiffeners will increase extra costs such as filler material and labour related to welding. After taking into consideration the labour, the overall costs of the external and internal columns are reduced sharply. The design results of the stiffened shells are largely determined by the constraints and the assumptions. For example, the design case of minimizing the costs in the fabrication considers the relevant costs of welding. Other fabrication conditions have not been considered such as installation or transportation. The effect of welding on fabrication is wide and depends on the different equipment and method of welding. The LCOE reduction of the project for FWTs can be further studied by a more optimized design considering more conditions, which is the initial motivation of this thesis. Furthermore, DNVGL provides a more conservative design result for the cylindrical shell with ring stiffeners compared with

EN1993-1-6 (2007) and EN1993-1-6 (2017) as the ring buckling check is neglected in these two Eurocode. EN1993-1-6 (2007) and EN1993-1-6 (2017) need to be improved if they are adopted for the stiffened shell of offshore structures.

CHAPTER 5 – ULTIMATE STRENGTH OF UNSTIFFENED CYLINDRICAL SHELL UNDER COMBINED COMPRESSION AND BENDING

Nonlinear structural response of floating offshore wind platforms under various actions of environmental forces has been studied in Chapter 3. After that, the external and internal columns, as primary structural components, are designed using various design codes in Chapter 4, based on the assumptions that those design codes are all fit for purpose. However, EN1993-1-6 is recommended for structures with $r/t < 160$, same as the DNVGL which follows the same recommended slenderness range (DNVGL-ST-0126, 2018). With the industry pushing towards larger wind turbines, large floating platforms with r/t exceeding 160 are likely to be in demand in order to meet the floatability and stability requirements. Therefore, the structural behaviour of shells, particularly the buckling load capacities, of a wide range of slenderness needs to be further investigated. Considering the complex load conditions that the offshore floating structures will experience during the life time, the buckling behaviour under combined compression and bending is going to be studied numerically. Although torsion is a critical failure mode for the wind tower, it is less critical for the floating platform due to its large torsional stiffness, which is therefore neglected in this chapter.

Firstly, the ultimate strength of unstiffened cylindrical shells with a wide range of ratio of r/t (*Radius/thickness*) (including r/t of the external and internal columns of WindFloat's platform) under combined compression and bending is studied based on FEA and code-based approach (DNVGL, EN1993-1-6 (2007) and EN1993-1-6 (2017)). Secondly, based on the data of the ultimate strength of cylindrical shells, the accuracy of these codes is evaluated. Thirdly, the reliability analysis of the shell design codes is carried out and recommended modification to partial safety factor is proposed to improve the design codes. Finally, a case study of the ultimate strength of stiffened cylindrical shells is presented, which is used to compare with the unstiffened cylindrical shell.

5.1 Code-based approach

In order to obtain the design strength of cylindrical shells, different design guidelines (DNVGL-RP-C202 (2019) (abbreviated as DNVGL), EN1993-1-6 (2007) and EN1993-1-6 (2017)) are used and compared with finite element models. The formulae for

calculating design buckling strength under axial compression, bending moment, and combined axial compression and bending moment have been presented in Chapter 4. This section presents the recommended tolerance of initial geometric imperfection as given by the design guidelines.

5.1.1 Tolerances of initial geometric imperfection

According to DNVGL (DNVGL, 2020) guidance, the maximum imperfection tolerance δ is given as:

$$\delta = \frac{0.01g}{1+g/r} \quad (5.1)$$

where:

g is the length of imperfection, and equal to $\min [s, 1.15\sqrt{l\sqrt{rt}}, \pi r/2]$ along the circumferential direction, or $\min [l, 4\sqrt{rt}]$ along the longitudinal direction;

s is the stringers (longitudinal stiffeners) spacing;

l is the distance between rings;

r is the radius shown in (a) (b)

Figure 5.1.

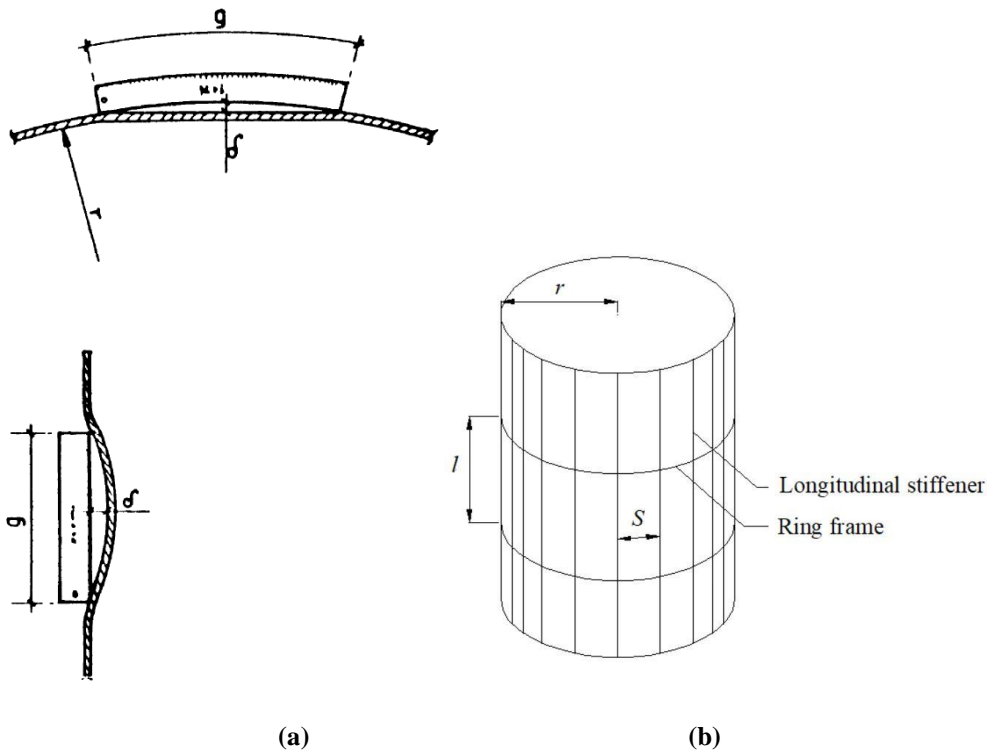


Figure 5.1 Definition of (a) δ and g , (b) s , l and r (DNVGL, 2020)

In both EN1993-1-6 (2007) and EN1993-1-6 (2017), the same parameters of the geometric imperfection are recommended. The maximum imperfection amplitude $\Delta w_{0,eq}$ should be the larger value of $\Delta w_{0,eq,1}$ and $\Delta w_{0,eq,2}$:

$$\Delta w_{0,eq,1} = l_g U_{n1} \quad (5.2)$$

$$\Delta w_{0,eq,2} = n_i t U_{n2} \quad (5.3)$$

where:

l_g is the relevant gauge lengths shown in Figure 5.2;

n_i is a multiplier to achieve an appropriate tolerance level ($n_i = 25$ is recommended);

U_{n1} and U_{n2} are the dimple imperfection amplitude parameters for the relevant fabrication tolerance quality class. The recommended values are given in Table 5.1.

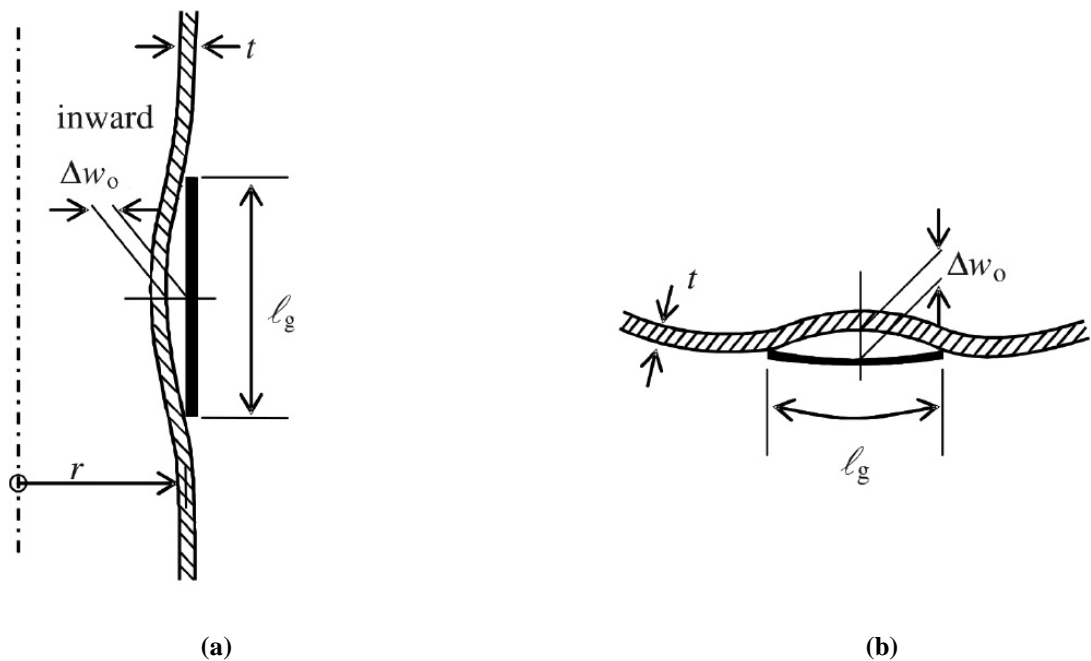


Figure 5.2 Gauge length l_g measured on (a) meridian and (b) circumferential circle (EN1993-1-6, 2017)

Table 5.1 Recommended values for dimple imperfection amplitude parameters U_{n1} and U_{n2}

Fabrication tolerance quality class	Description	Recommended value of U_{n1}	Recommended value of U_{n2}

Class A	Excellent	0.010	0.010
Class B	High	0.016	0.016
Class C	Normal	0.025	0.025

In buckling strength calculation, the fabrication quality parameter Q is used to calculate the elastic imperfection reduction factor α . Q is classified by fabrication tolerance quality class A, B and C, which should be consistent with the selection of U_{n1} and U_{n2} . In this study, Class B (High quality class) is adopted to study the ultimate strength of a cylinder.

5.2 Description of the numerical model

5.2.1 Material properties

High tensile structural steel, S355, was used for the studied shell, where the yield strength and elastic modulus are taken as 355 MPa and 210 GPa, respectively. Where strain hardening is included, a tangent modulus of 2.1 GPa (1% of the elastic modulus) is used. Figure 3.14 has plotted the nonlinear stress-strain curves of S355 structural steel.

5.2.2 Geometric imperfection

An eigenvalue buckling analysis based on the linear perturbation method is carried out first, and the first buckling mode is adopted as an imperfection profile of the cylinder. As the cylinders of FWTs work in a complex marine environment, they have to bear multiple loads including self-weight of wind turbine, wave loads, bending moment from tower base generated by wind loads, lateral forces from trusses or collisions with boats, etc. Thus, four different types of loads are used to generate the imperfection profiles: axial compressive load, lateral pressure, bending moment and lateral point load. Figure 5.3 plots the first buckling mode shapes of the cylinder subjected to the four different loads, which are to be used as the imperfection a, b, c, and d in later studies. As the focus of this chapter is to study the preliminary effect of the single imperfection profile of the cylinder, the combined imperfection has not been considered and it will be carried out in future work.

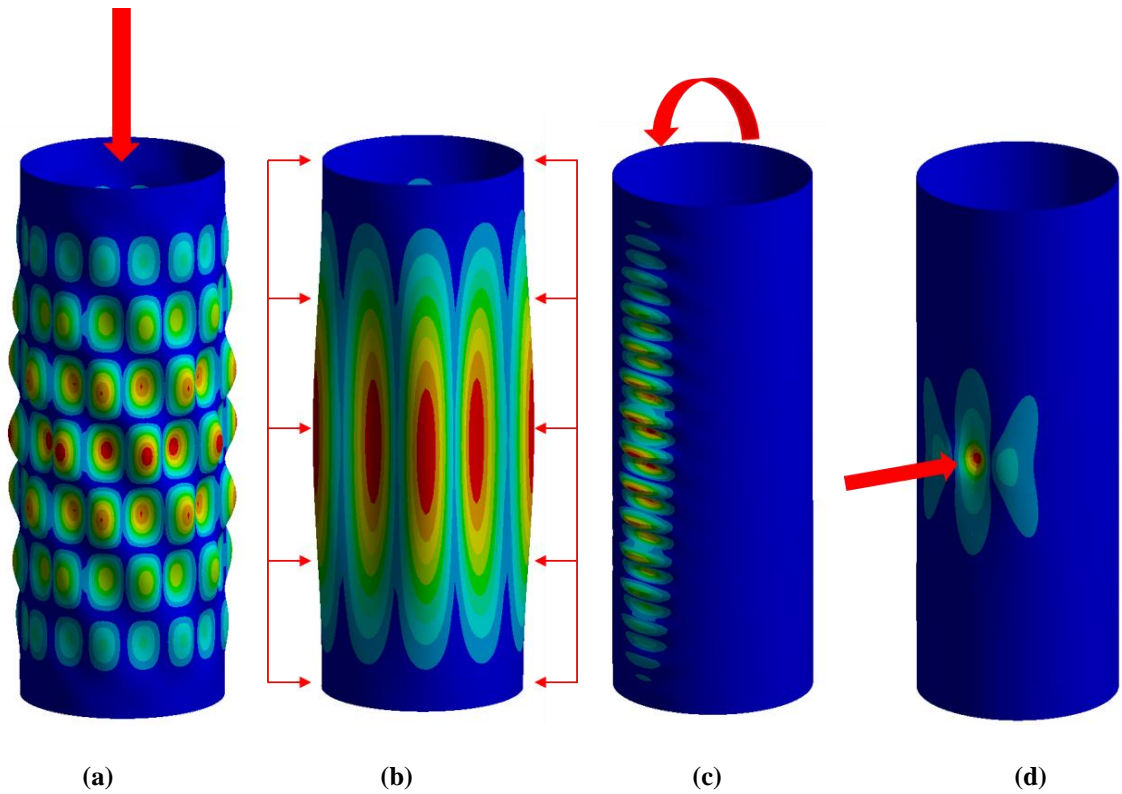


Figure 5.3 Imperfection profiles subjected to (a) axial compression load, (b) lateral pressure, (c) bending moment and (d) lateral point load (amplified by 50 times)

5.3 Finite element modelling

Nonlinear buckling analyses of simply supported cylindrical shells under combined axial compression and bending moment are performed using shell element (shell 181) in ANSYS. In order to facilitate the analysis (finite element analysis), only a half length of the cylindrical shell is analysed because of symmetric nature of the shell. As shown in Figure 5.4, the half model of the shell has two end sections; one represents the symmetric plane on which the longitudinal displacement and three rotations are constrained; the other is the simply supported plane on which the radial and circumferential displacements are constrained. For the presentation, however, the results such as stress contours are presented for the entire shell by using mirror function. To obtain the M-N interaction curves of the cylindrical shell under compression and bending, eccentric forces are applied on the top of the cylinder through a remote point, as shown in Figure 5.4. The compression is equal to the eccentric force and the bending is equal to the eccentric force multiplied by the eccentric distance S .

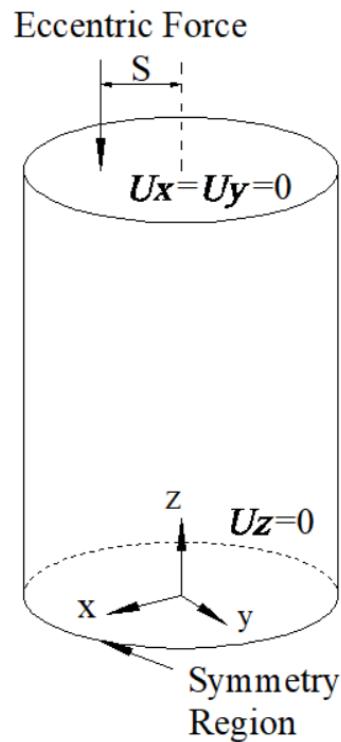


Figure 5.4 Boundary condition and loading mode

The simulation process is provided as follows: firstly, a static structural analysis based on a unit perturbation load is carried out; secondly, the results (pre-stress) were transferred to a linear eigenvalue buckling analysis to obtain the eigenvalue and corresponding buckling mode shapes; thirdly, the first eigenvalue buckling mode shape is adopted as the initial geometric imperfection, with a magnitude as defined by either Eurocode or DNVGL; lastly, a geometric and material nonlinear analysis (GMNA) is carried out in static structural module.

5.3.1 Case study of a FE model

In this section, a case study is carried out to justify the significance of the internal forces in the floating platform. Different from the shell element that is used in Chapter 3, the beam element is adopted to obtain the internal forces. In Chapter 3, two steel shells are used to represent the internal and external columns. According to the WindFloat concept in Figure 3.1, the internal columns, pontoons and bracings are connected as a load-bearing frame; the external columns cover the internal columns. In this case study, the external columns, wind turbine and heave plates have not been considered and the load-bearing frame is evaluated only. The simply supported boundary condition is applied at the end

of the internal column. The sketch of WindFloat platform shown in beam element is shown in Figure 5.5.

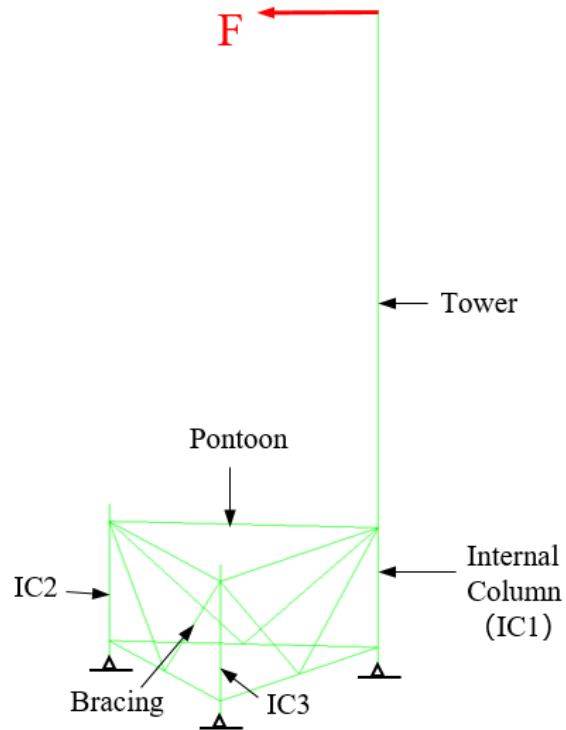


Figure 5.5 Sketch of WindFloat platform shown in beam element

To assess the internal forces of the components, a horizontal point load (800 kN, which is based on the maximum thrust of a 5 MW wind turbine shown in Figure 3.3) from 0° , 45° , 90° , 135° and 180° (refer to Figure 3.5) is applied on the top of the tower to simulate the wind load. After comparing of all components, IC1 is the most critical component which has the largest axial force, bending moment and torsional moment. The internal forces and the stresses induced by the forces of IC1 are summarized in Table 5.2. Compared with the stress induced by the axial force and the stress induced by the bending moment, the largest shear stress induced by the torsion is only 0.5 MPa, which is negligible. Thus, torsion has not been considered in the study of ultimate strength of the cylindrical shell.

Table 5.2 Summary of internal forces and stresses of IC1

Direction of point load	Maximum force (negative means compression)	axial (kN)	Normal stress due to axial force(MPa)	Maximum bending moment (kNm)	Normal stress due to bending moment (MPa)	Maximum torsional moment (kNm)	Shear stress due to torsion (MPa)
0°	-8695		-9.2	69892	50.2	8E-09	0
45°	-9347		-9.9	69828	50.1	1008	0.4
90°	-10923		-11.6	69765	50.1	1426	0.5
135°	-12499		-13.3	69828	50.2	1008	0.4
180°	-13151		-14.0	69892	50.2	8E-09	0

5.3.2 Test matrix

The tests of FEA can be categorized into two groups: Group A and B. In Group A, the parameters of models are determined according to the geometry of the external and internal columns, which is presented as follows:

- Radius to thickness ratio: $r/t = 50$ & 100 (5 m/ 0.1 m & 5 m/ 0.05 m for external columns; 3 m/ 0.06 m & 3 m/ 0.03 m for internal columns);
- Length to radius ratio: $L/r = 5.4$ & 9.0 (27 m/ 5 m for external columns; 27 m/ 3 m for internal columns);
- Maximum geometric imperfection amplitude based on two guidelines: DNVGL & Eurocode;
- Imperfection profiles: four imperfection profiles as shown in Figure 5.3.

Based on Group A, the effects of imperfection profiles and amplitudes can be determined. However, it is inadequate to assess the accuracy and reliability of the design standards due to the small range of geometrical slenderness that is covered in Group A. Hence, the geometrical parameters of cylinders are extended to carry more tests in Group B. In the literature ([Wang and Sadowski, 2018](#), [Wang et al., 2018a](#)), r/t is adopted ranging from 200 to 1000, so $r/t = 200$, 500 & 1000 are considered in Group B. Furthermore, three lengths of cylinders are adopted: short, medium and long cylinders based on Eurocode's recommendation. Only one imperfection profile (Imperfection c) has been used in Group B as it is concluded to be the most critical profile from Group A tests.

The geometrical properties of Group A and B are summarised in Table 5.3 and Table 5.4. There are 32 models in Group A and 18 models in Group B. To describe the strength capacity of cylindrical shell under combined axial load and bending moment, M-N interaction curve is adopted, which displays the maximum axial load and bending moment that a column could carry in x axis and y axis. It is necessary to have enough data to describe a M-N interaction curve. Based on the analysis experience of finite element modelling and related literature of cylindrical shell under combined loads (Garzón-Roca et al., 2012), around ten load cases were run to plot one M-N curve (one M-N curve represents one model). Therefore, in total 50 models and 469 test cases have been carried out.

Table 5.3 Geometrical properties of Group A

Series	L/r	r/t	L (m)	r (m)	t (mm)	Max. imperfection amplitude (mm)	Imperfect ion profiles
1	5.4	100	27	5	50	14.3 (DNVGL)	
2	5.4	100	27	5	50	32.0 (EN1993-1-6)	
3	5.4	50	27	5	100	18.1 (DNVGL)	Four imperfect ion profiles a, b, c and d
4	5.4	50	27	5	100	45.3 (EN1993-1-6)	
5	9.0	100	27	3	50	8.6 (DNVGL)	
6	9.0	100	27	3	50	19.2 (EN1993-1-6)	
7	9.0	50	27	3	100	10.8 (DNVGL)	
8	9.0	50	27	3	100	27.2 (EN1993-1-6)	

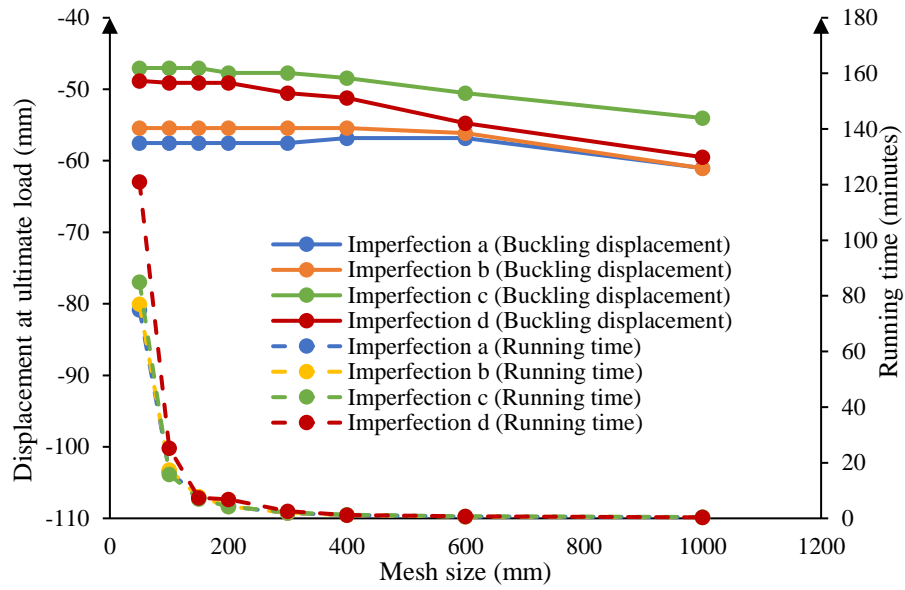
Table 5.4 Geometrical properties of Group B

Series	L/r	r/t	L (m)	r (m)	t (mm)	Length parameter ω	Cylinder types	Maximum imperfection amplitude of profile c (mm)
--------	-------	-------	---------	---------	----------	---------------------------	----------------	--

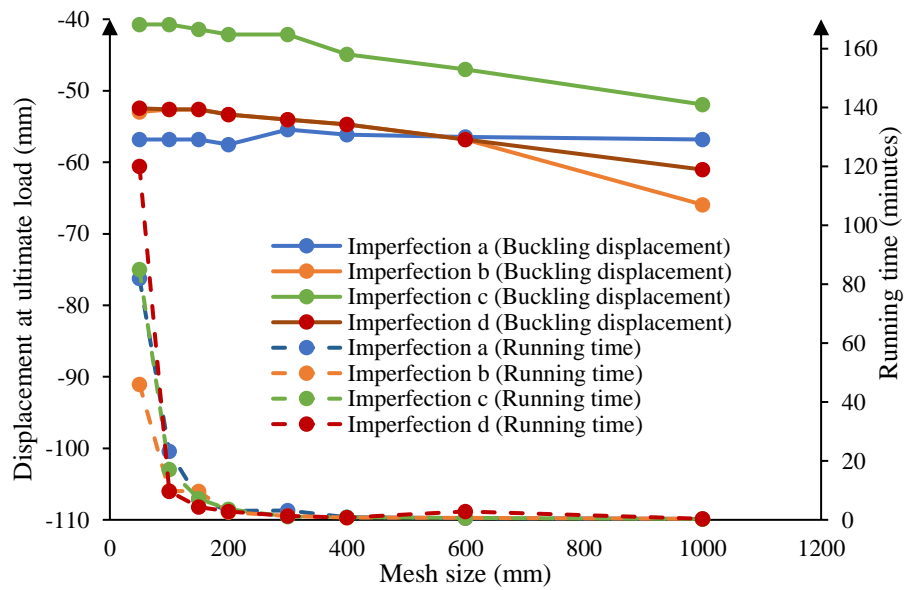
								DNVGL	EN1993-1-6 (2007) & (2017)
9	0.12	200	0.6	5	25	1.7	Short	4.79	22.62
10	3.54	200	17.68	5	25	50	Medium	11.02	22.62
11	14.14	200	70.71	5	25	200	Long	11.02	22.62
12	0.08	500	0.38	5	10	1.7	Short	3.14	14.31
13	5.59	500	27.95	5	10	125	Medium	7.59	14.31
14	22.36	500	111.80	5	10	500	Long	7.59	14.31
15	0.05	1000	0.27	5	5	1.7	Short	2.26	10.12
16	7.91	1000	39.53	5	5	250	Medium	5.61	10.12
17	31.62	1000	158.11	5	5	1000	Long	5.61	10.12

5.3.3 Mesh convergence study

Mesh convergence study is performed to obtain an optimal mesh element size. Two models with four imperfection profiles are selected for mesh convergence study: Series 3 ($L/r = 5.4$ and $r/t = 50$) and 6 ($L/r = 9$ and $r/t = 100$) shown in Table 5.3. The mesh element size ranges from 50 mm to 1000 mm. The results of mesh convergence study are presented in Figure 5.6 including the buckling displacement of the structure and the running time of the FE analysis. The maximum buckling displacement is converged when mesh size is smaller than 200 mm, while the running time increases exponentially accordingly. The largest difference of the ultimate displacement of Series 3 and 6 between mesh size 50 mm and 200 mm are 1.47% (Imperfection c) and 3.32% (Imperfection c) respectively. Balancing the accuracy of results and computational cost, a mesh size of 200 mm is adopted in all FE modelling.



(a) Series 3 $L/r = 5.4$ and $r/t = 50$



(b) Series 6 $L/r = 9$ and $r/t = 100$

Figure 5.6 Results of mesh convergence study

5.3.4 Validation of the model

In order to ensure the accuracy of FE modelling, the present model needs to be validated before carrying out parametric studies. The buckling behaviour is largely determined by the ratio of radius-to-thickness (r/t) of the shell. In this study, the results of cylindrical

shells with $r/t = 50, 100, 333$ and 796 obtained from ANSYS FE prediction are validated with the existing experimental or numerical predictions.

Ifayefunmi (2016) studied the buckling behaviour of cylindrical shells with $r/t = 50, 100$ under axial compression using experimental and numerical methods. In the cylinder compression testing shown in Figure 5.7, the cylinder specimen is clamped between two platens. The top movable platen is gently descended to apply axial load until the specimen collapses. The experimental results of the ultimate capacity of cylindrical shells with $r/t = 50$ and 100 are used in the following validation work. Wang et al. (2019) studied the imperfection generation approaches in order to provide an accurate prediction of the buckling load of cylindrical shells with $r/t = 333$ under axial compression. The worst multiple-perturbation load approach (WMPLA) (the most detrimental combination of three dimple-shape imperfections) is adopted to generate the initial geometric imperfection for the cylindrical shells with $r/t = 333$ in the present FE model in the validation work. Li et al. (2021) carried out the experiment and numerical simulation of a cylindrical shells with $r/t = 796$ under axial compression. The geometry of the cylinder is measured using 3D scanning technology. According to the measured imperfection profile, WMPLA is used to build the geometry of the cylindrical shell in the present FE model in the validation work.

The finite element model based on ANSYS has been presented in Figure 5.4 using a symmetric boundary condition. A displacement along the z axis is applied on the top end to produce the axial compression to obtain the load-displacement curve and the buckling capacity. In the mesh convergence study, the ratio of radius to mesh element size is $5m/0.2m = 25$. Following this ratio of radius to mesh element size, the mesh element sizes are 2mm, 2mm, 20mm and 30mm for the cylindrical shells with $r/t = 50, 100, 333$ and 796 , respectively.

Table 5.5 Geometries of validation model (Li et al., 2017, Ifayefunmi, 2016, Wang et al., 2019)

r/t	50	100	333	796
r (mm)	50.6	50.9	500	796

t (mm)	1	0.5	1.5	1
L (mm)	112.4	113.06	600	620
Maximum imperfection amplitude (mm)	0.5	0.47	0.374	20.53

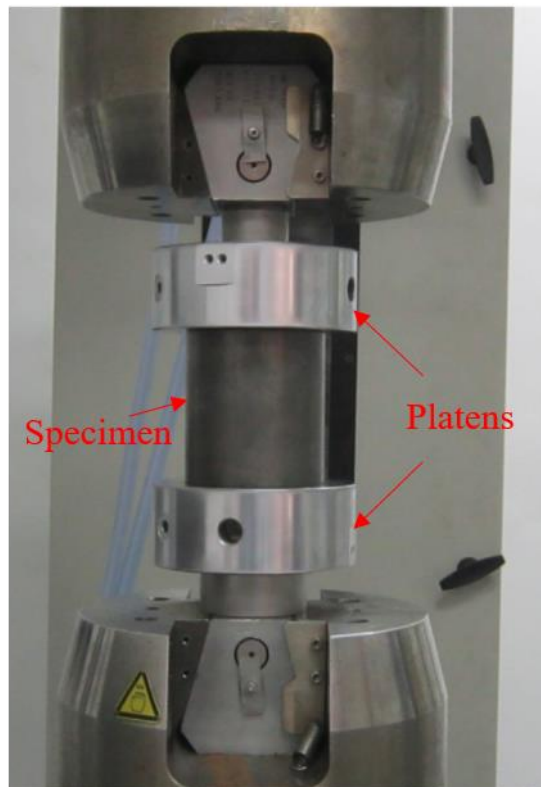
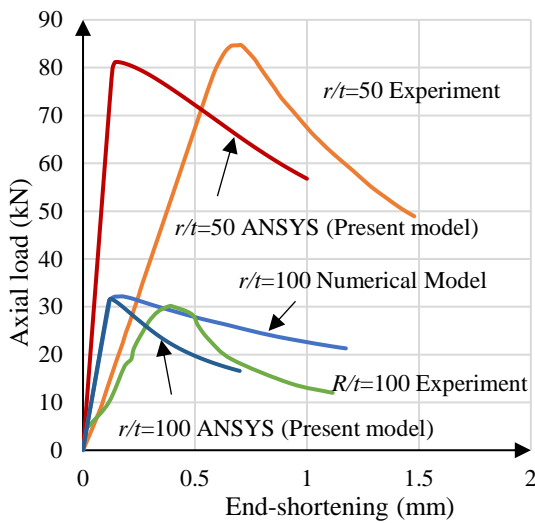


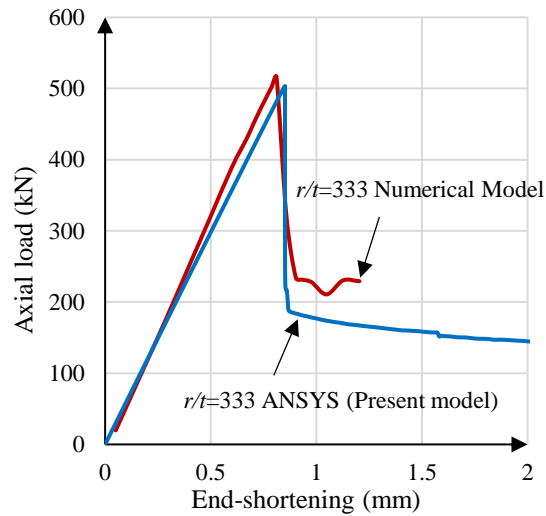
Figure 5.7 Test arrangement for cylinder provided by Ifayefunmi (2016)

Figure 5.8 shows the load-displacement curve of the cylindrical shells with $r/t = 50, 100, 333$ and 796 . In Figure 5.8 (a), the different inclined slopes between the FE prediction and experiment can be found. The main reason is that the boundary conditions of the specimen ends are not perfectly clamped as in the numerical model. As the testing goes on, the axial compression may not be transferred rapidly in the specimen. The plots of Figure 5.8 (b) follow a similar path up until collapse. In the post-buckling stage, the ultimate strength between the present model and the existing model has an apparent discrepancy. Figure 5.8 (c) has a similar comparison result to Figure 5.8 (b). The reason is that the thickness of the cylindrical shells with $r/t = 333$ and 796 are thin, and the imperfection profiles are more complex than the cylindrical shells with $r/t = 50$ and

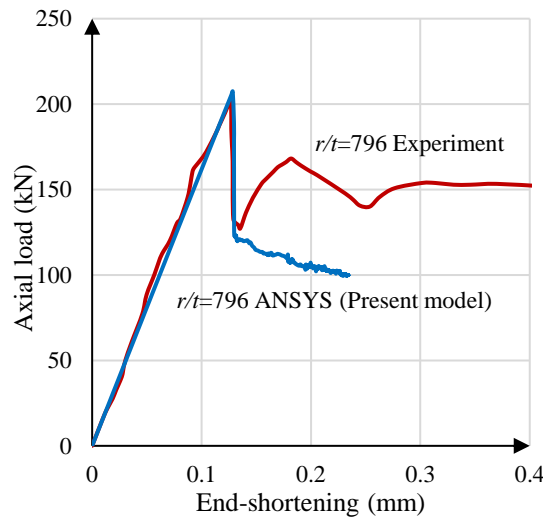
100. Different imperfection profiles lead to different buckling modes and post-buckling behaviours. Thus, the post-buckling behaviours of the cylindrical shells with large r/t are difficult to predict. Table 5.6 summarises the buckling load of the cylinders provided by the present ANSYS model and the existing experimental and numerical simulations. It can be found that there is a good agreement between these predictions with 5% maximum difference. Therefore, it can be concluded that the present model is adequate and can be adopted to carry out the following parametric studies.



(a) $r/t=50$ and 100 (Ifayefunmi, 2016)



(b) $r/t=333$ (Wang et al., 2019)



(c) $r/t=796$ (Li et al., 2021)

Figure 5.8 Load-displacement curves of the present model and existing studies

Table 5.6 Comparison of ANSYS predictions with the existing experimental and numerical predictions

r/t	E (GPa)	f_y (MPa)	F_{ANSYS} (kN)	F_{exp} or F_{num} (kN)	F_{ANSYS}/F_{exp} or F_{num}
50	214.0	256.2	81.19	84.67	0.96
100	193.7	203.1	31.60	30.13	1.05
333	75.538	357	503.43	516.05	0.98
796	200.0	600.0	207.30	202.39	1.02

5.4 Results and discussion of unstiffened cylindrical shells

5.4.1 Effect of imperfection profiles

Figure 5.9 presents the ultimate capacities of the cylindrical members under combined bending moment and axial compression by using different imperfection profiles and perfect shell. Overall, the cylinders with Imperfection b have the largest buckling strength compared with the other imperfection profiles. The buckling strength of the cylinders with Imperfection b is almost equal to the buckling strength of the perfect cylindrical shell. As for the models in Series 3 & 4, Series 5 & 6 and Series 7 & 8, the cylinders with Imperfection c have the smallest buckling strength. Furthermore, in model Series 1 & 2, Imperfection a and c become the most critical imperfection profiles. In general, Imperfection c is most detrimental to structural performance and the failure mode due to Imperfection c will be studied and compared with the other imperfection profiles.

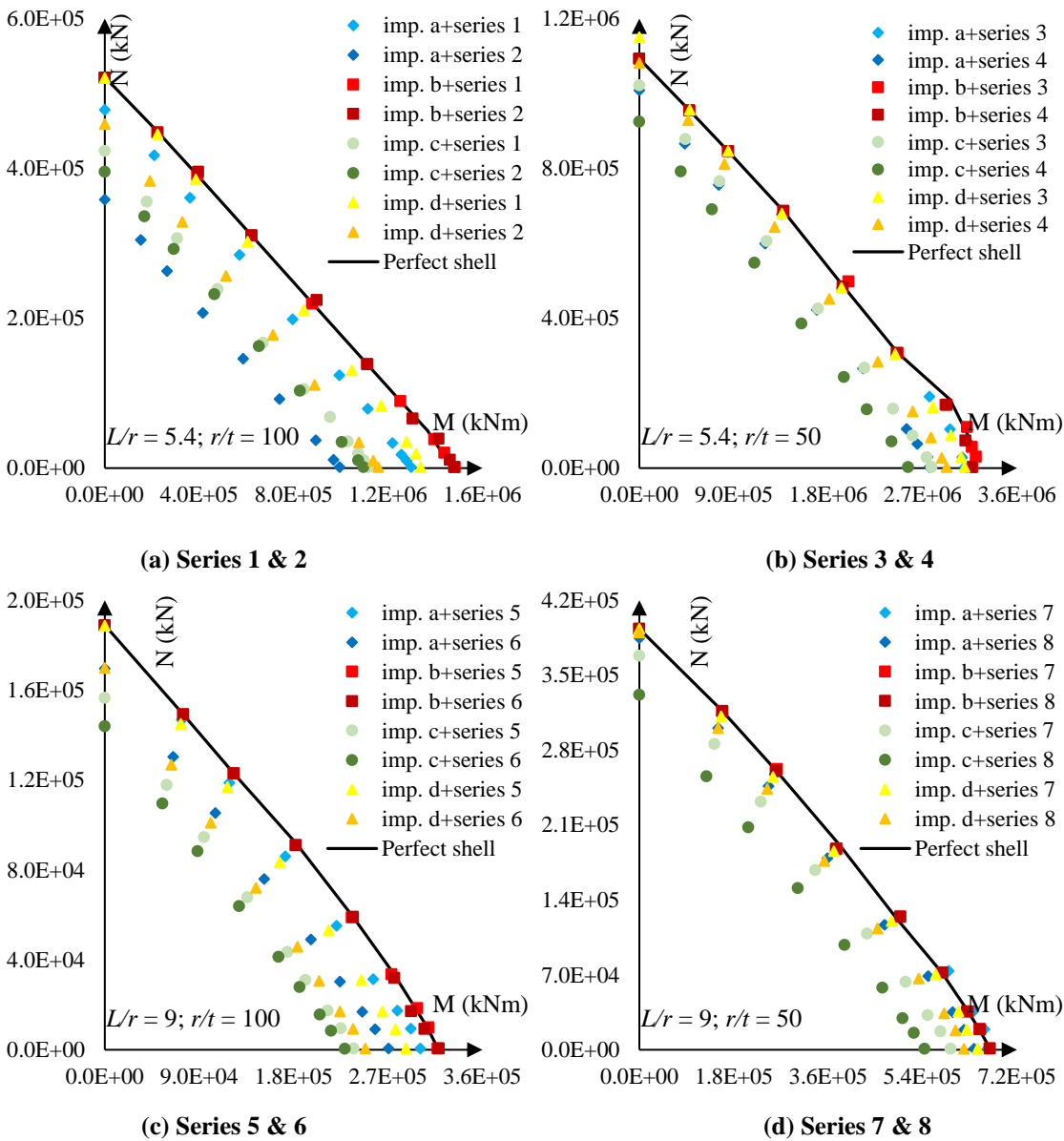


Figure 5.9 Ultimate capacity of cylinders under combined compression and bending moment

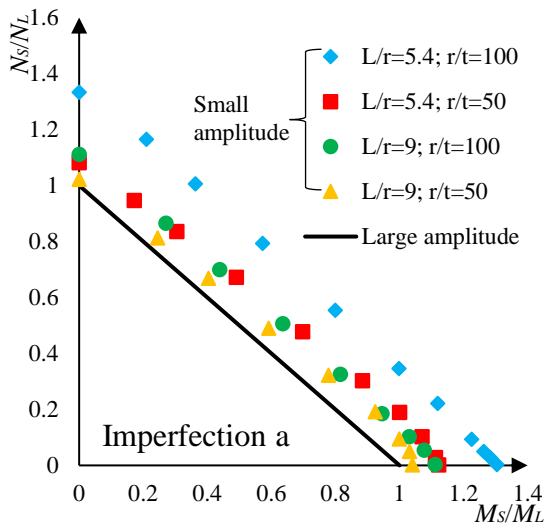
5.4.2 Effect of imperfection amplitudes

Figure 5.10 (a) to (d) shows the effect of different imperfection amplitudes based on FE analysis for Imperfection a, b, c and d respectively. The ultimate strength of the cylinder with a large imperfection amplitude is compared against the cylinder with a small imperfection amplitude. As summarized in Table 5.3, the maximum amplitude of imperfection according to Eurocode is more than twice as that based on DNVGL. Thus, the imperfection amplitude recommended by EN1993-1-6 (2007) and EN1993-1-6 (2017) corresponds to large amplitude, and amplitude recommended by DNVGL corresponds to small amplitude. N_S and N_L are the ultimate axial load capacities of the cylinder with small

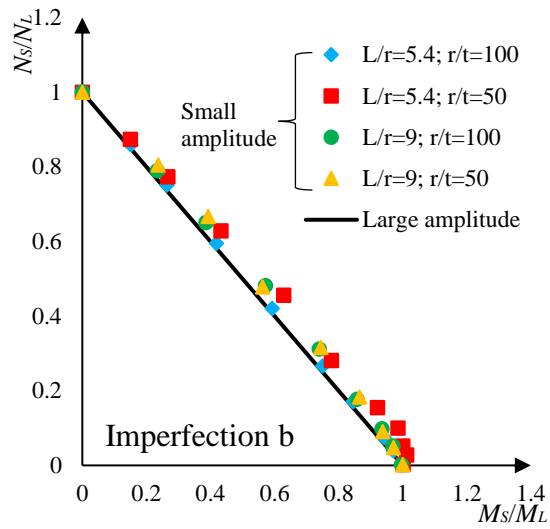
imperfection amplitude and large imperfection amplitude, respectively. M_S and M_L are the ultimate bending moment capacities of the cylinder with small imperfection amplitude and large imperfection amplitude, respectively.

It can be seen that all of dot data lies outside the solid line, which means that the ultimate strength of the models with small imperfection amplitude is larger than that of the models with large imperfection amplitude. In other words, a larger imperfection amplitude would significantly reduce the strength of the cylindrical shell. Among all four imperfection profiles, Imperfection b is the least sensitive to the imperfection amplitude. In addition, various colours of the dot data mean the model with various geometric dimensions. As can be seen from Figure 5.10 (a), with changing of the geometric dimensions, the dot data have a large difference on the ultimate strength. In other words, Imperfection a is more sensitive to geometric dimensions, while imperfection b is less sensitive to dimensions of the cylinder.

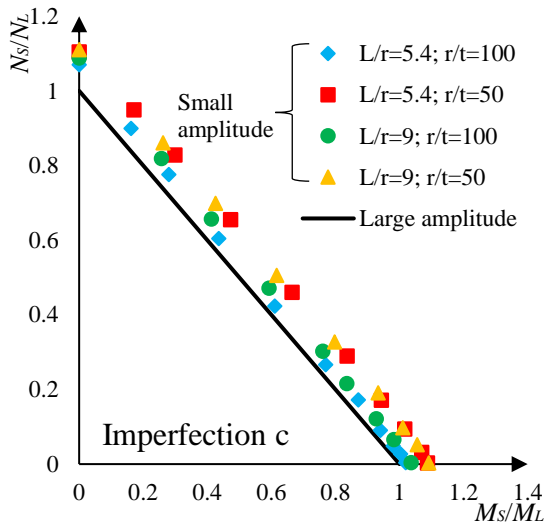
Figure 5.11 presents the ratio of the buckling strength between the small imperfection amplitude and large imperfection amplitude. f_S and f_L mean the FEA buckling strength with the small imperfection amplitude and large imperfection amplitude, respectively. The buckling strength of $L/r = 5.4$ and $r/t = 100$ is more sensitive to the imperfection profile as the ratio f_S/f_L of this model has the biggest fluctuation range from 1.01 to 1.34 with the mean value of 1.14. For the model of $L/r = 9$ and $r/t = 50$ it has the smallest mean value of f_S/f_L , and thus it is least affected by the imperfection amplitude.



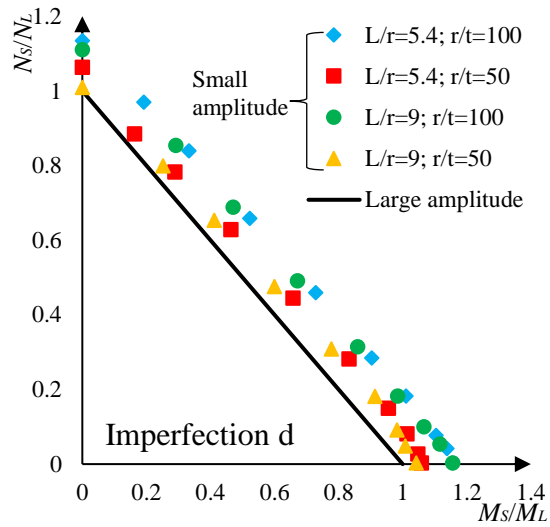
(a) Imperfection profile a



(b) Imperfection profile b



(c) Imperfection profile c



(d) Imperfection profile d

Figure 5.10 Comparison of the buckling resistance of cylinders under different imperfection amplitudes

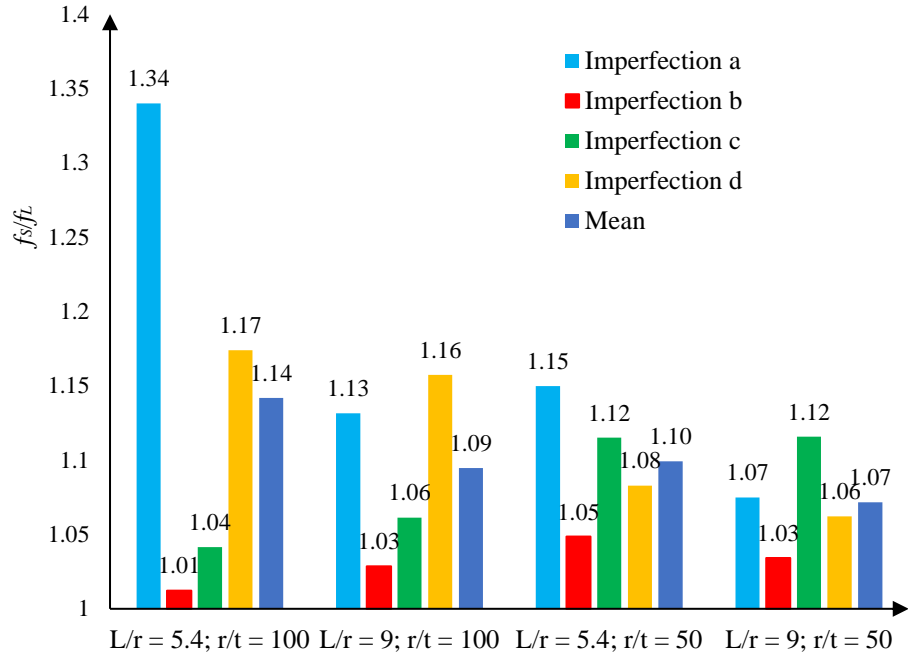


Figure 5.11 Ratio of the buckling strength between small imperfection amplitude and large imperfection amplitude

5.4.3 Comparison between design codes

The partial safety factor γ_M is used to ensure that the structural design possesses a certain target reliability level. It is defined as:

$$\gamma_M = \frac{f_{ks}}{f_{ksd}} \quad (5.4)$$

where f_{ks} is the characteristic buckling strength and f_{ksd} is the design buckling strength. According to DNVGL, γ_M is recommended as:

$$\begin{aligned} \gamma_M &= 1.15 && \text{for } \bar{\lambda}_s < 0.5 \\ \gamma_M &= 0.85 + 0.60\bar{\lambda}_s && \text{for } 0.5 \leq \bar{\lambda}_s \leq 1.0 \\ \gamma_M &= 1.45 && \text{for } \bar{\lambda}_s > 1.0 \end{aligned} \quad (5.5)$$

where $\bar{\lambda}_s$ is the reduced shell slenderness:

$$\bar{\lambda}_s = \sqrt{\frac{f_y}{\sigma_{j,sd}} \left[\frac{\sigma_{a0,sd}}{f_{Ea}} + \frac{\sigma_{m0,sd}}{f_{Em}} + \frac{\sigma_{h0,sd}}{f_{Eh}} + \frac{\tau_{sd}}{f_{E\tau}} \right]} \quad (5.6)$$

where $\sigma_{a0,sd}$, $\sigma_{m0,sd}$, $\sigma_{h0,sd}$ and τ_{sd} are the design stress due to axial forces, global bending moment, external pressure and shear force, respectively; f_{Ea} , f_{Em} , f_{Eh} and $f_{E\tau}$ are the elastic buckling strengths due to axial forces, global bending moment, external pressure and

shear force, respectively; $\sigma_{j,sd}$, is the design equivalent von Mises' stress. In this study, the calculated γ_M ranges from 1.18 to 1.45. According to EN1993-1-6 (2007) and EN1993-1-6 (2017), γ_M should not be smaller than 1.1. Therefore $\gamma_M=1.1$ is adopted in all cases.

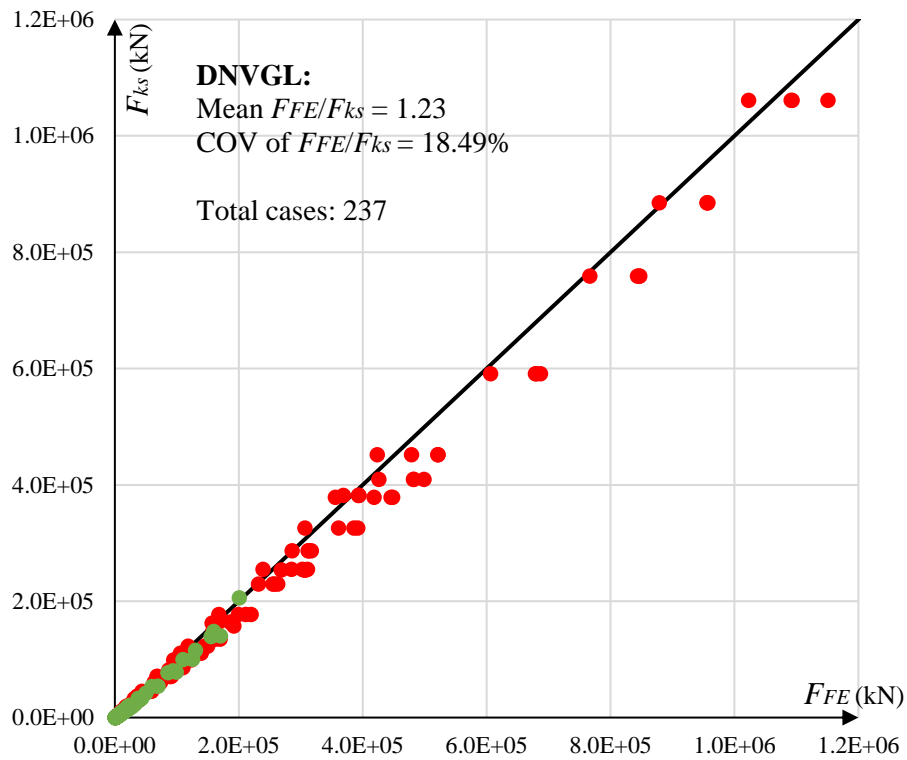
In this section, the accuracy of DNVGL, EN1993-1-6 (2007) and EN1993-1-6 (2017) design methods are assessed. Figure 5.12 plots the comparisons of the ultimate eccentric load capacity obtained from FEA (F_{FE}) and the characteristic load capacity (F_{ks}) predicted by DNVGL, EN1993-1-6 (2007) and EN1993-1-6 (2017), respectively. Note that in FE model the initial imperfection profiles (including all imperfection profiles a, b, c and d) and amplitudes are adopted based on corresponding code. Overall, EN1993-1-6 (2017) design method is found to outperform the others, with a mean value of F_{FE}/F_{ks} at 1.06 for EN1993-1-6 (2017), compared with 1.23 and 1.48 for DNVGL and EN1993-1-6 (2007). Eurocode has an obvious improvement from EN1993-1-6 (2007) to EN1993-1-6 (2017) in terms of both the mean value of F_{FE}/F_{ks} and the coefficient of variation (COV).

Compared with DNVGL, EN1993-1-6 (2007) and EN1993-1-6 (2017) have larger COV of F_{FE}/F_{ks} . This is because that, according to Figure 5.13, EN1993-1-6, whether 2007 version or 2017 version, has an overestimated prediction on thin and stocky cylindrical shell especially on the short cylinder with $r/t = 500$ and 1000. Note that N_{FE} and M_{FE} are the resistance of the axial load and bending moment in FE modelling, and N_{ks} and M_{ks} are the predicted characteristic buckling resistance of the axial load and bending moment, respectively based on the corresponding guidelines. The maximum value of N_{FE}/N_{ks} or M_{FE}/M_{ks} are 4.05 and 6.32 for EN1993-1-6 (2007) and EN1993-1-6 (2017) respectively. Except for thin and stocky cylindrical shell, the buckling strength of other cylindrical shells can be accurately predicted by using EN1993-1-6 (2017).

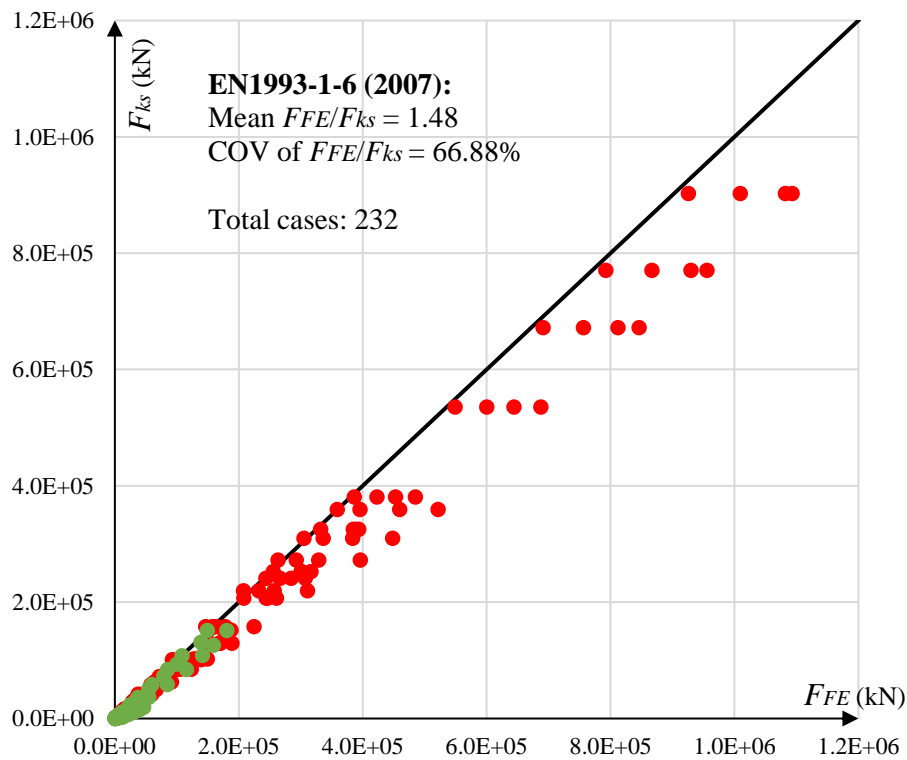
Figure 5.14 compares the ratio of F_{FE}/F_{ksd} against 1 in order to obtain an initial understanding of whether all cases meet the target reliability level by using the currently recommended partial safety factors in the design codes. Note that F_{FE} is the load capacity obtained from FEA, and F_{ksd} is the design strength calculated based on DNVGL and Eurocode design methods.

If $F_{FE}/F_{ksd} > 1$, it means that the design code provides a safe prediction for the structural design. The mean value of F_{FE}/F_{ksd} is 1.64 based on DNVGL, which is larger than EN1993-1-6 (2017) result 1.17 and EN1993-1-6 (2007) result 1.63. DNVGL provides the safe results for all 237 cases. However, 1.13% and 26.04% of code-based predictions based on EN1993-1-6 (2007) and EN1993-1-6 (2017) do not meet the safety requirement provided by FE modelling. Above design methods have not provided an accurate prediction on the cylinders with large r/t (500 and 1000), although the ratio of r/t of most offshore structures is less than 200. A comparison of the ultimate strength of unstiffened cylindrical shells predicted by DNVGL and EN1993-1-6 (2007) was also provided by [Li and Kim \(2022\)](#). This scholar found that DNVGL gave a more conservative design buckling strength than EN1993-1-6 (2007) for the cylindrical shells with $r/t = 50, 100, 200$ under pure compression, which is in good agreement with the present result.

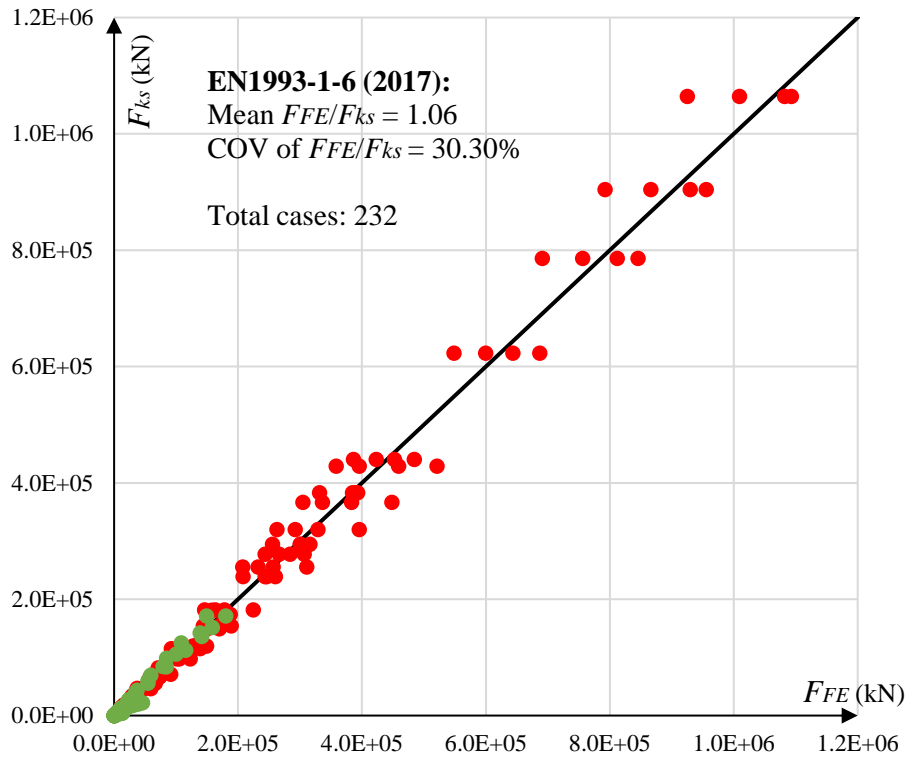
All in all, based on the FEM study, EN1993-1-6 (2017) provides a more accurate characteristic buckling capacity compared with the others. Furthermore, DNVGL provides a more reliable and safer design buckling capacity prediction. The partial safety factor γ_M needs to be improved in some cases in order to meet the target reliability level especially for Eurocode. All of above code-based approaches need to be improved on the buckling strength prediction for thin and stocky cylindrical shells. Of course, the ultimate load capacity F_{FE} is largely influenced by the imperfection amplitude, and DNVGL has adopted a more conservative imperfection amplitude than Eurocode. Therefore, the imperfection amplitude needs to be better understood based on the statistical analysis of real measurements.



(a)

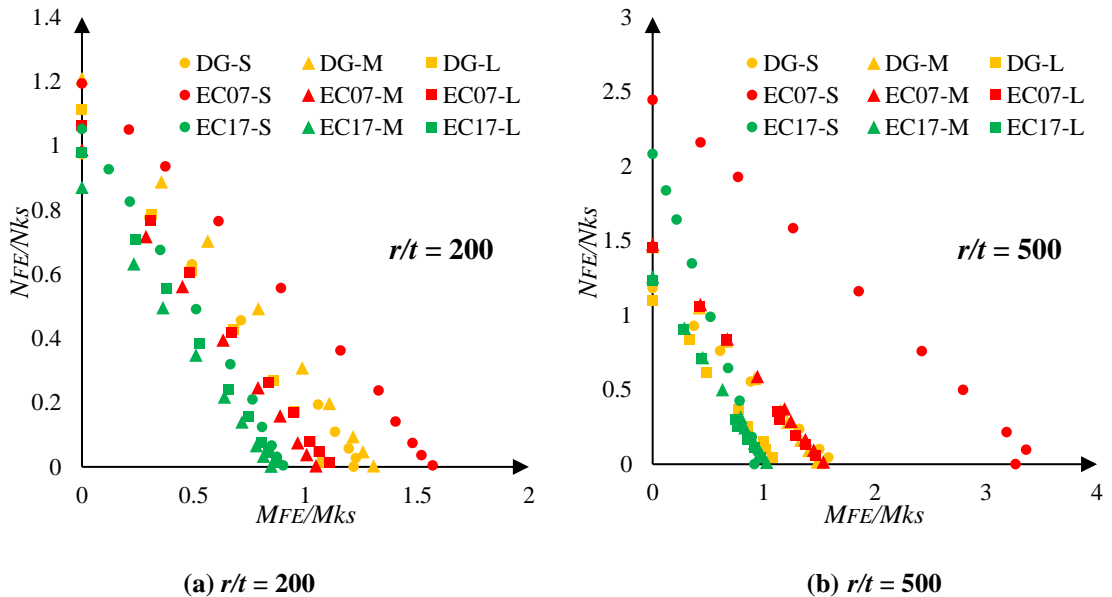


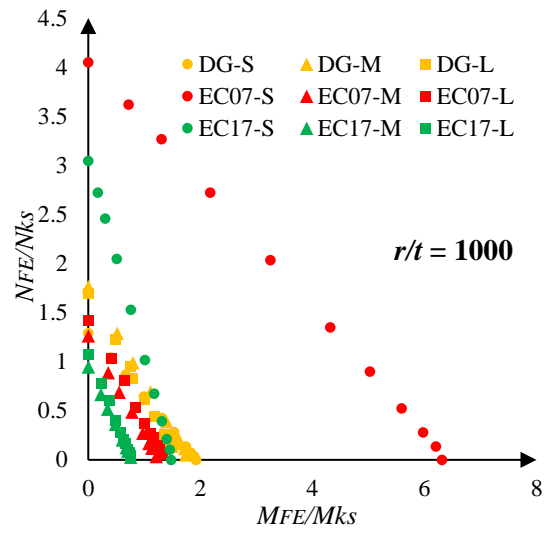
(b)



(c)

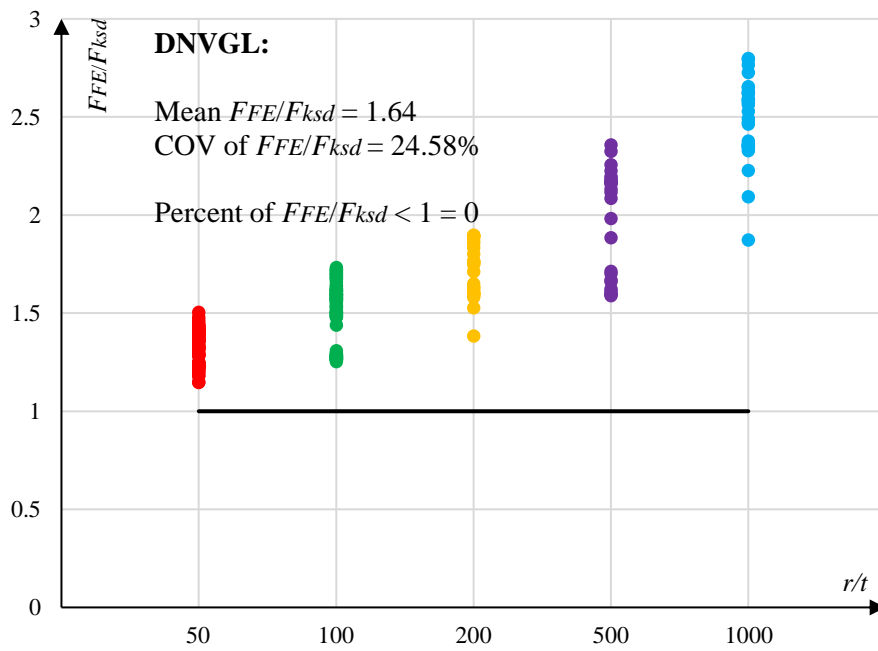
Figure 5.12 Buckling capacity of FEA results versus characteristic buckling capacity of (a) DNVGL (b) EN1993-1-6 (2007) (c) EN1993-1-6 (2017) subjected to eccentric compression (red and green data point obtained from Group A and B)



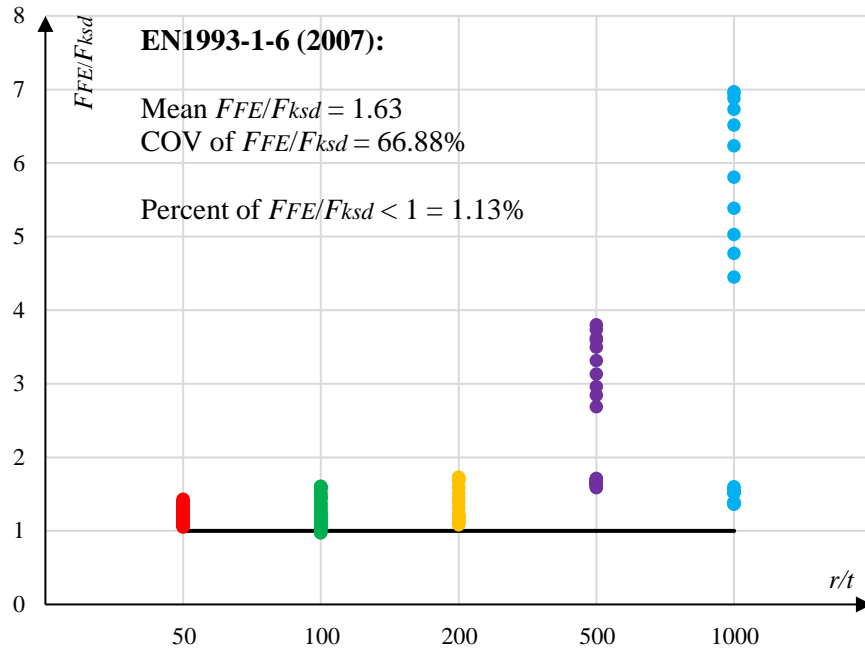


(c) $r/t = 1000$

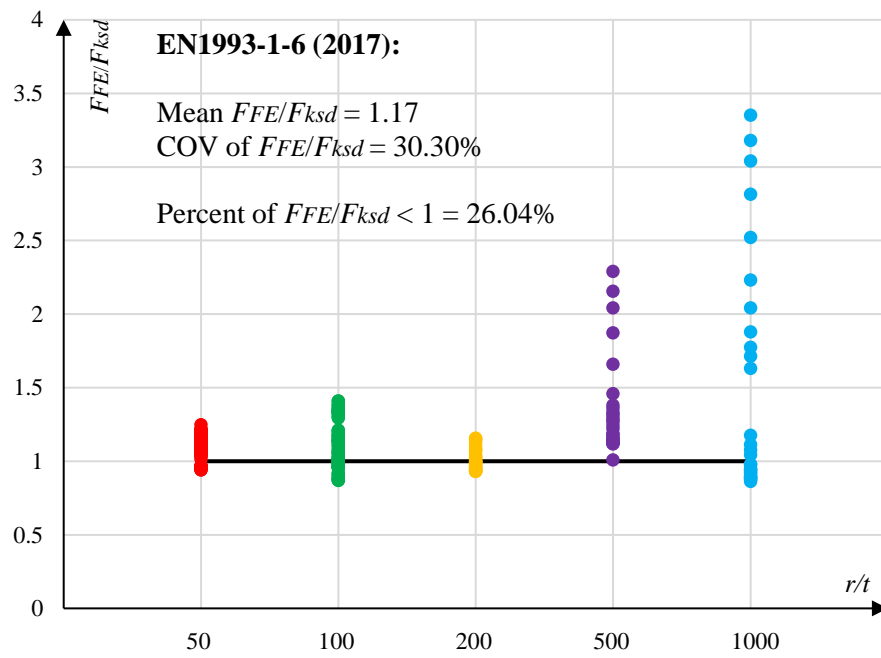
Figure 5.13 Comparison of M-N curve under different design guideline (DG-DNVGL, EC07-EN1993-1-6 (2007), EC17-EN1993-1-6 (2017), S-Short cylinder, M-Medium cylinder, L-Long cylinder)



(a)



(b)



(c)

Figure 5.14 Value of F_{FE}/F_{ksd} based on (a) DNVGL (b) EN1993-1-6 (2007) (c) EN1993-1-6 (2017)

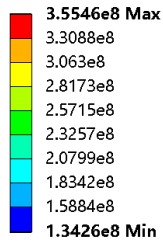
5.4.4 Failure modes of cylindrical shells

In the previous sections, the ultimate load capacities considering the effects of imperfection profiles and magnitudes are studied. In this section, the reasons that cause the above effects are investigated by studying the failure modes of each case. The models of $L/r = 5.4$ and $r/t = 100$ with different imperfection profiles and amplitudes (series 1 and 2 shown in Table 5.3) under pure axial compression are adopted in this section.

As can be seen in Figure 5.15, the models with Imperfections b and d and small imperfection amplitude experience bulge column buckling. Conversely, the failure modes of the models with Imperfections a and c are dominated by local shell buckling. Shell buckling occurs on the initial dimples, which takes less energy to deform. This explains why the buckling strength of the models with Imperfection b and d are larger than that of the models with Imperfections a and c.

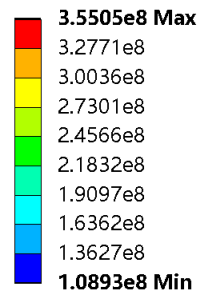
With the larger imperfection amplitude of models presented in Figure 5.16, the dominated buckling mode of the model with Imperfection d is changed from column bulge buckling to shell buckling, and the axial compression capacity is reduced by 11.9% according to Figure 5.17. The shell buckling of the model with Imperfections a and c becomes more obvious with increased imperfection magnitude, which results in a lower buckling strength with 27.5% and 6.4% reduction of the axial compression capacity. The buckling mode of the model with Imperfection b does not change, therefore the compression capacity has not been influenced.

K: Static Structural
 Equivalent Stress
 Type: Equivalent (von-Mises) Stress - Top/Bottom
 Unit: Pa
 Time: 0.64147



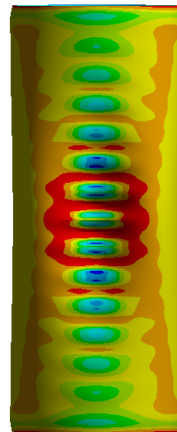
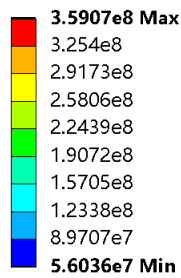
(a) Imperfection a

K: Static Structural
 Equivalent Stress
 Type: Equivalent (von-Mises) Stress - Top/Bottom
 Unit: Pa
 Time: 0.97178



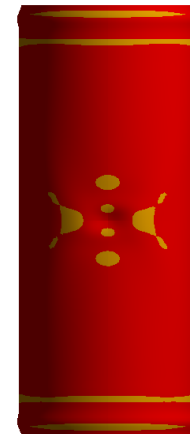
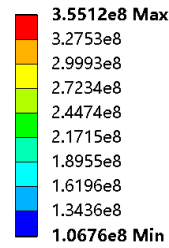
(b) Imperfection b

K: Static Structural
 Equivalent Stress
 Type: Equivalent (von-Mises) Stress - Top/Bottom
 Unit: Pa
 Time: 0.75178



(c) Imperfection c

K: Static Structural
 Equivalent Stress
 Type: Equivalent (von-Mises) Stress - Top/Bottom
 Unit: Pa
 Time: 0.97178

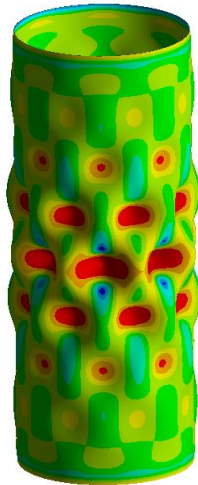


(d) Imperfection d

Figure 5.15 Failure modes of Series 1 (deformation is amplified by 50 times)

D: Static Structural
 Equivalent Stress
 Type: Equivalent (von-Mises) Stress - Top/Bottom
 Unit: Pa
 Time: 0.67178

3.6052e8 Max
 3.2671e8
 2.929e8
 2.5909e8
 2.2528e8
 1.9147e8
 1.5766e8
 1.2386e8
 9.0046e7
5.6237e7 Min



(a) Imperfection a

D: Static Structural
 Equivalent Stress
 Type: Equivalent (von-Mises) Stress - Top/Bottom
 Unit: Pa
 Time: 0.97178

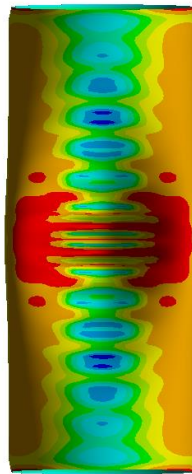
3.5513e8 Max
 3.2739e8
 2.9966e8
 2.7192e8
 2.4419e8
 2.1645e8
 1.8871e8
 1.6098e8
 1.3324e8
1.055e8 Min



(b) Imperfection b

D: Static Structural
 Equivalent Stress
 Type: Equivalent (von-Mises) Stress - Top/Bottom
 Unit: Pa
 Time: 0.76178

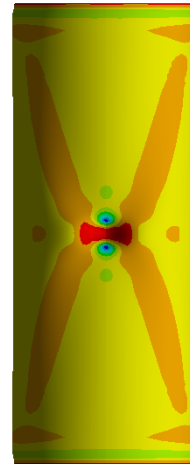
3.8031e8 Max
 3.3871e8
 2.9711e8
 2.5552e8
 2.1392e8
 1.7232e8
 1.3073e8
 8.9131e7
 4.7535e7
5.9382e6 Min



(c) Imperfection c

D: Static Structural
 Equivalent Stress
 Type: Equivalent (von-Mises) Stress - Top/Bottom
 Unit: Pa
 Time: 0.80246

3.6414e8 Max
 3.2992e8
 2.9569e8
 2.6146e8
 2.2723e8
 1.93e8
 1.5877e8
 1.2455e8
 9.0319e7
5.609e7 Min



(d) Imperfection d

Figure 5.16 Failure modes of Series 2 (deformation is amplified by 50 times)

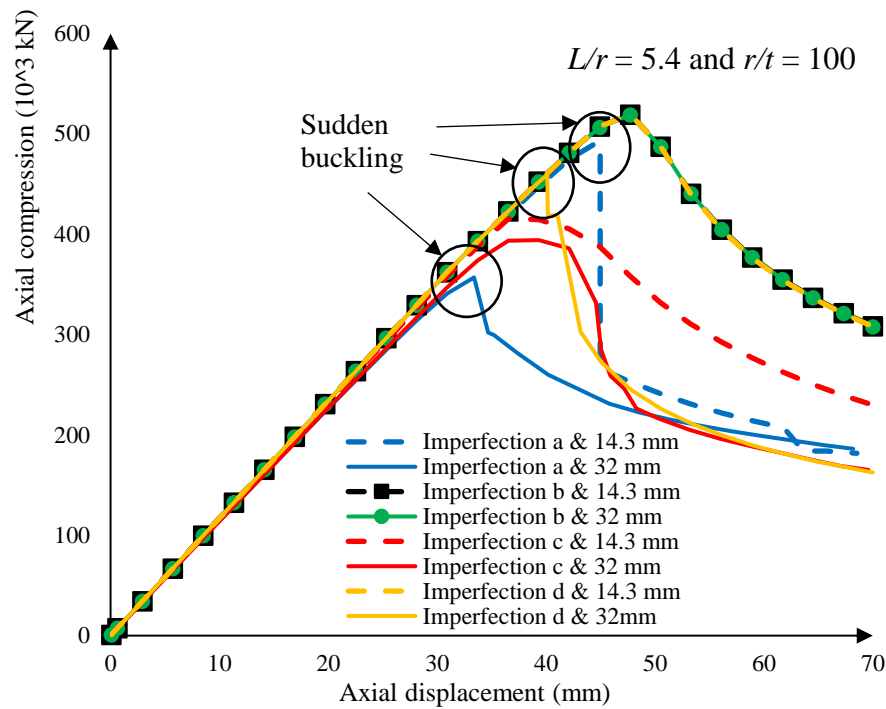
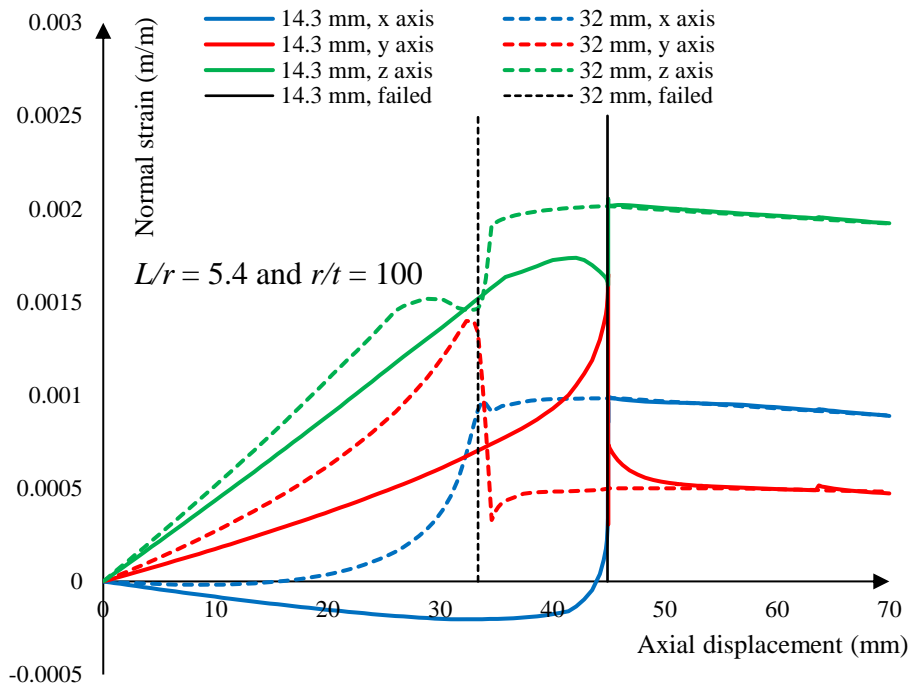


Figure 5.17 Load-displacement curve for unstiffened shell with different imperfection amplitude

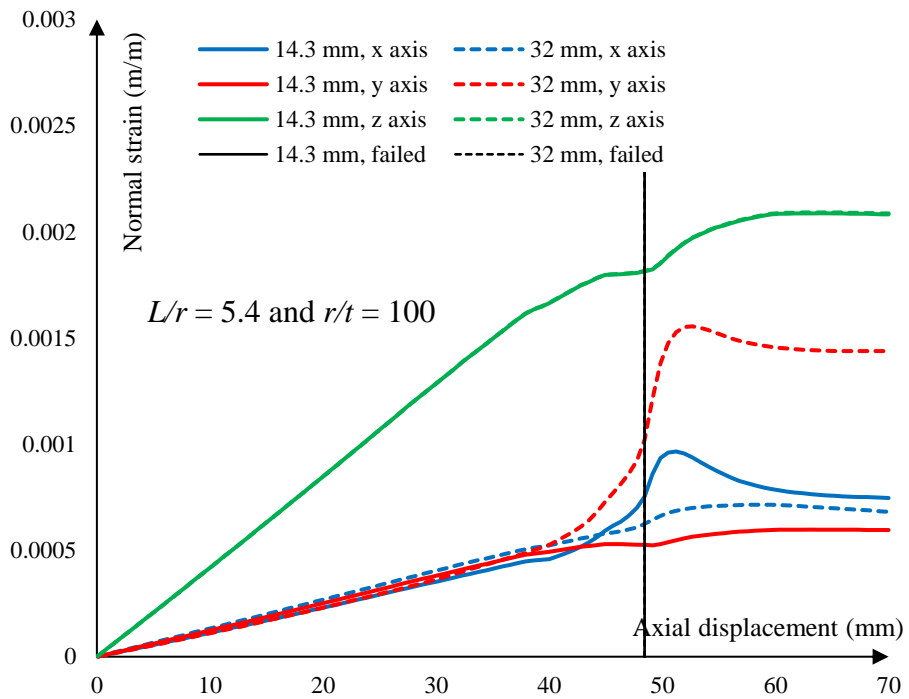
Strain-displacement curves of the most critical node when the stiffened shell buckles for $L/r = 5.4$ and $r/t = 100$ (Series 1 & 2) with different imperfection profiles are demonstrated in Figure 5.18. X- and y- axes are within the cross-section, and z- axis is the longitudinal axis (shown in Figure 5.4). Before buckling, the strain along z axis plays the most important role, which is in good agreement with what was reported by [Jin et al. \(2021\)](#). If the structures fail by bulge buckling (Figure 5.15 (b) and (d), Figure 5.16 (b)), the strain along x axis is almost equal to that along y axis on the pre-buckling, and they are about one third of the strain along z axis.

When the structures experience sudden buckling (Figure 5.17 Series 1 & 2 with Imperfection a, Series 2 with Imperfection d), the strain along z axis increases sharply. Conversely, the strain along y axis (tangential direction) decreases significantly.

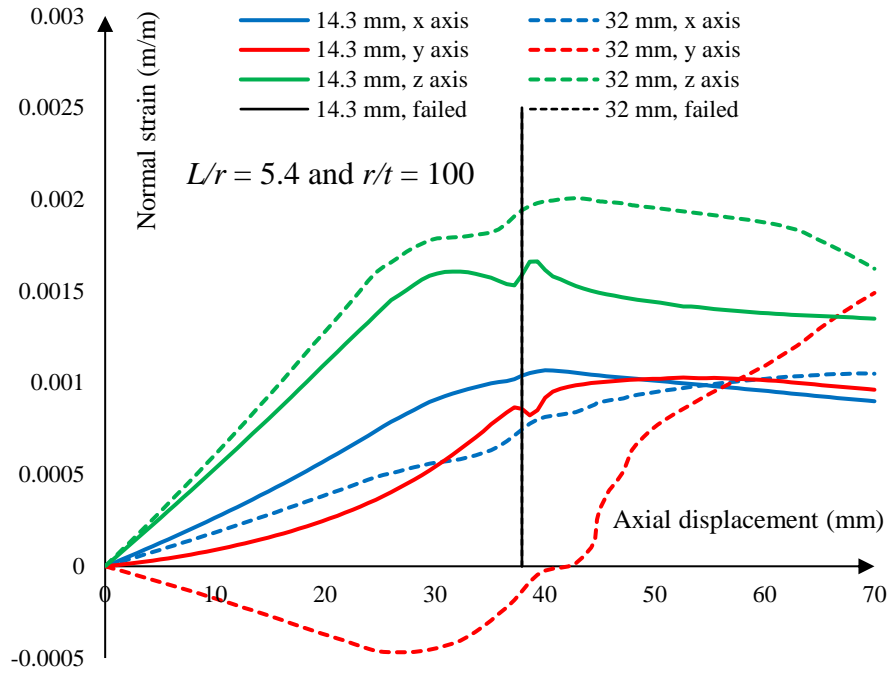
Figure 5.16 (c) has the largest horizontal deformation among all cases as presented in Figure 5.15 and Figure 5.16. According to Figure 5.18 (c), the strain along y- axis increases significantly after the buckling and even approach the z axis strain. It means that the horizontal strains are greatly influenced by the horizontal deformation.



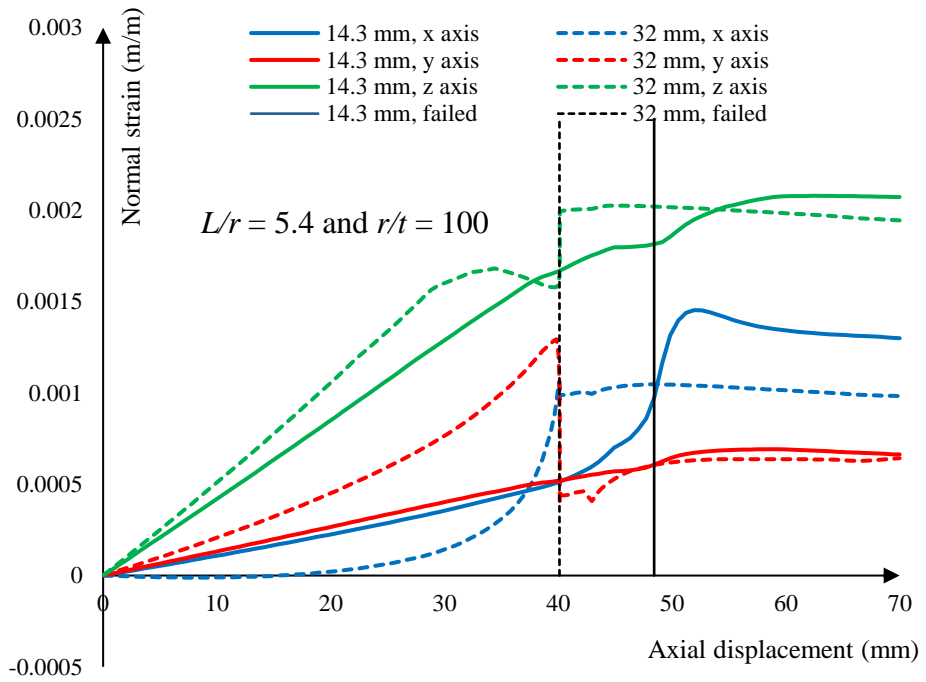
(a) Imperfection a



(b) Imperfection b



(c) Imperfection c



(d) Imperfection d

Figure 5.18 Strain-displacement curve for unstiffened shell $L/r = 5.4$ and $r/t = 100$ with different imperfection profiles and amplitudes (Series 1 & 2)

5.5 Reliability analysis

According to Section 5.4.3, it was concluded that DNVGL provides a safe prediction of design buckling capacity of shell structures, although some cases are overestimated, which may lead to overdesign. Conversely, 1.13% and 26.42% of code-based predictions based on EN1993-1-6 (2007) and EN1993-1-6 (2017) do not meet the safety requirement provided by FE modelling. Therefore, the reliability of these three codes is assessed based on [EN1990 \(2005\)](#) to provide a suitable partial safety factor γ_M for the structural design of offshore shell structures.

The basic limit state function Z is written as:

$$Z = K_R R - K_S (G + Q + W_A + W_I) \quad (5.7)$$

where K_R is the model uncertainty of the resistance effect R , K_S is the model uncertainty of $(G+Q+W_A+W_I)$, $G+Q+W_A+W_I$ are the dead load, live load, wave load and wind load, respectively. In order to have a clearer derivation of the following formulas, the function Z is defined using an alternative definition:

$$Z = \frac{K_R R}{K_S} - (G + Q + W_A + W_I) \quad (5.8)$$

The function of failure probability can be expressed as:

$$P_f = P(Z < 0) = \Phi(\beta) \quad (5.9)$$

where β is the reliability index and Φ is the cumulative distribution function of the standardised Normal distribution. According to [DNVGL-ST-0119 \(2018\)](#), the target safety level for structural design of floating wind turbine structures is a nominal annual probability of failure of 10^{-4} . Therefore, $P_f = 10^{-4} = \Phi(\beta_1)$ and $\beta_1 = 3.71$ ([Wang et al., 2022](#)). The target design life of 20 years ([DNVGL-ST-0119, 2018](#)) is used for a new floating wind turbine. Thus, the cumulative distribution function can be expressed as:

$$\Phi(\beta_{20}) = [\Phi(\beta_1)]^{20} \quad (5.10)$$

where β_{20} is the reliability index for 20 years, β_1 is the reliability index for one year. In this study, a reliability index of 2.87 is used to assess the partial safety factor γ_M .

The first order reliability method (FORM) is used to perform the reliability analysis in this study. The statistical properties of design variables are presented in Table 5.7.

Table 5.7 Statistical properties of design variables

Descriptio n	Variabl e	Distribution	Mean	COV	Reference
Dead load	G	Normal	G_n	0.06	BOMEL (2003)
Live load	Q	Normal	Q_n	0.1	BOMEL (2003)
Wave load	W_A	Normal	$0.9W_{An}$	0.2	JCSS (2021)
Wind load	W_I	Lognormal	W_{In}	0.125	JCSS (2021)
Resistance	R	Lognormal	R_n	-	Fitted by author
Uncertainty of R	K_R	Lognormal	-	-	Fitted by author
Uncertainty of S	K_S	Lognormal	1	0.1	JCSS (2021)
Young's modulus	E	Normal	E	0.05	N W Nichols (2014)
Material yield stress	f_y	Lognormal	$1.13 f_y$	0.0572	N W Nichols (2014)
Thickness	t	Normal	t	0.03	Yang et al. (2015)
Length	L	Normal	L	0.03	Yang et al. (2015)
Radius	r	Normal	r	0.03	Yang et al. (2015)

If the resistance effect and the load effect follow lognormal distribution, the reliability index can be obtained as follows (Cheng and Becque, 2016, Coile, 2015):

$$\beta = \frac{\mu_{\ln R'} - \mu_{\ln S}}{\sqrt{\sigma_{\ln R'}^2 + \sigma_{\ln S}^2}} = \frac{\ln\left(\frac{\mu_{R'}}{\mu_S} \sqrt{\frac{1+V_S^2}{1+V_{R'}^2}}\right)}{\sqrt{\ln[(1+V_{R'}^2)+(1+V_S^2)]}} \quad (5.11)$$

where

$$R' = \frac{K_R R}{K_S} \quad (5.12)$$

$$S = G + Q + W_A + W_I \quad (5.13)$$

$\mu_{\ln R'}$, $\mu_{\ln S}$, $\sigma_{\ln R'}$ and $\sigma_{\ln S}$ are the mean values and the standard deviations of natural logarithms of the resistance R' and the load S , and $\mu_{R'}$, μ_S , $V_{R'}$ and V_S are the mean values and COVs of the resistance R' and the load S , respectively. $\mu_{R'}$ and μ_S can be expressed as:

$$\mu_{R'} = \frac{\mu_{KR}\mu_R}{\mu_{KS}} = \frac{\mu_{KR}R_n}{\mu_{KS}} \quad (5.14)$$

$$\mu_S = \mu_G + \mu_Q + \mu_{WA} + \mu_{WI} = G_n + Q_n + 0.9W_{An} + W_{In} \quad (5.15)$$

In terms of offshore structures, the environmental loads (wave and wind loads) may dominate the structural design. It is assumed that $G_n/Q_n = 1$ (N W Nichols, 2014). Furthermore, a load ratio $\kappa = W_{An}/G_n = W_{In}/G_n$ is adopted. Eq. (5.15) can be expressed as:

$$\mu_S = G_n (1 + 1 + 0.9\kappa + \kappa) \quad (5.16)$$

In addition, the structural design shall be verified as follows:

$$R_d = \frac{R_n}{\gamma_M} \geq R_{Ed} = G_n + Q_n + 1.35W_{An} + 1.35W_{In} \quad (5.17)$$

where R_d and R_{Ed} are the design resistance and the design load effect, respectively. It should be noted that two load combinations (the other is $1.25G_n + 1.25Q_n + 0.7W_{An} + 0.7W_{In}$) are adopted in structural design in Chapter 4. According to the load ratio, $G_n + Q_n + 1.35W_{An} + 1.35W_{In}$ is adopted to ensure the safety of the structure under the maximum expected load effect. In structural design, $R_d = R_{Ed}$ is assumed to make full use of the resistance.

Therefore, Eq. (5.17) shall be transformed as:

$$\frac{R_n}{\gamma_M} = G_n + Q_n + 1.35W_{An} + 1.35W_{In} \quad (5.18)$$

or

$$\frac{R_n}{G_n} = \gamma_M(1 + 1 + 1.35\kappa + 1.35\kappa) \quad (5.19)$$

Based on Eqs. (5.14) to (5.19), the following equation could be derived as:

$$\frac{\mu_{R'}}{\mu_S} = \frac{\mu_{KR}\gamma_M(1+1+1.35\kappa+1.35\kappa)}{\mu_{KS}(1+1+0.9\kappa+\kappa)} \quad (5.20)$$

The COVs of S and R' are presented as following:

$$V_S = \frac{\sigma_S}{\mu_S} = \frac{\sqrt{(V_G\mu_G)^2 + (V_Q\mu_Q)^2 + (V_{WA}\mu_{WA})^2 + (V_{WI}\mu_{WI})^2}}{\mu_G + \mu_Q + \mu_{WA} + \mu_{WI}} = \frac{\sqrt{V_G^2 + V_Q^2 + V_{WA}^2(0.9\kappa)^2 + V_{WI}^2\kappa^2}}{1 + 1 + 0.9\kappa + \kappa} \quad (5.21)$$

$$V_{R'} = \sqrt{V_{KR}^2 + V_R^2 + V_{KS}^2} \quad (5.22)$$

$$V_R^2 = \frac{1}{g_R^2(X)} \times \sum_{i=1}^j \left(\frac{\partial g_R}{\partial X_i} \sigma_i \right)^2 = \frac{1}{g_R^2(X)} \left[\left(\frac{\partial g_R}{\partial E} \sigma_E \right)^2 + \left(\frac{\partial g_R}{\partial f_y} \sigma_{f_y} \right)^2 + \left(\frac{\partial g_R}{\partial t} \sigma_t \right)^2 + \left(\frac{\partial g_R}{\partial L} \sigma_L \right)^2 + \left(\frac{\partial g_R}{\partial r} \sigma_r \right)^2 \right] \quad (5.23)$$

where $g_R(X)$ is the resistance function (EN1990, 2005) of the basic variables X (shown in Table 5.7) and is used as the design model.

Based on Eqs. (5.11), (5.20)-(5.22), the reliability index could be derived as:

$$\beta = \frac{\ln \left\{ \left(\frac{\mu_{KR}\gamma_M a}{\mu_{KS} b} \right) \sqrt{1 + \frac{V_G^2 + V_Q^2 + V_{WA}^2(0.9\kappa)^2 + V_{WI}^2\kappa^2}{b^2}} \right\} / (1 + V_{KR}^2 + V_R^2 + V_{KS}^2)}{\sqrt{\ln \left[(1 + V_{KR}^2 + V_R^2 + V_{KS}^2) \left(1 + \frac{V_G^2 + V_Q^2 + V_{WA}^2(0.9\kappa)^2 + V_{WI}^2\kappa^2}{b^2} \right) \right]}} \quad (5.24)$$

where

$$a = 1 + 1 + 1.35\kappa + 1.35\kappa \quad (5.25)$$

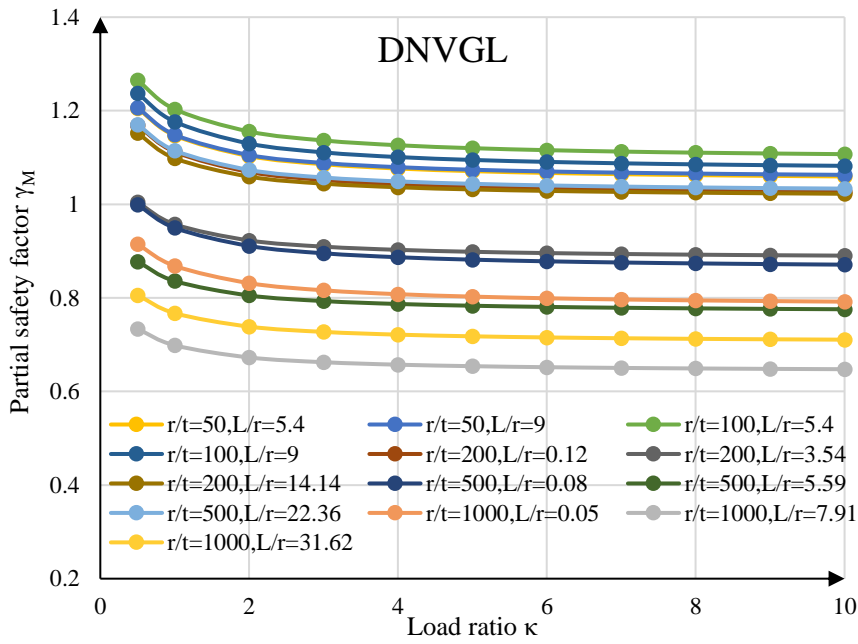
$$b = 1 + 1 + 0.9\kappa + \kappa \quad (5.26)$$

The partial safety factor can be derived as:

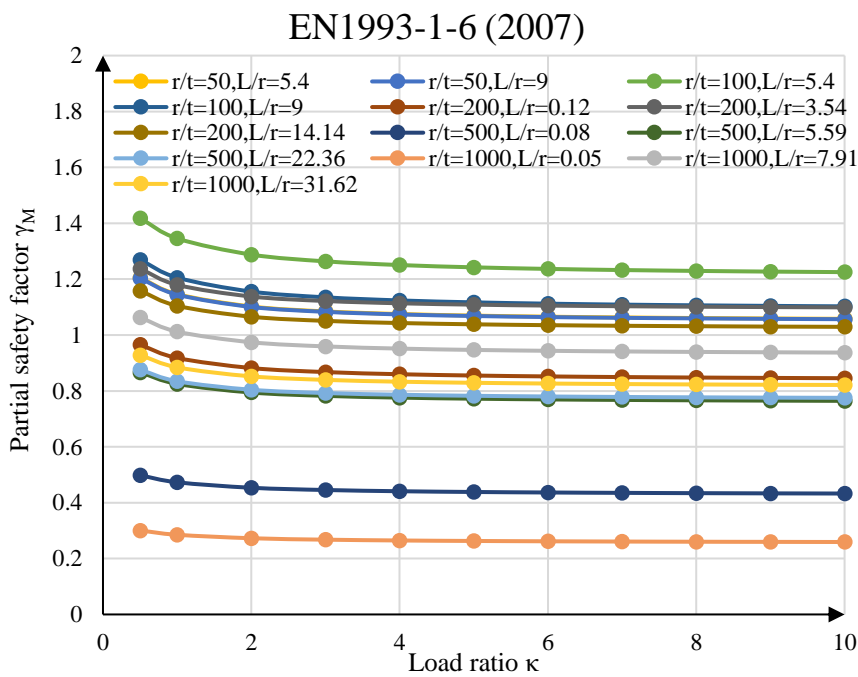
$$\gamma_M = \frac{\exp\left\{\beta \sqrt{\ln\left[\left(1+V_{KR}^2+V_R^2+V_{KS}^2\right)\left(1+\frac{V_G^2+V_Q^2+V_{WA}^2(0.9\kappa)^2+V_{WI}^2\kappa^2}{b^2}\right)\right]}\right\}}{\frac{\mu_{KR}a}{\mu_{KS}b} \sqrt{\left(1+\frac{V_G^2+V_Q^2+V_{WA}^2(0.9\kappa)^2+V_{WI}^2\kappa^2}{b^2}\right)} / (1+V_{KR}^2+V_R^2+V_{KS}^2)} \quad (5.27)$$

The process of calculation of the partial safety factor γ_M has been introduced. After that, γ_M is calculated based on the load ratio κ , the buckling capacity results of FE models and design codes and a target reliability index of 2.87. In Section 5.1, Class B of fabrication tolerance quality is adopted in FE models and code-based calculation, which is used to determine the imperfection amplitude. Thus, in this section, the partial safety factor γ_M is applicable for Class B of fabrication tolerance quality only. The results of γ_M are shown in Figure 5.19 in terms of the various κ ranging from 0.5 to 10 (N W Nichols, 2014) which are the typical ratio of environmental loads to dead load for offshore structures. Different geometries of the cylindrical shells have different FE models and code-based models. Hence, there are sixteen lines representing sixteen models. According to Figure 5.19, all values of γ_M reduce with the increasing of κ from 0.5 to 5 and remain relatively stable from 5 to 10. Due to the conservative prediction of the characteristic load capacity based on DNVGL and EN1993-1-6 (2007), the new γ_M for some geometries is lower than 1 especially for $r/t = 200, 500$ and 1000 . Conversely, in EN1993-1-6 (2017), the new γ_M is lower than 1 only when κ of the shell geometry with $r/t=1000$ and $L/r=0.05$ is larger than 0.5, which benefits from the relatively accurate prediction of the characteristic buckling capacity.

To ensure all design models meet the safety target under all load ratio, the maximum required value of the partial safety factor is adopted. A summary of reliability analysis results for this study is provided in Table 5.8. As DNVGL EN1993-1-6 (2007) provide a conservative prediction of characteristic load capacity of the shells with large r/t , the revised γ_M are smaller than the old ones. For EN1993-1-6 (2017), $\gamma_M = 1.1$ is mainly recommended for onshore structures. However, the environmental load conditions for offshore structures are more complicated and uncertain compared with onshore structures. Thus, the revised γ_M are larger than the original value 1.1 except for $r/t=1000$ with $L/r=0.05$.



(a)



(b)

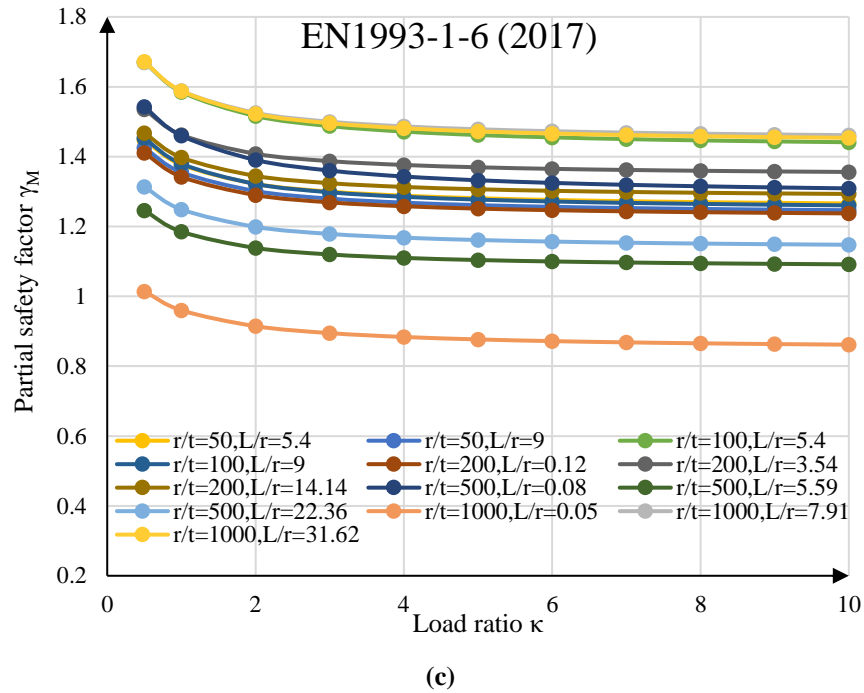


Figure 5.19 Partial safety factor-load ratio curves for (a) DNVGL (b) EN1993-1-6 (2007) (c) EN1993-1-6 (2017)

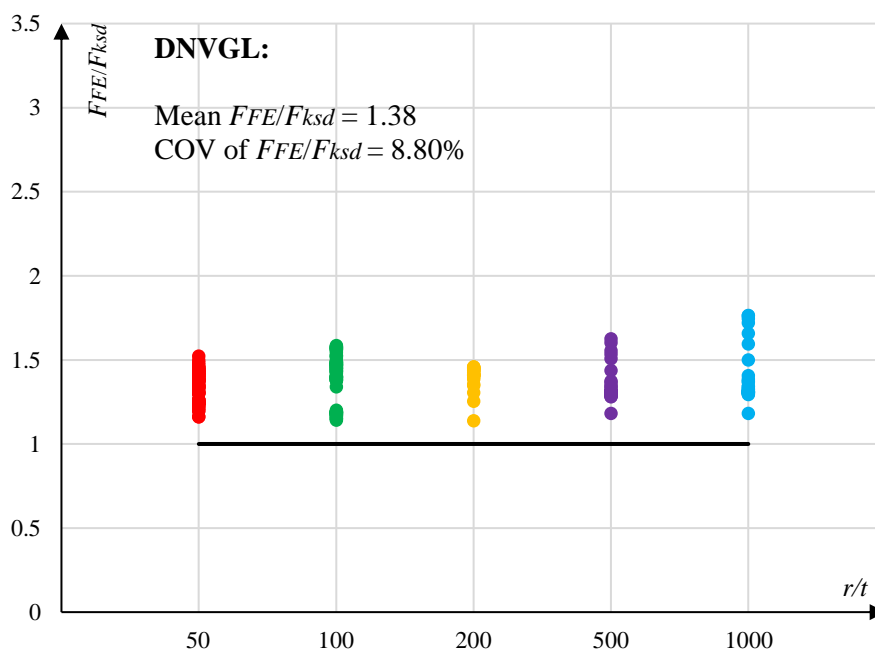
Table 5.8 Summary of reliability analysis results (note that the values in parentheses represent the original partial safety factor)

r/t	L/r	Partial safety factor γ_M		
		DNVGL	EN1993-1-6 (2007)	EN1993-1-6 (2017)
50	5.4	1.21 (1.19)	1.20 (1.1)	1.45 (1.1)
50	9	1.21 (1.19)	1.20 (1.1)	1.43 (1.1)
100	5.4	1.27 (1.36)	1.42 (1.1)	1.67 (1.1)
100	9	1.24 (1.36)	1.27 (1.1)	1.45 (1.1)
200	0.12	1.17 (1.42)	0.97 (1.1)	1.41 (1.1)
200	3.54	1.00 (1.31)	1.24 (1.1)	1.54 (1.1)
200	14.14	1.15 (1.31)	1.16 (1.1)	1.47 (1.1)
500	0.08	1.00 (1.45)	0.50 (1.1)	1.54 (1.1)
500	5.59	0.88 (1.45)	0.87 (1.1)	1.25 (1.1)
500	22.36	1.17 (1.45)	0.88 (1.1)	1.31 (1.1)
1000	0.05	0.91 (1.45)	0.30 (1.1)	1.01 (1.1)
1000	7.91	0.73 (1.45)	1.06 (1.1)	1.67 (1.1)
1000	31.62	0.81 (1.45)	0.93 (1.1)	1.67 (1.1)

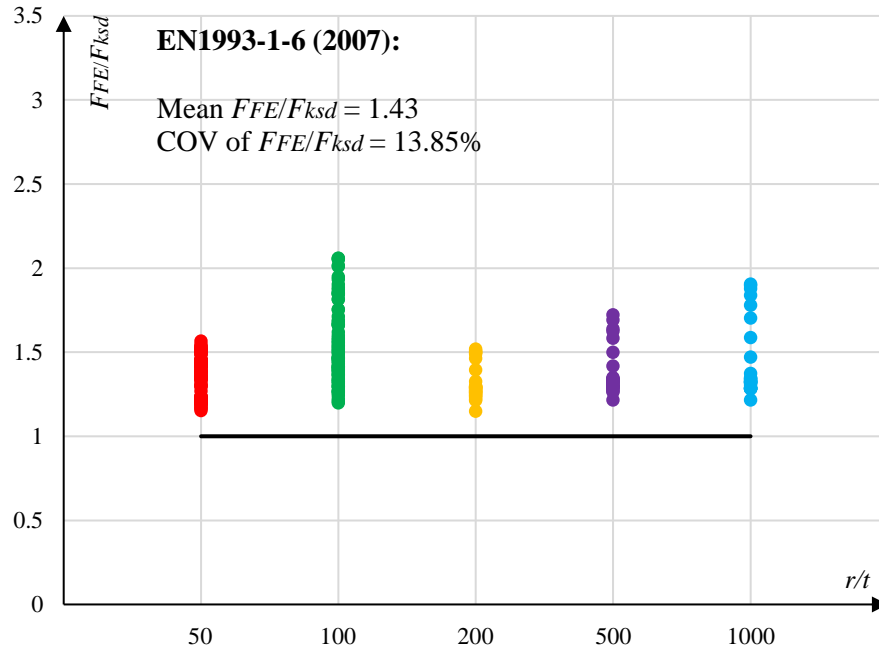
The revised partial safety factors are adopted to replace the old factors, and the values of F_{FE}/F_{ksd} based on DNVGL, EN1993-1-6 (2007) and EN1993-1-6 (2017) are provided in Figure 5.20 to re-evaluate the safety of this design code. After using new partial safety factors, the maximum value of F_{FE}/F_{ksd} is 1.76 which is lower than the maximum value

of F_{FE}/F_{ksd} (2.80) using the old partial safety factors Figure 5.14 (a). On the premise of ensuring safety, the lower mean value of F_{FE}/F_{ksd} can save more structural materials. Moreover, according to Figure 5.20, EN1993-1-6 (2007) and EN1993-1-6 (2017) provide safe predictions for the structural design. However, the mean value and COV of F_{FE}/F_{ksd} of DNVGL and EN1993-1-6 (2007) are smaller than that of EN1993-1-6 (2017). The main reason is that based on EN1993-1-6 (2017), the strength prediction of the cylinder with large r/t (500 and 1000) values is still conservative when axial compression dominates design forces.

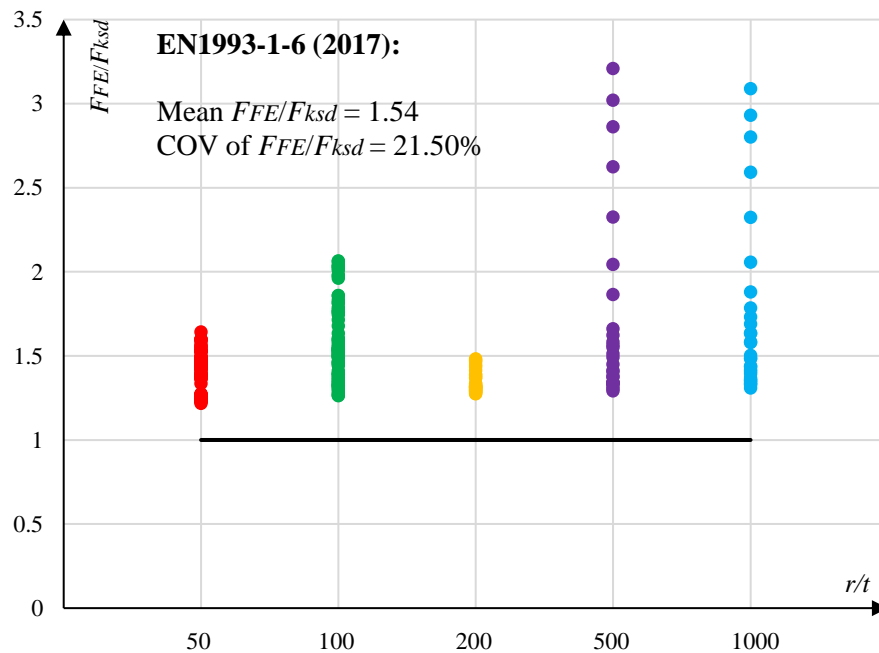
Furthermore, some limitations should be noted here. Firstly, although a wide range of r/t is considered in this study, only three typical L/r are considered representing short, medium and long columns for $L/r=200, 500$ and 1000 . Therefore, more geometries of cylinders need to be considered in future work. Secondly, Class B of fabrication tolerance quality is adopted only in this study. The other fabrication tolerance quality, Class A and C can be studied and compared further. Thirdly, more experiments can be carried out to obtain the more realistic data.



(a)



(b)



(c)

Figure 5.20 Value of F_{FE}/F_{ksd} based on (a) DNVGL (b) EN1993-1-6 (2007) (c) EN1993-1-6 (2017) using revised γ_M

5.6 Case study of stiffened cylindrical shells

The cylinder with $L/r = 5.4$ (length = 27 m, radius = 5 m), is adopted in the case study of the stiffened cylindrical shell. The structural scantlings of the stiffened cylindrical shell

are shown in Table 5.9. In this section, the buckling behaviour of the stiffened cylindrical shell under axial compression based on [DNVGL-RP-C202 \(2019\)](#) is studied. The design method is assessed by comparing the design solutions to FEA. The material properties, boundary condition and loading mode of the stiffened cylindrical shell are assumed to be the same as those used in unstiffened cylindrical shell described in the previous section.

Table 5.9 Structural scantlings of the stiffened cylindrical shell (unit: mm)

Shell thickness t	35
Distance of ring frames l	1400
Stringer web width h_s	360
Stringer web thickness t_{ws}	25
Spacing of stringer s	1040
Ring web width h_r	360
Ring web thickness t_{wr}	25

5.6.1 Axial compression capacity

Four types of geometric imperfection presented in section 5.2.2 are used as the initial imperfections. The axial compression capacity of the stiffened cylinder is compared with the unstiffened cylinder of series 1. The ratios of the ultimate eccentric load capacity obtained from FEA to the characteristic/design load capacity are presented in Figure 5.21 and Table 5.10. The cylinders with Imperfection a and Imperfection c have the lowest axial compression capacity for stiffened shell and unstiffened shell, respectively. The value of F_{FE}/F_{ks} for the stiffened shell is 0.987 with a COV of 4.40%, while the unstiffened shell has a larger F_{FE}/F_{ks} and COV, with 1.075 and 8.27%, respectively. A larger partial safety factor causes a lower design strength capacity, so the value from F_{FE}/F_{ks} to F_{FE}/F_{ksd} increases sharply from 1.075 to 1.461. It is clear that in this study DNVGL is more conservative on the buckling strength and safety factor calculation of the unstiffened shell. Furthermore, the results of the strength capacity are more discrete for the unstiffened shell in terms of the larger COV. One reason is that the imperfection amplitude recommendation for unstiffened shells is larger than that for stiffened shells

(14.3 mm for the unstiffened shell and 6 mm for the stiffened shell). Normally, a larger imperfection amplitude leads to a larger strength reduction, which has been discussed in section 5.4.2.

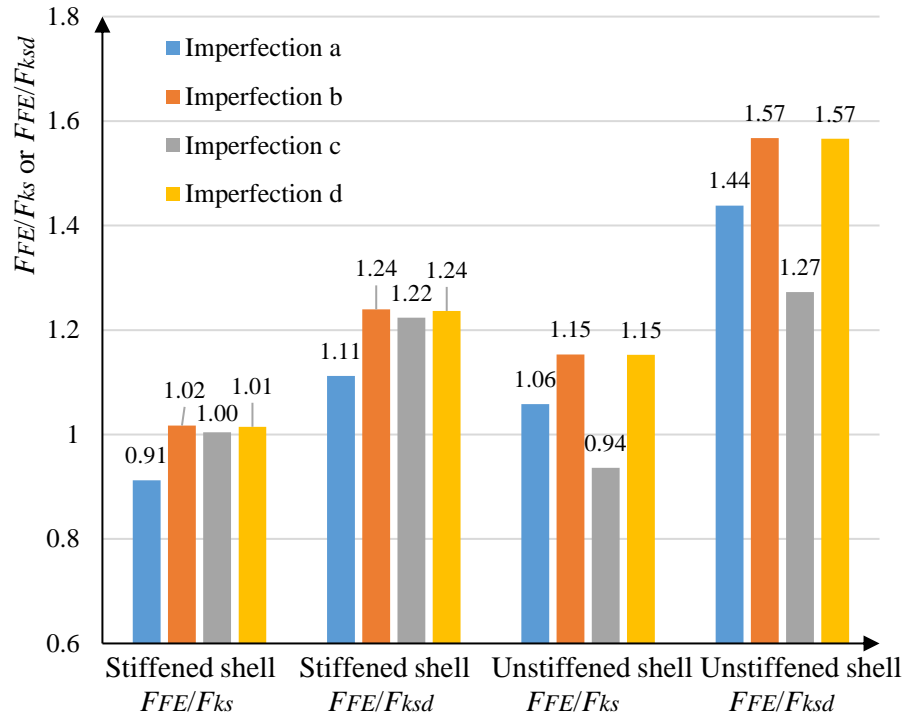


Figure 5.21 Comparison of F_{FE}/F_{ks} and F_{FE}/F_{ksd} between the stiffened and unstiffened shells

Table 5.10 Comparison of standard deviation, mean and COV for Figure 5.21

	Stiffened shell		Unstiffened shell	
	F_{FE}/F_{ks}	F_{FE}/F_{ksd}	F_{FE}/F_{ks}	F_{FE}/F_{ksd}
Standard Deviation	0.043	0.053	0.089	0.121
Mean	0.987	1.203	1.075	1.461
COV	4.40%	4.40%	8.27%	8.27%
γ_M	1.219		1.359	

5.6.2 Effect of imperfection amplitudes

In this section, 6 mm and 12 mm are used to examine the effect of imperfection amplitude on buckling behaviour. The load-displacement curve due to compressive loading for the stiffened shell is provided in Figure 5.22. The structure with 6mm imperfection amplitude buckles early compared with the structure with 12mm imperfection amplitude, with the compressive load capacity of 412260 kN. If the imperfection amplitude increases from 6mm to 12mm, the maximum compression capacity will reduce by 7.63% to 380820 kN.

The relationship between strain and end displacement for the most critical node when the stiffened shell buckles is demonstrated in Figure 5.23. As can be seen, the vertical strain is much larger than the horizontal strain. It is worth mentioning that the normal strain along the x axis for the stiffened shell with 12mm imperfection amplitude has a sharp increase before buckling, however the strains along the other axes increase gradually. It can be concluded that the horizontal strain may have a great effect on the buckling behaviour of the stiffened shell, which has a larger imperfection amplitude.

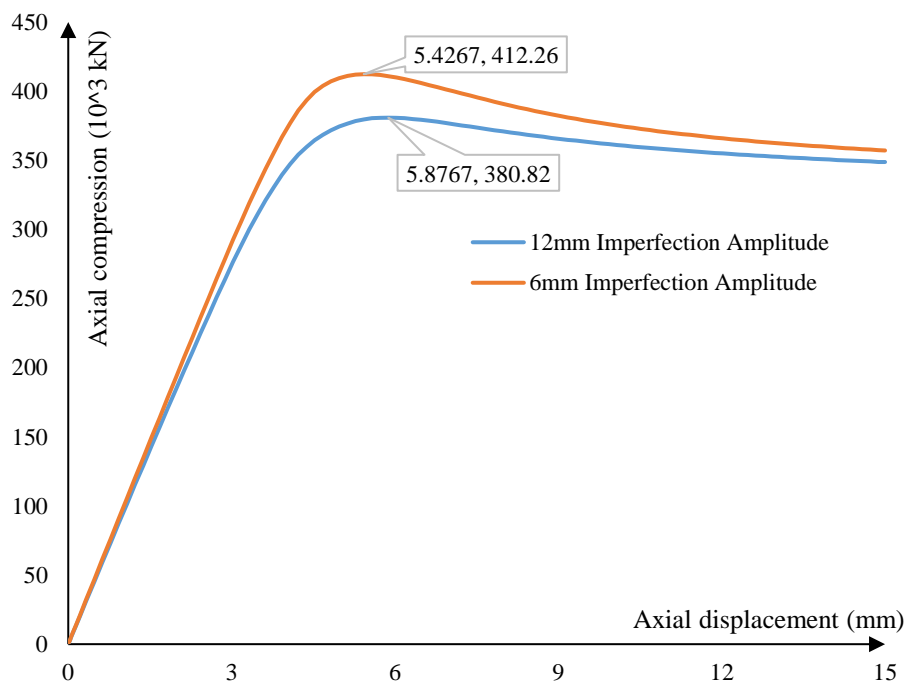


Figure 5.22 Load-displacement curve for stiffened shell with different imperfection amplitudes

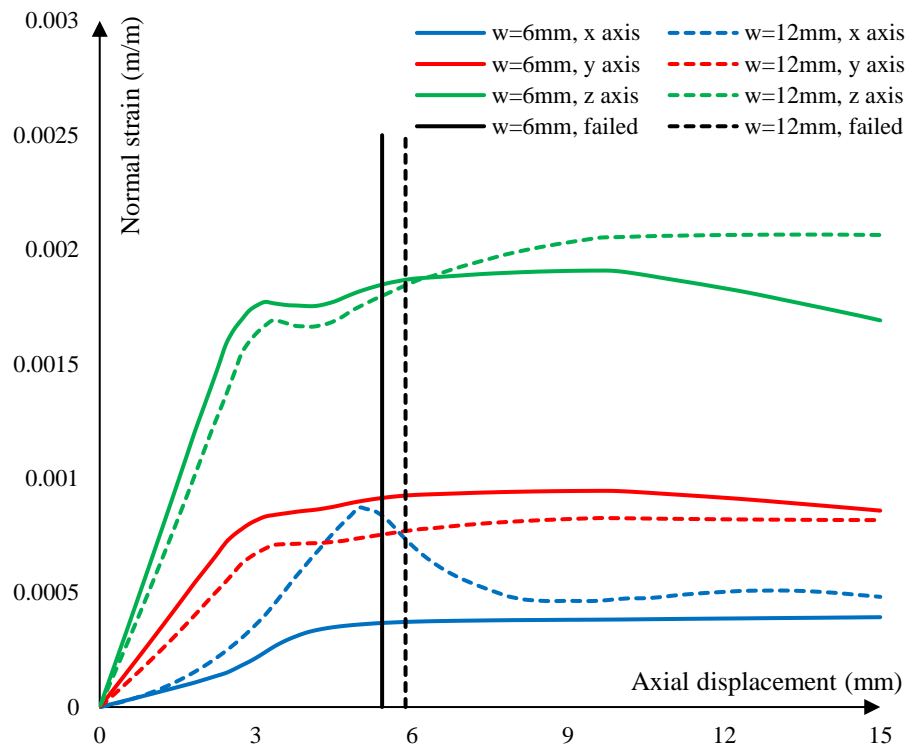


Figure 5.23 Strain-displacement curve for stiffened shell with different imperfection amplitudes

5.7 Conclusions

In this chapter, a numerical investigation considering geometrical and material nonlinearity on the buckling behaviour of unstiffened and stiffened cylindrical shells subjected to axial compression and bending moment has been carried out. Apart from FEM, three code-based approaches, the DNVGL, EN1993-1-6 (2007) and EN1993-1-6 (2017) codes, are used to evaluate the buckling strength of the shell. The accuracy and reliability of these design codes are assessed individually. The details of design process of unstiffened and stiffened cylindrical shells have been introduced in Chapter 4. Four imperfection profiles subjected to four perturbation loads are considered as initial imperfection in FEM. Finally, a case study of a stiffened cylinder is provided to study its buckling behaviour including the axial compression and the effect of imperfection amplitudes. Through this chapter the following conclusions can be drawn:

The imperfection profile has a significant effect on the ultimate strength and failure modes of the unstiffened and stiffened cylinders. Among the four imperfection profiles, Imperfection b (subjected to lateral pressure) is the safest profile for both the unstiffened

and stiffened cylinders. Imperfections a (subjected to axial compression) and c (subjected to bending moment) are the most critical profiles which lead to the lowest buckling strength of both stiffened and unstiffened cylinders. Imperfection a is quite sensitive to geometric dimensions, while Imperfection b is less sensitive to geometric dimensions of the cylinder. Furthermore, increasing imperfection amplitude would reduce the buckling strength of the cylindrical shell.

In terms of the design guidelines of shell structures, the calculation results of the characteristic buckling strength based on EN1993-1-6 (2017) agrees better with FEA result than DNVGL, despite the DNVGL has a more conservative imperfection amplitude. Due to a stricter setting of imperfection amplitude, DNVGL provides a more convergent result (a lower value of COV) of shell buckling strength. Moreover, owing to a more conservative consideration of partial safety factor, a larger safety factor recommended by DNVGL generates a safer result of the design buckling strength when compared with EN1993-1-6 (2017). Compared with EN1993-1-6 (2007), the accuracy and convergence characteristic buckling calculation of EN1993-1-6 (2017) are improved. The ultimate strength of the thin and stocky cylindrical shells needs to be better understood as all of above design standards could not provide accurate prediction.

The failure modes of unstiffened cylindrical shell are significantly affected by imperfection profiles and amplitudes. Different amplitudes for the same geometric dimensions would lead to different buckling modes (e.g. from column buckling to local buckling). The vertical strain plays a leading role when the shell structures experience buckling. When a sudden buckling occurs, the vertical strain increases sharply, but the tangential strain decreases sharply. On the post-buckling of the unstiffened shell, the greater the horizontal deformation, the greater the increase of horizontal strain.

According to the accuracy assessment of the design codes, DNVGL provides a safe design buckling capacity for every cylinder based on the FE modelling. However, some predictions of design buckling capacity are conservative. In addition, the predictions in some cases based on Eurocode cannot meet the safety requirement. Thus, a reliability analysis is performed for these three codes to improve the accuracy of the prediction of

the ultimate strength for cylindrical shells based on the first order reliability method. The new partial safety factor γ_M is provided for offshore structures (target design life of 20 years). After using the revised partial safety factor, the design load capacity predicted by DNVGL, EN1993-1-6 (2007) and EN1993-1-6 (2017) becomes more accurate and safer in terms of the studied cylindrical shells, although the strength prediction of the cylinder with large r/t using DNVGL, EN1993-1-6 (2007) and EN1993-1-6 (2017) is still conservative.

In the case study of stiffened cylindrical shell subjected to axial compression, DNVGL provides a relatively smaller safety factor and buckling strength than other design codes. An increase of imperfection amplitude decreases the maximum compression capacity of the stiffened cylinder, and the vertical strain plays a leading role when buckling occurs in a stiffened shell structure, which are in good agreement with the unstiffened shells.

CHAPTER 6 CONCLUSIONS AND FUTURE WORKS

The aim of this thesis was to improve understanding of the nonlinear structural behaviour of a semi-submersible platform for FWTs, compare and evaluate the relevant design codes. Considering two main environmental impacts hydrodynamic & aerodynamic forces and structural nonlinearity, a novel one-way coupled fluid structure interaction simulation in ANSYS is developed to obtain the structural behaviour of the entire floating system including the structural components and the connections between components, in which the failure behaviour and effect of environmental loads on the platform have been studied. Besides global structure analysis of floating platform, as the main components of the floating system, the columns fabricated by steel cylindrical shell have been evaluated at structural design, buckling behaviour and ultimate strength level. Specifically speaking, the code-based design solutions of the external and internal columns based on the shell design guideline of DNVGL and EN1993-1-6 (2007) & (2017) are compared and discussed. A cost-effectiveness design of the stiffened shell is proposed. Then, the ultimate strength of steel cylindrical shells with a wide geometric range under axial compression and bending were estimated by using FEM and design standard prediction. The effect of different imperfections on buckling behaviour and ultimate strength and reliability evaluation of the design guideline have been performed.

6.1 Summary of contributions

The main contribution of this thesis is to improve the knowledge and understanding of the nonlinear structural performance of a floating platform for FWTs, and to evaluate the relevant design codes. Specifically speaking, the most notable contributions could be summarised as follows:

- A novel one-way coupled fluid-structure interaction simulation including hydrodynamic and structural analysis has been developed and validated for structural performance study of FWTs. This analytical model considers the effects of wind, wave, mooring system, geometrical and material nonlinearity, which can also be adopted by other FWTs if they have similar design consideration.

- A series of nonlinear FE models with a wide geometric range have been carried out to study the buckling behaviour and ultimate strength of unstiffened and stiffened cylindrical shell under combined load effects. Different types of initial imperfections considering the realistic mechanical characteristics of marine structures have been adopted
- A comparison of the prevailing shell design codes is proposed based on a practical load case for a semi-submersible platform for FWTs.
- Assessment of the prevailing design guidelines of shell structure, DNVGL standard and Eurocode, has been conducted based on the comparison of the FEA results and the code-based prediction.
- Based on a reliability analysis, the recommended modifications for shell design code DNVGL and EN1993-1-6 (2007) & (2017) are proposed to ensure its safety and to be more applicable for OWTs.

6.2 Summary of findings

The main findings are summarised as follows:

Nonlinear structural analysis of floating wind platforms:

- Both in the linear and nonlinear structural analysis of the floating platform, the maximum stress occurs on the connections of pontoons and internal columns on the upper level of the platform.
- Compared with wave load, wind load has a larger effect on the structural behaviour especially for the tower base. The wave-wind misalignment has an adverse effect on the internal stress.

- After considering geometric and material nonlinearity in ultimate limit state, the stress in structure redistributes and the maximum stress is reduced, which maximize the strength of the material and reduce the material weight.

Code-based cylindrical shell design comparison:

- In an actual design case of offshore unstiffened cylindrical shell design in this study, DNVGL provide slightly more conservative prediction compared with EN1993-1-6 (2007) and EN1993-1-6 (2017) because of a larger partial safety factor of DNVGL.
- The EN1993-1-6 (2017) adopts a new method called Reference Resistance Design for meridional buckling, which sufficiently considers the effect of imperfections, plasticity, slenderness of shell structures. However, the design of the offshore shell structure may be dominated by circumferential buckling. Therefore, the EN1993-1-6 (2007) and EN1993-1-6 (2017) may predict the same shell thickness to resist the external forces.
- As for stiffened cylindrical shell, after considering the labour cost related to fabrication in optimization design, the total cost reduces sharply compared to the stiffened cylindrical shell neglecting the labour cost despite the weight of the structure itself increases significantly. The cost of the stiffened cylindrical shell is lower than the unstiffened cylindrical shell because of the lower cost of the steel.
- Eurocode need to be improved for the stiffened shell of offshore structures especially in stiffener design.

Ultimate strength of cylindrical shell under combined load effects:

- The initial imperfections of unstiffened cylindrical shell subjected to the perturbation load of bending moment and axial compression cause a larger reduction of buckling strength. The larger imperfection amplitude, the smaller buckling strength of the cylindrical shell.

- Among the shell structure design guidelines of the DNVGL code, EN1993-1-6 (2007) and EN1993-1-6 (2017), the characteristic buckling strength predicted by EN1993-1-6 (2017) are in best agreement with the FEA results. Because of a larger partial safety factor, the DNVGL code provides a safer prediction in the design buckling strength.
- Using the new partial safety factor based on a reliability analysis, EN1993-1-6 (2007) and EN1993-1-6 (2017) predict a safer ultimate strength of cylindrical shells, and DNVGL provides a more economical prediction in the design buckling strength.
- Different imperfection profiles and amplitudes may cause different buckling modes and post-buckling behaviour. The vertical strain develops sharply before and after buckling of the structure.
- As for the stiffened cylindrical shell, a more accurate and reliable value of buckling strength is provided by the DNVGL guideline compared with the unstiffened cylindrical shell.

6.3 Future works

According to the main findings and contributions summarized above, the primary objectives of this project have been achieved. Nevertheless, there are still some aspects over this study that need to be improved and further developed:

- The study performed in this thesis is based on numerical methods. Physical testing is needed to validate and improve the understanding of the structural performance of FWTs.
- The hydrodynamic calculation is relied on potential flow theory, which may not be accurate for extreme waves. A higher order approach for hydrodynamic analysis may be complemented in future with CFD or experimental modelling.

- The aerodynamic calculation is simplified in this thesis. A more accurate and realistic method of aerodynamic consideration is needed to enhance the structural analysis model of the FWT.
- Equivalent static structural analysis is used in the nonlinear structural study of floating offshore wind platforms, which does not induce significant inertia and damping effects. In future work, a time-dependent (transient) analysis will be undertaken.
- A case study of the stiffened cylindrical shell is provided in this thesis. More studies need to be conducted to improve the knowledge and understanding of the stiffened shell structure.
- As another important structural performance, the fatigue behaviour of floating offshore structure is highly valued to research in the future works.
- More design standards related to shell structures such as American Bureau of Shipping (ABS) and American Petroleum Institute (API) guideline need to be added and compared.
- Design formula and partial safety factor need to be improved to enhance the safety and reliability of the mentioned design guideline in this thesis.
- The effect of the single imperfection profile of the cylinder has been studied in Chapter 5, the combined imperfection will be carried out to have a more comprehensive understanding of the effect of imperfection on the cylindrical shell in future work.

APPENDIX A INTRODUCTION OF DESIGN CODES FOR SHELL STRUCTURE

A.1 Unstiffened shell structure design

The design processes of an unstiffened shell structure based on three design codes, the DNVGL, EN1993-1-6 (2007) and EN1993-1-6 (2017), are presented in this appendix.

A.1.1 DNVGL-RP-C202

The following equations from DNVGL-RP-C202 ([DNVGL-RP-C202, 2019](#)) were used to check the buckling strength of the structure design. The buckling modes of the unstiffened circular cylinders to be checked are: 1) shell buckling and 2) column buckling.

To meet the stability requirement of a structure, the design load effect must not exceed the design buckling strength. The stability requirement subjected to axial force, bending moment, circumferential compression and shear is given by:

$$\sigma_{j,sd} \leq f_{ksd} \quad (\text{A.1})$$

where $\sigma_{j,sd}$ is the design equivalent von Mises' stress and f_{ksd} is the design buckling strength of the shell.

The reduced buckling coefficient C related to the length, thickness and radius of shell can be used to consider geometrical and material imperfections. The reduced shell slenderness $\bar{\lambda}_S$ is the reduction factor for the characteristic buckling strength f_{ks} , it is also used to determine the partial safety factor γ_M . These important factors and the flowchart of shell buckling calculation are shown in Figure 7.1 ([Ye et al., 2019](#)).

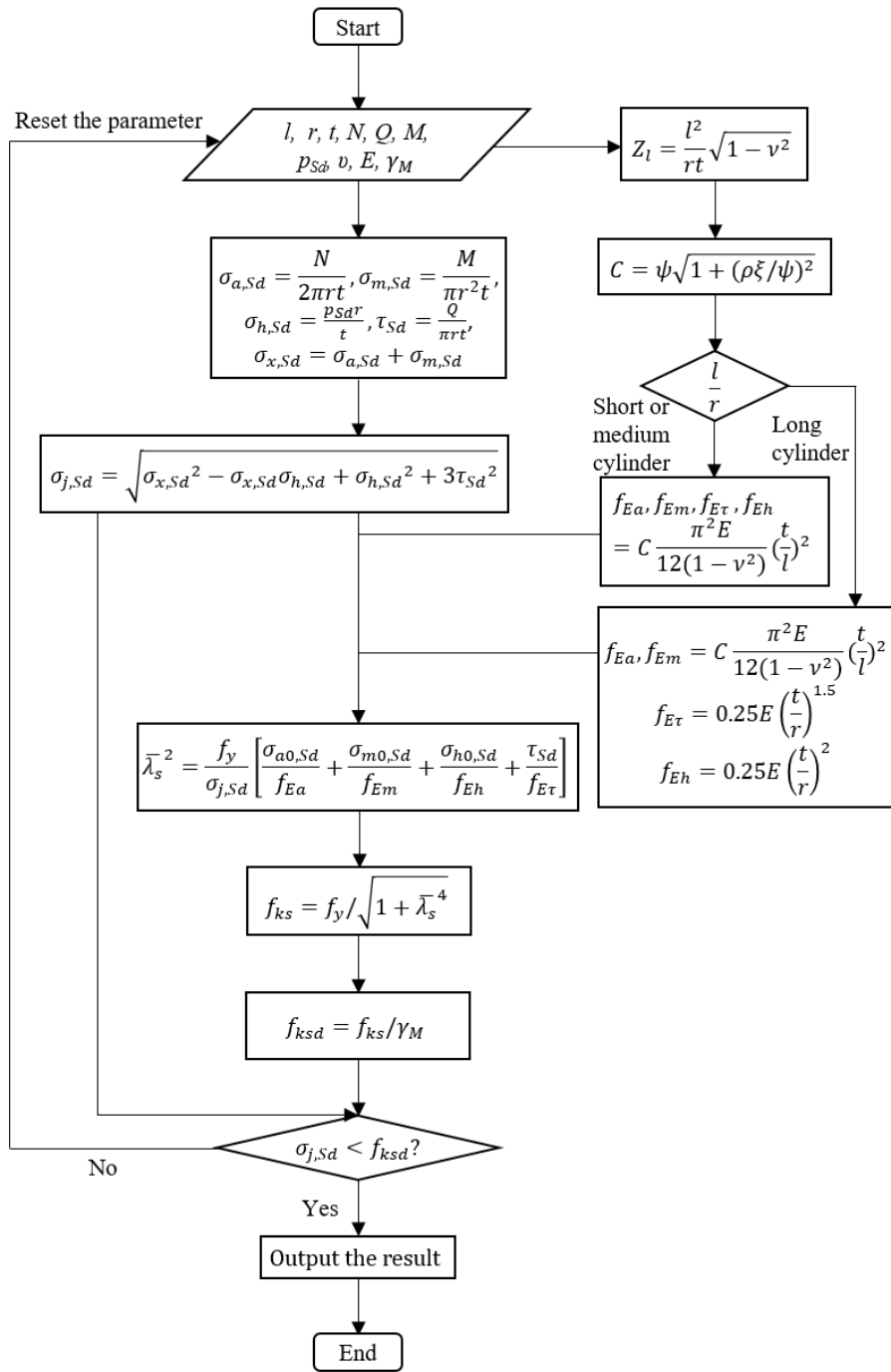


Figure 7.1 Flowchart of shell buckling calculation according to DNVGL (Ye et al., 2019)

Compared with the unstiffened curved panels, not only local buckling but also global buckling should be considered in unstiffened circular cylinders. The cylinders would be more unstable as the length increases so the maximum load effect, which the column can support, should be determined before it buckles. The column buckling strength should be assessed if

$$\left(\frac{kL_c}{i_c}\right)^2 \geq 2.5 \frac{E}{f_y} \quad (\text{A.2})$$

where k is the effective length factor, L_c is the length of cylinder, $i_c = \sqrt{I_c/A_c}$ is the radius of gyration of the cylinder section, I_c is the moment of inertia of the complete cylinder section (about the weakest axis), and A_c is the cross-sectional area of the complete cylinder section.

Furthermore, the stability requirement for a shell-column due to combined load effects must be checked:

$$\frac{\sigma_{a0,Sd}}{f_{kcd}} + \frac{1}{f_{akd}} \left[\left(\frac{\sigma_{m1,Sd}}{1 - \frac{\sigma_{a0,Sd}}{f_{E1}}} \right)^2 + \left(\frac{\sigma_{m2,Sd}}{1 - \frac{\sigma_{a0,Sd}}{f_{E2}}} \right)^2 \right]^{0.5} \leq 1 \quad (\text{A.3})$$

where $\sigma_{a0,Sd}$ is the design axial compression stress, $\sigma_{m,Sd}$ is the maximum design bending stress about the given axis, f_{akd} is the design local buckling strength, f_{kcd} is the design column buckling strength, and f_{E1} and f_{E2} are the Euler buckling strengths.

A.1.2 EN1993-1-6 (2007)

The following modes should be checked: 1) Meridional (axial) buckling, 2) Circumferential (hoop) buckling, 3) Shear buckling, 4) Meridional compression with coexistent internal pressure, 5) Combinations of meridional compression, circumferential compression and shear. Figure 7.2 shows the modes of meridional buckling, circumferential buckling and shear buckling.

The length of the shell segment is characterised in terms of the dimensionless length parameter ω :

$$\omega = \frac{l}{r} \sqrt{\frac{r}{t}} = \frac{l}{\sqrt{rt}} \quad (\text{A.4})$$

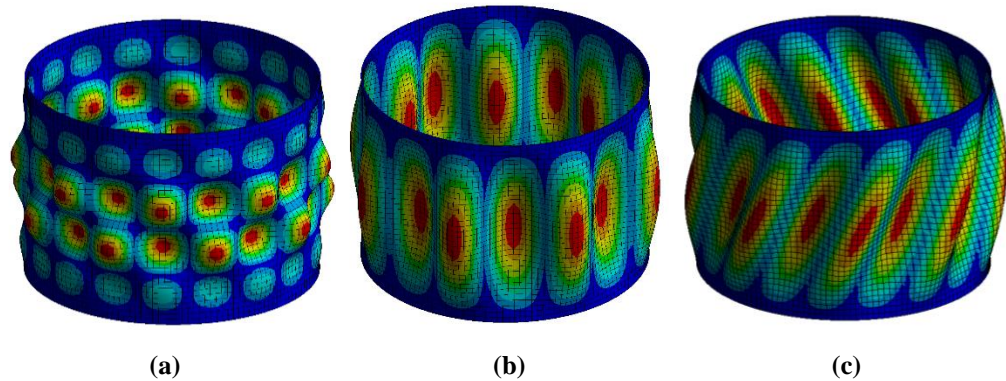


Figure 7.2 Buckling modes of (a) meridional buckling, (b) circumferential buckling, (c) Shear buckling obtained from FEA

A.1.2.1 Meridional buckling

Cylinders must be checked against meridional shell buckling if they satisfy:

$$\frac{r}{t} > 0.03 \frac{E}{f_{yk}} \quad (\text{A.5})$$

where f_{yk} is the characteristic yield strength. The critical meridional buckling stress should be obtained from:

$$\sigma_{xRc} = 0.605 E C_x \frac{t}{r} \quad (\text{A.6})$$

where C_x is the coefficient related to the length, thickness and radius of shell. The flowchart of meridional buckling calculation is shown in Figure 7.3.

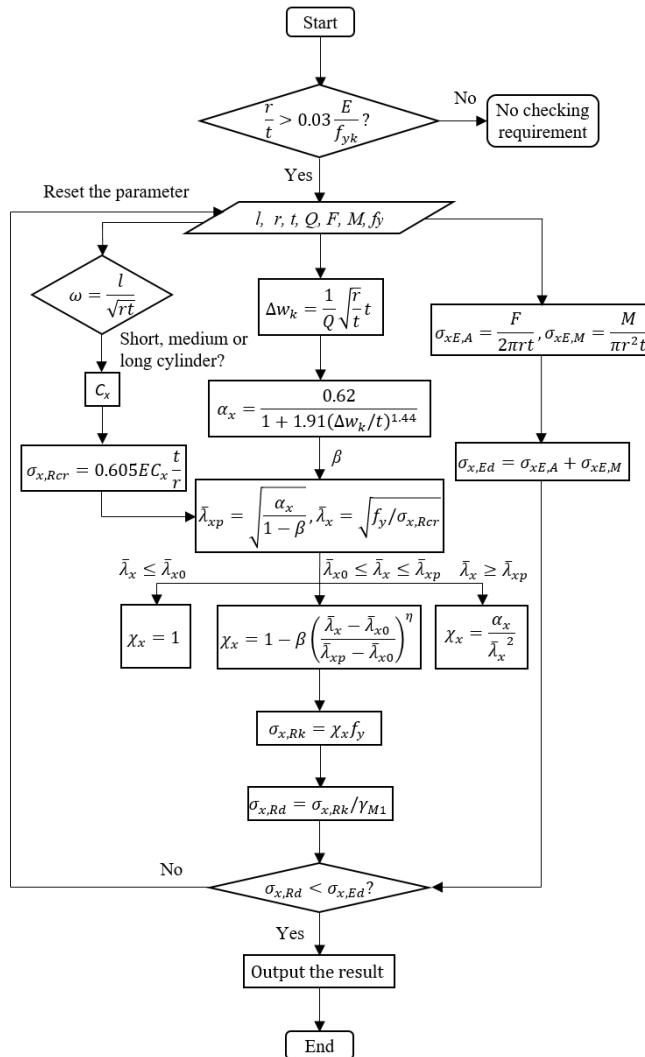


Figure 7.3 Flowchart of meridional buckling calculation according to EN1993-1-6 (2007)

A.1.2.2 Circumferential buckling

Cylinders must be checked against circumferential shell buckling if they satisfy:

$$\frac{r}{t} > 0.21 \sqrt{\frac{E}{f_{yk}}} \quad (\text{A.7})$$

The elastic critical circumferential buckling stress $\sigma_{\theta,Rcr}$ depends on the types of cylinders. Compared with short-cylinders and medium-length cylinders, the evaluation of the critical buckling stress for long cylinders is different, as shown in Table A.1. The value of the factor C_θ depends on the boundary conditions at the two ends of the cylinder. The flowchart of the circumferential buckling calculation is shown in Figure 7.4.

Table A.1 Elastic critical circumferential buckling stress

Type of cylinders	Criteria of length	$\sigma_{\theta,Rcr}$
Short-length	$\frac{\omega}{C_\theta} < 20$	$0.92E \left(\frac{C_\theta}{\omega}\right) \left(\frac{t}{r}\right)$
Medium-length	$20 \leq \frac{\omega}{C_\theta} \leq 1.63 \frac{r}{t}$	
Long-length	$\frac{\omega}{C_\theta} > 1.63 \frac{r}{t}$	$E \left(\frac{t}{r}\right)^2 \left[0.275 + 2.03 \left(\frac{C_\theta r}{\omega t}\right)^4\right]$

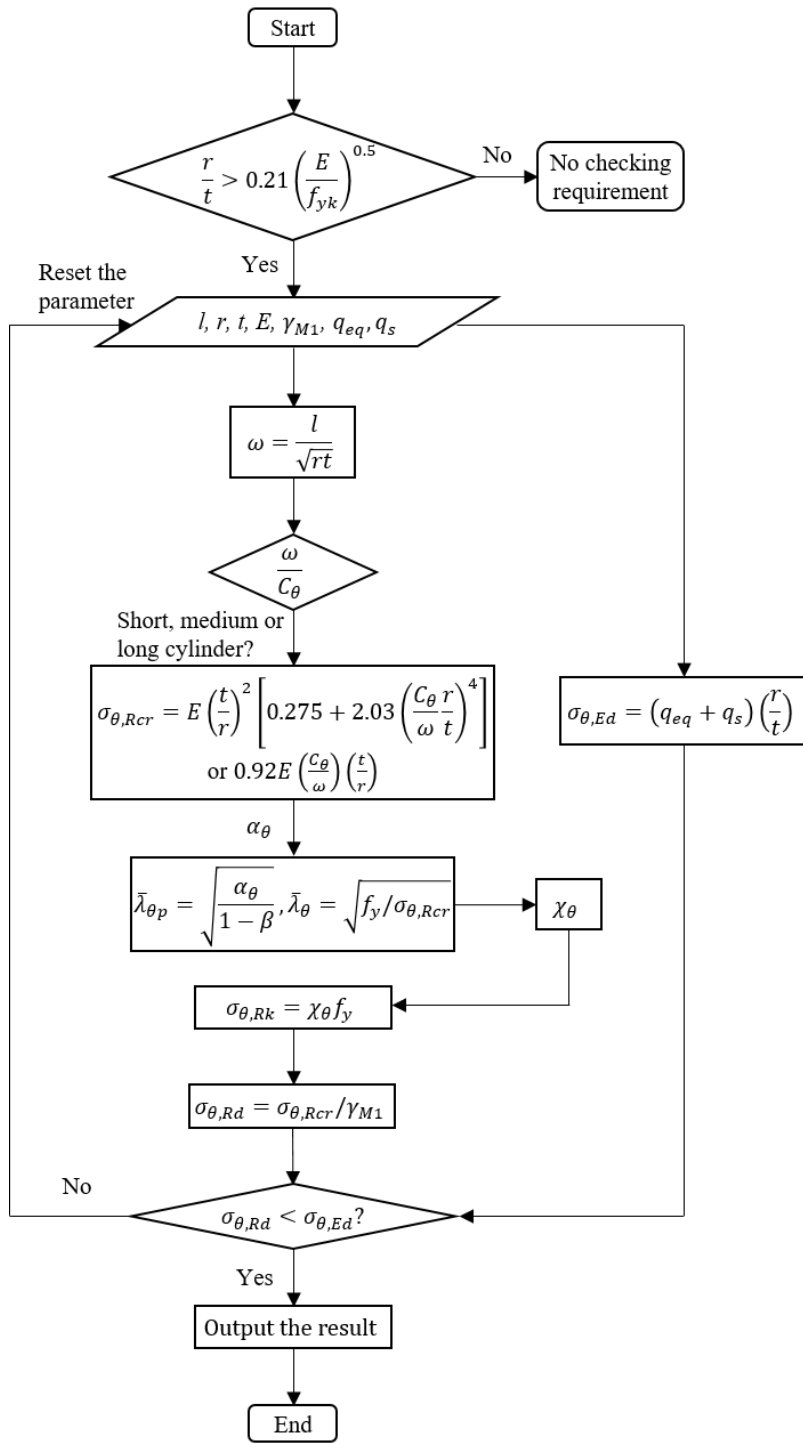


Figure 7.4 Flowchart of circumferential buckling calculation according to EN1993-1-6 (2007)

A.1.2.3 Shear buckling

Cylinders must be checked against shear shell buckling if they satisfy:

$$\frac{r}{t} > 0.16 \left(\frac{E}{f_{yk}} \right)^{0.67} \tag{A.8}$$

The elastic critical shear buckling stress should be obtained from:

$$\tau_{x\theta, Rcr} > 0.75EC_{\tau}\sqrt{\frac{1}{\omega}\left(\frac{t}{r}\right)} \quad (\text{A.9})$$

where E is the Young's modulus, ω is the dimensionless length parameter obtained from Eq. (A.4). The value of the factor C_{τ} may be found in Table A.2 for different types of cylinders. C_{τ} is a reduction factor for the elastic critical buckling stress induced by imperfection and slenderness of the cylindrical shell. According to different types of cylinders, the factor C_{τ} and the elastic critical shear buckling stress $\tau_{x\theta, Rcr}$ can be calculated. The flowchart of the meridional buckling calculation is shown in Figure 7.5.

Table A.2 Factor C_{τ}

Type of cylinders	Criteria of length	C_{τ}
Short-length	$\omega < 10$	$\sqrt{1 + \frac{42}{\omega^3}}$
Medium-length	$10 \leq \omega \leq 8.7\frac{r}{t}$	1.0
Long-length	$\omega > 8.7\frac{r}{t}$	$\frac{1}{3}\sqrt{\frac{t}{\omega r}}$

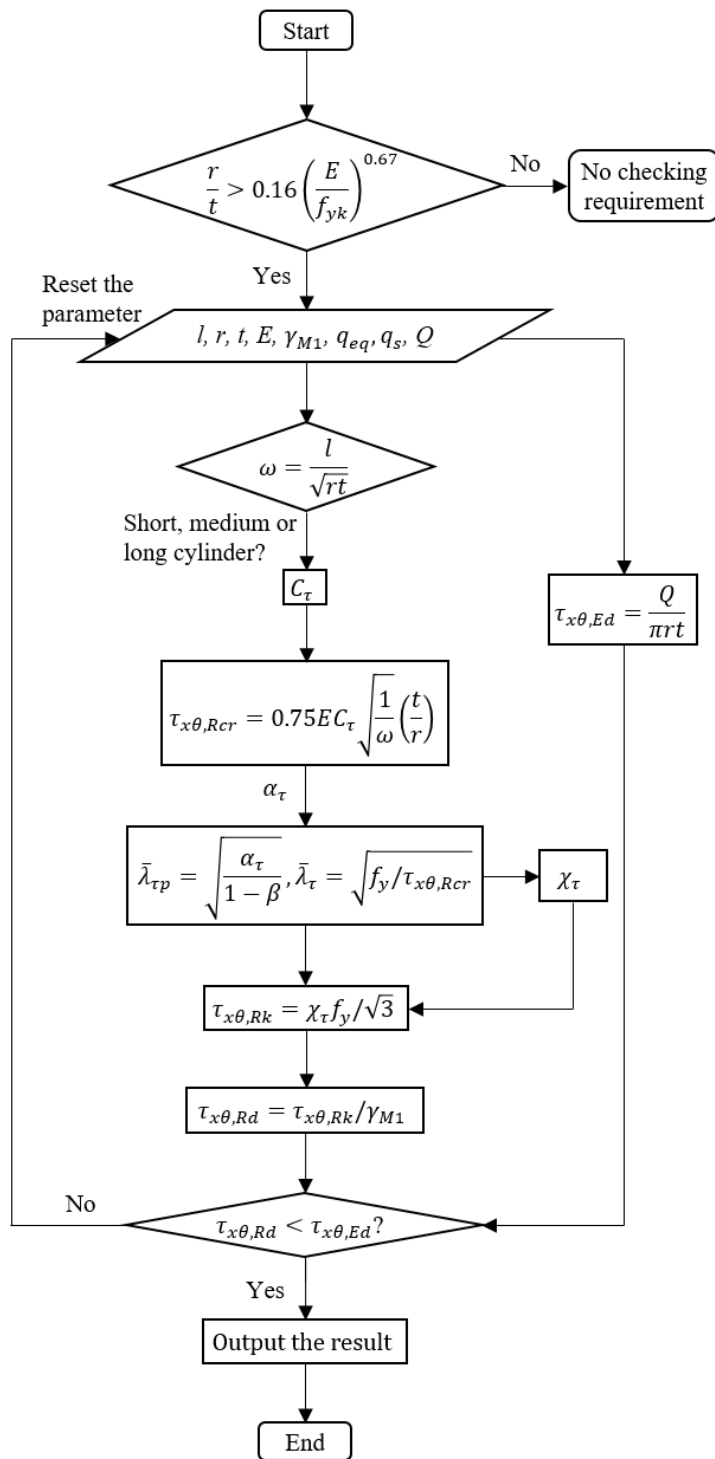


Figure 7.5 Flowchart of shear buckling calculation according to EN1993-1-6 (2007)

A.1.2.4 Combinations of meridional compression, circumferential compression and shear

Sometimes, the structure has to resist the combined effect of different forces. After checking the buckling strength due to meridional, circumferential compression and shear

individually, the buckling interaction due to these three load effects should be followed. The calculation process for the buckling interaction checking is shown in Figure 7.6.

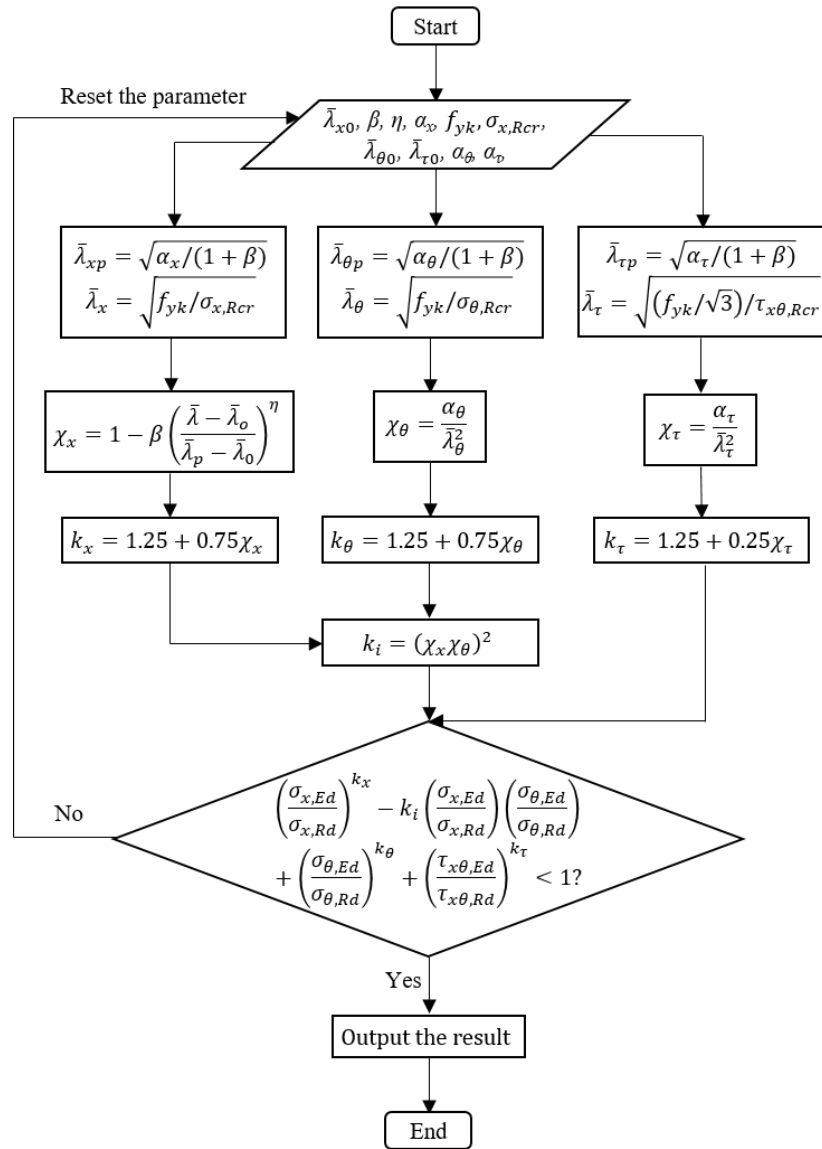


Figure 7.6 Flowchart for buckling interaction checking according to EN1993-1-6 (2007)

A.1.3 EN1993-1-6 (2017)

On the basis of the former version EN1993-1-6 (2007), the consideration of circumferential (hoop) buckling, shear buckling and combined effect of different forces have not been modified in EN1993-1-6 (2017). However, the calculation of meridional (axial) buckling has a major change.

Firstly, the values of the factor α_x (meridional elastic buckling reduction factor), β_x (plastic range factor) and η_x (interaction exponent) are changed in EN1993-1-6 (2017):

$$\alpha_x = \frac{0.83}{1+2.2(\Delta w_k/t)^{0.88}} \quad (\text{A.10})$$

$$\beta_x = 1 - \frac{0.95}{1+1.2(\Delta w_k/t)} \quad (\text{A.11})$$

$$\eta_x = \frac{5.4}{1+4.6(\Delta w_k/t)} \quad (\text{A.12})$$

where Δw_k is the characteristic imperfection amplitude given by:

$$\Delta w_k = \frac{1}{Q} \sqrt{rt} \quad (\text{A.13})$$

It means that β_x and η_x would change if the radius or thickness of the shell varies. However, in EN1993-1-6 (2007), β_x and η_x are taken as 0.6 and 1 respectively.

Secondly, a new method of Reference Resistance Design (RRD) is provided in EN1993-1-6 (2017) to consider the design resistance of bending moment. The only hand calculation method used in EN1993-1-6 (2007) is called ‘‘Stress Design’’, which is limited to be a purely elastic analysis. The cylindrical shell would occur a large plastic deformation under global bending. Therefore, the plastic behaviour of shell should be taken into account. In order to have a more realistic prediction of the buckling resistance, RRD is provided. RRD combines two reference values of linear elastic bifurcation analysis (LBA) and materially nonlinear small displacement theory analysis (MNA) and also consider the effect of imperfections, plasticity and slenderness of shell structures (Rotter, 2016).

A.2 Stiffened shell structure design

The design processes of stiffened shell structure based on three design codes, the DNVGL, EN1993-1-6 (2007) and EN1993-1-6 (2017), are presented as follows.

A.2.1 DNVGL-RP-C202

In DNVGL, the cylindrical shell may be stiffened by using longitudinal stiffeners and/or circumferential rings (Figure 7.7). For stiffened cylindrical shells the following buckling modes shown in Figure 7.8 should be checked: a) shell buckling (unstiffened curved panels), b) panel stiffener buckling, c) panel ring buckling, d) general buckling, e) column buckling. In this case, the panel ring stiffeners are used to strengthen the panel in the

circumferential direction. After ensuring the safety of the ring buckling strength, the check of general buckling can be avoided. Shell buckling and column buckling have been explained in A.1.1, and the others are described in the following section.

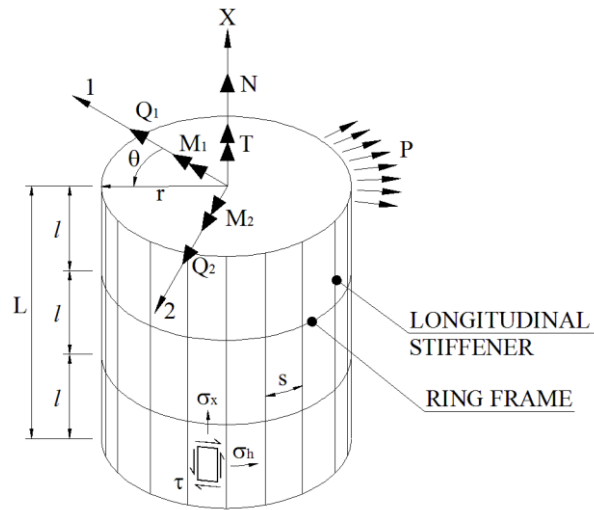


Figure 7.7 Stiffened cylindrical shell (DNVGL-RP-C202, 2019)

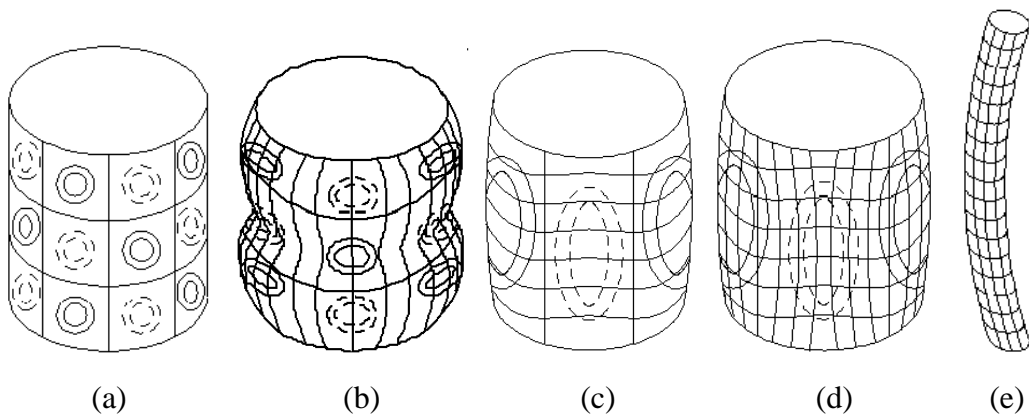


Figure 7.8 Buckling modes of (a) shell buckling, b) panel stiffener buckling, c) panel ring buckling, d) general buckling, e) column buckling (DNVGL-RP-C202, 2019)

A.2.1.1 Panel stiffener buckling

The panel stiffener is assumed to bear the longitudinal force subjected to axial force and bending moment (bending moment can be consisted of a couple of axial compression and tension) with the shell panel, so it is permissible to replace the shell thickness by using the equivalent thickness. The checking procedure is similar to that of the unstiffened shell structure, but different coefficients are used because of the change in equivalent thickness.

Additionally, the geometric proportions requirement of web and flange should be checked to prevent the local buckling of stiffeners. The calculation procedure of panel stiffener buckling is provided in Figure 7.9.

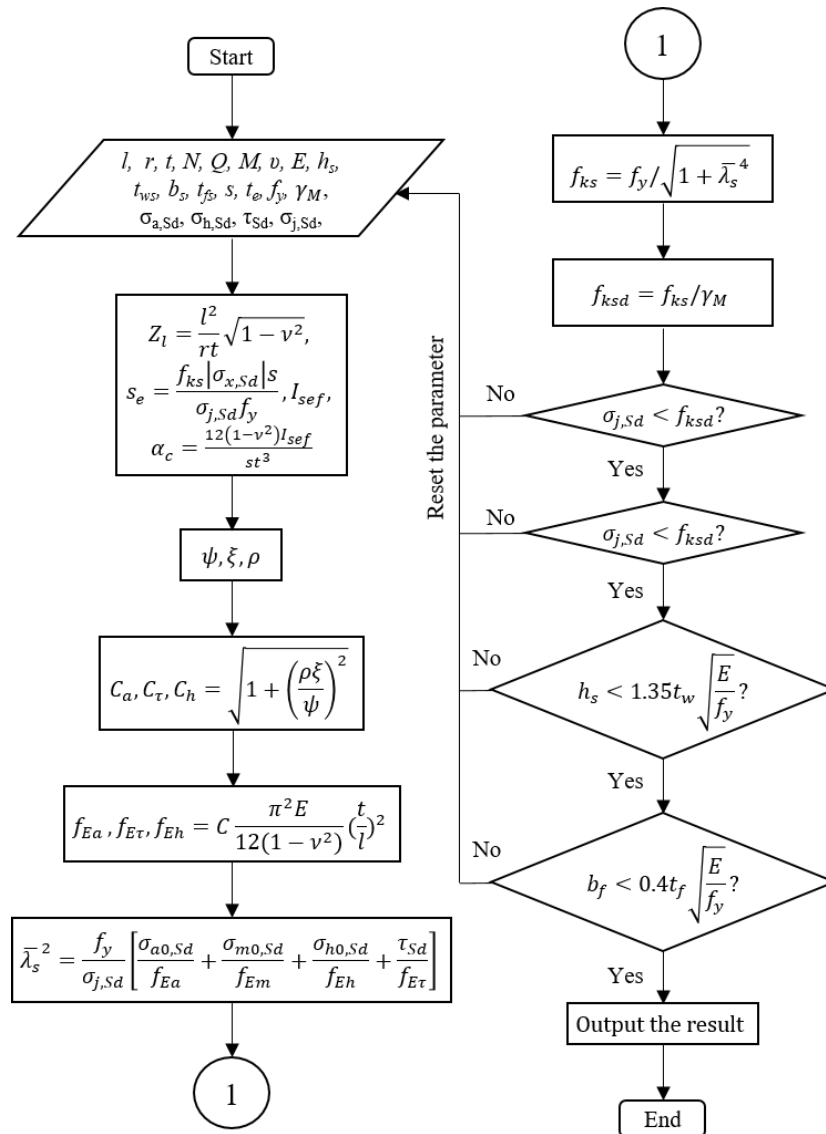


Figure 7.9 Flowchart of panel stiffener buckling calculation according to DNVGL

A.2.1.2 Panel ring buckling

On the basis of DNVGL-RP-C202, the panel ring stiffeners are assumed to bear the circumferential force subjected to lateral pressure. To avoid the panel ring buckling mode, the effective moment of inertia of the ring section should not be less than $I_R = I_x + I_{xh} + I_h$ (see Figure 7.10). I_x, I_{xh}, I_h represent the minimum requirement of the moment of inertia of ring frames subjected to axial compression with bending, shear and lateral pressure,

respectively. The calculation provided by the author in this study (Appendix B) has shown that I_h accounts for a large proportion (more than 90 %) in I_R . This means that compared with the other loads, lateral pressure is more critical in structural design.

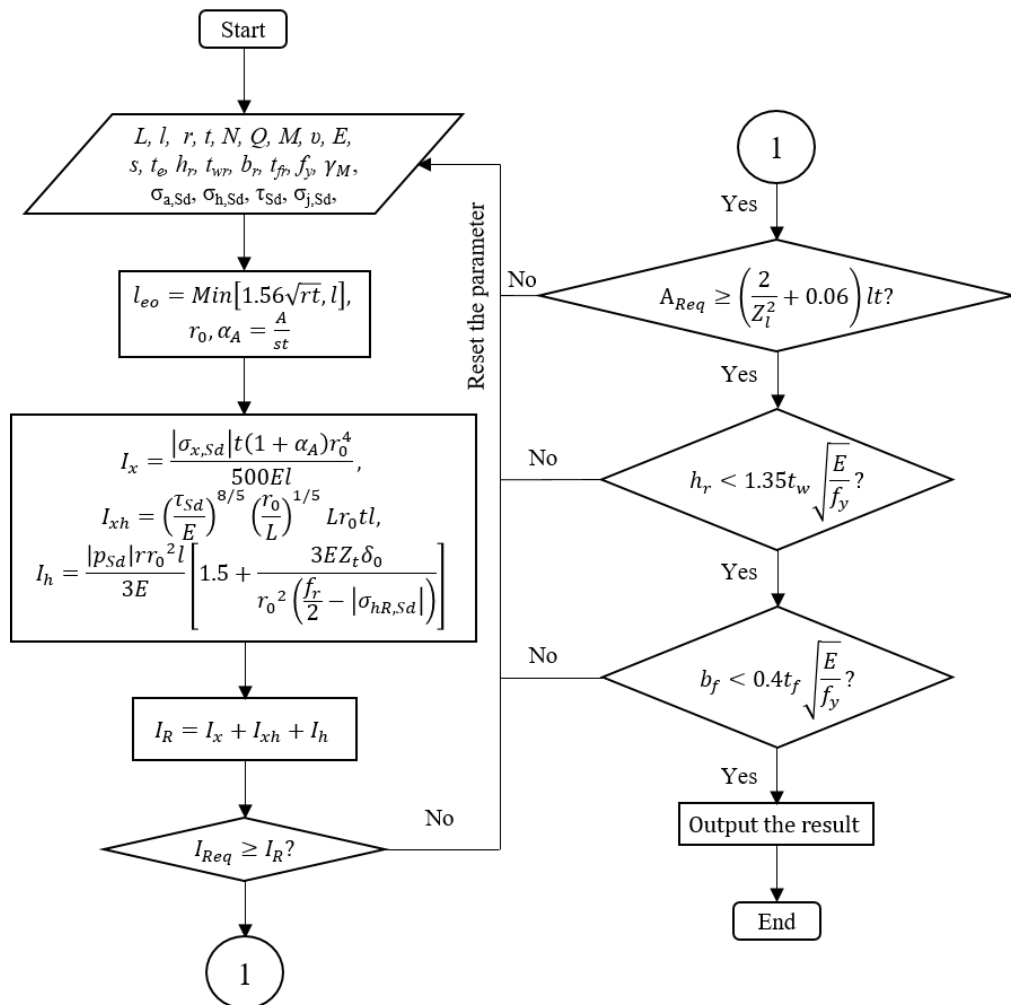


Figure 7.10 Flowchart of panel ring buckling calculation according to DNVGL

A.2.2 EN1993-1-6 (2007) & (2017)

EN1993-1-6 (2007) and EN1993-1-6 (2017) consider three load cases for ring stiffeners on a cylindrical shell: 1) radial force on ring, 2) axial loading, and 3) uniform pressure on surface. The design of longitudinal stiffeners has not been provided in this standard. Apart from the buckling modes that have been introduced in Section A.1.2, the strength check of the ring needs to be provided. In EN1993-1-6 (2007) and EN1993-1-6 (2017), the plastic resistance of the ring due to circumferential pressure is recommended to check.

APPENDIX B SPREADSHEET FOR SHELL STRUCTURE DESIGN

Spreadsheet lists:

1. Unstiffened cylindrical shell design for external column (DNVGL)
2. Unstiffened cylindrical shell design for internal column (DNVGL)
3. Unstiffened cylindrical shell design for external column (EN1993-1-6 (2007))
4. Unstiffened cylindrical shell design for internal column (EN1993-1-6 (2007))
5. Unstiffened cylindrical shell design for external column (EN1993-1-6 (2017))
6. Unstiffened cylindrical shell design for internal column (EN1993-1-6 (2017))
7. Stiffened cylindrical shell design for external column (DNVGL)
Case1: Mass minimization
Case2: Cost minimization
8. Stiffened cylindrical shell design for internal column (DNVGL)
Case1: Mass minimization
Case2: Cost minimization
9. Stiffened cylindrical shell design for external column (EN1993-1-6 (2007))
10. Stiffened cylindrical shell design for internal column (EN1993-1-6 (2007))
11. Stiffened cylindrical shell design for external column (EN1993-1-6 (2017))
12. Stiffened cylindrical shell design for internal column (EN1993-1-6 (2017))

1 Unstiffened cylindrical shell design for external column (DNVGL)						
Designed by:			Date:			
Checked by:						Reference
Design load on the column						Based on DNVGL-RP-C202
Distance of ring frames	l	=	27	m		
Shell thickness	t	=	43	mm		
Shell Radius	r	=	5	m		
Yield strength	f _y	=	355	MPa		
Young's modulus	E	=	210000000	kN/m ²		
Poisson's ratio	ν	=	0.3			
External column						
Axial force	F	=	4354	kN		
Shear force	V	=	1398	kN		
Bending moment	M	=	13664	kNm		
a) Shell buckling						
Stress due to axial force	σ _{a,Sd}	=	N _{Sd} /(2πrt)			
		=	3.22307266 MPa			
Stress due to bending	σ _{m,Sd}	=	M _{1,Sd} sinθ/(πr ² t)-M _{2,Sd} conθ/(πr ² t)			
		=	4.04594073 MPa			
Design longitudinal membrane stress	σ _{x,Sd}	=	σ _{a,Sd} +σ _{m,Sd}		eq. 2.2.1	
		=	7.26901339 MPa			
water level difference	h	=	9.8 m			
Design lateral pressure	p _{Sd}	=	0.09604 MPa			
Circumferential membrane stress	σ _{h,Sd}	=	p _{Sd} r/t		eq. 2.2.8	
		=	11.1674419 MPa			
Membrane shear stress	τ _{Sd}	=	τ _{T,Sd} +τ _{Q,Sd}		eq. 2.2.5	
		=	T _{Sd} /(2πr ² t)+[-Q _{1,Sd} sinθ/(πrt)+Q _{2,Sd} conθ/(πrt)]		eq. 2.2.6-7	
		=	2.06975452 MPa			
von Mises' stress	σ _{j,Sd}	=	$\sqrt{(\sigma_{a,Sd} + \sigma_{m,Sd})^2 - (\sigma_{a,Sd} + \sigma_{m,Sd})\sigma_{h,Sd} + \sigma_{h,Sd}^2 + 3\tau_{Sd}^2}$		eq. 3.2.3	
		=	10.451109 MPa			
Curvature parameter	Z _l	=	l ² √(1-ν ²)/(rt)		eq. 3.4.3	
		=	3234.51943			
Reduced buckling coefficient	C	=	ψ√(1+(ρξ/ψ) ²)		eq. 3.4.2	
	C _a	=	852.107316		axial	Table 3-2
	C _m	=	963.796743		bending	Table 3-2
	C _τ	=	220.348403			
	C _h	=	35.5449608			
Elastic buckling strength for axial force & bending moment	f _E	=	$C \frac{\pi^2 E}{12(1-\nu^2)} \left(\frac{t}{l}\right)^2$		eq. 3.4.1	
	f _{Ea}	=	410.204177 MPa			
	f _{Em}	=	463.97143 MPa			
	f _{Eτ}	=	106.075648			
	f _{Eh}	=	17.1113323			
reduced shell slenderness	$\bar{\lambda}_s^{-2}$	=	$\frac{f_y}{\sigma_{j,Sd}} \left[\frac{\sigma_{a0,Sd}}{f_{Ea}} + \frac{\sigma_{m0,Sd}}{f_{Em}} + \frac{\sigma_{h0,Sd}}{f_{Eh}} + \frac{\tau_{Sd}}{f_{E\tau}} \right]$		eq. 3.2.2	
		=	23.3943547			
	$\bar{\lambda}_s$	=	4.83677111			
Material factor	γ _M	=	1.45			
Characteristic buckling strength of a shell	f _{ks}	=	$f_y / \sqrt{1 + \bar{\lambda}_s^4}$			
		=	15.1607568 MPa			

1 Unstiffened cylindrical shell design for external column (DNVGL)							
Designed by:			Date:				
Checked by:							Reference
Design buckling strength of a shell	f_{ksd}	=	f_{ks}/γ_M				eq. 3.1.2
		=	10.4556943 MPa				
	$\sigma_{i,Sd}$	=	10.451109 <		f_{ksd}		eq. 3.1.1 OK
b) Column buckling							
Effective length factor	k	=	1				
Total cylinder length	L_c	=	27 m				
Moment of inertia of the cylinder section	I_c	=	$\frac{\pi(D^4 - d^4)}{64}$				
		=	16.6694765 m ⁴				
Cross sectional area of cylinder section	A_c	=	$\pi(R^2 - r^2)$				
		=	1.34507604 m ²				
Radius of gyration of cylinder section	i_c	=	$\sqrt{I_c/A_c}$				
		=	3.52036394 m				
			$\left(\frac{kL_c}{i_c}\right)^2$	=	58.8237086		eq. 3.8.1
			<	$2.5 \frac{E}{f_y} =$	1478.87324		No column buckling checking
The stability requirement for a shell-column							
		a	=	$1 + \frac{f_y^2}{f_E^2}$			eq. 3.8.9
			=	1.74895642			
		b	=	$\left(\frac{2f_y^2}{f_E f_{Eh}} - 1\right) \sigma_{h,sd}$			eq. 3.8.10
			=	-389.84376			
		c	=	$\sigma_{h,sd}^2 + \frac{f_y^2 \sigma_{h,sd}^2}{f_E^2} - f_y^2$			eq. 3.8.11
			=	-72222.272			
Reduced characteristic buckling strength	f_{ak}	=	$\frac{b + \sqrt{b^2 - 4ac}}{2a}$				eq. 3.8.8
		=	120.316053 MPa				
Reduced column slenderness	$\bar{\lambda}$	=	$\sqrt{\frac{f_{ak}}{f_E} = \frac{kL_c}{\pi i_c} \sqrt{\frac{f_{ak}}{E}}}$				eq. 3.8.7
		=	0.05843573				
Material factor	γ_M	=	1.15				
Design local buckling strength	f_{akd}	=	$\frac{f_{ak}}{\gamma_M}$				eq. 3.8.12
		=	104.622655 MPa				
Characteristic column buckling strength	f_{kc}	=	120.201015 MPa				eq. 3.8.5 & 3.8.6
Design column buckling strength	f_{kcd}	=	$\frac{f_{kc}}{\gamma_M}$				eq. 3.8.4
		=	104.522622 MPa				
Euler buckling strength	f_{E1}	=	$\frac{\pi^2 EI_{c,1}}{(kL_c)^2 A_c}$				eq. 3.8.3
		=	35234.3804 MPa				
			$\frac{\sigma_{a0,Sd}}{f_{kcd}} + \frac{1}{f_{akd}} \frac{\sigma_{m1,Sd}}{1 - \frac{\sigma_{a0,Sd}}{f_{E1}}}$	=	0.06951141 <		1 eq. 3.8.2 OK

2 Unstiffened cylindrical shell design for internal column (DNVGL)

Designed by:		Date:			
Checked by:					Reference
Design load on the column					Based on DNVGL-RP-C202
Distance of ring frames	l	=	27 m		
Shell thickness	t	=	33 mm		
Shell Radius	r	=	3 m		
Yield strength	f _y	=	355 MPa		
Young's modulus	E	=	210000000 kN/m ²		
Poisson's ratio	ν	=	0.3		
Internal column					
Axial force	F	=	11180 kN		
Shear force	V	=	1005 kN		
Bending moment	M	=	8867 kNm		
a) Shell buckling					
Stress due to axial force	σ _{a,Sd}	=	N _{Sd} /(2πrt)		
		=	17.9732552 MPa		
Stress due to bending	σ _{m,Sd}	=	M _{1,Sd} sinθ/(πr ² t)-M _{2,Sd} conθ/(πr ² t)		
		=	9.50321132 MPa		
Design longitudinal membrane stress	σ _{x,Sd}	=	σ _{a,Sd} +σ _{m,Sd}		eq. 2.2.1
		=	27.4764665 MPa		
water level difference	h	=	9.8 m		
Design lateral pressure	p _{Sd}	=	0.09604 MPa		
Circumferential membrane stress	σ _{h,Sd}	=	p _{Sd} r/t		eq. 2.2.8
		=	8.73090909 MPa		
Membrane shear stress	τ _{Sd}	=	τ _{T,Sd} +τ _{Q,Sd}		eq. 2.2.5
		=	T _{Sd} /((2πr ² t)+[-Q _{1,Sd} sinθ/(πrt)+Q _{2,Sd} conθ/(πrt)])		eq. 2.2.6-7
		=	3.23132763 MPa		
von Mises' stress	σ _{j,Sd}	=	$\sqrt{(\sigma_{a,Sd} + \sigma_{m,Sd})^2 - (\sigma_{a,Sd} + \sigma_{m,Sd})\sigma_{h,Sd} + \sigma_{h,Sd}^2 + 3\tau_{Sd}^2}$		eq. 3.2.3
		=	24.9522522 MPa		
Curvature parameter	Z _l	=	$l^2\sqrt{1-\nu^2}/(rt)$		eq. 3.4.3
		=	7024.46139		
Reduced buckling coefficient	C	=	$\psi\sqrt{1+(\rho\xi/\psi)^2}$		eq. 3.4.2
	C _a	=	1945.53585	axial	Table 3-2
	C _m	=	2159.94621	bending	Table 3-2
	C _τ	=	394.116535		
	C _h	=	52.3369533		
Elastic buckling strength for axial force & bending moment	f _E	=	$C \frac{\pi^2 E}{12(1-\nu^2)} \left(\frac{t}{l}\right)^2$		eq. 3.4.1
	f _{Ea}	=	551.614904 MPa		
	f _{Em}	=	612.406354 MPa		
	f _{Eτ}	=	111.743278		
	f _{Eh}	=	14.839019		
reduced shell slenderness	$\bar{\lambda}_s^{-2}$	=	$\frac{f_y}{\sigma_{j,Sd}} \left[\frac{\sigma_{a0,Sd}}{f_{Ea}} + \frac{\sigma_{m0,Sd}}{f_{Em}} + \frac{\sigma_{h0,Sd}}{f_{Eh}} + \frac{\tau_{Sd}}{f_{E\tau}} \right]$		eq. 3.2.2
		=	9.46666545		
	$\bar{\lambda}_s$	=	3.07679467		
Material factor	γ _M	=	1.45		
Characteristic buckling strength of a shell	f _{ks}	=	$f_y / \sqrt{1 + \bar{\lambda}_s^4}$		
		=	37.2925177 MPa		

2 Unstiffened cylindrical shell design for internal column (DNVGL)

Designed by:		Date:			
Checked by:					Reference
Design buckling strength of a shell	f_{ksd}	=	f_{ks}/γ_M = 25.7189777 MPa		eq. 3.1.2
	$\sigma_{i,Sd}$	=	24.9522522 <	f_{ksd}	eq. 3.1.1 OK
b) Column buckling					
Effective length factor	k	=	1		
Total cylinder length	L_c	=	27 m		
Moment of inertia of the cylinder section	I_c	=	$\frac{\pi(D^4 - d^4)}{64}$		
		=	2.7533107 m ⁴		
Cross sectional area of cylinder section	A_c	=	$\pi(R^2 - r^2)$		
		=	0.61861415 m ²		
Radius of gyration of cylinder section	i_c	=	$\sqrt{I_c/A_c}$		
		=	2.10968534 m		
	$\left(\frac{kL_c}{i_c}\right)^2$	=	163.7918		eq. 3.8.1
		<	$2.5 \frac{E}{f_y} = 1478.87324$		No column buckling checking
The stability requirement for a shell-column					
	a	=	$1 + \frac{f_y^2}{f_E^2}$ = 1.4141758		eq. 3.8.9
	b	=	$\left(\frac{2f_y^2}{f_E f_{Eh}} - 1\right) \sigma_{h,sd}$ = -260.11596		eq. 3.8.10
	c	=	$\sigma_{h,sd}^2 + \frac{f_y^2 \sigma_{h,sd}^2}{f_E^2} - f_y^2$ = -82320.776		eq. 3.8.11
Reduced characteristic buckling strength	f_{ak}	=	$\frac{b + \sqrt{b^2 - 4ac}}{2a}$ = 166.236313 MPa		eq. 3.8.8
Reduced column slenderness	$\bar{\lambda}$	=	$\sqrt{\frac{f_{ak}}{f_E}} = \frac{kL_c}{\pi i_c} \sqrt{\frac{f_{ak}}{E}}$ = 0.11461712		eq. 3.8.7
Material factor	γ_M	=	1.15		
Design local buckling strength	f_{akd}	=	$\frac{f_{ak}}{\gamma_M}$ = 144.553315 MPa		eq. 3.8.12
Characteristic column buckling strength	f_{kc}	=	165.624832 MPa		eq. 3.8.5 & 3.8.6
Design column buckling strength	f_{kcd}	=	$\frac{f_{kc}}{\gamma_M}$ = 144.021593 MPa		eq. 3.8.4
Euler buckling strength	f_{E1}	=	$\frac{\pi^2 EI_{c,1}}{(kL_c)^2 A_c}$		eq. 3.8.3
		=	12653.9724 MPa		
	$\frac{\sigma_{a0,Sd}}{f_{kcd}} + \frac{1}{f_{akd}} \frac{\sigma_{m1,Sd}}{1 - \frac{\sigma_{a0,Sd}}{f_{E1}}}$	=	0.19063098 <	1	eq. 3.8.2 OK

3 Unstiffened cylindrical shell design for external column (EN1993-1-6 (2007))

Designed by:		Date:			
Checked by:					Reference
Design load on the column					Based on EN 1993-1-6
Distance of ring frames	l	=	27 m		
Shell thickness	t	=	37 mm		
Shell Radius	r	=	5 m		
Yield strength	f_y	=	355 MPa		
Young's modulus	E	=	210000000 kN/m ²		
Poisson's ratio	ν	=	0.3		
External column					
Axial force	F	=	4354 kN		
Shear force	V	=	1398 kN		
Bending moment	M	=	13664 kNm		
a) Critical meridional (axial) buckling					
Length parameter	ω	=	$\frac{l}{r} \sqrt{\frac{r}{l}} = \frac{l}{\sqrt{rt}}$	0.5r/t	eq. D.1
		=	62.7737249	67.567568	medium cylinder
Factor	C_x	=	1		eq. D.3-D.10
Elastic critical meridional buckling stress	$\sigma_{x,Rcr}$	=	$0.605EC_x t/r$		eq. D.2
		=	940.17 MPa		
Characteristic imperfection amplitude	Δw_k	=	$\frac{1}{Q} \sqrt{\frac{r}{t}}$		eq. D.15
		=	0.01720465 m		
Meridional elastic imperfection reduction factor	α_x	=	$\frac{0.62}{1 + 1.91(\Delta w_k/t)^{1.44}}$		eq. D.14
		=	0.37941538		
	r/t	=	135.135135		eq. D.18 Meridional shell buckling checking
		>	$0.03E/f_{yk} =$	17.746479	
Meridional shell slenderness parameters	$\bar{\lambda}_x$	=	$\sqrt{f_{yk}/\sigma_{x,Rcr}}$		eq. 8.17
		=	0.61448457		
Meridional squash limit slenderness	$\bar{\lambda}_{x0}$	=	0.2		eq. D.16
Plastic range factor	β	=	0.6		eq. D.16
Interaction exponent	η	=	1		eq. D.16
Meridional plastic limit relative slenderness	$\bar{\lambda}_{xp}$	=	$\sqrt{\alpha_x/(1-\beta)}$		eq. 8.16
		=	0.97392939		
	$\bar{\lambda}_x$	\in	$(\bar{\lambda}_0, \bar{\lambda}_p)$		eq. 8.13-8.15
Buckling reduction factor	χ_x	=	$1 - \beta \left(\frac{\bar{\lambda} - \bar{\lambda}_0}{\bar{\lambda}_p - \bar{\lambda}_0} \right)^\eta$		eq. 8.13-8.15
		=	0.67866482		
Buckling interaction parameter	k_x	=	$1.25 + 0.75\chi_x$		eq. D.46
		=	1.75899861		
Meridional characteristic buckling stress	$\sigma_{x,Rk}$	=	$\chi_x f_{yk}$		ch. 8.5.2
		=	240.92601 MPa		
Partical factor	γ_{M1}	=	1.1		ch. 8.5.2
Meridional design buckling stress	$\sigma_{x,Rd}$	=	$\sigma_{x,Rk}/\gamma_{M1}$		eq. 8.11
		=	219.023646 MPa		
Design value of the meridional stress due to axial force	σ_{xEA}	=	$\frac{F}{2\pi r t}$		
		=	3.74573309 MPa		
Design value of the	σ	=	$\frac{M}{I}$		

3 Unstiffened cylindrical shell design for external column (EN1993-1-6 (2007))						
Designed by:			Date:			
Checked by:						Reference
meridional stress due to bending	$\sigma_{x,E,M}$	=	$\frac{\pi r^2 t}{\pi r^2 t}$			
		=	4.70203923 MPa			
Design value of meridional stress	$\sigma_{x,Ed}$	=	$\sigma_{x,E,A} + \sigma_{x,E,M}$			
		=	8.44777232 MPa			
		<	$\sigma_{x,Rd}$	219.023646 MPa		OK
b) Critical circumferential (hoop) buckling						due to hoop compression
Length parameter	ω	=	$\frac{l \sqrt{r}}{r \sqrt{l}} = \frac{l}{\sqrt{rt}}$			eq. D.1
		=	62.7737249			
Buckling factors	C_θ	=	1			
	ω/C_θ	<	1.63r/t	=	220.27027	medium cylinder
Elastic critical circumferential buckling stress	$\sigma_{\theta,Rcr}$	=	$0.92E \left(\frac{C_\theta}{\omega} \right) \left(\frac{t}{r} \right)$			eq. D.25
		=	22.7751341 MPa			
Circumferential elastic imperfection reduction factor	α_θ	=	0.65			Table D.5
	r/t	=	135.135135			eq. D.27 Circumferential shell buckling checking
		>	$0.21(E/f_{yk})^{0.5} =$		5.1075752	
Circumferential shell slenderness parameters	$\bar{\lambda}_\theta$	=	$\sqrt{f_{yk}/\sigma_{\theta,Rcr}}$			eq. 8.17
		=	3.94805965			
Circumferential squash limit slenderness	$\bar{\lambda}_{\theta 0}$	=	0.4			eq. D.26
Plastic range factor	β	=	0.6			eq. D.26
Interaction exponent	η	=	1			eq. D.26
Circumferential plastic limit relative slenderness	$\bar{\lambda}_{\theta p}$	=	$\sqrt{\alpha_\theta/(1+\beta)}$			eq. 8.16
		=	0.63737744			
	$\bar{\lambda}_\theta$	\in	$(\bar{\lambda}_p, +\infty)$			eq. 8.13-8.15
Buckling reduction factor	χ_θ	=	$\frac{\alpha_\theta}{\bar{\lambda}_\theta^2}$			eq. 8.13-8.15
		=	0.04170095			
Buckling interaction parameter	k_θ	=	$1.25+0.75\chi_\theta$			eq. D.47
		=	1.28127571			
Circumferential characteristic buckling stress	$\sigma_{\theta,Rk}$	=	$\chi_\theta f_{yk}$			ch. 8.5.2
		=	14.8038371 MPa			
Partical factor	γ_{M1}	=	1.1			ch. 8.5.2
Circumferential design buckling stress	$\sigma_{\theta,Rd}$	=	$\sigma_{\theta,Rk}/\gamma_{M1}$			eq. 8.11
		=	13.4580338 MPa			
External water pressure	q_{eq}	=	166.6 kPa			bottom of column
Internal water pressure	q_s	=	70.56 kPa			
Circumferential design stress	$\sigma_{\theta,Ed}$	=	$(q_{eq}+q_s)(r/t)$			eq. D.30
		=	12.9783784 MPa			
		<	$\sigma_{\theta,Rd}$	13.4580338 MPa		OK

3 Unstiffened cylindrical shell design for external column (EN1993-1-6 (2007))

Designed by:		Date:			
Checked by:					Reference
c) Critical shear buckling					ch. D.1.4
Length parameter	ω	$= \frac{l}{r} \sqrt{\frac{r}{l}} = \frac{l}{\sqrt{rt}}$			eq. D.31
		$= 62.7737249$	$>$	10	eq. D.33
		$< 8.7r/t$	$=$	1175.6757	medium-length cylinder
Factor	C_τ	$= 1$			eq. D.34
Elastic critical shear buckling stress	$\tau_{x\theta,Rcr}$	$= 0.75EC_\tau \sqrt{\frac{1}{\omega} \left(\frac{t}{r}\right)}$			eq. D.32
		$= 147.103609$ MPa			
Shear elastic imperfection reduction factor	α_τ	$= 0.65$			Table D.6
	r/t	$= 135.135135$			eq. D.40 Shear shell buckling checking
		$> 0.16(E/f_{yk})^{0.67} =$		11.517386	
Shell slenderness parameters of shear	$\bar{\lambda}_\tau$	$= \sqrt{(f_{yk}/\sqrt{3})/\tau_{x\theta,Rcr}}$			eq. 8.17
		$= 1.18038097$			
Shear squash limit slenderness	$\bar{\lambda}_{\tau 0}$	$= 0.4$			eq. D.39
Plastic range factor	β	$= 0.6$			eq. D.39
Interaction exponent	η	$= 1$			eq. D.39
Shear plastic limit relative slenderness	$\bar{\lambda}_{\tau p}$	$= \sqrt{\alpha_\tau/(1+\beta)}$			eq. 8.16
		$= 0.63737744$			
	$\bar{\lambda}_\tau$	$\in (\bar{\lambda}_p, +\infty)$			eq. 8.13-8.15
Buckling reduction factor	χ_τ	$= \frac{\alpha_\tau}{\bar{\lambda}_\tau^2}$			eq. 8.13-8.15
		$= 0.46651859$			
Buckling interaction parameter	k_τ	$= 1.75+0.25\chi_\tau$			eq. D.48
		$= 1.86662965$			
Shear characteristic buckling stress	$\tau_{x\theta,Rk}$	$= \chi_\tau f_{yk}/\sqrt{3}$			ch. 8.5.2
		$= 95.6173459$ MPa			
Partical factor	γ_{M1}	$= 1.1$			ch. 8.5.2
Shear design buckling resistance stress	$\tau_{x\theta,Rd}$	$= \tau_{x\theta,Rk}/\gamma_{M1}$			eq. 8.11
		$= 86.9248599$ MPa			
Design value of shear stress	$\tau_{x\theta,Ed}$	$= Q/(\pi rt)$			
		$= 2.40539038$ MPa			
		$< \tau_{x\theta,Rd} =$	86.9248599	MPa	OK
d) Combinations of meridional (axial) compression, circumferential (hoop) compression and shear					ch. D.1.6
Buckling interaction parameter	k_i	$= (\chi_x \chi_\theta)^2$			eq. D.49
		$= 0.00080094$			
Interaction check					eq. 8.19
		$\left(\frac{\sigma_{x,Ed}}{\sigma_{x,Rd}}\right)^{k_x} - k_i \left(\frac{\sigma_{x,Ed}}{\sigma_{x,Rd}}\right) \left(\frac{\sigma_{\theta,Ed}}{\sigma_{\theta,Rd}}\right) + \left(\frac{\sigma_{\theta,Ed}}{\sigma_{\theta,Rd}}\right)^{k_\theta} + \left(\frac{\tau_{x\theta,Ed}}{\tau_{x\theta,Rd}}\right)^{k_\tau}$			
		$= 0.95903095$			OK

4 Unstiffened cylindrical shell design for internal column (EN1993-1-6 (2007))

Designed by:		Date:			
Checked by:					Reference
Design load on the column					Based on EN 1993-1-6
Distance of ring frames	l	=	27 m		
Shell thickness	t	=	28 mm		
Shell Radius	r	=	3 m		
Yield strength	f_y	=	355 MPa		
Young's modulus	E	=	210000000 kN/m ²		
Poisson's ratio	ν	=	0.3		
Internal column					
Axial force	F	=	11180 kN		
Shear force	V	=	1005 kN		
Bending moment	M	=	8867 kNm		
a) Critical meridional (axial) buckling					
Length parameter	ω	=	$\frac{l}{r} \sqrt{\frac{r}{l}} = \frac{l}{\sqrt{rt}}$	0.5r/t	eq. D.1
		=	93.1588505	53.57143	long cylinder
Factor	C_x	=	0.73834692		eq. D.3-D.10
Elastic critical meridional buckling stress	$\sigma_{x,Rcr}$	=	$0.605EC_x t/r$		eq. D.2
		=	875.531778 MPa		
Characteristic imperfection amplitude	Δw_k	=	$\frac{1}{Q} \sqrt{\frac{r}{t}}$		eq. D.15
		=	0.0115931 m		
Meridional elastic imperfection reduction factor	α_x	=	$\frac{0.62}{1 + 1.91(\Delta w_k/t)^{1.44}}$		eq. D.14
		=	0.40351333		
	r/t	=	107.142857		eq. D.18 Meridional shell buckling checking
		>	$0.03E/f_{yk} =$	17.74648	
Meridional shell slenderness parameters	$\bar{\lambda}_x$	=	$\sqrt{f_{yk}/\sigma_{x,Rcr}}$		eq. 8.17
		=	0.63676359		
Meridional squash limit slenderness	$\bar{\lambda}_{x0}$	=	0.23458673		eq. D.16
Plastic range factor	β	=	0.6		eq. D.16
Interaction exponent	η	=	1		eq. D.16
Meridional plastic limit relative slenderness	$\bar{\lambda}_{xp}$	=	$\sqrt{\alpha_x/(1-\beta)}$		eq. 8.16
		=	1.00438206		
	$\bar{\lambda}_x$	\in	$(\bar{\lambda}_0, \bar{\lambda}_p)$		eq. 8.13-8.15
Buckling reduction factor	χ_x	=	$1 - \beta \left(\frac{\bar{\lambda} - \bar{\lambda}_0}{\bar{\lambda}_p - \bar{\lambda}_0} \right)^\eta$		eq. 8.13-8.15
		=	0.68653212		
Buckling interaction parameter	k_x	=	$1.25 + 0.75\chi_x$		eq. D.46
		=	1.76489909		
Meridional characteristic buckling stress	$\sigma_{x,Rk}$	=	$\chi_x f_{yk}$		ch. 8.5.2
		=	243.718901 MPa		
Partical factor	γ_{M1}	=	1.1		ch. 8.5.2
Meridional design buckling stress	$\sigma_{x,Rd}$	=	$\sigma_{x,Rk}/\gamma_{M1}$		eq. 8.11
		=	221.562637 MPa		
Design value of the meridional stress due to axial force	σ_{xEA}	=	$\frac{F}{2\pi r t}$		
		=	21.182765 MPa		
Design value of the	σ	=	$\frac{M}{I}$		

4 Unstiffened cylindrical shell design for internal column (EN1993-1-6 (2007))

Designed by:		Date:				
Checked by:						Reference
meridional stress due to bending	$\sigma_{x,E,M}$	$= \frac{\pi r^2 t}{\pi r^2 t}$				
		$= 11.2002133$	MPa			
Design value of meridional stress	$\sigma_{x,Ed}$	$= \sigma_{x,E,A} + \sigma_{x,E,M}$				
		$= 32.3829784$	MPa			
		$< \sigma_{x,Rd} =$	221.562637	MPa		OK
b) Critical circumferential (hoop) buckling						due to hoop compression
Length parameter	ω	$= \frac{l \sqrt{r}}{r \sqrt{l}} = \frac{l}{\sqrt{rt}}$				eq. D.1
		$= 93.1588505$				
Buckling factors	C_θ	$= 1$				
	ω/C_θ	$< 1.63r/t$	$=$	174.6429		medium cylinder
						eq. D.25
Elastic critical circumferential buckling stress	$\sigma_{\theta,Rcr}$	$= 0.92E \left(\frac{C_\theta}{\omega} \right) \left(\frac{t}{r} \right)$				
		$= 19.3561856$	MPa			
Circumferential elastic imperfection reduction factor	α_θ	$= 0.65$				Table D.5
	r/t	$= 107.142857$				eq. D.27 Circumferential shell buckling checking
		$> 0.21(E/f_{yk})^{0.5} =$		5.107575		eq. 8.17
Circumferential shell slenderness parameters	$\bar{\lambda}_\theta$	$= \sqrt{f_{yk}/\sigma_{\theta,Rcr}}$				
		$= 4.2825682$				
Circumferential squash limit slenderness	$\bar{\lambda}_{\theta 0}$	$= 0.4$				eq. D.26
Plastic range factor	β	$= 0.6$				eq. D.26
Interaction exponent	η	$= 1$				eq. D.26
Circumferential plastic limit relative slenderness	$\bar{\lambda}_{\theta p}$	$= \sqrt{\alpha_\theta/(1+\beta)}$				eq. 8.16
		$= 0.63737744$				
	$\bar{\lambda}_\theta$	$\in (\bar{\lambda}_p, +\infty)$				eq. 8.13-8.15
Buckling reduction factor	χ_θ	$= \frac{\alpha_\theta}{\bar{\lambda}_\theta^2}$				eq. 8.13-8.15
		$= 0.0354409$				
Buckling interaction parameter	k_θ	$= 1.25 + 0.75\chi_\theta$				eq. D.47
		$= 1.27658068$				
Circumferential characteristic buckling stress	$\sigma_{\theta,Rk}$	$= \chi_\theta f_{yk}$				ch. 8.5.2
		$= 12.5815206$	MPa			
Partical factor	γ_{M1}	$= 1.1$				ch. 8.5.2
Circumferential design buckling stress	$\sigma_{\theta,Rd}$	$= \sigma_{\theta,Rk}/\gamma_{M1}$				eq. 8.11
		$= 11.437746$	MPa			
External water pressure	q_{eq}	$= 166.6$	kPa			bottom of column
Internal water pressure	q_s	$= 70.56$	kPa			
Circumferential design stress	$\sigma_{\theta,Ed}$	$= (q_{eq} + q_s)(r/t)$				eq. D.30
		$= 10.29$	MPa			
		$< \sigma_{\theta,Rd} =$	11.437746	MPa		OK

4 Unstiffened cylindrical shell design for internal column (EN1993-1-6 (2007))

Designed by:		Date:				
Checked by:						Reference
c) Critical shear buckling						ch. D.1.4
Length parameter	ω	$= \frac{l}{r} \sqrt{\frac{r}{l}} = \frac{l}{\sqrt{rt}}$				eq. D.31
		$= 93.1588505$	$>$	10		eq. D.33
		$< 8.7r/t$	$=$	932.1429		medium-length cylinder
Factor	C_τ	$= 1$				eq. D.34
Elastic critical shear buckling stress	$\tau_{x\theta,Rcr}$	$= 0.75EC_\tau \sqrt{\frac{1}{\omega} \left(\frac{t}{r}\right)}$				eq. D.32
		$= 152.301883$ MPa				
Shear elastic imperfection reduction factor	α_τ	$= 0.65$				Table D.6
	r/t	$= 107.142857$				eq. D.40 Shear shell buckling checking
		$> 0.16(E/f_{yk})^{0.67} =$		11.51739		eq. 8.17
Shell slenderness parameters of shear	$\bar{\lambda}_\tau$	$= \sqrt{(f_{yk}/\sqrt{3})/\tau_{x\theta,Rcr}}$				
		$= 1.16006207$				
Shear squash limit slenderness	$\bar{\lambda}_{\tau 0}$	$= 0.4$				eq. D.39
Plastic range factor	β	$= 0.6$				eq. D.39
Interaction exponent	η	$= 1$				eq. D.39
Shear plastic limit relative slenderness	$\bar{\lambda}_{\tau p}$	$= \sqrt{\alpha_\tau/(1+\beta)}$				eq. 8.16
		$= 0.63737744$				
	$\bar{\lambda}_\tau$	$\in (\bar{\lambda}_p, +\infty)$				eq. 8.13-8.15
Buckling reduction factor	χ_τ	$= \frac{\alpha_\tau}{\bar{\lambda}_\tau^2}$				eq. 8.13-8.15
		$= 0.4830042$				
Buckling interaction parameter	k_τ	$= 1.75+0.25\chi_\tau$				eq. D.48
		$= 1.87075105$				
Shear characteristic buckling stress	$\tau_{x\theta,Rk}$	$= \chi_\tau f_{yk}/\sqrt{3}$				ch. 8.5.2
		$= 98.9962243$ MPa				
Partical factor	γ_{M1}	$= 1.1$				ch. 8.5.2
Shear design buckling resistance stress	$\tau_{x\theta,Rd}$	$= \tau_{x\theta,Rk}/\gamma_{M1}$				eq. 8.11
		$= 89.9965675$ MPa				
Design value of shear stress	$\tau_{x\theta,Ed}$	$= Q/(\pi rt)$				
		$= 3.80835042$ MPa				
		$< \tau_{x\theta,Rd} =$	89.9965675 MPa			OK
d) Combinations of meridional (axial) compression, circumferential (hoop) compression and shear						ch. D.1.6
Buckling interaction parameter	k_i	$= (\chi_x \chi_\theta)^2$				eq. D.49
		$= 0.00059201$				
Interaction check						eq. 8.19
		$\left(\frac{\sigma_{x,Ed}}{\sigma_{x,Rd}}\right)^{k_x} - k_i \left(\frac{\sigma_{x,Ed}}{\sigma_{x,Rd}}\right) \left(\frac{\sigma_{\theta,Ed}}{\sigma_{\theta,Rd}}\right) + \left(\frac{\sigma_{\theta,Ed}}{\sigma_{\theta,Rd}}\right)^{k_\theta} + \left(\frac{\tau_{x\theta,Ed}}{\tau_{x\theta,Rd}}\right)^{k_\tau}$				
		$= 0.90991154$				OK

5 Unstiffened cylindrical shell design for external column (EN1993-1-6 (2017))						
Designed by:			Date:			
Checked by:						Reference
Design load on the column						Based on BS EN 1993-1-6: 2007+A1: 2017
Distance of ring frames	l	=	27	m		
Shell thickness	t	=	37	mm		
Shell Radius	r	=	5	m		
Yield strength	f _y	=	355	MPa		
Young's modulus	E	=	210000000	kN/m ²		
Poisson's ratio	v	=	0.3			
External column						
Axial force	F	=	4354	kN		
Shear force	V	=	1398	kN		
Bending moment	M	=	13664	kNm		
a) Critical meridional (axial) buckling due to axial compression						
Length parameter	ω	=	$\frac{l}{r} \sqrt{\frac{r}{l}} = \frac{l}{r\sqrt{l}} = \frac{l}{\sqrt{rt}}$		0.5r/t=	eq. D.1
		=	62.7737249		67.56757	medium cylinder
Factor	C _x	=	1			eq. D.3-D.10
Elastic critical meridional buckling stress	σ _{x,Rcr}	=	0.605EC _x t/r			eq. D.2
		=	940.17	MPa		
Characteristic imperfection amplitude	Δw _k	=	$\frac{1}{Q} \sqrt{rt}$			eq. D.15
		=	0.01720465	m		
Geometrical reduction factor	α _{xG}	=	0.83			eq. D.14a
Imperfection reduction factor	α _{xl}	=	$\frac{1}{1 + 2.2(\Delta w_k/t)^{0.88}}$			eq. D.14b
		=	0.47137938			
Meridional elastic buckling reduction factor	α _x	=	α _{xG} α _{xl}			
		=	0.39124489			
Plastic range factor	β _x	=	$1 - \frac{0.95}{1 + 1.2\Delta w_k/t}$			eq. D.14c
		=	0.39023947			
Interaction exponent	η _x	=	$\frac{5.4}{1 + 4.6\Delta w_k/t}$			eq. D.14d
		=	1.7203169			
Hardening limit	χ _{xh}	=	1			eq. D.14d
Plastic limit relative slenderness	λ _p	=	$\sqrt{\frac{\alpha}{1 - \beta}}$			eq. 8.16
		=	0.80102244			
Squash limit relative slenderness	λ _{x0}	=	0.2			eq. D.16
Meridional shell slenderness parameters	λ _x	=	$\sqrt{f_{yk}/\sigma_{x,Rcr}}$			eq. 8.17
		=	0.61448457			
	λ _x	∈	[λ ₀ , λ _p]			
Elastic-plastic buckling reduction factor	χ _x	=	0.79407814			eq. 8.13-8.15
Buckling interaction parameter	k _x	=	1.25+0.75χ _x			eq. D.46
		=	1.8455586			
Characteristic stress	σ _{x,Rk}	=	χ _x f _{yk}			eq. 8.12
		=	281.897738			
Partial factor	γ _{M1}	=	1.1			ch. 8.5.2
Meridional design	σ _{x,Rd}	=	σ _{x,Rk} /γ _{M1}			eq. 8.11

5 Unstiffened cylindrical shell design for external column (EN1993-1-6 (2017))

Designed by:		Date:			
Checked by:					Reference
buckling stress		=	256.270671 MPa		
	r/t	=	135.135135		eq. D.18 Meridional shell
		>	0.03E/f _{yk} =	17.74648	buckling checking
Design value of the meridional stress due to axial force	σ _{xEA}	=	$\frac{F}{2\pi r t}$		
		=	3.74573309 MPa		
		<	σ _{x,Rd} =	256.270671 MPa	OK
b) Critical meridional (axial) buckling due to bending					
Plastic reference moment	M _{R,pl}	=	4r ² tf _{y,k}		eq. E.2
		=	1313500 kNm		
First dimensionless length	ω	=	$\frac{l}{r} \sqrt{\frac{r}{L}} = \frac{l}{r \sqrt{L}}$		eq. E.5
		=	$\frac{62.7737249}{\sqrt{rt}}$		
Factor	C _m	=	$1 + \frac{4}{\omega^2}$		eq. E.4
		=	1.00101509		
Elastic reference moment	M _{R,cr}	=	1.9C _m Ert ²		eq. E.3
		=	2734704.38 kNm		
	M _{Ed}	=	13664 kNm		
Reference plastic resistance	R _{pl}	=	$\frac{M_{R,pl}}{M_{Ed}}$		eq. E.13
		=	96.1285129		
Reference elastic critical resistance	R _{cr}	=	$\frac{M_{R,cr}}{M_{Ed}}$		eq. E.13
		=	200.139372		
Slenderness	λ̄	=	$\sqrt{\frac{R_{pl}}{R_{cr}}} = \sqrt{\frac{M_{R,pl}}{M_{R,cr}}}$		eq. E.14
		=	0.69304246		
Second dimensionless length	Ω	=	$\frac{L}{r} \sqrt{\frac{t}{r}} = \frac{t}{r} \omega$		eq. E.6
		=	0.46452556		
	ω	<	0.5 $\left(\frac{r}{t}\right)$	=	67.56757 Table E.1
		0.5 ≤ Ω < 7			
Geometrical reduction fact	α _G	=	0.95546731		Table E.1
	Δw _k	=	$\frac{1}{Q} \sqrt{rt}$		eq. E.8
		=	17.2046505 mm		
Imperfection reduction factor	α _I	=	$\frac{1}{1 + 2(\Delta w_k/t)^{0.8}}$		eq. E.7
		=	0.47987173		
Elastic buckling reduction f	α	=	α _G α _I		eq. E.9
		=	0.45850174		
Plastic range factor	β	=	$1 - \frac{0.6}{1 + 1.2(\Delta w_k/t)^{0.8}}$		eq. E.10
		=	0.63643726		
	η	=	0.65 + 0.2 $\left(\frac{\Delta w_k}{t}\right)$		eq. E.11
		=	0.74299811		

5 Unstiffened cylindrical shell design for external column (EN1993-1-6 (2017))						
Designed by:			Date:			
Checked by:						Reference
Hardening limit	χ_h	=	1			eq. E.11
Plastic limit relative slenderness	$\bar{\lambda}_p$	=	$\sqrt{\frac{\alpha}{1-\beta}}$			eq. 8.29
		=	1.12300273			
Squash limit relative	$\bar{\lambda}_0$	=	0.3			eq. E.12
Elastic-plastic buckling reduction factor	$\bar{\lambda}$	\in	$[\lambda_0, \lambda_p]$			eq. 8.26-8.28
		χ	=	0.63247949		eq. 8.26-8.28
Characteristic resistance	R_k	=	χR_{pl}			eq. 8.30
		=	60.7993125			
Design resistance	R_d	=	R_k/γ_{M1}			eq. 8.31
		=	55.2721022 >		1	OK
c) Critical circumferential (hoop) buckling						due to hoop compression
Length parameter	ω	=	$\frac{l}{r} \sqrt{\frac{r}{l}} = \frac{l}{\sqrt{rt}}$			eq. D.1
		=	62.7737249			
Buckling factors	C_θ	=	1			
		ω/C_θ	<	1.63r/t =	220.2703	medium cylinder
Elastic critical circumferential buckling stress	$\sigma_{\theta,Rcr}$	=	$0.92E \left(\frac{C_\theta}{\omega}\right) \left(\frac{t}{r}\right)$			eq. D.25
		=	22.7751341 MPa			
Circumferential elastic imperfection reduction factor	α_θ	=	0.65			Table D.5
		r/t	=	135.135135		
Circumferential shell slenderness parameters	$\bar{\lambda}_\theta$	>	$0.21(E/f_{yk})^{0.5} =$	5.107575		eq. D.27 Circumferential shell buckling checking
		=	$\sqrt{f_{yk}/\sigma_{\theta,Rcr}}$			eq. 8.17
Circumferential squash limit slenderness	$\bar{\lambda}_{\theta 0}$	=	0.4			eq. D.26
Plastic range factor	β	=	0.6			eq. D.26
Interaction exponent	η	=	1			eq. D.26
Circumferential plastic limit relative slenderness	$\bar{\lambda}_{\theta p}$	=	$\sqrt{\alpha_\theta/(1+\beta)}$			eq. 8.16
		=	0.63737744			
Buckling reduction factor	χ_θ	\in	$(\bar{\lambda}_p, +\infty)$			eq. 8.13-8.15
		=	$\frac{\alpha_\theta}{\bar{\lambda}_\theta^2}$			eq. 8.13-8.15
		=	0.04170095			
Buckling interaction parameter	k_θ	=	$1.25+0.75\chi_\theta$			eq. D.47
Circumferential characteristic buckling stress	$\sigma_{\theta,Rk}$	=	1.28127571			
		=	$\chi_\theta f_{yk}$			ch. 8.5.2
Partical factor	γ_{M1}	=	1.1			ch. 8.5.2
Circumferential design buckling stress	$\sigma_{\theta,Rd}$	=	$\sigma_{\theta,Rk}/\gamma_{M1}$			eq. 8.11
		=	13.4580338 MPa			
External water pressure	q_{eq}	=	166.6 kPa			bottom of column

5 Unstiffened cylindrical shell design for external column (EN1993-1-6 (2017))

Designed by:		Date:			
Checked by:					Reference
Internal water pressure	q_s	=	70.56	kPa	
Circumferential design stress	$\sigma_{\theta,Ed}$	=	$(q_{eq}+q_s)/(r/t)$		eq. D.30
		=	12.9783784	MPa	
		<	$\sigma_{\theta,Rd}$	13.4580338	MPa
					OK
d) Critical shear buckling					ch. D.1.4
Length parameter	ω	=	$\frac{l}{r} \sqrt{\frac{r}{L}} = \frac{l}{r \sqrt{L}}$		eq. D.31
		=	$\frac{62.7737249}{\sqrt{1175.676}}$	>	10
		<	$8.7r/t$	=	1175.676
Factor	C_τ	=	1		eq. D.34
Elastic critical shear buckling stress	$\tau_{x\theta,Rcr}$	=	$0.75EC_\tau \sqrt{\frac{1}{\omega} \left(\frac{t}{r}\right)}$		eq. D.32
		=	147.103609	MPa	
Shear elastic imperfection reduction factor		α_τ	=	0.65	Table D.6
		r/t	=	135.135135	
		>	$0.16(E/f_{yk})^{0.67}$	11.51739	eq. D.40 Shear shell buckling checking
Shell slenderness parameters of shear	$\bar{\lambda}_\tau$	=	$\sqrt{(f_{yk}/\sqrt{3})/\tau_{x\theta,Rcr}}$		eq. 8.17
		=	1.18038097		
Shear squash limit slenderness	$\bar{\lambda}_{\tau 0}$	=	0.4		eq. D.39
Plastic range factor	β	=	0.6		eq. D.39
Interaction exponent	η	=	1		eq. D.39
Shear plastic limit relative slenderness	$\bar{\lambda}_{\tau p}$	=	$\sqrt{\alpha_\tau/(1+\beta)}$		eq. 8.16
		=	0.63737744		
	$\bar{\lambda}_\tau$	\in	$(\bar{\lambda}_p, +\infty)$		eq. 8.13-8.15
Buckling reduction factor	χ_τ	=	$\frac{\alpha_\tau}{\bar{\lambda}_\tau^2}$		eq. 8.13-8.15
		=	0.46651859		
Buckling interaction parameter	k_τ	=	$1.75+0.25\chi_\tau$		eq. D.48
		=	1.86662965		
Shear characteristic buckling stress	$\tau_{x\theta,Rk}$	=	$\chi_\tau f_{yk}/\sqrt{3}$		ch. 8.5.2
		=	95.6173459	MPa	
Partical factor	γ_{M1}	=	1.1		ch. 8.5.2
Shear design buckling resistance stress	$\tau_{x\theta,Rd}$	=	$\tau_{x\theta,Rk}/\gamma_{M1}$		eq. 8.11
		=	86.9248599	MPa	
Design value of shear stress	$\tau_{x\theta,Ed}$	=	$Q/(\pi r t)$		
		=	2.40539038	MPa	
		<	$\tau_{x\theta,Rd}$	86.9248599	MPa
e) Combinations of meridional (axial) compression, circumferential (hoop) compression and shear					ch. D.1.6
Buckling interaction parameter	k_i	=	$(\chi_x \chi_\theta)^2$		eq. D.49
		=	0.00109652		
Interaction check					eq. 8.19
					$\left(\frac{\sigma_{x,Ed}}{\sigma_{x,Rd}}\right)^{k_x} - k_i \left(\frac{\sigma_{x,Ed}}{\sigma_{x,Rd}}\right) \left(\frac{\sigma_{\theta,Ed}}{\sigma_{\theta,Rd}}\right) + \left(\frac{\sigma_{\theta,Ed}}{\sigma_{\theta,Rd}}\right)^{k_\theta} + \left(\frac{\tau_{x\theta,Ed}}{\tau_{x\theta,Rd}}\right)^{k_\tau}$

5 Unstiffened cylindrical shell design for external column (EN1993-1-6 (2017))

Designed by:			Date:				
Checked by:							Reference
	$\sqrt{\sigma_{x,Rd}}$	$\sqrt{\sigma_{x,Rd}}$	$\sqrt{\sigma_{\theta,Rd}}$	$\sqrt{\sigma_{\theta,Rd}}$	$\sqrt{\tau_{x\theta,Rd}}$		
			=	0.9575805			OK

6 Unstiffened cylindrical shell design for internal column (EN1993-1-6 (2017))

Designed by:		Date:			
Checked by:					Reference
Design load on the column					Based on BS EN 1993-1-6: 2007+A1: 2017
Distance of ring frames	l	=	27 m		
Shell thickness	t	=	28 mm		
Shell Radius	r	=	3 m		
Yield strength	f_y	=	355 MPa		
Young's modulus	E	=	210000000 kN/m ²		
Poisson's ratio	ν	=	0.3		
Internal column					
Axial force	F	=	11180 kN		
Shear force	V	=	1005 kN		
Bending moment	M	=	8867 kNm		
a) Critical meridional (axial) buckling due to axial compression					
Length parameter	ω	=	$\frac{l}{r} \sqrt{\frac{r}{l}} = \frac{l}{r\sqrt{l}} = \frac{l}{\sqrt{rt}}$	0.5r/t=	eq. D.1
		=	93.1588505	53.57143	long cylinder
Factor	C_x	=	0.73834692		eq. D.3-D.10
Elastic critical meridional buckling stress	$\sigma_{x,Rcr}$	=	$0.605EC_x t/r$		eq. D.2
		=	875.531778 MPa		
Characteristic imperfection amplitude	Δw_k	=	$\frac{1}{Q} \sqrt{rt}$		eq. D.15
		=	0.0115931 m		
Geometrical reduction factor	α_{xG}	=	0.83		eq. D.14a
Imperfection reduction factor	α_{xl}	=	$\frac{1}{1 + 2.2(\Delta w_k/t)^{0.88}}$		eq. D.14b
		=	0.49688045		
Meridional elastic buckling reduction factor	α_x	=	$\alpha_{xG} \alpha_{xl}$		
		=	0.41241077		
Plastic range factor	β_x	=	$1 - \frac{0.95}{1 + 1.2\Delta w_k/t}$		eq. D.14c
		=	0.36533268		
Interaction exponent	η_x	=	$\frac{5.4}{1 + 4.6\Delta w_k/t}$		eq. D.14d
		=	1.85913221		
Hardening limit	χ_{xh}	=	1		eq. D.14d
Plastic limit relative slenderness	$\bar{\lambda}_p$	=	$\sqrt{\frac{\alpha}{1 - \beta}}$		eq. 8.16
		=	0.80610559		
Squash limit relative slenderness	$\bar{\lambda}_{x0}$	=	0.2		eq. D.16
Meridional shell slenderness parameters	$\bar{\lambda}_x$	=	$\sqrt{f_{yk}/\sigma_{x,Rcr}}$		eq. 8.17
		=	0.63676359		
	$\bar{\lambda}_x$	∈	$[\lambda_0, \lambda_p]$		
Elastic-plastic buckling reduction factor	χ_x	=	0.8013308		eq. 8.13-8.15
Buckling interaction parameter	k_x	=	$1.25 + 0.75\chi_x$		eq. D.46
		=	1.8509981		
Characteristic stress	$\sigma_{x,Rk}$	=	$\chi_x f_{yk}$		eq. 8.12
		=	284.472434		
Partial factor	γ_{M1}	=	1.1		ch. 8.5.2
Meridional design	$\sigma_{x,Rd}$	=	$\sigma_{x,Rk}/\gamma_{M1}$		eq. 8.11

6 Unstiffened cylindrical shell design for internal column (EN1993-1-6 (2017))

Designed by:		Date:			
Checked by:					Reference
buckling stress		=	258.611304 MPa		
	r/t	=	107.142857		eq. D.18 Meridional shell buckling checking
		>	0.03E/f _{yk} =	17.74648	
Design value of the meridional stress due to axial force	σ _{xEA}	=	$\frac{F}{2\pi r t}$		
		=	21.182765 MPa		
		<	σ _{x,Rd} =	258.611304 MPa	OK
b) Critical meridional (axial) buckling due to bending					
Plastic reference moment	M _{R,pl}	=	4r ² t f _{y,k}		eq. E.2
		=	357840 kNm		
First dimensionless length	ω	=	$\frac{l}{r} \sqrt{\frac{r}{l}} = \frac{l}{r \sqrt{l}} = \frac{l}{\sqrt{r t}}$		eq. E.5
		=	93.1588505		
Factor	C _m	=	$1 + \frac{4}{\omega^2}$		eq. E.4
		=	1.00046091		
Elastic reference moment	M _{R,cr}	=	1.9 C _m E r t ²		eq. E.3
		=	939147.375 kNm		
	M _{Ed}	=	8867 kNm		
Reference plastic resistance	R _{pl}	=	$\frac{M_{R,pl}}{M_{Ed}}$		eq. E.13
		=	40.3563776		
Reference elastic critical resistance	R _{cr}	=	$\frac{M_{R,cr}}{M_{Ed}}$		eq. E.13
		=	105.914895		
Slenderness	λ̄	=	$\sqrt{\frac{R_{pl}}{R_{cr}}} = \sqrt{\frac{M_{R,pl}}{M_{R,cr}}}$		eq. E.14
		=	0.61727341		
Second dimensionless length	Ω	=	$\frac{L}{r} \sqrt{\frac{t}{r}} = \frac{t}{r} \omega$		eq. E.6
		=	0.8694826		
	ω	>	0.5 $\left(\frac{r}{t}\right)$	=	53.57143 Table E.1
			0.5 ≤ Ω < 7		
Geometrical reduction factor	α _G	=	0.84164152		Table E.1
	Δw _k	=	$\frac{1}{Q} \sqrt{r t}$		eq. E.8
		=	11.5931014 mm		
Imperfection reduction factor	α _I	=	$\frac{1}{1 + 2(\Delta w_k/t)^{0.8}}$		eq. E.7
		=	0.50307203		
Elastic buckling reduction factor	α	=	α _G α _I		eq. E.9
		=	0.42340631		
Plastic range factor	β	=	$1 - \frac{0.6}{1 + 1.2(\Delta w_k/t)^{0.8}}$		eq. E.10
		=	0.62327464		
	η	=	0.65 + 0.2 $\left(\frac{\Delta w_k}{t}\right)$		eq. E.11
		=	0.73280787		

6 Unstiffened cylindrical shell design for internal column (EN1993-1-6 (2017))						
Designed by:			Date:			
Checked by:						Reference
Hardening limit	χ_h	=	1			eq. E.11
Plastic limit relative slenderness	$\bar{\lambda}_p$	=	$\sqrt{\frac{\alpha}{1-\beta}}$			eq. 8.29
		=	1.06014734			
Squash limit relative	$\bar{\lambda}_0$	=	0.3			eq. E.12
Elastic-plastic buckling reduction factor	$\bar{\lambda}$	\in	$[\lambda_0, \lambda_p]$			eq. 8.26-8.28
		χ	=	0.6714472		eq. 8.26-8.28
Characteristic resistance	R_k	=	χR_{pl}			eq. 8.30
		=	27.0971768			
Design resistance	R_d	=	R_k/γ_{M1}			eq. 8.31
		=	24.6337971 >		1	OK
c) Critical circumferential (hoop) buckling						due to hoop compression
Length parameter	ω	=	$\frac{l}{r} \sqrt{\frac{r}{l}} = \frac{l}{\sqrt{rt}}$			eq. D.1
		=	93.1588505			
Buckling factors	C_θ	=	1			
		ω/C_θ	<	1.63r/t =	174.6429	medium cylinder
Elastic critical circumferential buckling stress	$\sigma_{\theta,Rcr}$	=	$0.92E \left(\frac{C_\theta}{\omega}\right) \left(\frac{t}{r}\right)$			eq. D.25
		=	19.3561856 MPa			
Circumferential elastic imperfection reduction factor	α_0	=	0.65			Table D.5
		r/t	=	107.142857		
Circumferential shell slenderness parameters	$\bar{\lambda}_\theta$	>	$0.21(E/f_{yk})^{0.5} =$	5.107575		eq. D.27 Circumferential shell buckling checking
		=	$\sqrt{f_{yk}/\sigma_{\theta,Rcr}}$			eq. 8.17
Circumferential squash limit slenderness	$\bar{\lambda}_{\theta 0}$	=	0.4			eq. D.26
Plastic range factor	β	=	0.6			eq. D.26
Interaction exponent	η	=	1			eq. D.26
Circumferential plastic limit relative slenderness	$\bar{\lambda}_{\theta p}$	=	$\sqrt{\alpha_\theta/(1+\beta)}$			eq. 8.16
		=	0.63737744			
Buckling reduction factor	χ_θ	\in	$(\bar{\lambda}_p, +\infty)$			eq. 8.13-8.15
		=	$\frac{\alpha_\theta}{\bar{\lambda}_\theta^2}$			eq. 8.13-8.15
		=	0.0354409			
Buckling interaction parameter	k_θ	=	$1.25+0.75\chi_\theta$			eq. D.47
		=	1.27658068			
Circumferential characteristic buckling stress	$\sigma_{\theta,Rk}$	=	$\chi_\theta f_{yk}$			ch. 8.5.2
		=	12.5815206 MPa			
Partical factor	γ_{M1}	=	1.1			ch. 8.5.2
Circumferential design buckling stress	$\sigma_{\theta,Rd}$	=	$\sigma_{\theta,Rk}/\gamma_{M1}$			eq. 8.11
		=	11.437746 MPa			
External water pressure	q_{eq}	=	166.6 kPa			bottom of column

6 Unstiffened cylindrical shell design for internal column (EN1993-1-6 (2017))

Designed by:		Date:				
Checked by:					Reference	
Internal water pressure	q_s	=	70.56 kPa			
Circumferential design stress	$\sigma_{\theta,Ed}$	=	$(q_{eq}+q_s)(r/t)$		eq. D.30	
		=	10.29 MPa			
		<	$\sigma_{\theta,Rd}$ =	11.437746 MPa	OK	
d) Critical shear buckling						
Length parameter	ω	=	$\frac{l}{r} \sqrt{\frac{r}{t}} = \frac{l}{r \sqrt{t}}$		ch. D.1.4 eq. D.31	
		=	93.1588505	>	10	eq. D.33
		<	8.7r/t	=	932.1429	medium cylinder
Factor	C_τ	=	1		eq. D.34	
Elastic critical shear buckling stress	$\tau_{x\theta,Rcr}$	=	$0.75 E C_\tau \sqrt{\frac{1}{\omega} \left(\frac{t}{r}\right)}$		eq. D.32	
		=	152.301883 MPa			
Shear elastic imperfection reduction factor	α_τ	=	0.65		Table D.6	
		r/t	=	107.142857		
Shell slenderness parameters of shear	$\bar{\lambda}_\tau$	>	$0.16(E/f_{yk})^{0.67} =$	11.51739	eq. D.40 Shear shell buckling checking	
		=	$\sqrt{(f_{yk}/\sqrt{3})/\tau_{x\theta,Rcr}}$		eq. 8.17	
Shear squash limit slenderness	$\bar{\lambda}_{\tau 0}$	=	0.4		eq. D.39	
Plastic range factor	β	=	0.6		eq. D.39	
Interaction exponent	η	=	1		eq. D.39	
Shear plastic limit relative slenderness	$\bar{\lambda}_{\tau p}$	=	$\sqrt{\alpha_\tau/(1+\beta)}$		eq. 8.16	
		=	0.63737744			
Buckling reduction factor	χ_τ	$\bar{\lambda}_\tau \in$	$(\bar{\lambda}_p, +\infty)$		eq. 8.13-8.15	
		=	$\frac{\alpha_\tau}{\bar{\lambda}_\tau^2}$		eq. 8.13-8.15	
		=	0.4830042			
Buckling interaction parameter	k_τ	=	1.75+0.25 χ_τ		eq. D.48	
Shear characteristic buckling stress	$\tau_{x\theta,Rk}$	=	$\chi_\tau f_{yk}/\sqrt{3}$		ch. 8.5.2	
		=	98.9962243 MPa			
Partical factor	γ_{M1}	=	1.1		ch. 8.5.2	
Shear design buckling resistance stress	$\tau_{x\theta,Rd}$	=	$\tau_{x\theta,Rk}/\gamma_{M1}$		eq. 8.11	
		=	89.9965675 MPa			
Design value of shear stress	$\tau_{x\theta,Ed}$	=	$Q/(\pi r t)$			
		=	3.80835042 MPa			
		<	$\tau_{x\theta,Rd}$ =	89.9965675 MPa	OK	
e) Combinations of meridional (axial) compression, circumferential (hoop) compression and shear						
Buckling interaction parameter	k_i	=	$(\chi_x \chi_\theta)^2$		ch. D.1.6	
		=	0.00080655		eq. D.49	
Interaction check					eq. 8.19	
					$\left(\frac{\sigma_{x,Ed}}{\sigma_{x,Rd}}\right)^{k_x} - k_i \left(\frac{\sigma_{x,Ed}}{\sigma_{x,Rd}}\right) \left(\frac{\sigma_{\theta,Ed}}{\sigma_{\theta,Rd}}\right) + \left(\frac{\sigma_{\theta,Ed}}{\sigma_{\theta,Rd}}\right)^{k_\theta} + \left(\frac{\tau_{x\theta,Ed}}{\tau_{x\theta,Rd}}\right)^{k_\tau}$	

6 Unstiffened cylindrical shell design for internal column (EN1993-1-6 (2017))

Designed by:			Date:				
Checked by:							Reference
	$\sqrt{\sigma_{x,Rd}}$	$\sqrt{\sigma_{x,Rd}}$	$\sqrt{\sigma_{\theta,Rd}}$	$\sqrt{\sigma_{\theta,Rd}}$	$\sqrt{\tau_{x\theta,Rd}}$		
			=	0.89684699			OK

7 Stiffened cylindrical shell design for external column (DNVGL) case1						
Designed by:			Date:			
Checked by:						Reference
Design Information						Based on DNVGL-RP-C202
Distance of ring frames	l	=	2.09776023	m		
Distance between eff. supports of the cylinder	L	=	27	m		
Shell thickness	t	=	2.85545301	mm		
Stringer web width	h _s	=	18.8145057	mm		
Stringer web thickness	t _{ws}	=	0.57301181	mm		
Stringer flange width	b _s	=	9.63928598	mm		
Stringer flange thickness	t _{fs}	=	0.60939441	mm		
Spacing of stringer	s	=	42.0678197	mm		
Equivalent thickness	t _e	=	t+A/s			eq. 2.2.4
		=	3.25136278	mm		
Ring web width	h _r	=	399.80321	mm		
Ring web thickness	t _{wr}	=	12.1763476	mm		
Ring flange width	b _r	=	12.1763476	mm		
Ring flange thickness	t _{fr}	=	0	mm		
Shell Radius	r	=	5	m		
Yield strength	f _y	=	355	MPa		
Young's modulus	E	=	210000000	kN/m ²		
Poisson's ratio	v	=	0.3			
Load comb. Case: 1.0G + 1.0Q+ 1.35E						
Axial force	F	=	4354	kN		
Shear force	V	=	1398	kN		
Bending moment	M	=	13664	kNm		
a) Shell buckling						
Stress due to axial force	σ _{a,Sd}	=	N _{Sd} /(2πrt)			eq. 2.2.2
		=	42.6258569	MPa		
Stress due to bending	σ _{m,Sd}	=	M _{1,Sd} sinθ/(πr ² t)-M _{2,Sd} conθ/(πr ² t)			eq. 2.2.3
		=	53.5084711	MPa		
Design longitudinal membrane stress	σ _{x,Sd}	=	σ _{a,Sd} +σ _{m,Sd}			eq. 2.2.1
		=	96.134328	MPa		
water level difference	h	=	9.8	m		
Design lateral pressure	p _{Sd}	=	0.09604	MPa		
Circumferential membrane stress	σ _{h,Sd}	=	p _{Sd} r/t			eq. 2.2.8
		=	168.169463	MPa		
Membrane shear stress	τ _{Sd}	=	τ _{T,Sd} +τ _{Q,Sd}			eq. 2.2.5
		=	T _{Sd} /(2πr ² t)+[-Q _{1,Sd} sinθ/(πrt)+			eq. 2.2.6-7
		=	Q _{2,Sd} conθ/(πrt)]			
		=	31.1682399	MPa		
von Mises' stress	σ _{i,Sd}	=	$\sqrt{(\sigma_{a,sd} + \sigma_{m,sd})^2 - (\sigma_{a,sd} + \sigma_{m,sd})\sigma_{h,sd} + \sigma_{h,sd}^2 + 3\tau_{sd}^2}$			
	σ _{j,Sd}	=	160.760512	MPa	for panel	eq. 3.2.3
Curvature parameter	Z _s	=	s ² √(1-v ²)/(rt)			eq. 3.3.3
		=	0.11824307			
Reduced buckling coefficient	C	=	ψ√(1+(ρξ/ψ) ²)			eq. 3.3.2
	C _a	=	4.00001699		axial	Table 3-1
	C _τ	=	5.34893644		shear	Table 3-1
	C _h	=	1.00295363		hydrostatic pressure	Table 3-1
Elastic buckling strength for	f _E	=	C $\frac{\pi^2 E}{12(1-v^2)}$ $\left(\frac{t}{s}\right)^2$			eq. 3.3.1

7 Stiffened cylindrical shell design for external column (DNVGL) case1							
Designed by:			Date:				
Checked by:							Reference
axial force & bending moment	f_{Ea}	=	3497.90705 MPa				
	$f_{E\tau}$	=	4677.50076 MPa				
	f_{Eh}	=	877.055919 MPa				
reduced shell slenderness	$\bar{\lambda}_s^{-2}$	=	$\frac{f_y}{\sigma_{j,sd}} \left[\frac{\sigma_{a0,sd}}{f_{Ea}} + \frac{\sigma_{m0,sd}}{f_{Em}} + \frac{\sigma_{h0,sd}}{f_{Eh}} + \frac{\tau_{sd}}{f_{E\tau}} \right]$				eq. 3.2.2
		=	0.4650421				
Characteristic buckling strength of a shell	f_{ks}	=	$f_y / \sqrt{1 + \bar{\lambda}_s^4}$				
		=	321.895125 MPa				
Design buckling strength of a shell	f_{ksd}	=	f_{ks} / γ_M				eq. 3.1.2
		=	279.908805 MPa				
	$\sigma_{j,sd}$	=	160.760512 <	f_{ksd}			eq. 3.1.1 OK
b) Panel Stiffener Buckling							
Curvature parameter	Z_l	=	$l^2 \sqrt{1 - \nu^2} / (rt)$				eq. 3.6.5
		=	258.22421				
Effective shell width	S_e	=	$f_{ks} \sigma_{x,sd} s / (\sigma_{j,sd} f_y)$				eq. 3.6.7
		=	0.02281052 m				
Moment of inertia	I_{sef}	=	3.7865E-07 m ⁴				
Coefficient	α_c	=	$12(1 - \nu^2) I_{sef} / (st^3)$				eq. 3.6.6
		=	2859.6359				
Reduced buckling coefficient	C	=	$\psi \sqrt{1 + (\rho \xi / \psi)^2}$				eq. 3.6.4
	C_a	=	2337.79666		axial		Table 3-3
	C_τ	=	4748.69606		shear		Table 3-3
	C_h	=	109.430202		hydrostatic pressure		Table 3-3
Elastic buckling strength for axial force & bending moment	f_E	=	$C \frac{\pi^2 E}{12(1 - \nu^2)} \left(\frac{t}{l} \right)^2$				eq. 3.6.3
	f_{Ea}	=	1065.91432 MPa				
	$f_{E\tau}$	=	2165.15972 MPa				
	f_{Eh}	=	49.8945107 MPa				
reduced shell slenderness	$\bar{\lambda}_s^{-2}$	=	$\frac{f_y}{\sigma_{j,sd}} \left[\frac{\sigma_{a0,sd}}{f_{Ea}} + \frac{\sigma_{m0,sd}}{f_{Em}} + \frac{\sigma_{h0,sd}}{f_{Eh}} + \frac{\tau_{sd}}{f_{E\tau}} \right]$				eq. 3.2.2
		=	1.63928255				
Characteristic buckling strength of a shell	f_{ks}	=	$f_y / \sqrt{1 + \bar{\lambda}_s^4}$				
		=	184.874589 MPa				
Design buckling strength of a shell	f_{ksd}	=	f_{ks} / γ_M				eq. 3.1.2
		=	160.760512 MPa				
	$\sigma_{j,sd}$	=	160.760512 >	f_{ksd}			eq. 3.1.1 OK
Geometric proportions requirement (web)	h_s	=	18.8145057 mm				
		<	$1.35 t_w \sqrt{\frac{E}{f_y}} =$	19 mm			eq. 3.10.7 OK
Geometric proportions requirement (flange)	b_f	=	4.53313709 mm				
		<	$0.4 t_f \sqrt{\frac{E}{f_y}} =$	6 mm			eq. 3.10.8 OK
c) Panel Ring Buckling							
Cross sectional area	A_R	=	0.00486814 m ²				
Required cross sectional area		\geq	$A_{Req} = (2/Z_l^2 + 0.06) l t$				eq. 3.5.1
		=	0.00035958 m ²				

7 Stiffened cylindrical shell design for external column (DNVGL) case1							
Designed by:				Date:			
Checked by:						Reference	
Effective width of shell	l_{ef}	=	$\frac{1.56\sqrt{rt}}{1 + \frac{12t}{r}}$	or l (smaller one)	eq. 3.5.3		
		=	$\frac{0.18513179}{0.18513179} m$				
Equivalent length	l_{eo}	=	$\frac{1.56\sqrt{rt}}{0.18640052}$	or l (smaller one)	eq. 3.5.3		
		=	$0.18640052 m$				
	r_0	=	$4.99813959 m$				
	α_A	=	$A/(st)$		eq. 3.5.6		
		=	0.13865043				
Moment of inertia subjected to axial compression and bending	I_x	=	$\frac{ \sigma_{x,sd} t(1 + \alpha_A)r_0^4}{500El}$		eq. 3.5.5		
		=	$8.8559E-07 m^4$				
Moment of inertia subjected to shear	I_{xh}	=	$\left(\frac{\tau_{sd}}{E}\right)^{8/5} \left(\frac{r_0}{L}\right)^{1/5} Lr_0tl$		eq. 3.5.7		
		=	$1.0851E-16 m^4$				
Initial out-of-roundness parameter	δ_0	=	$0.005r$		eq. 3.5.13		
		=	0.025				
Moment of inertia subjected to external lateral pressure	I_h	=	$\frac{ p_{sd} rr_0^2l}{3E} \left[1.5 + \frac{3EZ_t\delta_0}{r_0^2 \left(\frac{f_r}{2} - \sigma_{hR,sd} \right)} \right]$		eq. 3.5.8		
		=	$6.4938E-05 m^4$				
Effective moment of inertia	I_R	=	$6.5823E-05 m^4$				
		<	$I_x + I_{xh} + I_h$		OK		
Geometric proportions requirement (web)	h_r	=	$399.80321 mm$				
		<	$1.35t_w \sqrt{\frac{E}{f_y}} = 400 mm$		eq. 3.10.7 OK		
Geometric proportions requirement (flange)	b_f	=	$0 mm$				
		<	$0.4t_f \sqrt{\frac{E}{f_y}} = 0 mm$		eq. 3.10.8 OK		
d) Column Buckling							
I of the complete section	I_c	=	$1.27556231 m^4$				
Area of complete section	A_c	=	$0.10211136 m^2$				
Radius of gyration	i_c	=	$3.53438456 m$				
			$\left(\frac{kL_c}{i_c}\right)^2 = 58.3579362$		eq. 3.8.1		
			$< 2.5E/f_y$		No buckling strength design requirement		
			$= 1478.87324$				
The stability requirement for a shell-column							
Stress due to axial force	$\sigma_{a,Sd}$	=	$N_{sd}/(2\pi rt)$		eq. 2.2.2		
		=	$48.53595 MPa$				
Stress due to bending	$\sigma_{m,Sd}$	=	$M_{1,Sd}\sin\theta/(\pi r^2 t) - M_{2,Sd}\cos\theta/(\pi r^2 t)$		eq. 2.2.3		
		=	$60.9274434 MPa$				
Reduced column slenderness	$\bar{\lambda}$	=	$\sqrt{\frac{f_{ak}}{f_E} = \frac{kL_c}{\pi i_c} \sqrt{\frac{f_{ak}}{E}}}$		eq. 3.8.7		
		=	0.08877664				
Characteristic column buckling strength	f_{kc}	=	$[1.0 - 0.28\bar{\lambda}^2]f_{ak}$		eq. 3.8.5		
		=	$279.291113 MPa$				

7 Stiffened cylindrical shell design for external column (DNVGL) case1							
Designed by:				Date:			
Checked by:							Reference
Design column buckling strength	f_{kcd}	=	f_{kc}/γ_M				eq. 3.8.6
		=	192.61456 MPa				
Euler buckling strength	f_{E1}	=	$\frac{\pi^2 EI_{c,1}}{(k_1 L_1)^2 A_c}$				eq. 3.8.3
		=	35515.5966 MPa				
Curvature parameter	Z_l	=	$l^2 \sqrt{1 - \nu^2} / (rt)$				eq. 3.4.3
		=	294.027107				
Reduced buckling coefficient	C	=	$\psi \sqrt{1 + (\rho \xi / \psi)^2}$				eq. 3.4.2
	C_a	=	29.0070268		axial		Table 3-2
Elastic buckling strength for axial force	f_E	=	$C \frac{\pi^2 E}{12(1 - \nu^2)} \left(\frac{t}{l}\right)^2$				eq. 3.4.1
	f_{Ea}	=	10.2008875 MPa				
Elastic buckling strength for lateral pressure	l/r	=	0.41955205				
		>	$2.25(r/t)^{0.5}$		0.0941521		
	f_{Eh}	=	$0.25E(t/r)^2$				eq. 3.4.5
		=	0.01712258 MPa				
Design local buckling strength	f_{akd}	=	f_{ak}/γ_M				
		=	160.760512 MPa				
	$\frac{\sigma_{a0,Sd}}{f_{kcd}} + \frac{1}{f_{akd}} \frac{\sigma_{m1,Sd}}{1 - \frac{\sigma_{a0,Sd}}{f_{E1}}}$	=	0.63143534	<	1	eq. 3.8.2	OK
e) The Cost of Steel Structure							
Volume of column	V_c	=	2.42208095 m ³				
Volume of stringer	V_s	=	0.33582255 m ³				
Volume of ring	V_r	=	1.96843511 m ³				
Total volume	V	=	4.72633862 m ³				
Density of steel	ρ	=	7850 kg/m ³				
Total mass	m_s	=	37101.7581 kg				
Cost of steel	C_s	=	37101.7581 €			1 €/kg	
f) The Cost of Filler material							
Length of welding	L_s	=	80653.5754 m			for stringer	
	L_r	=	808.700636 m			for ring	
	L	=	$L_s + L_r$				
		=	81462.276 m				
leg length of weld	a	=	2 mm				
Mass of weld	m_w	=	$A * L * \rho$				
		=	1278.95773 kg				
Cost of Filler material	C_w	=	2557.91547 €			2 €/kg	
g) The Cost of Labour welding							
	T	=	13577.046 h				
Cost of labour welding	C_l	=	271540.92 €				
h) Total Cost							
	C	=	311200.594 €				

7 Stiffened cylindrical shell design for external column (DNVGL) case2						
Designed by:			Date:			
Checked by:						Reference
Design Information						Based on DNVGL-RP-C202
Distance of ring frames	l	=	1.42	m		
Distance between eff. supports of the cylinder	L	=	27	m		
Shell thickness	t	=	11	mm		
Stringer web width	h _s	=	0	mm		
Stringer web thickness	t _{ws}	=	0	mm		
Stringer flange width	b _s	=	0	mm		
Stringer flange thickness	t _{fs}	=	0	mm		
Spacing of stringer	s	=	2.3113E+10	mm		
Equivalent thickness	t _e	=	t+A/s			eq. 2.2.4
		=	11	mm		
Ring web width	h _r	=	360	mm		
Ring web thickness	t _{wr}	=	11	mm		
Ring flange width	b _r	=	11	mm		
Ring flange thickness	t _{fr}	=	0	mm		
Shell Radius	r	=	5	m		
Yield strength	f _y	=	355	MPa		
Young's modulus	E	=	210000000	kN/m ²		
Poisson's ratio	ν	=	0.3			
Load comb. Case: 1.0G + 1.0Q + 1.35E						
Axial force	F	=	4354	kN		
Shear force	V	=	1398	kN		
Bending moment	M	=	13664	kNm		
a) Shell buckling						
Stress due to axial force	σ _{a,Sd}	=	N _{Sd} /(2πrt)			eq. 2.2.2
		=	12.599284	MPa		
Stress due to bending	σ _{m,Sd}	=	M _{1,Sd} sinθ/(πr ² t)-M _{2,Sd} conθ/(πr ² t)			eq. 2.2.3
		=	15.8159501	MPa		
Design longitudinal membrane stress	σ _{x,Sd}	=	σ _{a,Sd} +σ _{m,Sd}			eq. 2.2.1
		=	28.4152342	MPa		
water level difference	h	=	9.8	m		
Design lateral pressure	p _{Sd}	=	0.09604	MPa		
Circumferential membrane stress	σ _{h,Sd}	=	p _{Sd} r/t			eq. 2.2.8
		=	43.6545455	MPa		
Membrane shear stress	τ _{Sd}	=	τ _{T,Sd} +τ _{Q,Sd}			eq. 2.2.5
		=	T _{Sd} /(2πr ² t)+[-Q _{1,Sd} sinθ/(πrt)+			eq. 2.2.6-7
		=	Q _{2,Sd} conθ/(πrt)]			
		=	8.09085856	MPa		
von Mises' stress	σ _{i,Sd}	=	$\sqrt{(\sigma_{a,Sd} + \sigma_{m,Sd})^2 - (\sigma_{a,Sd} + \sigma_{m,Sd})\sigma_{h,Sd} + \sigma_{h,Sd}^2 + 3\tau_{Sd}^2}$			
	σ _{j,Sd}	=	41.362196	MPa	for panel	eq. 3.2.3
Curvature parameter	Z _s	=	s ² √(1-ν ²)/(rt)			eq. 3.3.3
		=	9.2657E+15			
Reduced buckling coefficient	C	=	ψ√(1+(ρξ/ψ) ²)			eq. 3.3.2
	C _a	=	1.62E+15		axial	Table 3-1
	C _τ	=	1.788E+15		shear	Table 3-1
	C _h	=	7.0192E+28		hydrostatic pressure	Table 3-1
Elastic buckling strength for	f _E	=	C $\frac{\pi^2 E}{12(1-\nu^2)}$ $\left(\frac{t}{s}\right)^2$			eq. 3.3.1

7 Stiffened cylindrical shell design for external column (DNVGL) case2

Designed by:		Date:			
Checked by:					Reference
axial force & bending moment	$f_{Ea} = 69.643092$ MPa $f_{E\tau} = 76.8645513$ MPa $f_{Eh} = 3.0175E+15$ MPa				
reduced shell slenderness	$\bar{\lambda}_s^{-2} = \frac{f_y}{\sigma_{j,sd}} \left[\frac{\sigma_{a0,sd}}{f_{Ea}} + \frac{\sigma_{m0,sd}}{f_{Em}} + \frac{\sigma_{h0,sd}}{f_{Eh}} + \frac{\tau_{sd}}{f_{E\tau}} \right]$ $= 2.45614544$				eq. 3.2.2
Characteristic buckling strength of a shell	$f_{ks} = \frac{f_y}{\sqrt{1 + \bar{\lambda}_s^4}}$ $= 133.865553$ MPa				
Design buckling strength of a shell	$f_{ksd} = f_{ks}/\gamma_M$ $= 92.3210714$ MPa				eq. 3.1.2
	$\sigma_{j,sd} = 41.362196 <$		f_{ksd}		eq. 3.1.1 OK
b) Panel Stiffener Buckling					
Curvature parameter	$Z_l = \frac{l^2 \sqrt{1 - \nu^2}}{rt}$ $= 34.9731456$				eq. 3.6.5
Effective shell width	$S_e = \frac{f_{ks} \sigma_{x,sd} s}{(\sigma_{j,sd} f_y)}$ $= 5987532.94$ m				eq. 3.6.7
Moment of inertia	$I_{sef} = 0.6641172$ m ⁴				
Coefficient	$\alpha_c = \frac{12(1 - \nu^2) I_{sef}}{st^3}$ $= 0.23573796$				eq. 3.6.6
Reduced buckling coefficient	$C = \frac{\psi \sqrt{1 + (\rho \xi / \psi)^2}}{12.337616}$			axial	eq. 3.6.4 Table 3-3
	$C_\tau = 18.7391702$			shear	Table 3-3
	$C_h = 5.60836478$			hydrostatic pressure	Table 3-3
					eq. 3.6.3
Elastic buckling strength for axial force & bending moment	$f_E = C \frac{\pi^2 E}{12(1 - \nu^2)} \left(\frac{t}{l}\right)^2$ $f_{Ea} = 140.519414$ MPa $f_{E\tau} = 213.429988$ MPa $f_{Eh} = 63.8765331$ MPa				
reduced shell slenderness	$\bar{\lambda}_s^{-2} = \frac{f_y}{\sigma_{j,sd}} \left[\frac{\sigma_{a0,sd}}{f_{Ea}} + \frac{\sigma_{m0,sd}}{f_{Em}} + \frac{\sigma_{h0,sd}}{f_{Eh}} + \frac{\tau_{sd}}{f_{E\tau}} \right]$ $= 3.61215864$				eq. 3.2.2
Characteristic buckling strength of a shell	$f_{ks} = \frac{f_y}{\sqrt{1 + \bar{\lambda}_s^4}}$ $= 94.7165553$ MPa				
Design buckling strength of a shell	$f_{ksd} = f_{ks}/\gamma_M$ $= 65.3217622$ MPa				eq. 3.1.2
	$\sigma_{j,sd} = 41.362196 <$		f_{ksd}		eq. 3.1.1 OK
Geometric proportions requirement (web)	$h_s = 0$ mm $< 1.35 t_w \sqrt{\frac{E}{f_y}} = 0$ mm				eq. 3.10.7 OK
Geometric proportions requirement (flange)	$b_f = 0$ mm $< 0.4 t_f \sqrt{\frac{E}{f_y}} = 0$ mm				eq. 3.10.8 OK
c) Panel Ring Buckling					
Cross sectional area	$A_R = 0.00396$ m ²				
Required cross sectional area	$\geq A_{Req} = (2/Z_l^2 + 0.06) l t$ $= 0.00096274$ m ²				eq. 3.5.1

7 Stiffened cylindrical shell design for external column (DNVGL) case2

Designed by:		Date:			
Checked by:					Reference
Effective width of shell	l_{ef}	=	$\frac{1.56\sqrt{rt}}{1 + \frac{12t}{r}}$ or l (smaller one)		eq. 3.5.3
		=	$\frac{0.35644235}{1.56\sqrt{rt}}$ m		
Equivalent length	l_{eo}	=	$\frac{1.56\sqrt{rt}}{0.36585243}$ or l (smaller one)		
		=	0.36585243 m		
	r_0	=	4.9945 m		
	α_A	=	$A/(st)$		eq. 3.5.6
		=	0		
Moment of inertia subjected to axial compression and bending	I_x	=	$\frac{ \sigma_{x,sd} t(1 + \alpha_A)r_0^4}{500El}$		eq. 3.5.5
		=	1.3045E-06 m ⁴		
Moment of inertia subjected to shear	I_{xh}	=	$\left(\frac{\tau_{sd}}{E}\right)^{8/5} \left(\frac{r_0}{L}\right)^{1/5} Lr_0tl$		eq. 3.5.7
		=	3.2674E-17 m ⁴		
Initial out-of-roundness parameter	δ_0	=	0.005r		eq. 3.5.13
		=	0.025		
Moment of inertia subjected to external lateral pressure	I_h	=	$\frac{ p_{sd} rr_0^2l}{3E} \left[1.5 + \frac{3EZ_t\delta_0}{r_0^2 \left(\frac{f_r}{2} - \sigma_{hR,sd} \right)} \right]$		eq. 3.5.8
		=	4.12E-05 m ⁴		
Effective moment of inertia	I_R	=	4.3543E-05 m ⁴		
		\geq	$I_x + I_{xh} + I_h$		
		=	4.2504E-05 m ⁴		OK
Geometric proportions requirement (web)	h_r	=	360 mm		eq. 3.10.7
		<	$1.35t_w \sqrt{\frac{E}{f_y}} = 361$ mm		
Geometric proportions requirement (flange)	b_f	=	0 mm		eq. 3.10.8
		<	$0.4t_f \sqrt{\frac{E}{f_y}} = 0$ mm		
d) Column Buckling					
I of the complete section	I_c	=	4.30545582 m ⁴		
Area of complete section	A_c	=	0.34519506 m ²		
Radius of gyration	i_c	=	3.53164696 m		
		$\left(\frac{kL_c}{i_c}\right)^2$	= 58.4484451		eq. 3.8.1
		<	$2.5E/f_y$		No buckling strength design requirement
		=	1478.87324		
The stability requirement for a shell-column					
Stress due to axial force	$\sigma_{a,Sd}$	=	$N_{sd}/(2\pi rt)$		eq. 2.2.2
		=	12.599284 MPa		
Stress due to bending	$\sigma_{m,Sd}$	=	$M_{1,Sd}\sin\theta/(\pi r^2t) - M_{2,Sd}\cos\theta/(\pi r^2t)$		eq. 2.2.3
		=	15.8159501 MPa		
Reduced column slenderness	$\bar{\lambda}$	=	$\sqrt{\frac{f_{ak}}{f_E} = \frac{kL_c}{\pi i_c} \sqrt{\frac{f_{ak}}{E}}}$		eq. 3.8.7
		=	0.05102434		
Characteristic column buckling strength	f_{kc}	=	$[1.0 - 0.28\bar{\lambda}^2]f_{ak}$		eq. 3.8.5
		=	92.2537716 MPa		

7 Stiffened cylindrical shell design for external column (DNVGL) case2

Designed by:		Date:			
Checked by:					Reference
Design column buckling strength	f_{kcd}	= f_{kc}/γ_M = 63.6232907 MPa			eq. 3.8.6
Euler buckling strength	f_{E1}	= $\frac{\pi^2 E I_{c,1}}{(k_L L_{c0})^2 A}$ = 35460.5998 MPa			eq. 3.8.3
Curvature parameter	Z_l	= $l^2 \sqrt{1 - \nu^2} / (rt)$ = 34.9731456			eq. 3.4.3
Reduced buckling coefficient	C C_a	= $\psi \sqrt{1 + (\rho \xi / \psi)^2}$ = 6.19590013		axial	eq. 3.4.2 Table 3-2
Elastic buckling strength for axial force	f_E f_{Ea}	= $C \frac{\pi^2 E}{12(1 - \nu^2)} \left(\frac{t}{l}\right)^2$ = 70.5682735 MPa			eq. 3.4.1
Elastic buckling strength for lateral pressure	l/r f_{Eh}	= 0.284 = $0.25E(t/r)^2$ = 0.2541 MPa	> 2.25(r/t)^0.5	0.0479702	eq. 3.4.5
Design local buckling strength	f_{akd}	= f_{ak}/γ_M = 65.3217622 MPa			
	$\frac{\sigma_{a0,Sd}}{f_{kcd}} + \frac{1}{f_{akd}} \frac{\sigma_{m1,Sd}}{1 - \frac{\sigma_{a0,Sd}}{f_{E1}}}$	= 0.44023924	<	1	eq. 3.8.2 OK
e) The Cost of Steel Structure					
Volume of column	V_c	= 9.33053018 m ³			
Volume of stringer	V_s	= 0 m ³			
Volume of ring	V_r	= 2.36548652 m ³			
Total volume	V	= 11.6960167 m ³			
Density of steel	ρ	= 7850 kg/m ³			
Total mass	m_s	= 91813.7311 kg			
Cost of steel	C_s	= 91813.7311 €			1 €/kg
f) The Cost of Filler material					
Length of welding	L_s	= 7.3398E-05 m			for stringer
	L_r	= 1194.69016 m			for ring
	L	= $L_s + L_r$ = 1194.69024 m			
leg length of weld	a	= 8 mm			
Mass of weld	m_w	= $A * L * \rho$ = 300.106188 kg			
Cost of Filler material	C_w	= 600.212375 €			2 €/kg
g) The Cost of Labour welding					
	T	= 199.11504 h			
Cost of labour welding	C_l	= 3982.30079 €			
h) Total Cost					
	C	= 96396.2443 €			

8 Stiffened shell structure design for internal column (DNVGL) case1

Designed by:		Date:	
Checked by:			
Design Information			Reference
			Based on DNVGL-RP-C202
Distance of ring frames	l	= 1.70473361 m	
Distance between eff. supports of the cylinder	L	= 27 m	
Shell thickness	t	= 2.88317798 mm	
Stringer web width	h_s	= 20.8101924 mm	
Stringer web thickness	t_{ws}	= 0.63379215 mm	
Stringer flange width	b_s	= 11.180524 mm	
Stringer flange thickness	t_{fs}	= 0.62809942 mm	
Spacing of stringer	s	= 45.8474301 mm	
Equivalent thickness	t_e	= $t + A/s$ = 3.3240275 mm	eq. 2.2.4
Ring web width	h_r	= 379.944205 mm	
Ring web thickness	t_{wr}	= 11.5715247 mm	
Ring flange width	b_r	= 11.5715247 mm	
Ring flange thickness	t_{fr}	= 5 mm	
Shell Radius	r	= 3 m	
Yield strength	f_y	= 355 MPa	
Young's modulus	E	= 210000000 kN/m ²	
Poisson's ratio	ν	= 0.3	
Load comb. Case: 1.0G + 1.0Q + 1.35E			
Axial force	F	= 11180 kN	
Shear force	V	= 1005 kN	
Bending moment	M	= 8867 kNm	
a) Shell buckling			
Stress due to axial force	$\sigma_{a,Sd}$	= $N_{Sd}/(2\pi r t)$ = 178.433368 MPa	eq. 2.2.2
Stress due to bending	$\sigma_{m,Sd}$	= $M_{1,Sd} \sin\theta / (\pi r^2 t) - M_{2,Sd} \cos\theta / (\pi r^2 t)$ = 94.3451803 MPa	eq. 2.2.3
Design longitudinal membrane stress	$\sigma_{x,Sd}$	= $\sigma_{a,Sd} + \sigma_{m,Sd}$ = 272.778548 MPa	eq. 2.2.1
water level difference	h	= 9.8 m	
Design lateral pressure	p_{Sd}	= 0.09604 MPa	
Circumferential membrane stress	$\sigma_{h,Sd}$	= $p_{Sd} r / t$ = 99.9313957 MPa	eq. 2.2.8
Membrane shear stress	τ_{Sd}	= $ \tau_{T,Sd} + \tau_{Q,Sd} $	eq. 2.2.5
		= $T_{Sd} / (2\pi r^2 t) + [-Q_{1,Sd} \sin\theta / (\pi r t) + Q_{2,Sd} \cos\theta / (\pi r t)]$	eq. 2.2.6-7
		= 36.9848176 MPa	
von Mises' stress	$\sigma_{j,Sd}$	= $\sqrt{(\sigma_{a,Sd} + \sigma_{m,Sd})^2 - (\sigma_{a,Sd} + \sigma_{m,Sd})\sigma_{h,Sd} + \sigma_{h,Sd}^2 + 3\tau_{Sd}^2}$ = 167.622449 MPa	eq. 3.2.3
Curvature parameter	Z_s	= $s^2 \sqrt{1 - \nu^2} / (r t)$ = 0.23182378	eq. 3.3.3
	C	= $\psi \sqrt{1 + (\rho \xi / \psi)^2}$	eq. 3.3.2
Reduced buckling coefficient	C_a	= 4.00010428	axial Table 3-1
	C_τ	= 5.35694467	shear Table 3-1
	C_h	= 1.0054791	hydrostatic pressure Table 3-1
Elastic buckling strength for	f_E	= $C \frac{\pi^2 E}{12(1 - \nu^2)} \left(\frac{t}{s}\right)^2$	eq. 3.3.1

8 Stiffened shell structure design for internal column (DNVGL) case1

Designed by:		Date:			
Checked by:					Reference
axial force & bending moment	$f_{Ea} = 3002.48348$ MPa $f_{E\tau} = 4020.92964$ MPa $f_{Eh} = 754.713922$ MPa				
reduced shell slenderness	$\bar{\lambda}_s^{-2} = \frac{f_y}{\sigma_{j,sd}} \left[\frac{\sigma_{a0,sd}}{f_{Ea}} + \frac{\sigma_{m0,sd}}{f_{Em}} + \frac{\sigma_{h0,sd}}{f_{Eh}} + \frac{\tau_{sd}}{f_{E\tau}} \right]$ $= 0.42576569$				eq. 3.2.2
Characteristic buckling strength of a shell	$f_{ks} = \frac{f_y}{\sqrt{1 + \bar{\lambda}_s^4}}$ $= 326.627378$ MPa				
Design buckling strength of a shell	$f_{ksd} = f_{ks}/\gamma_M$ $= 284.023807$ MPa				eq. 3.1.2
	$\sigma_{j,sd} = 167.622449 <$		f_{ksd}		eq. 3.1.1 OK
b) Panel Stiffener Buckling					
Curvature parameter	$Z_l = \frac{l^2 \sqrt{1 - \nu^2}}{rt}$ $= 278.001976$				eq. 3.6.5
Effective shell width	$S_e = \frac{f_{ks} \sigma_{x,sd} s}{(\sigma_{j,sd} f_y)}$ $= 0.06864632$ m				eq. 3.6.7
Moment of inertia	$I_{sef} = 5.7173E-07$ m ⁴				
Coefficient	$\alpha_c = \frac{12(1-\nu^2) I_{sef}}{st^3}$ $= 3707.67923$				eq. 3.6.6
Reduced buckling coefficient	$C = \frac{\psi \sqrt{1 + (\rho \xi / \psi)^2}}{3408.30124}$			axial	eq. 3.6.4 Table 3-3
	$C_\tau = 3504.16468$			shear	Table 3-3
	$C_h = 124.234277$			hydrostatic pressure	Table 3-3
					eq. 3.6.3
Elastic buckling strength for axial force & bending moment	$f_E = C \frac{\pi^2 E}{12(1-\nu^2)} \left(\frac{t}{l}\right)^2$ $f_{Ea} = 2459.52103$ MPa $f_{E\tau} = 2528.69864$ MPa $f_{Eh} = 89.6507661$ MPa				
reduced shell slenderness	$\bar{\lambda}_s^{-2} = \frac{f_y}{\sigma_{j,sd}} \left[\frac{\sigma_{a0,sd}}{f_{Ea}} + \frac{\sigma_{m0,sd}}{f_{Em}} + \frac{\sigma_{h0,sd}}{f_{Eh}} + \frac{\tau_{sd}}{f_{E\tau}} \right]$ $= 1.11104812$				eq. 3.2.2
Characteristic buckling strength of a shell	$f_{ks} = \frac{f_y}{\sqrt{1 + \bar{\lambda}_s^4}}$ $= 237.489918$ MPa				
Design buckling strength of a shell	$f_{ksd} = f_{ks}/\gamma_M$ $= 206.512972$ MPa				eq. 3.1.2
	$\sigma_{j,sd} = 167.622449 <$		f_{ksd}		eq. 3.1.1 OK
Geometric proportions requirement (web)	$h_s = 20.8101924$ mm				
	$> 1.35 t_w \sqrt{\frac{E}{f_y}} = 21$ mm				eq. 3.10.7 OK
Geometric proportions requirement (flange)	$b_f = 5.27336593$ mm				
	$< 0.4 t_f \sqrt{\frac{E}{f_y}} = 6$ mm				eq. 3.10.8 OK
c) Panel Ring Buckling					
Cross sectional area	$A_R = 0.00445439$ m ²				
Required cross sectional area	$\geq A_{Req} = (2/Z_l^2 + 0.06) l t$ $= 0.00029503$ m ²				eq. 3.5.1

8 Stiffened shell structure design for internal column (DNVGL) case1

Designed by:		Date:			
Checked by:					Reference
Effective width of shell	l_{ef}	=	$\frac{1.56\sqrt{rt}}{1 + \frac{12t}{r}}$ or l (smaller one)		eq. 3.5.3
		=	$\frac{0.14343034}{0.14343034} m$		
Equivalent length	l_{eo}	=	$\frac{1.56\sqrt{rt}}{0.14508448}$ or l (smaller one)		
		=	$0.14508448 m$		
	r_0	=	$2.99784072 m$		
	α_A	=	$A/(st)$		eq. 3.5.6
		=	0.15290402		
Moment of inertia subjected to axial compression and bending	I_x	=	$\frac{ \sigma_{x,sd} t(1 + \alpha_A)r_0^4}{500El}$		eq. 3.5.5
		=	$4.0913E-07 m^4$		
Moment of inertia subjected to shear	I_{xh}	=	$\left(\frac{\tau_{sd}}{E}\right)^{8/5} \left(\frac{r_0}{L}\right)^{1/5} Lr_0tl$		eq. 3.5.7
		=	$6.3398E-17 m^4$		
Initial out-of-roundness parameter	δ_0	=	$0.005r$		eq. 3.5.13
		=	0.015		
Moment of inertia subjected to external lateral pressure	I_h	=	$\frac{ p_{sd} rr_0^2l}{3E} \left[1.5 + \frac{3EZ_t\delta_0}{r_0^2 \left(\frac{f_r}{2} - \sigma_{hR,sd} \right)} \right]$		eq. 3.5.8
		=	$1.0715E-05 m^4$		
Effective moment of inertia	I_R	=	$5.3751E-05 m^4$		
		\geq	$I_x + I_{xh} + I_h$		
		=	$1.1124E-05 m^4$		OK
Geometric proportions requirement (web)	h_r	=	$379.944205 mm$		
		<	$1.35t_w \sqrt{\frac{E}{f_y}} = 380 mm$		
Geometric proportions requirement (flange)	b_f	=	$0 mm$		
		<	$0.4t_f \sqrt{\frac{E}{f_y}} = 49 mm$		
d) Column Buckling					
I of the complete section	I_c	=	$0.28148572 m^4$		
Area of complete section	A_c	=	$0.06262173 m^2$		
Radius of gyration	i_c	=	$2.12014545 m$		
	$\left(\frac{kL_c}{i_c}\right)^2$	=	162.179597		eq. 3.8.1
		<	$2.5E/f_y$		No buckling strength design requirement
		=	1478.87324		
The stability requirement for a shell-column					
Stress due to axial force	$\sigma_{a,Sd}$	=	$N_{sd}/(2\pi rt)$		eq. 2.2.2
		=	$205.716548 MPa$		
Stress due to bending	$\sigma_{m,Sd}$	=	$M_{1,Sd}\sin\theta/(\pi r^2t) - M_{2,Sd}\cos\theta/(\pi r^2t)$		eq. 2.2.3
		=	$108.770938 MPa$		
Reduced column slenderness	$\bar{\lambda}$	=	$\sqrt{\frac{f_{ak}}{f_E} = \frac{kL_c}{\pi i_c} \sqrt{\frac{f_{ak}}{E}}}$		eq. 3.8.7
		=	0.14907882		
Characteristic column buckling strength	f_{kc}	=	$[1.0 - 0.28\bar{\lambda}^2]f_{ak}$		eq. 3.8.5
		=	$282.256367 MPa$		

8 Stiffened shell structure design for internal column (DNVGL) case1							
Designed by:			Date:				
Checked by:							Reference
Design column buckling strength	f_{kcd}	=	f_{kc}/γ_M				eq. 3.8.6
		=	194.659563 MPa				
Euler buckling strength	f_{E1}	=	$\frac{\pi^2 EI_{c,1}}{(k_1 L_{c,1})^2 A}$				eq. 3.8.3
		=	$\frac{(12779)^2 \cdot 437}{12779^2}$ MPa				
Curvature parameter	Z_l	=	$l^2 \sqrt{1 - \nu^2} / (rt)$				eq. 3.4.3
		=	320.509597				
Reduced buckling coefficient	C	=	$\psi \sqrt{1 + (\rho \xi / \psi)^2}$				eq. 3.4.2
	C_a	=	39.9449467		axial		Table 3-2
Elastic buckling strength for axial force	f_E	=	$C \frac{\pi^2 E}{12(1 - \nu^2)} \left(\frac{t}{l}\right)^2$				eq. 3.4.1
	f_{Ea}	=	21.6864319 MPa				
Elastic buckling strength for lateral pressure	l/r	=	0.56824454				
		>	$2.25(r/t)^{0.5}$		0.0725784		
	f_{Eh}	=	$0.25E(t/r)^2$				eq. 3.4.5
		=	0.04849084 MPa				
Design local buckling strength	f_{akd}	=	f_{ak}/γ_M				
		=	206.512972 MPa				
	$\frac{\sigma_{a0,Sd}}{f_{kcd}} + \frac{1}{f_{akd}} \frac{\sigma_{m1,Sd}}{1 - \frac{\sigma_{a0,Sd}}{f_{E1}}}$	=	0.99096239	<	1	eq. 3.8.2	OK
e) The Cost of Steel Structure							
Volume of column	V_c	=	1.46735886 m ³				
Volume of stringer	V_s	=	0.22436507 m ³				
Volume of ring	V_r	=	1.32983186 m ³				
Total volumn	V	=	3.0215558 m ³				
Density of steel	ρ	=	7850 kg/m ³				
Total mass	m_s	=	23719.213 kg				
Cost of steel	C_s	=	23719.213 €			1 €/kg	
f) The Cost of Filler material							
Length of welding	L_s	=	44402.7514 m			for stringer	
	L_r	=	1194.17604 m			for ring	
	L	=	$L_s + L_r$				
		=	45596.9274 m				
leg length of weld	a	=	2 mm				
Mass of weld	m_w	=	$A * L * \rho$				
		=	715.87176 kg				
Cost of Filler material	C_w	=	1431.74352 €			2 €/kg	
g) The Cost of Labour welding							
	T	=	7599.4879 h				
Cost of labour welding	C_l	=	151989.758 €				
h) Total Cost							
	C	=	177140.715 €				

8 Stiffened shell structure design for internal column (DNVGL) case2

Designed by:		Date:	
Checked by:			
Design Information			Reference
Distance of ring frames	l	= 1.96927005 m	Based on DNVGL-RP-C202
Distance between eff. supports of the cylinder	L	= 27 m	
Shell thickness	t	= 12 mm	
Stringer web width	h_s	= 0 mm	
Stringer web thickness	t_{ws}	= 0 mm	
Stringer flange width	b_s	= 0 mm	
Stringer flange thickness	t_{fs}	= 0 mm	
Spacing of stringer	s	= 7.4716E+17 mm	
Equivalent thickness	t_e	= $t+A/s$	eq. 2.2.4
		= 12 mm	
Ring web width	h_r	= 388 mm	
Ring web thickness	t_{wr}	= 11.8168708 mm	
Ring flange width	b_r	= 11.8168708 mm	
Ring flange thickness	t_{fr}	= 0 mm	
Shell Radius	r	= 5 m	
Yield strength	f_y	= 355 MPa	
Young's modulus	E	= 210000000 kN/m ²	
Poisson's ratio	ν	= 0.3	
Load comb. Case: 1.0G + 1.0Q+ 1.35E			
Axial force	F	= 11180 kN	
Shear force	V	= 1005 kN	
Bending moment	M	= 8867 kNm	
a) Shell buckling			
Stress due to axial force	$\sigma_{a,Sd}$	= $N_{Sd}/(2\pi r t)$ = 29.6558711 MPa	eq. 2.2.2
Stress due to bending	$\sigma_{m,Sd}$	= $M_{1,Sd}\sin\theta/(\pi r^2 t) - M_{2,Sd}\cos\theta/(\pi r^2 t)$ = 9.4081792 MPa	eq. 2.2.3
Design longitudinal membrane stress	$\sigma_{x,Sd}$	= $\sigma_{a,Sd} + \sigma_{m,Sd}$ = 39.0640503 MPa	eq. 2.2.1
water level difference	h	= 9.8 m	
Design lateral pressure	p_{Sd}	= 0.09604 MPa	
Circumferential membrane stress	$\sigma_{h,Sd}$	= $p_{Sd}r/t$ = 40.0166667 MPa	eq. 2.2.8
Membrane shear stress	τ_{Sd}	= $ \tau_{T,Sd} + \tau_{Q,Sd} $	eq. 2.2.5
		= $T_{Sd}/(2\pi r^2 t) + [-Q_{1,Sd}\sin\theta/(\pi r t) + Q_{2,Sd}\cos\theta/(\pi r t)]$	eq. 2.2.6-7
		= 5.33169059 MPa	
von Mises' stress	$\sigma_{j,Sd}$	= $\sqrt{(\sigma_{a,Sd} + \sigma_{m,Sd})^2 - (\sigma_{a,Sd} + \sigma_{m,Sd})\sigma_{h,Sd} + \sigma_{h,Sd}^2 + 3\tau_{Sd}^2}$ = 37.1396818 MPa for panel	eq. 3.2.3
Curvature parameter	Z_s	= $s^2\sqrt{1 - \nu^2}/(rt)$ = 8.8756E+30	eq. 3.3.3
Reduced buckling coefficient	C	= $\psi\sqrt{1 + (\rho\xi/\psi)^2}$	eq. 3.3.2
	C_a	= 1.6028E+30	axial Table 3-1
	C_τ	= 1.1262E+30	shear Table 3-1
	C_h	= 2.0722E+58	hydrostatic pressure Table 3-1
Elastic buckling strength for	f_E	= $C \frac{\pi^2 E}{12(1 - \nu^2)} \left(\frac{t}{s}\right)^2$	eq. 3.3.1

8 Stiffened shell structure design for internal column (DNVGL) case2

Designed by:		Date:			
Checked by:					Reference
axial force & bending moment	$f_{Ea} = 78.4724573$ MPa $f_{E\tau} = 55.136058$ MPa $f_{Eh} = 1.0145E+30$ MPa				
reduced shell slenderness	$\bar{\lambda}_s^{-2} = \frac{f_y}{\sigma_{j,Sd}} \left[\frac{\sigma_{a0,Sd}}{f_{Ea}} + \frac{\sigma_{m0,Sd}}{f_{Em}} + \frac{\sigma_{h0,Sd}}{f_{Eh}} + \frac{\tau_{Sd}}{f_{E\tau}} \right]$ $= 4.53661202$				eq. 3.2.2
Characteristic buckling strength of a shell	$f_{ks} = \frac{f_y}{\sqrt{1 + \bar{\lambda}_s^4}}$ $= 76.4177231$ MPa				
Design buckling strength of a shell	$f_{ksd} = f_{ks}/\gamma_M$ $= 52.701878$ MPa				eq. 3.1.2
	$\sigma_{j,Sd} = 37.1396818 <$		f_{ksd}		eq. 3.1.1 OK
b) Panel Stiffener Buckling					
Curvature parameter	$Z_l = \frac{l^2 \sqrt{1 - \nu^2}}{rt}$ $= 61.6566602$				eq. 3.6.5
Effective shell width	$S_e = \frac{f_{ks} \sigma_{x,Sd} s}{(\sigma_{j,Sd} f_y)}$ $= 1.6917E+14$ m				eq. 3.6.7
Moment of inertia	$I_{sef} = 24360214.7$ m ⁴				
Coefficient	$\alpha_c = \frac{12(1 - \nu^2) I_{sef}}{st^3}$ $= 0.20603748$				eq. 3.6.6
Reduced buckling coefficient	$C = \frac{\psi \sqrt{1 + (\rho \xi / \psi)^2}}{21.6750667}$			axial	eq. 3.6.4 Table 3-3
	$C_\tau = 32.1139481$			shear	Table 3-3
	$C_h = 6.45115127$			hydrostatic pressure	Table 3-3
					eq. 3.6.3
Elastic buckling strength for axial force & bending moment	$f_E = C \frac{\pi^2 E}{12(1 - \nu^2)} \left(\frac{t}{l} \right)^2$ $f_{Ea} = 152.759696$ MPa $f_{E\tau} = 226.329959$ MPa $f_{Eh} = 45.4658766$ MPa				
reduced shell slenderness	$\bar{\lambda}_s^{-2} = \frac{f_y}{\sigma_{j,Sd}} \left[\frac{\sigma_{a0,Sd}}{f_{Ea}} + \frac{\sigma_{m0,Sd}}{f_{Em}} + \frac{\sigma_{h0,Sd}}{f_{Eh}} + \frac{\tau_{Sd}}{f_{E\tau}} \right]$ $= 4.66654892$				eq. 3.2.2
Characteristic buckling strength of a shell	$f_{ks} = \frac{f_y}{\sqrt{1 + \bar{\lambda}_s^4}}$ $= 74.3846209$ MPa				
Design buckling strength of a shell	$f_{ksd} = f_{ks}/\gamma_M$ $= 51.2997385$ MPa				eq. 3.1.2
	$\sigma_{j,Sd} = 37.1396818 <$		f_{ksd}		eq. 3.1.1 OK
Geometric proportions requirement (web)	$h_s = 0$ mm				
	$< 1.35 t_w \sqrt{\frac{E}{f_y}} = 0$ mm				eq. 3.10.7 OK
Geometric proportions requirement (flange)	$b_f = 0$ mm				
	$< 0.4 t_f \sqrt{\frac{E}{f_y}} = 0$ mm				eq. 3.10.8 OK
c) Panel Ring Buckling					
Cross sectional area	$A_R = 0.00458495$ m ²				
Required cross sectional area	$\geq A_{Req} = (2/Z_l^2 + 0.06) l t$ $= 0.00143031$ m ²				eq. 3.5.1

8 Stiffened shell structure design for internal column (DNVGL) case2

Designed by:		Date:	
Checked by:			
			Reference
Effective width of shell	l_{ef}	$= \frac{1.56\sqrt{rt}}{1 + \frac{12t/r}{0.37142341}}$ or l (smaller one)	eq. 3.5.3
		$= 1.42341$ m	
Equivalent length	l_{eo}	$= \frac{1.56\sqrt{rt}}{0.3821204}$ or l (smaller one)	
		$= 1204$ m	
	r_0	$= 4.994$ m	
	α_A	$= A/(st)$	eq. 3.5.6
		$= 0$	
Moment of inertia subjected to axial compression and bending	I_x	$= \frac{ \sigma_{x,sd} t(1 + \alpha_A)r_0^4}{500El}$	eq. 3.5.5
		$= 1.4101E-06$ m ⁴	
Moment of inertia subjected to shear	I_{xh}	$= \left(\frac{\tau_{sd}}{E}\right)^{8/5} \left(\frac{r_0}{L}\right)^{1/5} Lr_0tl$	eq. 3.5.7
		$= 2.536E-17$ m ⁴	
Initial out-of-roundness parameter	δ_0	$= 0.005r$	eq. 3.5.13
		$= 0.025$	
Moment of inertia subjected to external lateral pressure	I_h	$= \frac{ p_{sd} rr_0^2l}{3E} \left[1.5 + \frac{3EZ_t\delta_0}{r_0^2 \left(\frac{f_r}{2} - \sigma_{hR,sd} \right)} \right]$	eq. 3.5.8
		$= 5.7185E-05$ m ⁴	
Effective moment of inertia	I_R	$= 5.8492E-05$ m ⁴	
		$< I_x + I_{xh} + I_h$	OK
		$= 5.8595E-05$ m ⁴	
Geometric proportions requirement (web)	h_r	$= 388$ mm	
		$< 1.35t_w \sqrt{\frac{E}{f_y}} = 388$ mm	eq. 3.10.7 OK
Geometric proportions requirement (flange)	b_f	$= 0$ mm	
		$< 0.4t_f \sqrt{\frac{E}{f_y}} = 0$ mm	eq. 3.10.8 OK
d) Column Buckling			
I of the complete section	I_c	$= 4.69545151$ m ⁴	
Area of complete section	A_c	$= 0.37653873$ m ²	
Radius of gyration	i_c	$= 3.53129381$ m	
		$\left(\frac{kL_c}{i_c}\right)^2 = 58.460136$	eq. 3.8.1
		$< 2.5E/f_y$	No buckling strength design requirement
		$= 1478.87324$	
The stability requirement for a shell-column			
Stress due to axial force	$\sigma_{a,Sd}$	$= N_{sd}/(2\pi rt)$	eq. 2.2.2
		$= 29.6558711$ MPa	
Stress due to bending	$\sigma_{m,Sd}$	$= M_{1,Sd}\sin\theta/(\pi r^2 t) - M_{2,Sd}\cos\theta/(\pi r^2 t)$	eq. 2.2.3
		$= 9.4081792$ MPa	
Reduced column slenderness	$\bar{\lambda}$	$= \sqrt{\frac{f_{ak}}{f_E} = \frac{kL_c}{\pi i_c} \sqrt{\frac{f_{ak}}{E}}}$	eq. 3.8.7
		$= 0.03855524$	
Characteristic column buckling strength	f_{kc}	$= [1.0 - 0.28\bar{\lambda}^2]f_{ak}$	eq. 3.8.5
		$= 52.6799423$ MPa	

8 Stiffened shell structure design for internal column (DNVGL) case2

Designed by:		Date:					
Checked by:							Reference
Design column buckling strength	f_{kcd}	=	f_{kc}/γ_M				eq. 3.8.6
		=	36.3309947 MPa				
Euler buckling strength	f_{E1}	=	$\frac{\pi^2 EI_{c,1}}{(k_1 L_{E1})^2}$				eq. 3.8.3
		=	$\frac{35458.5084}{55458.5084}$ MPa				
Curvature parameter	Z_l	=	$l^2 \sqrt{1 - \nu^2} / (rt)$				eq. 3.4.3
		=	61.6566602				
Reduced buckling coefficient	C	=	$\psi \sqrt{1 + (\rho \xi / \psi)^2}$				eq. 3.4.2
	C_a	=	11.1792691		axial		Table 3-2
Elastic buckling strength for axial force	f_E	=	$C \frac{\pi^2 E}{12(1 - \nu^2)} \left(\frac{t}{l}\right)^2$				eq. 3.4.1
	f_{Ea}	=	78.788304 MPa				
Elastic buckling strength for lateral pressure	l/r	=	0.39385401				
		>	$2.25(r/t)^{0.5}$		0.0459279		
	f_{Eh}	=	$0.25E(t/r)^2$				eq. 3.4.5
		=	0.3024 MPa				
Design local buckling strength	f_{akd}	=	f_{ak}/γ_M				
		=	51.2997385 MPa				
	$\frac{\sigma_{a0,sd}}{f_{kcd}} + \frac{1}{f_{akd}} \frac{\sigma_{m1,sd}}{1 - \frac{\sigma_{a0,sd}}{f_{E1}}}$	=	0.99981895	<	1	eq. 3.8.2	OK
e) The Cost of Steel Structure							
Volume of column	V_c	=	10.1787602 m ³				
Volume of stringer	V_s	=	0 m ³				
Volume of ring	V_r	=	1.97488847 m ³				
Total volumn	V	=	12.1536487 m ³				
Density of steel	ρ	=	7850 kg/m ³				
Total mass	m_s	=	95406.142 kg				
Cost of steel	C_s	=	95406.142 €			1 €/kg	
f) The Cost of Filler material							
Length of welding	L_s	=	1.1353E-11 m			for stringer	
	L_r	=	861.466428 m			for ring	
	L	=	$L_s + L_r$				
		=	861.466428 m				
leg length of weld	a	=	8 mm				
Mass of weld	m_w	=	$A * L * \rho$				
		=	216.400367 kg				
Cost of Filler material	C_w	=	432.800733 €			2 €/kg	
g) The Cost of Labour welding							
	T	=	143.577738 h				
Cost of labour welding	C_l	=	2871.55476 €				
h) Total Cost							
	C	=	98710.4975 €				

9 Stiffened cylindrical shell design for external column (EN1993-1-6 (2007))						
Designed by:				Date:		
Checked by:						Reference
Design load on the column						Based on EN 1993-1-6
Distance of ring frames	l	=	1.25	m		
Distance of cylinder	L	=	27	m		
Shell thickness	t	=	11	mm		
Shell Radius	r	=	5	m		
Ring web width	h _r	=	360	mm		
Ring web thickness	t _{wr}	=	6	mm		
Yield strength	f _y	=	355	MPa		
Young's modulus	E	=	210000000	kN/m ²		
Poisson's ratio	ν	=	0.3			
External column						
Axial force	F	=	4354	kN		
Shear force	V	=	1398	kN		
Bending moment	M	=	13664	kNm		
a) Critical meridional (axial) buckling						
Length parameter	ω	=	$\frac{l}{r} \sqrt{\frac{r}{l}} = \frac{l}{\sqrt{rt}}$		0.5r/t	eq. D.1
		=	5.33001791		227.27273	medium cylinder
Factor	C _x	=	1			eq. D.3-D.10
Elastic critical meridional buckling stress	σ _{x,Rcr}	=	0.605EC _x t/r			eq. D.2
		=	279.51	MPa		
Characteristic imperfection amplitude	Δw _k	=	$\frac{1}{Q} \sqrt{\frac{r}{t}}$			eq. D.15
		=	0.00938083	m		
Meridional elastic imperfection reduction factor	α _x	=	$\frac{0.62}{1 + 1.91(\Delta w_k/t)^{1.44}}$			eq. D.14
		=	0.2461644			
	r/t	=	454.545455			eq. D.18 Meridional shell buckling checking
		>	0.03E/f _{yk} =		17.746479	
Meridional shell slenderness parameters	λ̄ _x	=	$\sqrt{f_{yk}/\sigma_{x,Rcr}}$			eq. 8.17
		=	1.12697816			
Meridional squash limit slenderness	λ̄ _{x0}	=	0.2			eq. D.16
Plastic range factor	β	=	0.6			eq. D.16
Interaction exponent	η	=	1			eq. D.16
Meridional plastic limit relative slenderness	λ̄ _{xp}	=	$\sqrt{\alpha_x/(1-\beta)}$			eq. 8.16
		=	0.78448135			
	λ̄ _x	∈	(λ̄ ₀ , λ̄ _p)			eq. 8.13-8.15
Buckling reduction factor	χ _x	=	$1 - \beta \left(\frac{\lambda - \lambda_0}{\lambda_p - \lambda_0} \right)^\eta$			eq. 8.13-8.15
		=	0.19381806			
Buckling interaction parameter	k _x	=	1.25+0.75χ _x			eq. D.46
		=	1.39536354			
Meridional characteristic buckling stress	σ _{x,Rk}	=	χ _x f _{yk}			ch. 8.5.2
		=	68.8054101	MPa		
Partical factor	γ _{M1}	=	1.1			ch. 8.5.2
Meridional design buckling stress	σ _{x,Rd}	=	σ _{x,Rk} /γ _{M1}			eq. 8.11
		=	62.5503728	MPa		

9 Stiffened cylindrical shell design for external column (EN1993-1-6 (2007))						
Designed by:			Date:			
Checked by:						Reference
Design value of the meridional stress due to axial force	$\sigma_{x,E,A}$	=	$\frac{F}{2\pi r t}$			
		=	$\frac{12.599284}{12.599284}$ MPa			
Design value of the meridional stress due to bending	$\sigma_{x,E,M}$	=	$\frac{M}{\pi r^2 t}$			
		=	15.8159501 MPa			
Design value of meridional stress	$\sigma_{x,Ed}$	=	$\sigma_{x,E,A} + \sigma_{x,E,M}$			
		=	28.4152342 MPa			
		<	$\sigma_{x,Rd}$	62.5503728 MPa		OK
b) Critical circumferential (hoop) buckling						due to hoop compression
Length parameter	ω	=	$\frac{l \sqrt{r}}{r \sqrt{l}} = \frac{l}{\sqrt{r t}}$			eq. D.1
		=	5.33001791			
Buckling factors	C_θ	=	1.31335567			
	ω/C_θ	<	1.63r/t	=	740.90909	short cylinder eq. D.25
Elastic critical circumferential buckling stress	$\sigma_{\theta,Rcr}$	=	$0.92E \left(\frac{C_\theta}{\omega}\right) \left(\frac{t}{r}\right)$			
		=	104.732986 MPa			
Circumferential elastic imperfection reduction factor	α_θ	=	0.65			Table D.5
	r/t	=	454.545455			eq. D.27 Circumferential shell buckling checking
		>	$0.21(E/f_{yk})^{0.5} =$	5.1075752		
Circumferential shell slenderness parameters	$\bar{\lambda}_\theta$	=	$\sqrt{f_{yk}/\sigma_{\theta,Rcr}}$			eq. 8.17
		=	1.84107904			
Circumferential squash limit slenderness	$\bar{\lambda}_{\theta 0}$	=	0.4			eq. D.26
Plastic range factor	β	=	0.6			eq. D.26
Interaction exponent	η	=	1			eq. D.26
Circumferential plastic limit relative slenderness	$\bar{\lambda}_{\theta p}$	=	$\sqrt{\alpha_\theta/(1+\beta)}$			eq. 8.16
		=	0.63737744			
	$\bar{\lambda}_\theta$	\in	$(\bar{\lambda}_p, +\infty)$			eq. 8.13-8.15
Buckling reduction factor	χ_θ	=	$\frac{\alpha_\theta}{\bar{\lambda}_\theta^2}$			eq. 8.13-8.15
		=	0.19176462			
Buckling interaction parameter	k_θ	=	$1.25 + 0.75\chi_\theta$			eq. D.47
		=	1.39382347			
Circumferential characteristic buckling stress	$\sigma_{\theta,Rk}$	=	$\chi_\theta f_{yk}$			ch. 8.5.2
		=	68.0764411 MPa			
Partical factor	γ_{M1}	=	1.1			ch. 8.5.2
Circumferential design buckling stress	$\sigma_{\theta,Rd}$	=	$\sigma_{\theta,Rk}/\gamma_{M1}$			eq. 8.11
		=	61.8876737 MPa			
External water pressure	q_{eq}	=	166.6 kPa			bottom of column
Internal water pressure	q_s	=	70.56 kPa			

9 Stiffened cylindrical shell design for external column (EN1993-1-6 (2007))						
Designed by:			Date:			
Checked by:						Reference
Circumferential design stress	$\sigma_{\theta,Ed}$	=	$(q_{eq}+q_s)(r/t)$ = 43.6545455 MPa			eq. D.30
Deformation	w_0	=	$\sigma_{MT\theta}/E$ = 0.00103939 m			C.5.3
Ratio of ring area to total area	κ	=	$\frac{A_r}{A_r + (b + 2b_m)t}$ = 0.34615064			C.5.3
Deformation	w_r	=	$w_0(1-\kappa)$ = 0.00067961 m			C.5.3
Deformation	w	=	$w_r - w_0$ = -0.0003598 m			C.5.3
von Mises equivalent stress of surface stresses	$\sigma_{eq,s}$	=	$k_{eq,s}\sigma_{MT\theta}$ = 44.0776548			C.5.3
		<	$\sigma_{\theta,Rd}$ = 61.8876737 MPa			OK
c) Critical shear buckling						ch. D.1.4
Length parameter	ω	=	$\frac{l}{r} \sqrt{\frac{r}{l}} = \frac{l}{\sqrt{rt}}$ = 5.33001791 < 10			eq. D.31
		<	$8.7r/t$ = 3954.5455			short cylinder
Factor	C_τ	=	1.13020902			eq. D.34
Elastic critical shear buckling stress	$\tau_{x\theta,Rcr}$	=	$0.75EC_\tau \sqrt{\frac{1}{\omega} \left(\frac{t}{r}\right)}$ = 169.628051 MPa			eq. D.32
Shear elastic imperfection reduction factor	α_τ	=	0.65			Table D.6
	r/t	=	454.545455			eq. D.40 Shear shell buckling checking
		>	$0.16(E/f_{yk})^{0.67} = 11.517386$			eq. 8.17
Shell slenderness parameters of shear	$\bar{\lambda}_\tau$	=	$\sqrt{(f_{yk}/\sqrt{3})/\tau_{x\theta,Rcr}}$ = 1.09922102			
Shear squash limit slenderness	$\bar{\lambda}_{\tau 0}$	=	0.4			eq. D.39
Plastic range factor	β	=	0.6			eq. D.39
Interaction exponent	η	=	1			eq. D.39
Shear plastic limit relative slenderness	$\bar{\lambda}_{\tau p}$	=	$\sqrt{\alpha_\tau/(1+\beta)}$ = 0.63737744			eq. 8.16
	$\bar{\lambda}_\tau$	∈	$(\bar{\lambda}_p, +\infty)$			eq. 8.13-8.15
Buckling reduction factor	χ_τ	=	$\frac{\alpha_\tau}{\bar{\lambda}_\tau^2}$ = 0.53795172			eq. 8.13-8.15
Buckling interaction parameter	k_τ	=	$1.75+0.25\chi_\tau$ = 1.88448793			eq. D.48
Shear characteristic buckling stress	$\tau_{x\theta,Rk}$	=	$\chi_\tau f_{yk}/\sqrt{3}$ = 110.258233 MPa			ch. 8.5.2
Partical factor	γ_{M1}	=	1.1			ch. 8.5.2

10 Stiffened cylindrical shell design for internal column (EN1993-1-6 (2007))

Designed by:		Date:			
Checked by:					Reference
Design load on the column					Based on EN 1993-1-6
Distance of ring frames	l	=	2.7 m		
Distance of cylinder	L	=	27 m		
Shell thickness	t	=	12 mm		
Shell Radius	r	=	3 m		
Ring web width	h_r	=	388 mm		
Ring web thickness	t_{wr}	=	3 mm		
Yield strength	f_y	=	355 MPa		
Young's modulus	E	=	210000000 kN/m ²		
Poisson's ratio	ν	=	0.3		
Internal column					
Axial force	F	=	11180 kN		
Shear force	V	=	1005 kN		
Bending moment	M	=	8867 kNm		
a) Critical meridional (axial) buckling					
Length parameter	ω	=	$\frac{l}{r} \sqrt{\frac{r}{l}} = \frac{l}{\sqrt{rt}}$	0.5r/t	eq. D.1
		=	14.2302495	125	medium cylinder
Factor	C_x	=	1		eq. D.3-D.10
Elastic critical meridional buckling stress	$\sigma_{x,Rcr}$	=	$0.605EC_x t/r$		eq. D.2
		=	508.2 MPa		
Characteristic imperfection amplitude	Δw_k	=	$\frac{1}{Q} \sqrt{\frac{r}{t}}$		eq. D.15
		=	0.00758947 m		
Meridional elastic imperfection reduction factor	α_x	=	$\frac{0.62}{1 + 1.91(\Delta w_k/t)^{1.44}}$		eq. D.14
		=	0.31195702		
	r/t	=	250		eq. D.18 Meridional shell buckling checking
		>	$0.03E/f_{yk} =$	17.746479	
Meridional shell slenderness parameters	$\bar{\lambda}_x$	=	$\sqrt{f_{yk}/\sigma_{x,Rcr}}$		eq. 8.17
		=	0.83578938		
Meridional squash limit slenderness	$\bar{\lambda}_{x0}$	=	0.2		eq. D.16
Plastic range factor	β	=	0.6		eq. D.16
Interaction exponent	η	=	1		eq. D.16
Meridional plastic limit relative slenderness	$\bar{\lambda}_{xp}$	=	$\sqrt{\alpha_x/(1-\beta)}$		eq. 8.16
		=	0.88311525		
	$\bar{\lambda}_x$	∈	$(\bar{\lambda}_0, \bar{\lambda}_p)$		eq. 8.13-8.15
Buckling reduction factor	χ_x	=	$1 - \beta \left(\frac{\bar{\lambda} - \bar{\lambda}_0}{\bar{\lambda}_p - \bar{\lambda}_0} \right)^\eta$		eq. 8.13-8.15
		=	0.44156769		
Buckling interaction parameter	k_x	=	$1.25 + 0.75\chi_x$		eq. D.46
		=	1.58117577		
Meridional characteristic buckling stress	$\sigma_{x,Rk}$	=	$\chi_x f_{yk}$		ch. 8.5.2
		=	156.756531 MPa		
Partical factor	γ_{M1}	=	1.1		ch. 8.5.2
Meridional design buckling stress	$\sigma_{x,Rd}$	=	$\sigma_{x,Rk}/\gamma_{M1}$		eq. 8.11
		=	142.505937 MPa		

10 Stiffened cylindrical shell design for internal column (EN1993-1-6 (2007))						
Designed by:			Date:			
Checked by:						Reference
Design value of the meridional stress due to axial force	$\sigma_{x,E,A}$	=	$\frac{F}{2\pi r t}$			
		=	49.4264518 MPa			
Design value of the meridional stress due to bending	$\sigma_{x,E,M}$	=	$\frac{M}{\pi r^2 t}$			
		=	26.1338311 MPa			
Design value of meridional stress	$\sigma_{x,Ed}$	=	$\sigma_{x,E,A} + \sigma_{x,E,M}$			
		=	75.5602829 MPa			
		<	$\sigma_{x,Rd}$	142.505937 MPa		OK
b) Critical circumferential (hoop) buckling						due to hoop compression
Length parameter	ω	=	$\frac{l \sqrt{r}}{r \sqrt{l}} = \frac{l}{\sqrt{r t}}$			eq. D.1
		=	14.2302495			
Buckling factors	C_θ	=	1.08323086			
	ω/C_θ	<	$1.63r/t$	=	407.5	short cylinder
						eq. D.25
Elastic critical circumferential buckling stress	$\sigma_{\theta,Rcr}$	=	$0.92E \left(\frac{C_\theta}{\omega}\right) \left(\frac{t}{r}\right)$			
		=	58.8268538 MPa			
Circumferential elastic imperfection reduction factor	α_θ	=	0.65			Table D.5
	r/t	=	250			
		>	$0.21(E/f_{yk})^{0.5}$	=	5.1075752	eq. D.27 Circumferential shell buckling checking
						eq. 8.17
Circumferential shell slenderness parameters	$\bar{\lambda}_\theta$	=	$\sqrt{f_{yk}/\sigma_{\theta,Rcr}}$			
		=	2.45655428			
Circumferential squash limit slenderness	$\bar{\lambda}_{\theta 0}$	=	0.4			eq. D.26
Plastic range factor	β	=	0.6			eq. D.26
Interaction exponent	η	=	1			eq. D.26
Circumferential plastic limit relative slenderness	$\bar{\lambda}_{\theta p}$	=	$\sqrt{\alpha_\theta/(1+\beta)}$			eq. 8.16
		=	0.63737744			
	$\bar{\lambda}_\theta$	\in	$(\bar{\lambda}_p, +\infty)$			eq. 8.13-8.15
Buckling reduction factor	χ_θ	=	$\frac{\alpha_\theta}{\bar{\lambda}_\theta^2}$			eq. 8.13-8.15
		=	0.10771114			
Buckling interaction parameter	k_θ	=	$1.25 + 0.75\chi_\theta$			eq. D.47
		=	1.33078336			
Circumferential characteristic buckling stress	$\sigma_{\theta,Rk}$	=	$\chi_\theta f_{yk}$			ch. 8.5.2
		=	38.237455 MPa			
Partical factor	γ_{M1}	=	1.1			ch. 8.5.2
Circumferential design buckling stress	$\sigma_{\theta,Rd}$	=	$\sigma_{\theta,Rk}/\gamma_{M1}$			eq. 8.11
		=	34.7613227 MPa			
External water pressure	q_{eq}	=	166.6 kPa			bottom of column
Internal water pressure	q_s	=	70.56 kPa			

10 Stiffened cylindrical shell design for internal column (EN1993-1-6 (2007))						
Designed by:			Date:			
Checked by:						Reference
Circumferential design stress	$\sigma_{\theta,Ed}$	=	$(q_{eq}+q_s)(r/t)$			eq. D.30
		=	24.01 MPa			
Deformation	w_0	=	$\sigma_{MT\theta}r/E$			C.5.3
		=	0.000343 m			
Ratio of ring area to total area	κ	=	$\frac{A_r}{A_r + (b + 2b_m)t}$			C.5.3
		=	0.24542656			
Deformation	w_r	=	$w_0(1-\kappa)$			C.5.3
		=	0.00025882 m			
Deformation	w	=	$w_r - w_0$			C.5.3
		=	-8.418E-05 m			
von Mises equivalent stress of surface stresses	$\sigma_{eq,s}$	=	$k_{eq,s}\sigma_{MT\theta}$			C.5.3
		=	24.1749954			
		<	$\sigma_{\theta,Rd}$	34.7613227 MPa		OK
c) Critical shear buckling						ch. D.1.4
Length parameter	ω	=	$\frac{l}{r} \sqrt{\frac{r}{l}} = \frac{l}{\sqrt{rt}}$			eq. D.31
		=	14.2302495	>	10	eq. D.33
		<	$8.7r/t$	=	2175	medium cylinder
Factor	C_τ	=	1			eq. D.34
Elastic critical shear buckling stress	$\tau_{x\theta,Rcr}$	=	$0.75EC_\tau \sqrt{\frac{1}{\omega} \left(\frac{t}{r}\right)}$			eq. D.32
		=	167.006853 MPa			
Shear elastic imperfection reduction factor	α_τ	=	0.65			Table D.6
	r/t	=	250			eq. D.40 Shear shell buckling checking
		>	$0.16(E/f_{yk})^{0.67}$		11.517386	
Shell slenderness parameters of shear	$\bar{\lambda}_\tau$	=	$\sqrt{(f_{yk}/\sqrt{3})/\tau_{x\theta,Rcr}}$			eq. 8.17
		=	1.10781366			
Shear squash limit slenderness	$\bar{\lambda}_{\tau 0}$	=	0.4			eq. D.39
Plastic range factor	β	=	0.6			eq. D.39
Interaction exponent	η	=	1			eq. D.39
Shear plastic limit relative slenderness	$\bar{\lambda}_{\tau p}$	=	$\sqrt{\alpha_\tau/(1+\beta)}$			eq. 8.16
		=	0.63737744			
	$\bar{\lambda}_\tau$	∈	$(\bar{\lambda}_p, +\infty)$			eq. 8.13-8.15
Buckling reduction factor	χ_τ	=	$\frac{\alpha_\tau}{\bar{\lambda}_\tau^2}$			eq. 8.13-8.15
		=	0.52963896			
Buckling interaction parameter	k_τ	=	$1.75+0.25\chi_\tau$			eq. D.48
		=	1.88240974			
Shear characteristic buckling stress	$\tau_{x\theta,Rk}$	=	$\chi_\tau f_{yk}/\sqrt{3}$			ch. 8.5.2
		=	108.554454 MPa			
Partical factor	γ_{M1}	=	1.1			ch. 8.5.2

11 Stiffened cylindrical shell design for external column (EN1993-1-6 (2017))						
Designed by:			Date:			
Checked by:						Reference
Design load on the column						Based on BS EN 1993-1-6: 2007+A1: 2017
Distance of ring frames	l	=	1.42 m			
Distance of cylinder	L	=	27 m			
Shell thickness	t	=	11 mm			
Shell Radius	r	=	5 m			
Ring web width	h_r	=	360 mm			
Ring web thickness	t_{wr}	=	6 mm			
Yield strength	f_y	=	355 MPa			
Young's modulus	E	=	210000000 kN/m ²			
Poisson's ratio	ν	=	0.3			
External column						
Axial force	F	=	4354 kN			
Shear force	V	=	1398 kN			
Bending moment	M	=	13664 kNm			
a) Critical meridional (axial) buckling due to axial compression						
Length parameter	ω	=	$\frac{l\sqrt{r}}{r\sqrt{l}} = \frac{l}{\sqrt{rt}}$	0.5r/t=		eq. D.1
		=	6.05490034	227.27273		medium cylinder
Factor	C_x	=	1			eq. D.3-D.10
Elastic critical meridional buckling stress	$\sigma_{x,Rcr}$	=	$0.605EC_x t/r$			eq. D.2
		=	279.51 MPa			
Characteristic imperfection amplitude	Δw_k	=	$\frac{1}{Q}\sqrt{rt}$			eq. D.15
		=	0.00938083 m			
Geometrical reduction factor	α_{xG}	=	0.83			eq. D.14a
Imperfection reduction factor	α_{xl}	=	$\frac{1}{1 + 2.2(\Delta w_k/t)^{0.88}}$			eq. D.14b
		=	0.34336423			
Meridional elastic buckling reduction factor	α_x	=	$\alpha_{xG} \alpha_{xl}$			
		=	0.28499231			
Plastic range factor	β_x	=	$1 - \frac{0.95}{1 + 1.2\Delta w_k/t}$			eq. D.14c
		=	0.53048475			
Interaction exponent	η_x	=	$\frac{5.4}{1 + 4.6\Delta w_k/t}$			eq. D.14d
		=	1.09691594			
Hardening limit	χ_{xh}	=	1			eq. D.14d
Plastic limit relative slenderness	$\bar{\lambda}_p$	=	$\sqrt{\frac{\alpha}{1 - \beta}}$			eq. 8.16
		=	0.77909733			
Squash limit relative slenderness	$\bar{\lambda}_{x0}$	=	0.2			eq. D.16
Meridional shell slenderness parameters	$\bar{\lambda}_x$	=	$\sqrt{f_{yk}/\sigma_{x,Rcr}}$			eq. 8.17
		=	1.12697816			
		$\bar{\lambda}_x$	$\in [\lambda_p, +\infty]$			
Elastic-plastic buckling reduction factor	χ_x	=	0.2243893			eq. 8.13-8.15
Buckling interaction parameter	k_x	=	$1.25 + 0.75\chi_x$			eq. D.46
		=	1.41829197			
Characteristic meridional	$\sigma_{x,Rk}$	=	$\chi_x f_{yk}$			eq. 8.12

11 Stiffened cylindrical shell design for external column (EN1993-1-6 (2017))

Designed by:		Date:			
Checked by:					Reference
buckling stress		=	79.6582		
Partical factor	γ_{M1}	=	1.1		ch. 8.5.2
Meridional design buckling stress	$\sigma_{x,Rd}$	=	$\sigma_{x,Rk}/\gamma_{M1}$		eq. 8.11
		=	72.4165454 MPa		
	r/t	=	454.545455		eq. D.18 Meridional shell buckling checking
		>	$0.03E/f_{yk} =$	17.746479	
Design value of the meridional stress due to axial force	$\sigma_{x,E,A}$	=	$\frac{F}{2\pi r t}$		
		=	12.599284 MPa		
		<	$\sigma_{x,Rd} =$	72.4165454 MPa	OK
b) Critical meridional (axial) buckling due to bending					
Plastic reference moment	$M_{R,pl}$	=	$4r^2 t f_{y,k}$		eq. E.2
		=	390500 kNm		
First dimensionless length	ω	=	$\frac{l}{r} \sqrt{\frac{r}{l}} = \frac{l}{r \sqrt{l}}$		eq. E.5
		=	6.05490034		
Factor	C_m	=	$1 + \frac{4}{\omega^2}$		eq. E.4
		=	1.10910534		
Elastic reference moment	$M_{R,cr}$	=	$1.9 C_m E r t^2$		eq. E.3
		=	267808.575 kNm		
	M_{Ed}	=	13664 kNm		
Reference plastic resistance	R_{pl}	=	$\frac{M_{R,pl}}{M_{Ed}}$		eq. E.13
		=	28.5787471		
Reference elastic critical resistance	R_{cr}	=	$\frac{M_{R,cr}}{M_{Ed}}$		eq. E.13
		=	19.5995737		
Slenderness	$\bar{\lambda}$	=	$\sqrt{\frac{R_{pl}}{R_{cr}}} = \sqrt{\frac{M_{R,pl}}{M_{R,cr}}}$		eq. E.14
		=	1.20753097		
Second dimensionless length	Ω	=	$\frac{L}{r} \sqrt{\frac{t}{r}} = \frac{t}{r} \omega$		eq. E.6
		=	0.01332078		
	ω	<	$0.5 \left(\frac{r}{t}\right)$	=	227.27273 Table E.1
		$0.5 \leq \Omega < 7$			
Geometrical reduction fact	α_G	=	1		Table E.1
	Δw_k	=	$\frac{1}{Q} \sqrt{r t}$		eq. E.8
		=	9.38083152 mm		
Imperfection reduction factor	α_I	=	$\frac{1}{1 + 2(\Delta w_k/t)^{0.8}}$		eq. E.7
		=	0.36221444		
Elastic buckling reduction f	α	=	$\alpha_G \alpha_I$		eq. E.9
		=	0.36221444		
Plastic range factor	β	=	$1 - \frac{0.6}{1 + 1.2(\Delta w_k/t)^{0.8}}$		eq. E.10
		=	0.70823894		

11 Stiffened cylindrical shell design for external column (EN1993-1-6 (2017))						
Designed by:			Date:			
Checked by:						Reference
		η	$= 0.65 + 0.2 \left(\frac{\Delta w_k}{t} \right)$			eq. E.11
			$= 0.82056057$			
Hardening limit		χ_h	$= 1$			eq. E.11
Plastic limit relative slenderness		$\bar{\lambda}_p$	$= \sqrt{\frac{\alpha}{1-\beta}}$			eq. 8.29
			$= 1.11421555$			
Squash limit relative		$\bar{\lambda}_0$	$= 0.3$			eq. E.12
Elastic-plastic buckling reduction factor		$\bar{\lambda}$	$\in [\lambda_p, +\infty]$			eq. 8.26-8.28
		χ	$= 0.24841007$			eq. 8.26-8.28
Characteristic resistance		R_k	$= \chi R_{pl}$			eq. 8.30
			$= 7.09924867$			
Design resistance		R_d	$= R_k / \gamma_{M1}$			eq. 8.31
			$= 6.45386243 >$		1	OK
c) Critical circumferential (hoop) buckling						due to hoop compression
Length parameter		ω	$= \frac{l \sqrt{r}}{r \sqrt{l}} = \frac{l}{\sqrt{rt}}$			eq. D.1
			$= 6.05490034$			
Buckling factors		C_θ	$= 1.26380122$			
		ω/C_θ	$< 1.63r/t =$	740.90909		short cylinder
Elastic critical circumferential buckling stress		$\sigma_{\theta,Rcr}$	$= 0.92E \left(\frac{C_{\theta S}}{\omega} \right) \left(\frac{t}{r} \right)$			eq. D.25
			$= 88.7159229 \text{ MPa}$			
Circumferential elastic imperfection reduction factor		α_θ	$= 0.65$			Table D.5
		r/t	$= 454.545455$			eq. D.27 Circumferential shell buckling checking
			$> 0.21(E/f_{yk})^{0.5} =$	5.1075752		
Circumferential shell slenderness parameters		$\bar{\lambda}_\theta$	$= \sqrt{f_{yk}/\sigma_{\theta,Rcr}}$			eq. 8.17
			$= 2.00038408$			
Circumferential squash limit slenderness		$\bar{\lambda}_{\theta 0}$	$= 0.4$			eq. D.26
Plastic range factor		β	$= 0.6$			eq. D.26
Interaction exponent		η	$= 1$			eq. D.26
Circumferential plastic limit relative slenderness		$\bar{\lambda}_{\theta p}$	$= \sqrt{\alpha_\theta/(1+\beta)}$			eq. 8.16
			$= 0.63737744$			
Buckling reduction factor		$\bar{\lambda}_\theta$	$\in (\bar{\lambda}_p, +\infty)$			eq. 8.13-8.15
		χ_θ	$= \frac{\alpha_\theta}{\bar{\lambda}_\theta^2}$			eq. 8.13-8.15
			$= 0.16243761$			
Buckling interaction parameter		k_θ	$= 1.25 + 0.75\chi_\theta$			eq. D.47
			$= 1.3718282$			
Circumferential characteristic buckling stress		$\sigma_{\theta,Rk}$	$= \chi_\theta f_{yk}$			ch. 8.5.2
			$= 57.6653499 \text{ MPa}$			
Partical factor		γ_{M1}	$= 1.1$			ch. 8.5.2

11 Stiffened cylindrical shell design for external column (EN1993-1-6 (2017))						
Designed by:			Date:			
Checked by:						Reference
Circumferential design buckling stress	$\sigma_{\theta,Rd}$	=	$\sigma_{\theta,Rk}/\gamma_{M1}$			eq. 8.11
		=	52.4230453 MPa			
External water pressure	q_{eq}	=	166.6 kPa			bottom of column
Internal water pressure	q_s	=	70.56 kPa			
Circumferential design stress	$\sigma_{MT\theta}$	=	$(q_{eq}+q_s)(r/t)$			eq. D.30
		=	43.6545455 MPa			
Deformation	w_0	=	$\sigma_{MT\theta}/E$			C.5.3
		=	0.00103939 m			
Ratio of ring area to total area	κ	=	$\frac{A_r}{A_r + (b + 2b_m)t}$			C.5.3
		=	0.34615064			
Deformation	w_r	=	$w_0(1-\kappa)$			C.5.3
		=	0.00067961 m			
Deformation	w	=	$w_r - w_0$			C.5.3
		=	-0.0003598 m			
von Mises equivalent stress of surface stresses	$\sigma_{eq,s}$	=	$k_{eq,s}\sigma_{MT\theta}$			C.5.3
		=	44.0776548			
		<	$\sigma_{\theta,Rd}$	52.4230453 MPa		OK
d) Critical shear buckling						
Length parameter	ω	=	$\frac{l}{r} \sqrt{\frac{r}{l}} = \frac{l}{r\sqrt{l}}$			ch. D.1.4 eq. D.31
		=	$\frac{6.05490034}{8.7r/t}$	<	10	eq. D.33
		<	8.7r/t	=	3954.5455	short cylinder
Factor	C_τ	=	1.0905059			eq. D.34
Elastic critical shear buckling stress	$\tau_{x\theta,Rcr}$	=	$0.75EC_\tau \sqrt{\frac{1}{\omega} \left(\frac{t}{r}\right)}$			eq. D.32
		=	153.559878 MPa			
Shear elastic imperfection reduction factor	α_τ	=	0.65			Table D.6
	r/t	=	454.545455			eq. D.40 Shear shell buckling checking
		>	$0.16(E/f_{yk})^{0.67}$	=	11.517386	
Shell slenderness parameters of shear	$\bar{\lambda}_\tau$	=	$\sqrt{(f_{yk}/\sqrt{3})/\tau_{x\theta,Rcr}}$			eq. 8.17
		=	1.15530056			
Shear squash limit slenderness	$\bar{\lambda}_{\tau 0}$	=	0.4			eq. D.39
Plastic range factor	β	=	0.6			eq. D.39
Interaction exponent	η	=	1			eq. D.39
Shear plastic limit relative slenderness	$\bar{\lambda}_{\tau p}$	=	$\sqrt{\alpha_\tau/(1+\beta)}$			eq. 8.16
		=	0.63737744			
	$\bar{\lambda}_\tau$	∈	$(\bar{\lambda}_{\tau p}, +\infty)$			eq. 8.13-8.15
Buckling reduction factor	χ_τ	=	$\frac{\alpha_\tau}{\bar{\lambda}_\tau^2}$			eq. 8.13-8.15
		=	0.48699375			
Buckling interaction parameter	k_τ	=	$1.75+0.25\chi_\tau$			eq. D.48
		=	1.87174844			
Shear characteristic buckling stress	$\tau_{x\theta,Rk}$	=	$\chi_\tau f_{yk}/\sqrt{3}$			ch. 8.5.2
		=	99.8139208 MPa			

11 Stiffened cylindrical shell design for external column (EN1993-1-6 (2017))							
Designed by:			Date:				
Checked by:							Reference
Partical factor		γ_{M1}	=	1.1			ch. 8.5.2
Shear design buckling resistance stress		$\tau_{x\theta,Rd}$	=	$\tau_{x\theta,Rk}/\gamma_{M1}$			eq. 8.11
			=	90.739928 MPa			
Design value of shear stress		$\tau_{x\theta,Ed}$	=	$Q/(\pi r t)$			
			=	8.09085856 MPa			
			<	$\tau_{x\theta,Rd}$	=	90.739928 MPa	OK
e) Combinations of meridional (axial) compression, circumferential (hoop) compression and shear							ch. D.1.6
Buckling interaction parameter		k_i	=	$(\chi_x \chi_\theta)^2$			eq. D.49
			=	0.00132855			
Interaction check							eq. 8.19
							OK
f) Plastic resistance of ring due to circumferential pressure							
Axial membrane stress		p_x/t	=	$\frac{F}{2\pi r t} + \frac{M}{\pi r^2 t}$			
			=	-28.415234 MPa			
Dimensionless axial stress parameter		S_x	=	$\frac{p_x}{f_y t}$			B.3.3
			=	-0.0800429			
Circumferential membrane stress		$p_n r/t$	=	$(q_{eq} + q_s)(r/t)$			
			=	-43.654545 MPa			
Dimensionless circumferential stress parameter		S_θ	=	$\frac{p_n r}{f_y t}$			B.3.3
			=	-0.1229706			
Dimensionless von Mises equivalent stress parameter		S_e	=	$\sqrt{S_\theta^2 + S_x^2 - S_x S_\theta}$			B.3.3
			=	0.10810043			
Effective length of shell without a ring		l_0	=	$0.975 \sqrt{r t}$			
			=	0.22865777 m			
Factor		A	=	$-S_x - 2S_\theta - 1.5$			B.3.3
			=	-1.174016			
Dimensionless combined stress parameter		S_m	=	$A + \sqrt{A^2 + 4(1 - S_e^2)}$			B.3.3
			=	1.13500344			
Effective length of shell with a ring		l_m	=	$l_0 \left(\frac{S_m}{1 + S_\theta} \right)$			B.3.3
			=	0.29591635 m			
			=	$p_{nR} + p_n(b + 2l_m)$			B.3.3
Resistance of ring			<	$f_y \left(\frac{A_r + (b + 2l_m)t}{r} \right)$			OK
			=	153.36 kN			

12 Stiffened cylindrical shell design for internal column (EN1993-1-6 (2017))						
Designed by:				Date:		
Checked by:						Reference
Design load on the column						Based on BS EN 1993-1-6: 2007+A1: 2017
Distance of ring frames	l	=	2.95	m		
Distance of cylinder	L	=	27	m		
Shell thickness	t	=	12	mm		
Shell Radius	r	=	3	m		
Ring web width	h _r	=	388	mm		
Ring web thickness	t _{wr}	=	3	mm		
Yield strength	f _y	=	355	MPa		
Young's modulus	E	=	210000000	kN/m ²		
Poisson's ratio	ν	=	0.3			
Internal column						
Axial force	F	=	11180	kN		
Shear force	V	=	1005	kN		
Bending moment	M	=	8867	kNm		
a) Critical meridional (axial) buckling due to axial compression						
Length parameter	ω	=	$\frac{l\sqrt{r}}{r\sqrt{l}} = \frac{l}{\sqrt{rt}}$		0.5r/t=	eq. D.1
		=	15.5478652		125	medium cylinder
Factor	C _x	=	1			eq. D.3-D.10
Elastic critical meridional buckling stress	σ _{x,Rcr}	=	0.605EC _x t/r			eq. D.2
		=	508.2	MPa		
Characteristic imperfection amplitude	Δw _k	=	$\frac{1}{Q}\sqrt{rt}$			eq. D.15
		=	0.00758947	m		
Geometrical reduction factor	α _{xG}	=	0.83			eq. D.14a
Imperfection reduction factor	α _{xl}	=	$\frac{1}{1 + 2.2(\Delta w_k/t)^{0.88}}$			eq. D.14b
		=	0.40485178			
Meridional elastic buckling reduction factor	α _x	=	α _{xG} α _{xl}			
		=	0.33602698			
Plastic range factor	β _x	=	$1 - \frac{0.95}{1 + 1.2\Delta w_k/t}$			eq. D.14c
		=	0.45990402			
Interaction exponent	η _x	=	$\frac{5.4}{1 + 4.6\Delta w_k/t}$			eq. D.14d
		=	1.38132307			
Hardening limit	χ _{xh}	=	1			eq. D.14d
Plastic limit relative slenderness	λ _p	=	$\sqrt{\frac{\alpha}{1 - \beta}}$			eq. 8.16
		=	0.78877222			
Squash limit relative slenderness	λ _{x0}	=	0.2			eq. D.16
Meridional shell slenderness parameters	λ _x	=	$\sqrt{f_{yk}/\sigma_{x,Rcr}}$			eq. 8.17
		=	0.83578938			
		λ _x	∈ [λ _p , +∞]			
Elastic-plastic buckling reduction factor	χ _x	=	0.48103919			eq. 8.13-8.15
Buckling interaction parameter	k _x	=	1.25+0.75χ _x			eq. D.46
		=	1.61077939			
Characteristic meridional	σ _{x,Rk}	=	χ _x f _{yk}			eq. 8.12

12 Stiffened cylindrical shell design for internal column (EN1993-1-6 (2017))

Designed by:		Date:			
Checked by:					Reference
buckling stress		=	170.768912		
Partical factor	γ_{M1}	=	1.1		ch. 8.5.2
Meridional design buckling stress	$\sigma_{x,Rd}$	=	$\sigma_{x,Rk}/\gamma_{M1}$		eq. 8.11
		=	155.244465 MPa		
	r/t	=	250		eq. D.18 Meridional shell buckling checking
		>	$0.03E/f_{yk} =$	17.746479	
Design value of the meridional stress due to axial force	$\sigma_{x,E,A}$	=	$\frac{F}{2\pi r t}$		
		=	49.4264518 MPa		
		<	$\sigma_{x,Rd} =$	155.244465 MPa	OK
b) Critical meridional (axial) buckling due to bending					
Plastic reference moment	$M_{R,pl}$	=	$4r^2 t f_{y,k}$		eq. E.2
		=	153360 kNm		
First dimensionless length	ω	=	$\frac{l}{r} \sqrt{\frac{r}{t}} = \frac{l}{r \sqrt{t}}$		eq. E.5
		=	15.5478652		
Factor	C_m	=	$1 + \frac{4}{\omega^2}$		eq. E.4
		=	1.01654697		
Elastic reference moment	$M_{R,cr}$	=	$1.9 C_m E r t^2$		eq. E.3
		=	175269.967 kNm		
	M_{Ed}	=	8867 kNm		
Reference plastic resistance	R_{pl}	=	$\frac{M_{R,pl}}{M_{Ed}}$		eq. E.13
		=	17.2955904		
Reference elastic critical resistance	R_{cr}	=	$\frac{M_{R,cr}}{M_{Ed}}$		eq. E.13
		=	19.7665465		
Slenderness	$\bar{\lambda}$	=	$\sqrt{\frac{R_{pl}}{R_{cr}}} = \sqrt{\frac{M_{R,pl}}{M_{R,cr}}}$		eq. E.14
		=	0.93541062		
Second dimensionless length	Ω	=	$\frac{L}{r} \sqrt{\frac{t}{r}} = \frac{t}{r} \omega$		eq. E.6
		=	0.06219146		
	ω	<	$0.5 \left(\frac{r}{t}\right)$	=	125
		$0.5 \leq \Omega < 7$			Table E.1
Geometrical reduction fact	α_G	=	1		Table E.1
	Δw_k	=	$\frac{1}{Q} \sqrt{r t}$		eq. E.8
		=	7.58946638 mm		
Imperfection reduction factor	α_1	=	$\frac{1}{1 + 2(\Delta w_k/t)^{0.8}}$		eq. E.7
		=	0.41906061		
Elastic buckling reduction f	α	=	$\alpha_G \alpha_1$		eq. E.9
		=	0.41906061		
Plastic range factor	β	=	$1 - \frac{0.6}{1 + 1.2(\Delta w_k/t)^{0.8}}$		eq. E.10
		=	0.67244864		

12 Stiffened cylindrical shell design for internal column (EN1993-1-6 (2017))								
Designed by:				Date:				
Checked by:							Reference	
		η	=	$0.65 + 0.2\left(\frac{\Delta w_k}{t}\right)$			eq. E.11	
			=	0.77649111				
Hardening limit		χ_h	=	1			eq. E.11	
Plastic limit relative slenderness		$\bar{\lambda}_p$	=	$\sqrt{\frac{\alpha}{1-\beta}}$			eq. 8.29	
			=	1.13109404				
Squash limit relative		$\bar{\lambda}_0$	=	0.3			eq. E.12	
Elastic-plastic buckling reduction factor		$\bar{\lambda}$	∈	$[\lambda_0, \lambda_p]$			eq. 8.26-8.28	
		χ	=	0.4540868			eq. 8.26-8.28	
Characteristic resistance		R_k	=	χR_{pl}			eq. 8.30	
			=	7.85369927				
Design resistance		R_d	=	R_k/γ_{M1}			eq. 8.31	
			=	7.13972661 >		1	OK	
c) Critical circumferential (hoop) buckling								due to hoop compression
Length parameter		ω	=	$\frac{l}{r} \sqrt{\frac{r}{l}} = \frac{l}{\sqrt{rt}}$			eq. D.1	
			=	15.5478652				
Buckling factors		C_θ	=	1.07385259				
		ω/C_θ	<	$1.63r/t$	=	407.5	short cylinder	
Elastic critical circumferential buckling stress		$\sigma_{\theta,Rcr}$	=	$0.92E \left(\frac{C_{\theta S}}{\omega}\right) \left(\frac{t}{r}\right)$			eq. D.25	
			=	53.3753844 MPa				
Circumferential elastic imperfection reduction factor		α_θ	=	0.65			Table D.5	
r/t			=	250			eq. D.27 Circumferential shell buckling checking	
			>	$0.21(E/f_{yk})^{0.5} =$		5.1075752		
Circumferential shell slenderness parameters		$\bar{\lambda}_\theta$	=	$\sqrt{f_{yk}/\sigma_{\theta,Rcr}}$			eq. 8.17	
			=	2.57895443				
Circumferential squash limit slenderness		$\bar{\lambda}_{\theta 0}$	=	0.4			eq. D.26	
Plastic range factor		β	=	0.6			eq. D.26	
Interaction exponent		η	=	1			eq. D.26	
Circumferential plastic limit relative slenderness		$\bar{\lambda}_{\theta p}$	=	$\sqrt{\alpha_\theta/(1+\beta)}$			eq. 8.16	
			=	0.63737744				
Buckling reduction factor		$\bar{\lambda}_\theta$	∈	$(\bar{\lambda}_p, +\infty)$			eq. 8.13-8.15	
		χ_θ	=	$\frac{\alpha_\theta}{\bar{\lambda}_\theta^2}$			eq. 8.13-8.15	
			=	0.09772958				
Buckling interaction parameter		k_θ	=	$1.25+0.75\chi_\theta$			eq. D.47	
			=	1.32329718				
Circumferential characteristic buckling stress		$\sigma_{\theta,Rk}$	=	$\chi_\theta f_{yk}$			ch. 8.5.2	
			=	34.6939999 MPa				
Partical factor		γ_{M1}	=	1.1			ch. 8.5.2	

12 Stiffened cylindrical shell design for internal column (EN1993-1-6 (2017))

Designed by:		Date:			
Checked by:					Reference
Circumferential design buckling stress	$\sigma_{\theta,Rd}$	= $\sigma_{\theta,Rk}/\gamma_{M1}$ = 31.5399999 MPa			eq. 8.11
External water pressure	q_{eq}	= 166.6 kPa			bottom of column
Internal water pressure	q_s	= 70.56 kPa			
Circumferential design stress	$\sigma_{MT\theta}$	= $(q_{eq}+q_s)(r/t)$ = 24.01 MPa			eq. D.30
Deformation	w_0	= $\sigma_{MT\theta}r/E$ = 0.000343 m			C.5.3
Ratio of ring area to total area	κ	= $\frac{A_r}{A_r + (b + 2b_m)t}$ = 0.24542656			C.5.3
Deformation	w_r	= $w_0(1-\kappa)$ = 0.00025882 m			C.5.3
Deformation	w	= $w_r - w_0$ = -8.418E-05 m			C.5.3
von Mises equivalent stress of surface stresses	$\sigma_{eq,s}$	= $k_{eq,s}\sigma_{MT\theta}$ = 24.1749954			C.5.3
		< $\sigma_{\theta,Rd}$ = 31.5399999 MPa			OK
d) Critical shear buckling					
Length parameter	ω	= $\frac{l}{r} \sqrt{\frac{r}{l}} = \frac{l}{r\sqrt{l}} = \frac{l}{\sqrt{r}l}$ = $\frac{15.54786652}{8.7r/t} > 10$			ch. D.1.4 eq. D.31
Factor	C_τ	= 1		2175	eq. D.33 medium cylinder
Elastic critical shear buckling stress	$\tau_{x\theta,Rcr}$	= $0.75EC_\tau \sqrt{\frac{1}{\omega} \left(\frac{t}{r}\right)}$ = 159.773654 MPa			eq. D.34 eq. D.32
Shear elastic imperfection reduction factor	α_τ	= 0.65			Table D.6
	r/t	= 250 > $0.16(E/f_{yk})^{0.67} = 11.517386$			eq. D.40 Shear shell buckling checking
Shell slenderness parameters of shear	$\bar{\lambda}_\tau$	= $\sqrt{(f_{yk}/\sqrt{3})/\tau_{x\theta,Rcr}}$ = 1.13261232			eq. 8.17
Shear squash limit slenderness	$\bar{\lambda}_{\tau 0}$	= 0.4			eq. D.39
Plastic range factor	β	= 0.6			eq. D.39
Interaction exponent	η	= 1			eq. D.39
Shear plastic limit relative slenderness	$\bar{\lambda}_{\tau p}$	= $\sqrt{\alpha_\tau/(1+\beta)}$ = 0.63737744			eq. 8.16
	$\bar{\lambda}_\tau$	$\in (\bar{\lambda}_p, +\infty)$			eq. 8.13-8.15
Buckling reduction factor	χ_τ	= $\frac{\alpha_\tau}{\bar{\lambda}_\tau^2}$ = 0.50669988			eq. 8.13-8.15
Buckling interaction parameter	k_τ	= $1.75+0.25\chi_\tau$ = 1.87667497			eq. D.48
Shear characteristic buckling stress	$\tau_{x\theta,Rk}$	= $\chi_\tau f_{yk}/\sqrt{3}$ = 103.852875 MPa			ch. 8.5.2

12 Stiffened cylindrical shell design for internal column (EN1993-1-6 (2017))

Designed by:		Date:			
Checked by:					Reference
Partical factor	γ_{M1}	=	1.1		ch. 8.5.2
Shear design buckling resistance stress	$\tau_{x\theta,Rd}$	=	$\tau_{x\theta,Rk}/\gamma_{M1}$ = 94.4117044 MPa		eq. 8.11
Design value of shear stress	$\tau_{x\theta,Ed}$	=	$Q/(\pi r t)$ = 8.88615099 MPa		
		<	$\tau_{x\theta,Rd}$ = 94.4117044 MPa		OK
e) Combinations of meridional (axial) compression, circumferential (hoop) compression and shear					ch. D.1.6
Buckling interaction parameter	k_i	=	$(\chi_x \chi_\theta)^2$ = 0.00221011		eq. D.49
Interaction check					eq. 8.19
			$\left(\frac{\sigma_{x,Ed}}{\sigma_{x,Rd}}\right)^{k_x} - k_i \left(\frac{\sigma_{x,Ed}}{\sigma_{x,Rd}}\right) \left(\frac{\sigma_{\theta,Ed}}{\sigma_{\theta,Rd}}\right) + \left(\frac{\sigma_{\theta,Ed}}{\sigma_{\theta,Rd}}\right)^{k_\theta} + \left(\frac{\tau_{x\theta,Ed}}{\tau_{x\theta,Rd}}\right)^{k_\tau}$		
		=	0.99278815		OK
f) Plastic resistance of ring due to circumferential pressure					
Axial membrane stress	p_x/t	=	$\frac{F}{2\pi r t} + \frac{M}{\pi r^2 t}$ = -75.560283 MPa		
Dimensionless axial stress parameter	S_x	=	$\frac{p_x}{f_y t}$ = -0.2128459		B.3.3
Circumferential membrane stress	$p_n r/t$	=	$(q_{eq} + q_s)(r/t)$ = -24.01 MPa		
Dimensionless circumferential stress parameter	S_θ	=	$\frac{p_n r}{f_y t}$ = -0.0676338		B.3.3
Dimensionless von Mises equivalent stress parameter	S_e	=	$\sqrt{S_\theta^2 + S_x^2 - S_x S_\theta}$ = 0.18836698		B.3.3
Effective length of shell without a ring	l_0	=	$0.975\sqrt{r t}$ = 0.18499324 m		
Factor	A	=	$-S_x - 2S_\theta - 1.5$ = -1.1518865		B.3.3
Dimensionless combined stress parameter	S_m	=	$A + \sqrt{A^2 + 4(1 - S_e^2)}$ = 1.12515412		B.3.3
Effective length of shell with a ring	l_m	=	$l_0 \left(\frac{S_m}{1 + S_\theta}\right)$ = 0.2232448 m		B.3.3
Resistance of ring	$p_{nR} + p_n(b + 2l_m)$	=	106.600956 kN		B.3.3
		<	$f_y \left(\frac{A_r + (b + 2l_m)t}{r}\right)$ = 137.74 kN		OK

REFERENCE

- ABDALLAH, I., NATARAJAN, A. & SØRENSEN, J. D. 2016. Influence of the control system on wind turbine loads during power production in extreme turbulence: Structural reliability. *Renewable Energy*, 87, 464-477.
- ABS 2020. Guide for Building and Classing Floating Offshore Wind Turbines. USA: American Bureau of Shipping.
- ABS 2021. Floating Offshore Wind Turbine Development Assessment. Washington: American Bureau of Shipping.
- ADAM, F., MYLAND, T., DAHLHAUS, F. & GROßMANN, J. 2015. GICON®-TLP for wind turbines – the path of development. 651-656.
- ADAM, F., MYLAND, T., SCHULDT, B., GROSSMANN, J. & DAHLHAUS, F. 2014. Evaluation of internal force superposition on a TLP for wind turbines. *Renewable Energy*, 71, 271-275.
- ANDRIANOV, I. V., VERBONOL, V. M. & AWREJCEWICZ, J. 2006. Buckling analysis of discretely stringer-stiffened cylindrical shells. *International Journal of Mechanical Sciences*, 48, 1505-1515.
- API 2014. Recommended practice for planning, designing and constructing fixed offshore platforms-working stress design, API Recommended Practice 2A WSD (RP 2A WSD). Washington: API.
- ARANY, L., BHATTACHARYA, S., MACDONALD, J. & HOGAN, S. J. 2017. Design of monopiles for offshore wind turbines in 10 steps. *Soil Dynamics and Earthquake Engineering*, 92, 126-152.
- ASGARIAN, B., AGHAEIDOOST, V. & SHOKRGOZAR, H. R. 2016. Damage detection of jacket type offshore platforms using rate of signal energy using wavelet packet transform. *Marine Structures*, 45, 1-21.
- AUBAULT, A., ALVES, M., SARMENTO, A., RODDIER, D. & PEIFFER, A. 2011. Modeling of an Oscillating Water Column on the Floating Foundation Windfloat. *the ASME 2011 30th International Conference on Ocean, Offshore and Arctic Engineering*. Rotterdam, The Netherlands.
- AUBAULT, A., CERMELLI, C., RODDIER, D., YU, B. B., NARAYANAN, S. & LAHIJANIAN, A. 2018. *Floating wind turbine platform structure with optimized transfer of wave and wind loads*. USA patent application.
- AZCONA, J., BOUCHOTROUCH, F., GONZÁLEZ, M., GARCIA DÍA, J., MUNDUATE, X., KELBERLAU, F. & NYGAARD, T. A. 2014. Aerodynamic Thrust Modelling in Wave Tank Tests of Offshore Floating Wind Turbines Using a Ducted Fan. *Journal of Physics: Conference Series*, 524, 012089.
- BAKICA, A., MALENICA, Š. & VLADIMIR, N. 2020. Hydro-structure coupling of CFD and FEM - Quasi-static approach. *Ocean Engineering*, 217.

- BENITZ, M. A., SCHMIDT, D. P., LACKNER, M. A., STEWART, G. M., JONKMAN, J. & ROBERTSON, A. 2014. Comparison of Hydrodynamic Load Predictions between Reduced Order Engineering Models and Computational Fluid Dynamics for the Oc4-Deepcwind Semi-submersible. *ASME 2014 33rd International Conference on Ocean, Offshore and Arctic Engineering*. San Francisco, California, USA.
- BENITZ, M. A., SCHMIDT, D. P., LACKNER, M. A., STEWART, G. M., JONKMAN, J. & ROBERTSON, A. 2015. Validation of Hydrodynamic Load Models Using CFD for the OC4-DeepCwind Semisubmersible. *ASME 2015 34th International Conference on Ocean, Offshore and Arctic Engineering*. St. John's, Newfoundland, Canada.
- BENTO, N. & FONTES, M. 2019. Emergence of floating offshore wind energy: Technology and industry. *Renewable and Sustainable Energy Reviews*, 99, 66-82.
- BILGILI, M., YASAR, A. & SIMSEK, E. 2011. Offshore wind power development in Europe and its comparison with onshore counterpart. *Renewable and Sustainable Energy Reviews*, 15, 905-915.
- BOMEL 2003. System-based calibration of North West European annex environmental load factors for the ISO fixed steel offshore structures code 19902.
- BORG, M. & COLLU, M. 2015. A comparison between the dynamics of horizontal and vertical axis offshore floating wind turbines. *Philos Trans A Math Phys Eng Sci*, 373.
- BOTS, M. 2020. *Comparison of Potential Flow and CFD for a Column With Heave Plate*. Master, Norwegian University of Science and Technology.
- BRUINSMA, N., PAULSEN, B. T. & JACOBSEN, N. G. 2018. Validation and application of a fully nonlinear numerical wave tank for simulating floating offshore wind turbines. *Ocean Engineering*, 147, 647-658.
- BV 2019. NI 572 Classification and Certification of Floating Offshore Wind Turbines. France: BV(Bureau Veritas).
- BV 2021. NI615 Buckling Assessment of Plated Structures. France: BV(Bureau Veritas).
- CAMPANILE, A., PISCOPO, V. & SCAMARDELLA, A. 2018. Mooring design and selection for floating offshore wind turbines on intermediate and deep water depths. *Ocean Engineering*, 148, 349-360.
- CERIK, B. C. 2015. Ultimate strength of locally damaged steel stiffened cylinders under axial compression. *Thin-Walled Structures*, 95, 138-151.
- CEVASCO, D., COLLU, M., RIZZO, C. M. & HALL, M. 2018. On mooring line tension and fatigue prediction for offshore vertical axis wind turbines: A comparison of lumped mass and quasi-static approaches. *Wind Engineering*, 42, 97-107.
- CHATZIOANNOU, K., KARAMANOS, S. A. & HUANG, Y. 2019. Ultra low-cycle fatigue performance of S420 and S700 steel welded tubular X-joints. *International Journal of Fatigue*, 129.

- CHATZIOANNOU, K., KARAMANOS, S. A. & HUANG, Y. 2021. Coupled numerical simulation of low-cycle fatigue damage in metal components. *Engineering Structures*, 229.
- CHEN, H. & HALL, M. 2022. CFD simulation of floating body motion with mooring dynamics: Coupling MoorDyn with OpenFOAM. *Applied Ocean Research*, 124.
- CHEN, J., HU, Z., LIU, G. & WAN, D. 2019. Coupled aero-hydro-servo-elastic methods for floating wind turbines. *Renewable Energy*, 130, 139-153.
- CHEN, L. & BASU, B. 2018. Fatigue load estimation of a spar-type floating offshore wind turbine considering wave-current interactions. *International Journal of Fatigue*, 116, 421-428.
- CHEN, M., CHEN, K., YOU, Y.-X. & YU, H.-T. 2018. Experimental study of forces on a multi-column floating platform in internal solitary waves. *Applied Ocean Research*, 78, 192-200.
- CHEN, Z., WANG, X., GUO, Y. & KANG, S. 2021. Numerical analysis of unsteady aerodynamic performance of floating offshore wind turbine under platform surge and pitch motions. *Renewable Energy*, 163, 1849-1870.
- CHENG, P., HUANG, Y. & WAN, D. 2019a. A numerical model for fully coupled aero-hydrodynamic analysis of floating offshore wind turbine. *Ocean Engineering*, 173, 183-196.
- CHENG, S. & BECQUE, J. 2016. A design methodology for side wall failure of RHS truss X-joints accounting for compressive chord pre-load. *Engineering Structures*, 126, 689-702.
- CHENG, Z., MADSEN, H. A., CHAI, W., GAO, Z. & MOAN, T. 2017. A comparison of extreme structural responses and fatigue damage of semi-submersible type floating horizontal and vertical axis wind turbines. *Renewable Energy*, 108, 207-219.
- CHENG, Z., WEN, T. R., ONG, M. C. & WANG, K. 2019b. Power performance and dynamic responses of a combined floating vertical axis wind turbine and wave energy converter concept. *Energy*, 171, 190-204.
- CHEW, K.-H., TAI, K., NG, E. Y. K. & MUSKULUS, M. 2015. Optimization of Offshore Wind Turbine Support Structures Using an Analytical Gradient-based Method. *Energy Procedia*, 80, 100-107.
- COILE, R. V. 2015. *Reliability-Based Decision Making for Concrete Elements Exposed to Fire*. PhD, University of Gent.
- CORIGLIANO, P., EPASTO, G., GUGLIELMINO, E. & RISITANO, G. 2017. Fatigue analysis of marine welded joints by means of DIC and IR images during static and fatigue tests. *Engineering Fracture Mechanics*, 183, 26-38.
- DIAZ-CASAS, L. C.-S. 2016. *Floating Offshore Wind Farms*, Springer International Publishing.

- DIN 2005. Baugrund Sicherheitsnachweise im Erd und Guntbau, DIN 1054. Berlin, Germany: DIN.
- DING, Q. 2019. *Research on dynamic response of floating wind turbine platform under the coupling effect of wind, wave and its stability improvement*. Doctor of Philosophy, University of Shanghai for Science and Technology.
- DING, R., LIU, C. R., ZHANG, H. C., XU, D. L., SHI, Q. J., YAN, D. L., YANG, W. Y., CHEN, W. P. & WU, Y. S. 2020. Experimental investigation on characteristic change of a scale-extendable chain-type floating structure. *Ocean Engineering*, 213.
- DNVGL-RP-C202 2019. DNVGL-RP-C202 Buckling strength of shells. DNV GL.
- DNVGL-RP-C203 2016. DNVGL-RP-C203 Fatigue design of offshore steel structures. DNV GL.
- DNVGL-RP-C205 2020. DNVGL-RP-C205 Environmental conditions and environmental loads. DNV GL.
- DNVGL-ST-0119 2018. DNVGL-ST-0119 Floating wind turbine structures. DNV GL.
- DNVGL-ST-0126 2018. Support structures for wind turbines. DNVGL.
- DNVGL 2010. DNV-RP-C201 Buckling strength of plated structures. Norway: Det Norske Veritas.
- DNVGL 2015. DNVGL-OS-C102 Structural design of offshore ships. Oslo, Norway: DNVGL.
- DNVGL 2016. DNVGL-RP-0416 Corrosion protection for wind turbines. Norway: DNVGL.
- DNVGL 2019. DNVGL-OS-B101 Metallic materials. Norway: DNVGL.
- DNVGL 2020. DNVGL-OS-C401 Fabrication and testing of offshore structures. Norway: DNVGL.
- DO, Q. T., HUYNH, V. V., CHO, S.-R., VU, M. T., VU, Q.-V. & THAI, D.-K. 2021. Residual ultimate strength formulations of locally damaged steel stiffened cylinders under combined loads. *Ocean Engineering*, 225.
- DONG, J., VIRÉ, A., FERREIRA, C. S., LI, Z. & VAN BUSSEL, G. 2019. A Modified Free Wake Vortex Ring Method for Horizontal-Axis Wind Turbines. *Energies*, 12.
- DOSE, B., RAHIMI, H., HERRÁEZ, I., STOEVE SANDT, B. & PEINKE, J. 2018. Fluid-structure coupled computations of the NREL 5 MW wind turbine by means of CFD. *Renewable Energy*, 129, 591-605.
- ECCS 2013. Buckling of steel shells-European design recommendations. Multicomp Lda, Mem Martins: European design recommendations.

- EDWARDS, E. C., HOLCOMBE, A., BROWN, S., RANSLEY, E., HANN, M. & GREAVES, D. 2023. Evolution of floating offshore wind platforms: A review of at-sea devices. *Renewable and Sustainable Energy Reviews*, 183.
- EN1990 2005. Eurocode-Basis of structural design. Brussels.
- EN1993-1-1 2005. EN 1993-1-1 (2005): Eurocode 3: Design of steel structures. Brussels: European Committee for Standardization (CEN).
- EN1993-1-6 2007. Eurocode 3: Design of steel structures—part 1-6: Strength and stability of shell structures. Brussels: European Committee Standardization.
- EN1993-1-6 2017. Eurocode 3: Design of steel structures—part 1-6: Strength and stability of shell structures. Brussels: The European Committee for Standardization (CEN).
- EN1993-4-1 2007. en.1993.4.1.2007 Design of steel structures silos. Brussels: European Committee Standardization.
- EN1993-4-2 2007. en.1993.4.2.2007 Design of steel structures tank. Brussels: European Committee Standardization.
- EN 2005. EN 1993-1-9 (2005): Eurocode 3: Design of steel structures - Part 1-9: Fatigue. Brussels: EN (The European Union).
- EN 2006. EN 1993-1-5 (2006): Eurocode 3: Design of steel structures - Part 1-5: General rules - Plated structural elements. Brussels: The European Union.
- EN 2007. EN 1993-1-7 (2007): Eurocode 3: Design of steel structures - Part 1-7: Strength and stability of planar plated structures subject to out of plane loading. Brussels: The European Union.
- EVKIN, A., KRASOVSKY, V., LYKHACHOVA, O. & MARCHENKO, V. 2019. Local buckling of axially compressed cylindrical shells with different boundary conditions. *Thin-Walled Structures*, 141, 374-388.
- EVKIN, A. & LYKHACHOVA, O. 2021. Energy barrier method for estimation of design buckling load of axially compressed elasto-plastic cylindrical shells. *Thin-Walled Structures*, 161.
- EWEA 2013. Deep water The next step for offshore wind energy. Brussels, Belgium: European Wind Energy Association.
- FAIZI, K., FARAMARZI, A., DIRAR, S. & CHAPMAN, D. 2019. Investigating the monotonic behaviour of hybrid tripod suction bucket foundations for offshore wind towers in sand. *Applied Ocean Research*, 89, 176-187.
- FAJUYITAN, O. K., SADOWSKI, A. J. & ROTTER, J. M. 2015. A Study of Imperfect Cylindrical Steel Tube under Global Bending and Varying Support Conditions. *Eighth International Conference on Advances in steel structures*. Lisbon, Portugal.
- FAJUYITAN, O. K., SADOWSKI, A. J., WADEE, M. A. & ROTTER, J. M. 2018. Nonlinear behaviour of short elastic cylindrical shells under global bending. *Thin-Walled Structures*, 124, 574-587.

- FARRUGIA, R., SANT, T. & MICALLEF, D. 2016. A study on the aerodynamics of a floating wind turbine rotor. *Renewable Energy*, 86, 770-784.
- FATEMI, S. M., SHOWKATI, H. & MAALI, M. 2013. Experiments on imperfect cylindrical shells under uniform external pressure. *Thin-Walled Structures*, 65, 14-25.
- FELIX-GONZALEZ, I. & MERCIER, R. S. 2016. Optimized design of statically equivalent mooring systems. *Ocean Engineering*, 111, 384-397.
- FROUDE, R. E. 1889. On the Part Played in Propulsion by Difference in Pressure. *Transactions of the Institution of Naval Architects*, 390-423.
- GAO, B., YE, G., ZHANG, Q., XIE, Y. & YAN, B. 2021. Numerical simulation of suction bucket foundation response located in liquefiable sand under earthquakes. *Ocean Engineering*, 235.
- GARZÓN-ROCA, J., ADAM, J. M., CALDERÓN, P. A. & VALENTE, I. B. 2012. Finite element modelling of steel-caged RC columns subjected to axial force and bending moment. *Engineering Structures*, 40, 168-186.
- GHAFAARI, H. R., GHASSEMI, H. & HE, G. 2021. Numerical study of the Wavestar wave energy converter with multi-point-absorber around DeepCwind semisubmersible floating platform. *Ocean Engineering*, 232.
- GOUPEE, A. J., KOO, B. J., KIMBALL, R. W., LAMBRAKOS, K. F. & DAGHER, H. J. 2014. Experimental Comparison of Three Floating Wind Turbine Concepts. *Journal of Offshore Mechanics and Arctic Engineering*, 136.
- GUPTA, B. K. & BASU, D. 2020. Offshore wind turbine monopile foundations: Design perspectives. *Ocean Engineering*, 213.
- HäFELE, J., GEBHARDT, C. G. & ROLFES, R. 2019. A comparison study on jacket substructures for offshore wind turbines based on optimization. *Wind Energy Science*, 4, 23-40.
- HäFELE, J., HÜBLER, C., GEBHARDT, C. G. & ROLFES, R. 2018. A comprehensive fatigue load set reduction study for offshore wind turbines with jacket substructures. *Renewable Energy*, 118, 99-112.
- HAN, Y., LE, C., DING, H., CHENG, Z. & ZHANG, P. 2017. Stability and dynamic response analysis of a submerged tension leg platform for offshore wind turbines. *Ocean Engineering*, 129, 68-82.
- HAN, Z., ZHAO, Y., SU, J., HE, Y., XU, Y., WU, F. & JIANG, Z. 2022. On the hydrodynamic responses of a multi-column TLP floating offshore wind turbine model. *Ocean Engineering*, 253.
- HAO, E. & LIU, C. 2017. Evaluation and comparison of anti-impact performance to offshore wind turbine foundations: Monopile, tripod, and jacket. *Ocean Engineering*, 130, 218-227.

- HEGSETH, J. M. & BACHYNSKI, E. E. 2019. A semi-analytical frequency domain model for efficient design evaluation of spar floating wind turbines. *Marine Structures*, 64, 186-210.
- HERONEMUS, W. E. 1972. *Pollution-free energy from the offshore winds*, Washington, D.C., Marine Technology Society.
- HIRDARIS, S. E., BAI, W., DESSI, D., ERGIN, A., GU, X., HERMUNDSTAD, O. A., HUIJSMANS, R., IJIMA, K., NIELSEN, U. D., PARUNOV, J., FONSECA, N., PAPANIKOLAOU, A., ARGYRIADIS, K. & INCECIK, A. 2014. Loads for use in the design of ships and offshore structures. *Ocean Engineering*, 78, 131-174.
- HU, R., LE, C., ZHANG, P. & DING, H. 2022. Hydrodynamic modeling effect analysis of a fully submerged tension leg concept integrating the DTU 10 MW offshore wind turbine. *Marine Structures*, 83.
- HU, Z.-Q., LIU, Y. & WANG, J. 2016. An integrated structural strength analysis method for Spar type floating wind turbine. *China Ocean Engineering*, 30, 217-230.
- HUANG, S., JIAO, J. & GUEDES SOARES, C. 2022. Uncertainty analyses on the CFD–FEA co-simulations of ship wave loads and whipping responses. *Marine Structures*, 82.
- HUSSEIN, K. R., HUSSEIN, A. W., HEGAZY, E. H. & AMIN, A. A. 2013. *Structural design of a floating foundation for offshore wind turbines in red sea*, Boca Raton, Crc Press-Taylor & Francis Group.
- IET 2019. PD IEC TS 61400-3-2-2019 Wind energy generation systems Part 3-2: Design requirements for floating offshore wind turbines. UK: International Electrotechnical Commission.
- IFAYEFUNMI, O. 2016. Buckling behavior of axially compressed cylindrical shells: Comparison of theoretical and experimental data. *Thin-Walled Structures*, 98, 558-564.
- ISHIHARA, T. 2016. *The challenge to the world's first floating wind farm* [Online]. Tokyo: The University of Tokyo. [Accessed].
- ISHIHARA, T. & ZHANG, S. 2019. Prediction of dynamic response of semi-submersible floating offshore wind turbine using augmented Morison's equation with frequency dependent hydrodynamic coefficients. *Renewable Energy*, 131, 1186-1207.
- ISO 2013. ISO 898-1: 2013 Mechanical properties of fasteners made of carbon steel and alloy steel-Part 1: Bolts, screws and studs with specified property classes-Coarse thread and fine pitch thread. Switzerland: ISO (International Standard).
- ISO 2020. ISO 19902:2020 Petroleum and natural gas industries — Fixed steel offshore structures. Switzerland: ISO (International Standard).
- J. MORISON, J. J., S. SCHAAF 1950. The Force Exerted by Surface Waves on Piles. *Journal of Petroleum Technology*, 2, 149-154.

- JAWAD, M. H. 2004. *Design of plate and shell structures*, New York, USA, The American Society of Mechanical Engineers.
- JCSS 2021. JCSS (Joint Committee on Structural Safety) probabilistic model code.
- JEON, M., LEE, S. & LEE, S. 2014. Unsteady aerodynamics of offshore floating wind turbines in platform pitching motion using vortex lattice method. *Renewable Energy*, 65, 207-212.
- JESSEN, K., LAUGESEN, K., M. MORTENSEN, S., K. JENSEN, J. & N. SOLTANI, M. 2019. Experimental Validation of Aero-Hydro-Servo-Elastic Models of a Scaled Floating Offshore Wind Turbine. *Applied Sciences*, 9.
- JIANG, X., DAY, S., CLELLAND, D. & LIANG, X. 2019. Analysis and real-time prediction of the full-scale thrust for floating wind turbine based on artificial intelligence. *Ocean Engineering*, 175, 207-216.
- JIANG, Z. 2021. Installation of offshore wind turbines: A technical review. *Renewable and Sustainable Energy Reviews*, 139.
- JIAO, J., HUANG, S. & GUEDES SOARES, C. 2021. Viscous fluid–flexible structure interaction analysis on ship springing and whipping responses in regular waves. *Journal of Fluids and Structures*, 106.
- JIN, S., CHENG, P., SANEIAN, M. & BAI, Y. 2021. Mechanical behavior of thin tubes under combined axial compression and bending. *Thin-Walled Structures*, 159.
- JOHNSTON, B., FOLEY, A., DORAN, J. & LITTLER, T. 2020. Levelised cost of energy, A challenge for offshore wind. *Renewable Energy*, 160, 876-885.
- JONKMAN, J., BUTTERFIELD, S., MUSIAL, W. & SCOTT, G. 2009. Definition of a 5-MW Reference Wind Turbine for Offshore System Development. Golden, CO, USA: National Renewable Energy Laboratory.
- KARIMIRAD, M. & MICHAELIDES, C. 2015. V-shaped semisubmersible offshore wind turbine: An alternative concept for offshore wind technology. *Renewable Energy*, 83, 126-143.
- KAVEH, A. & SABETI, S. 2018. Structural optimization of jacket supporting structures for offshore wind turbines using colliding bodies optimization algorithm. *The Structural Design of Tall and Special Buildings*, 27.
- KHALID, S.-S., ZHANG, L., ZHANG, X.-W. & SUN, K. 2013. Three-dimensional numerical simulation of a vertical axis tidal turbine using the two-way fluid structure interaction approach. *Journal of Zhejiang University SCIENCE A*, 14, 574-582.
- KIM, D. H. & PAIK, J. K. 2017. Ultimate limit state-based multi-objective optimum design technology for hull structural scantlings of merchant cargo ships. *Ocean Engineering*, 129, 318-334.
- KIM, G.-J. & KWAK, H.-G. 2022. Feasibility assessment for design of a circular one-cell concrete submerged floating tunnel structure. *Ocean Engineering*, 245.

- KIM, G.-J., KWAK, H.-G., JIN, C., KANG, H. & CHUNG, W. 2021. Three-dimensional equivalent static analysis for design of submerged floating tunnel. *Marine Structures*, 80.
- KOH, J. H. & NG, E. Y. K. 2016. Downwind offshore wind turbines: Opportunities, trends and technical challenges. *Renewable and Sustainable Energy Reviews*, 54, 797-808.
- KOK HON CHEW, E. Y. K. N. A. K. T. 2014. Offshore Wind Turbine Jacket Substructure: A Comparison Study Between Four-Legged and Three-Legged Designs. *Journal of Ocean and Wind Energy*, 1, 74-81.
- KOO, B., GOUPEE, A. J., LAMBRAKOS, K. & KIMBALL, R. W. 2012. Model Tests for a Floating Windturbine on Three Different Floaters. *OMAE2012, Volume 7, Ocean Renewable Energy*.
- KOPPERSTAD, K. M., KUMAR, R. & SHOELE, K. 2020. Aerodynamic characterization of barge and spar type floating offshore wind turbines at different sea states. *Wind Energy*, 23, 2087-2112.
- KUMAR YADAV, K. & GERASIMIDIS, S. 2019. Instability of thin steel cylindrical shells under bending. *Thin-Walled Structures*, 137, 151-166.
- KVITTEM, M. I. & MOAN, T. 2015. Time domain analysis procedures for fatigue assessment of a semi-submersible wind turbine. *Marine Structures*, 40, 38-59.
- LAMEI, A. & HAYATDAVOODI, M. 2020. On motion analysis and elastic response of floating offshore wind turbines. *Journal of Ocean Engineering and Marine Energy*, 6, 71-90.
- LEE, D.-C., CHO, S., YANG, H.-I., NA, S.-K. & KIM, C.-W. 2020. Load analysis and structural strength evaluation of semi-submersible platform for wind turbines in Jeju Island sea states using hydrodynamic-structure interaction analysis. *Journal of Mechanical Science and Technology*, 34, 1227-1235.
- LEE, H. & LEE, D.-J. 2019. Effects of platform motions on aerodynamic performance and unsteady wake evolution of a floating offshore wind turbine. *Renewable Energy*, 143, 9-23.
- LEE, K., HUQUE, Z., KOMMALAPATI, R. & HAN, S.-E. 2017. Fluid-structure interaction analysis of NREL phase VI wind turbine: Aerodynamic force evaluation and structural analysis using FSI analysis. *Renewable Energy*, 113, 512-531.
- LEE, Y.-S., GONZÁLEZ, J. A., LEE, J. H., KIM, Y. I., PARK, K. C. & HAN, S. 2016. Structural topology optimization of the transition piece for an offshore wind turbine with jacket foundation. *Renewable Energy*, 85, 1214-1225.
- LEFEBVRE, S. & COLLU, M. 2012. Preliminary design of a floating support structure for a 5MW offshore wind turbine. *Ocean Engineering*, 40, 15-26.

- LERCH, M., DE-PRADA-GIL, M., MOLINS, C. & BENVENISTE, G. 2018. Sensitivity analysis on the levelized cost of energy for floating offshore wind farms. *Sustainable Energy Technologies and Assessments*, 30, 77-90.
- LI, C. B. & CHOUNG, J. 2016. Fatigue damage analysis for a floating offshore wind turbine mooring line using the artificial neural network approach. *Ships and Offshore Structures*, 12, S288-S295.
- LI, H. & BACHYNSKI-POLIĆ, E. E. 2021. Validation and application of nonlinear hydrodynamics from CFD in an engineering model of a semi-submersible floating wind turbine. *Marine Structures*, 79.
- LI, H., HU, Z., WANG, J. & MENG, X. 2018a. Short-term fatigue analysis for tower base of a spar-type wind turbine under stochastic wind-wave loads. *International Journal of Naval Architecture and Ocean Engineering*, 10, 9-20.
- LI, H., YANG, S., ZHANG, S., ZHANG, B., JIANG, Z., FENG, H., HAN, P. & LI, J. 2017. Microstructure evolution and mechanical properties of friction stir welding super-austenitic stainless steel S32654. *Materials & Design*, 118, 207-217.
- LI, L., CHENG, Z., YUAN, Z. & GAO, Y. 2018b. Short-term extreme response and fatigue damage of an integrated offshore renewable energy system. *Renewable Energy*, 126, 617-629.
- LI, L., RUZZO, C., COLLU, M., GAO, Y., FAILLA, G. & ARENA, F. 2020a. Analysis of the coupled dynamic response of an offshore floating multi-purpose platform for the Blue Economy. *Ocean Engineering*, 217.
- LI, S. & KIM, D. K. 2022. Ultimate strength characteristics of unstiffened cylindrical shell in axial compression. *Ocean Engineering*, 243.
- LI, X., ZHU, C., FAN, Z., CHEN, X. & TAN, J. 2020b. Effects of the yaw error and the wind-wave misalignment on the dynamic characteristics of the floating offshore wind turbine. *Ocean Engineering*, 199.
- LI, Y., ZHU, Q., LIU, L. & TANG, Y. 2018c. Transient response of a SPAR-type floating offshore wind turbine with fractured mooring lines. *Renewable Energy*, 122, 576-588.
- LI, Z., PASTERNAK, H. & JÄGER-CAÑÁS, A. 2021. Buckling of ring-stiffened cylindrical shell under axial compression: Experiment and numerical simulation. *Thin-Walled Structures*, 164.
- LIAN, J., CHEN, F. & WANG, H. 2014. Laboratory tests on soil–skirt interaction and penetration resistance of suction caissons during installation in sand. *Ocean Engineering*, 84, 1-13.
- LIU, F., LI, H., LI, W. & WANG, B. 2014. Experimental study of improved modal strain energy method for damage localisation in jacket-type offshore wind turbines. *Renewable Energy*, 72, 174-181.

- LIU, L., ZHAO, H., XU, W., YUAN, R. & GUO, Y. 2018. Structural Strength Analysis of a Tri-Floater Floating Foundation for Offshore VAWT. *Journal of Ocean University of China*, 17, 753-762.
- LIU, X., LU, C., LI, G., GODBOLE, A. & CHEN, Y. 2017. Effects of aerodynamic damping on the tower load of offshore horizontal axis wind turbines. *Applied Energy*, 204, 1101-1114.
- LONG, H. & MOE, G. 2012. Preliminary Design of Bottom-Fixed Lattice Offshore Wind Turbine Towers in the Fatigue Limit State by the Frequency Domain Method. *Journal of Offshore Mechanics and Arctic Engineering*, 134.
- LOPEZ-PAVON, C. & SOUTO-IGLESIAS, A. 2015. Hydrodynamic coefficients and pressure loads on heave plates for semi-submersible floating offshore wind turbines: A comparative analysis using large scale models. *Renewable Energy*, 81, 864-881.
- LUAN, C., GAO, Z. & MOAN, T. 2017. Development and verification of a time-domain approach for determining forces and moments in structural components of floaters with an application to floating wind turbines. *Marine Structures*, 51, 87-109.
- LUAN, C., GAO, Z. & MOAN, T. 2018. Comparative analysis of numerically simulated and experimentally measured motions and sectional forces and moments in a floating wind turbine hull structure subjected to combined wind and wave loads. *Engineering Structures*, 177, 210-233.
- M. AGHAJANI DELAVAR, K. B. 2018. Prediction of Local Seismic Damage in Jacket-type Offshore Platforms. *AUT Journal of Civil Engineering*, 2, 241-250.
- MA, J., ZHOU, D., HAN, Z., ZHANG, K., BAO, Y. & DONG, L. 2019a. Fluctuating wind and wave simulations and its application in structural analysis of a semi-submersible offshore platform. *International Journal of Naval Architecture and Ocean Engineering*, 11, 624-637.
- MA, Z., LI, W., REN, N. & OU, J. 2017. The typhoon effect on the aerodynamic performance of a floating offshore wind turbine. *Journal of Ocean Engineering and Science*, 2, 279-287.
- MA, Z., WANG, S., WANG, Y., REN, N. & ZHAI, G. 2019b. Experimental and numerical study on the multi-body coupling dynamic response of a Novel Serbuoys-TLP wind turbine. *Ocean Engineering*, 192.
- MADSEN, F. J., NIELSEN, T. R. L., KIM, T., BREDMOSE, H., PEGALAJAR-JURADO, A., MIKKELSEN, R. F., LOMHOLT, A. K., BORG, M., MIRZAEI, M. & SHIN, P. 2020. Experimental analysis of the scaled DTU10MW TLP floating wind turbine with different control strategies. *Renewable Energy*, 155, 330-346.
- MALEKJAFARIAN, A., JALILVAND, S., DOHERTY, P. & IGOE, D. 2021. Foundation damping for monopile supported offshore wind turbines: A review. *Marine Structures*, 77.

- MARINO, E., GIUSTI, A. & MANUEL, L. 2017. Offshore wind turbine fatigue loads: The influence of alternative wave modeling for different turbulent and mean winds. *Renewable Energy*, 102, 157-169.
- MCA 2020. Construction and outfit standards Part 5 welding. UK: Maritime and Coastguard Agency.
- MEI, X. & XIONG, M. 2021. Effects of Second-Order Hydrodynamics on the Dynamic Responses and Fatigue Damage of a 15 MW Floating Offshore Wind Turbine. *Journal of Marine Science and Engineering*, 9.
- MIAN, H. H., WANG, G., ZHOU, H. & WU, X. 2021. Optimization of thin electric propeller using physics-based surrogate model with space mapping. *Aerospace Science and Technology*, 111.
- MICHAILIDES, C., GAO, Z. & MOAN, T. 2016. Experimental and numerical study of the response of the offshore combined wind/wave energy concept SFC in extreme environmental conditions. *Marine Structures*, 50, 35-54.
- MITRA, A., SARKAR, S., CHAKRABORTY, A. & DAS, S. 2021. Sway vibration control of floating horizontal axis wind turbine by modified spar-torus combination. *Ocean Engineering*, 219.
- MOGHADDAM, B. T., HAMEDANY, A. M., TAYLOR, J., MEHMANPARAST, A., BRENNAN, F., DAVIES, C. M. & NIKBIN, K. 2020. Structural integrity assessment of floating offshore wind turbine support structures. *Ocean Engineering*, 208.
- MULIAWAN, M. J., KARIMIRAD, M. & MOAN, T. 2013. Dynamic response and power performance of a combined Spar-type floating wind turbine and coaxial floating wave energy converter. *Renewable Energy*, 50, 47-57.
- N-004 2004. Norsok standard N-004 Design of steel structures. Norway: Standards Norway.
- N W NICHOLS, R. K., A A RAHMAN, M K M AKRAM & DR K CHEN 2014. Load resistance factor design LRFD calibration of load factors for extreme storm loading in Malaysian waters. *Journal of Marine Engineering & Technology*, 13.
- NATARAJAN, A., STOLPE, M. & NJOMO WANDJI, W. 2019. Structural optimization based design of jacket type sub-structures for 10 MW offshore wind turbines. *Ocean Engineering*, 172, 629-640.
- NEJAD, A. R., BACHYNSKI, E. E., KVITTEM, M. I., LUAN, C., GAO, Z. & MOAN, T. 2015. Stochastic dynamic load effect and fatigue damage analysis of drivetrains in land-based and TLP, spar and semi-submersible floating wind turbines. *Marine Structures*, 42, 137-153.
- NEMATBAKHSH, A., BACHYNSKI, E. E., GAO, Z. & MOAN, T. 2015. Comparison of wave load effects on a TLP wind turbine by using computational fluid dynamics and potential flow theory approaches. *Applied Ocean Research*, 53, 142-154.

- NIKLAS, K. 2017. Strength analysis of a large-size supporting structure for an offshore wind turbine. *Polish maritime research*, 24, 156-165.
- OEST, J., SANDAL, K., SCHAFHIRT, S., STIENG, L. E. S. & MUSKULUS, M. 2018. On gradient-based optimization of jacket structures for offshore wind turbines. *Wind Energy*, 21, 953-967.
- OKULOV, V. L., SØRENSEN, J. N. & WOOD, D. H. 2015. The rotor theories by Professor Joukowski: Vortex theories. *Progress in Aerospace Sciences*, 73, 19-46.
- PARK, S., LACKNER, M. A., CROSS-WHITER, J., TSOUROUKDISSIAN, A. R. & CAVA, W. L. 2016. An Investigation of Passive and Semi-Active Tuned Mass Dampers for a Tension Leg Platform Floating Offshore Wind Turbine in ULS Conditions. *International Conference on Ocean, Offshore and Arctic Engineering*. Busan, South Korea: The American Society of mechanical engineers.
- PEIFFER, A. & RODDIER, D. 2012. Design of an Oscillating Wave Surge Converter on the WindFloat Structure. *4th International Conference on Ocean Energy*. Dublin.
- PÉREZ-COLLAZO, C., GREAVES, D. & IGLESIAS, G. 2015. A review of combined wave and offshore wind energy. *Renewable and Sustainable Energy Reviews*, 42, 141-153.
- PLAZA, B., BARDERA, R. & VISIEDO, S. 2015. Comparison of BEM and CFD results for MEXICO rotor aerodynamics. *Journal of Wind Engineering and Industrial Aerodynamics*, 145, 115-122.
- QI, T., HUANG, X. & LI, L. 2018. Spectral-based fatigue crack propagation prediction for very large floating structures. *Marine Structures*, 57, 193-206.
- QU, X., LI, Y., TANG, Y., CHAI, W. & GAO, Z. 2020. Comparative study of short-term extreme responses and fatigue damages of a floating wind turbine using two different blade models. *Applied Ocean Research*, 97.
- QUINTANA, J. A. 2016. *Alternative Installation Methods for offshore wind substation*. Master, University of Strathclyde.
- RANKINE, W. J. 1865. On the mechanical principles of the action of propellers. *Transaction of the Institute of Naval Architects*, 6, 13-39.
- RAO, M. N., SCHMIDT, R. & SCHRÖDER, K. U. 2015. Geometrically nonlinear static FE-simulation of multilayered magneto-electro-elastic composite structures. *Composite Structures*, 127, 120-131.
- REN, N., MA, Z., FAN, T., ZHAI, G. & OU, J. 2018. Experimental and numerical study of hydrodynamic responses of a new combined monopile wind turbine and a heave-type wave energy converter under typical operational conditions. *Ocean Engineering*, 159, 1-8.
- REN, N., MA, Z., SHAN, B., NING, D. & OU, J. 2020. Experimental and numerical study of dynamic responses of a new combined TLP type floating wind turbine

- and a wave energy converter under operational conditions. *Renewable Energy*, 151, 966-974.
- REZAEI, R., FROMME, P. & DUFFOUR, P. 2018. Fatigue life sensitivity of monopile-supported offshore wind turbines to damping. *Renewable Energy*, 123, 450-459.
- RHODRI JAMES, M. C. R. 2015. Floating offshore wind: market and technology review. UK: The Carbon Trust.
- ROALD, L., JONKMAN, J., ROBERTSON, A. & CHOKANI, N. 2013. The Effect of Second-order Hydrodynamics on Floating Offshore Wind Turbines. *Energy Procedia*, 35, 253-264.
- RODDIER, D., CERMELLI, C., AUBAULT, A. & WEINSTEIN, A. 2010a. WindFloat: A floating foundation for offshore wind turbines. *Journal of Renewable and Sustainable Energy*, 2, 34.
- RODDIER, D., CERMELLI, C. & WEINSTEIN, A. 2010b. Windfloat: A Floating Foundation for Offshore Wind Turbines. *Omae 2009, Vol 4, Pts a and B*, 845-853.
- ROTTER, J. M. 2016. The new method of Reference Resistance Design for shell structures. *Proc. SDSS 2016, International Colloquium on Stability and Ductility of Steel Structures*. Timisoara, Romania.
- RUZZO, C., FIAMMA, V., NAVA, V., COLLU, M., FAILLA, G. & ARENA, F. 2016. Progress on the experimental set-up for the testing of a floating offshore wind turbine scaled model in a field site. *Wind Engineering*, 40, 455-467.
- SANTO, G., PEETERS, M., VAN PAEPEGEM, W. & DEGROOTE, J. 2020. Fluid–Structure Interaction Simulations of a Wind Gust Impacting on the Blades of a Large Horizontal Axis Wind Turbine. *Energies*, 13.
- SARKER, B. R. & FAIZ, T. I. 2016. Minimizing maintenance cost for offshore wind turbines following multi-level opportunistic preventive strategy. *Renewable Energy*, 85, 104-113.
- SHE, G.-L., YUAN, F.-G. & REN, Y.-R. 2017. Nonlinear analysis of bending, thermal buckling and post-buckling for functionally graded tubes by using a refined beam theory. *Composite Structures*, 165, 74-82.
- SHEN, H.-S. 2004. Thermal postbuckling behavior of functionally graded cylindrical shells with temperature-dependent properties. *International Journal of Solids and Structures*, 41, 1961-1974.
- SHEN, H. S. 1998. Postbuckling analysis of stiffened laminated cylindrical shells under combined external liquid pressure and axial compression. *Engineering Structures*, 20, 14.
- SHEN, J. J., LIU, H. J. & CUI, F. 2010. Effect of welding speed on microstructure and mechanical properties of friction stir welded copper. *Materials & Design*, 31, 3937-3942.

- SHI, W., JIANG, J., SUN, K. & JU, Q. 2021. Aerodynamic performance of semi-submersible floating wind turbine under pitch motion. *Sustainable Energy Technologies and Assessments*, 48.
- SHI, W., ZHANG, L., KARIMIRAD, M., MICHAILIDES, C., JIANG, Z. & LI, X. 2023. Combined effects of aerodynamic and second-order hydrodynamic loads for floating wind turbines at different water depths. *Applied Ocean Research*, 130.
- SHI, X. H., ZHANG, J. & GUEDES SOARES, C. 2018. Numerical assessment of experiments on the ultimate strength of stiffened panels with pitting corrosion under compression. *Thin-Walled Structures*, 133, 52-70.
- SHUKLA, A. & KARKI, H. 2016. Application of robotics in offshore oil and gas industry— A review Part II. *Robotics and Autonomous Systems*, 75, 508-524.
- SIMOS, A. N., RUGGERI, F., WATAI, R. A., SOUTO-IGLESIAS, A. & LOPEZ-PAVON, C. 2018. Slow-drift of a floating wind turbine: An assessment of frequency-domain methods based on model tests. *Renewable Energy*, 116, 133-154.
- SONG, C. Y., TENG, J. G. & ROTTER, J. M. 2004. Imperfection sensitivity of thin elastic cylindrical shells subject to partial axial compression. *International Journal of Solids and Structures*, 41, 7155-7180.
- SOUTHWELL, R. V. 1914. V. On the general theory of elastic stability. *Philosophical transactions of the royal society A*, 213, 16.
- SUJA-THAUVIN, L., KROKSTAD, J. R. & BACHYNSKI, E. E. 2018. Critical assessment of non-linear hydrodynamic load models for a fully flexible monopile offshore wind turbine. *Ocean Engineering*, 164, 87-104.
- TANAKA, K., SATO, I., UTSUNOMIYA, T. & KAKUYA, H. 2020. Validation of dynamic response of a 2-MW hybrid-spar floating wind turbine during typhoon using full-scale field data. *Ocean Engineering*, 218.
- TEMAMI, O., AYOUB, A., HAMADI, D. & BENNOUI, I. 2018. Effect of Boundary Conditions on the Behavior of Stiffened and Un-Stiffened Cylindrical Shells. *International Journal of Steel Structures*, 19, 867-878.
- THANG DO, Q., MUTTAQIE, T., PARK, S.-H., SHIN, H. K. & CHO, S.-R. 2018. Ultimate strength of intact and dented steel stringer-stiffened cylinders under hydrostatic pressure. *Thin-Walled Structures*, 132, 442-460.
- TIAN, X., WANG, Q., LIU, G., LIU, Y., XIE, Y. & DENG, W. 2019. Topology optimization design for offshore platform jacket structure. *Applied Ocean Research*, 84, 38-50.
- TOFT, H. S., BRANNER, K., BERRING, P. & SØRENSEN, J. D. 2011. Defect distribution and reliability assessment of wind turbine blades. *Engineering Structures*, 33, 171-180.

- TRAN, T.-T. & KIM, D.-H. 2015. The platform pitching motion of floating offshore wind turbine: A preliminary unsteady aerodynamic analysis. *Journal of Wind Engineering and Industrial Aerodynamics*, 142, 65-81.
- UTSUNOMIYA, T., SATO, T., MATSUKUMA, H. & YAGO, K. 2009. Experimental Validation for Motion of a SPAR-Type Floating Offshore Wind Turbine Using 1/22.5 Scale Model. *OMAE2009, Volume 4, Parts A and B*, 951-959.
- VARDAROGLU, M., GAO, Z., AVOSSA, A. M. & RICCIARDELLI, F. 2022. Validation of a TLP wind turbine numerical model against model-scale tests under regular and irregular waves. *Ocean Engineering*, 256.
- VOLPI, S., DIEZ, M., SADAT-HOSSEINI, H., KIM, D. H., STERN, F., THODAL, R. S. & GRENESTEDT, J. L. 2017. Composite bottom panel slamming of a fast planing hull via tightly coupled fluid-structure interaction simulations and sea trials. *Ocean Engineering*, 143, 240-258.
- VON, M. R. & WINDENBURG, D. F. 1933. The Critical External Pressure of Cylindrical Tubes under Uniform Radial and Axial Load. *David Taylor Model Basin Translation WashintonDC*.
- VON, S. K. & GUNTHER, K. 1952. The strength of cylindrical shells, stiffened by frames and bulkheads, under uniform external pressure on all sides. *David Taylor Model Basin Translation*, 38.
- WALIA, D., SCHÜNEMANN, P., HARTMANN, H., ADAM, F. & GROßMANN, J. 2021. Numerical and Physical Modeling of a Tension-Leg Platform for Offshore Wind Turbines. *Energies*, 14.
- WANG, B., DU, K., HAO, P., TIAN, K., CHAO, Y. J., JIANG, L., XU, S. & ZHANG, X. 2019. Experimental validation of cylindrical shells under axial compression for improved knockdown factors. *International Journal of Solids and Structures*, 164, 37-51.
- WANG, J. & SADOWSKI, A. J. 2018. Elastic imperfect tip-loaded cantilever cylinders of varying length. *International Journal of Mechanical Sciences*, 140, 200-210.
- WANG, J., SADOWSKI, A. J. & ROTTER, J. M. 2018a. Influence of ovalisation on the plastic collapse of thick cylindrical tubes under uniform bending. *International Journal of Pressure Vessels and Piping*, 168, 94-99.
- WANG, K., MOAN, T. & HANSEN, M. O. L. 2016a. Stochastic dynamic response analysis of a floating vertical-axis wind turbine with a semi-submersible floater. *Wind Energy*, 19, 1853-1870.
- WANG, L., KOLIOS, A., LIU, X., VENETSANOS, D. & CAI, R. 2022. Reliability of offshore wind turbine support structures: A state-of-the-art review. *Renewable and Sustainable Energy Reviews*, 161.
- WANG, L., QUANT, R. & KOLIOS, A. 2016b. Fluid structure interaction modelling of horizontal-axis wind turbine blades based on CFD and FEA. *Journal of Wind Engineering and Industrial Aerodynamics*, 158, 11-25.

- WANG, X., YANG, X. & ZENG, X. 2017a. Lateral response of improved suction bucket foundation for offshore wind turbine in centrifuge modelling. *Ocean Engineering*, 141, 295-307.
- WANG, X., YANG, X. & ZENG, X. 2017b. Seismic centrifuge modelling of suction bucket foundation for offshore wind turbine. *Renewable Energy*, 114, 1013-1022.
- WANG, X., ZENG, X., LI, J., YANG, X. & WANG, H. 2018b. A review on recent advancements of substructures for offshore wind turbines. *Energy Conversion and Management*, 158, 103-119.
- WARIS, M. B. & ISHIHARA, T. 2012. Dynamic response analysis of floating offshore wind turbine with different types of heave plates and mooring systems by using a fully nonlinear model. *Coupled Systems Mechanics*, 1, 247-268.
- WEN, B., DONG, X., TIAN, X., PENG, Z., ZHANG, W. & WEI, K. 2018. The power performance of an offshore floating wind turbine in platform pitching motion. *Energy*, 154, 508-521.
- WEN, B., TIAN, X., DONG, X., PENG, Z. & ZHANG, W. 2017. Influences of surge motion on the power and thrust characteristics of an offshore floating wind turbine. *Energy*, 141, 2054-2068.
- WINDENBURG, D. F. & TRILLING, C. 1934. Collapse by instability of thin cylindrical shells under external pressure. *Trans ASME*, 56, 7.
- WINDEUROPE 2018. Offshore wind in Europe key trends and statistics 2017. Brussels, Belgium: WindEurope.
- WINTERSTETTER, T. A. & SCHMIDT, H. 2002. Stability of circular cylindrical steel shells under combined loading. *Thin-Walled Structures*, 40, 893-909.
- WU, X., HU, Y., LI, Y., YANG, J., DUAN, L., WANG, T., ADCOCK, T., JIANG, Z., GAO, Z., LIN, Z., BORTHWICK, A. & LIAO, S. 2019. Foundations of offshore wind turbines: A review. *Renewable and Sustainable Energy Reviews*, 104, 379-393.
- XU, K., GAO, Z. & MOAN, T. 2018. Effect of hydrodynamic load modelling on the response of floating wind turbines and its mooring system in small water depths. *EERA DeepWind'2018, 15th Deep Sea Offshore Wind R&D Conference*.
- XU, K., ZHANG, M., SHAO, Y., GAO, Z. & MOAN, T. 2019. Effect of wave nonlinearity on fatigue damage and extreme responses of a semi-submersible floating wind turbine. *Applied Ocean Research*, 91.
- YANG, H., ZHU, Y., LU, Q. & ZHANG, J. 2015. Dynamic reliability based design optimization of the tripod sub-structure of offshore wind turbines. *Renewable Energy*, 78, 16-25.
- YE, Q., CHENG, S., KIM, B., COLLINS, K. & IGLESIAS, G. 2019. Structural design and assessment of a floating foundation for offshore wind turbines. *ASME 2019 2nd International Offshore Wind Technical Conference*. St. Julian's, Malta.

- YETER, B., GARBATOV, Y. & GUEDES SOARES, C. 2015. Fatigue damage assessment of fixed offshore wind turbine tripod support structures. *Engineering Structures*, 101, 518-528.
- YOUNG, A. C., GOUPEE, A. J., DAGHER, H. J. & VISELLI, A. M. 2017. Methodology for optimizing composite towers for use on floating wind turbines. *Journal of Renewable and Sustainable Energy*, 9, 033305.
- YU, Z. & AMDAHL, J. 2018. Analysis and design of offshore tubular members against ship impacts. *Marine Structures*, 58, 109-135.
- ZHANG, L., SHI, W., KARIMIRAD, M., MICHAILIDES, C. & JIANG, Z. 2020. Second-order hydrodynamic effects on the response of three semisubmersible floating offshore wind turbines. *Ocean Engineering*, 207.
- ZHAO, C., THIES, P. R., YE, Q. & LARS, J. 2021. System integration and coupled effects of an OWT/WEC device. *Ocean Engineering*, 220.
- ZHAO, Y., CHEN, M., YANG, F., ZHANG, L. & FANG, D. 2017. Optimal design of hierarchical grid-stiffened cylindrical shell structures based on linear buckling and nonlinear collapse analyses. *Thin-Walled Structures*, 119, 315-323.
- ZHAO, Z., WANG, W., SHI, W. & LI, X. 2020. Effects of second-order hydrodynamics on an ultra-large semi-submersible floating offshore wind turbine. *Structures*, 28, 2260-2275.
- ZHOU, S., SHAN, B., XIAO, Y., LI, C., HU, G., SONG, X., LIU, Y. & HU, Y. 2017. Directionality Effects of Aligned Wind and Wave Loads on a Y-Shape Semi-Submersible Floating Wind Turbine under Rated Operational Conditions. *Energies*, 10, 2097.
- ZHU, Y., DAI, Y., MA, Q. & TANG, W. 2018. Buckling of externally pressurized cylindrical shell: A comparison of theoretical and experimental data. *Thin-Walled Structures*, 129, 309-316.
- ZOUNTOURIDOU, E. I., KIOKES, G. C., CHAKALIS, S., GEORGILAKIS, P. S. & HATZIARGYRIOU, N. D. 2015. Offshore floating wind parks in the deep waters of Mediterranean Sea. *Renewable and Sustainable Energy Reviews*, 51, 433-448.

PUBLICATIONS

Qi Ye*, Shanshan Cheng, Boksun Kim, Keri Collins, Gregorio Iglesias. Nonlinear structural response of floating offshore wind platforms. *Thin-Walled Structures*. Under review.

Qingsong Liu, Weipao Miao, Qi Ye, Chun Li. 2022. Performance assessment of an innovative Gurney flap for straight-bladed vertical axis wind turbine. *Renewable Energy*, 185, 1124-1138. DOI: 10.1016/j.renene.2021.12.098.

Chenyu Zhao, Philipp R. Thies, Qi Ye*, Johanning Lars. 2021. System integration and coupled effects of an OWT/WEC device. *Ocean Engineering*, 220. DOI: 10.1016/j.oceaneng.2020.108405.

Qi Ye, Shanshan Cheng, Boksun Kim, Keri Collins, Gregorio Iglesias. 2019. Structural design and assessment of a floating foundation for offshore wind turbines [C]. *ASME 2019 2nd International Offshore Wind Technical Conference*. St. Julian's, Malta.

* Corresponding author